SCUOLA DI DOTTORATO
UNIVERSITÀ DEGLI STUDI DI MILANO-BICOCCA

Department of Materials Science

PhD program in Materials Science and Nanotechnology Cycle XXXVI

CERAMIC-IN-POLYMER AND POLYMER-IN-CERAMIC SOLID-STATE ELECTROLYTES FOR LITHIUM-METAL BATTERIES

Surname: Mezzomo Name: Lorenzo

Registration number: 807229

Tutor: Prof. Riccardo Ruffo

Co-tutor: Prof. Piercarlo Mustarelli

Coordinator: Prof. Francesco Montalenti

ACADEMIC YEAR 2022/2023

Contents

1. Abstract:

Even if the continuous improvements experienced by lithium-ion batteries (LIBs) in the past decades have enabled a mass scale production of reliable and performant energy storage devices, the energy density of this system still falls short from the industry requirement, particularly for the specifications required by the automotive sector. Consequently, a lot of interest is currently devoted to the development of new categories of energy storage devices able to store and deliver higher quantities of energy for unit of mass and volume. A promising alternative is represented by lithium metal batteries (LMBs), i.e. rechargeable devices that exploit an anode of metallic lithium in place of the graphitic one commonly employed in LIBs. This replacement greatly improves the gravimetric and volumetric energy density of the batteries, simultaneously enabling the use of high-capacity conversion cathodes such as sulfur.
However, the high reactivity of metallic Li and the inhomogeneous deposition of Li-ions on its surface, which leads to the growth of dangerous dendrites responsible of short-circuiting, are hindering the implementation of LMBs based on liquid electrolytes. As a consequence, great attention is presently directed towards the development of solid state electrolytes (SSEs) that, possessing an improved mechanical stability coupled with reduced flammability, can mitigate the aforementioned shortcomings.
After a brief introduction on the current energy scenario (*Chap. 2*), on lithium batteries (*Chap. 3*), and on the state-of-the-art electrolytes *Chap. 4*), the two different approaches exploited during my PhD project in order to develop more performant and stable SSEs suitable for operation in LMBs will be discussed.
Firstly, ceramic-in-polymer nanocomposite SSEs comprising a polymer matrix and hybrid nanoparticles (NPs), such as SiO_2 and TiO_2 functionalized with short chains of polyethylene glycol (SiO_2@PEG and TiO_2@PEG), will be described in *Chap. 5*. In particular, PEO matrices were employed with both fillers to produce SSEs with an improved stability against dendrite piercing and satisfying cycling properties (*Sec. 5.1* and *Sec. 5.2*). The interaction of the hybrid NPs with the dendrites was investigated, demonstrating the beneficial effect imparted by filler dispersion on the mobility and on the strength of the electrolyte. Additionally, the study of PVdF-HFP based SSEs confirmed the suitability of this polymer as a feasible candidate to produce performant and durable electrolytes (*Sec. 5.3*). After having demonstrated that the presence of residual DMF resulted critical for the conductivity of the system, also the effect of the addition of SiO_2@PFOTES and SiO_2@PEG functionalized fillers was verified.
Secondly, thin solid electrolytes (TSEs) composed by Li_6PS_5Cl (LPSCl) and a polymer binder fabricated using two different manufacturing approaches (tape-casting and calendering) will be presented in *Chap. 6*. After having produced thin polymer-in-ceramic free-standing separators, the impact of these two industrially-relevant productive techniques was verified, particularly focusing on the mechanical properties of the TSEs and

on the possible scalability of the chosen process. Also the effects of variable binder content, needed to improve the processability of sulfide electrolytes, and of increasing densification pressures, required to ensure an intimate inter-particle contacts in the electrolyte, have been thoroughly characterised.
Overall, both filler encompassing into polymer matrix and the incorporation of a binder into a ceramic electrolyte enabled an effective decoupling of the electrochemical and of the mechanical properties of the electrolytes. As it will be described throughout this elaborate, both approaches resulted suitable for the improvements of the features of SSEs for LMBs. While the use of hybrid fillers permitted to overcome the intrinsic softness of polymer SSEs simultaneously improving some electrochemical properties, binder encompassing into ceramic electrolyte permitted to overcome some of the serious issues related to ISEs such as poor processability and bad electrode adhesion without sacrificing the high room temperature conductivity of LPSCl.

2. The energy scenario:

The recent years, characterised by a world pandemic and by Ukraine and Middle East crisis, have somehow exposed all the weaknesses of our current European energetic system, strongly dependent on fossil fuels and foreign countries. Without suitable compelling alternatives, any turmoil on the price of gas and oil in the next years is expected to have an even more severe impact both on the competitiveness of UE industrial sector and on the prices of energy bills for domestic users. Additionally, the present productive system results totally incompatible with the ambitious but necessary targets set by the International Energy Agency (IEA) and by the Intergovernmental Panel on Climate Change (IPCC), which are respectively the goal of Net Zero Emissions (NZE) by 2050 and a 1.5°C limitation of global temperature rising by the same deadline [1, 2].
As perfectly summarized in the introduction of 2022 International Renewable Energy Agency (IRENA) report [3]:

> *"We do not have the luxury of time to deal with each of these challenges separately. We can ill afford to invest in outdated ways of producing, distributing and consuming energy that are neither economical nor future proof."*

Therefore, it becomes necessary to take immediate and extensive actions in order to contrast the actual reliance on any form of polluting and non-renewable source.
Throughout this chapter, an up-to-date world energy scenario is delineated, particularly highlighting the most critical issues and devoting a peculiar attention to renewable energies (RE) and electric vehicles, topics that are expected to drive the demand for energy storage in next decades. Eventually, the future outlooks are outlined in order to present the main guidelines for a sustainable development.

2.1 The current situation:

Global energy demand is continuously experiencing a continuous growth that has only been partially reduced by the recent pandemic. Anyway, the 2020 contraction (-4%) has been more than off-setted by the 2021 recovery (+5.8%) mainly driven by the emerging economies [4]. As shown in *Fig. 2.1*, this quite unstoppable rise has only been occasionally tampered by major world event such as the Global Financial Crisis of 2008 and the aforementioned Covid-19 pandemic.
Moreover, it is possible to notice that the biggest share of primary energy consumption is still dominated by fossil fuels like coal (27.2%), oil (31.3%) and gas (24.6%). Overall, this means that more than the 73% of the global energy consumption is still dependent on these three non renewable sources responsible of greenhouse gases (GHG) emissions such as CO_2, CH_4, N_2O,and fluorinated gases. As a consequence, also the global anthropogenic emissions have experienced a similar uphill trend with a $\sim 2\%$ yr^{-1} average

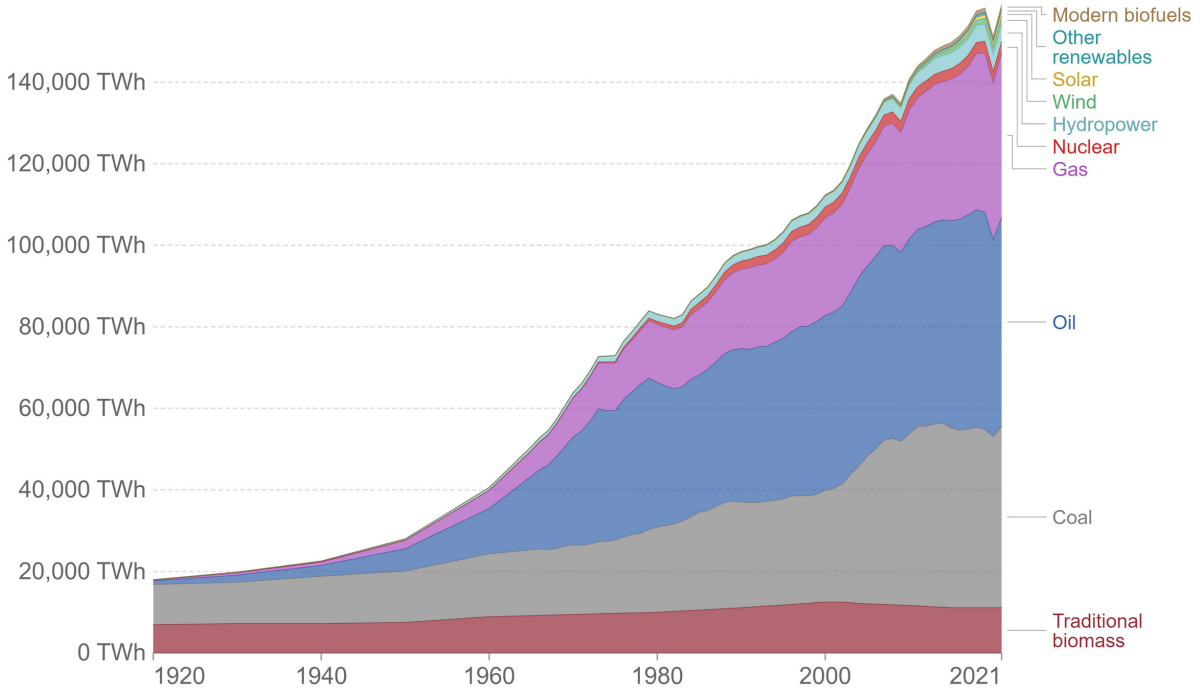

Figure 2.1: Global direct primary energy consumption from 1920 to 2021 [5].

annual growth until reaching 59 $GtCO_2$-eq in 2019. Of these, more of the 50% came from energy supply and transport sectors that therefore represent two aspects that must be addressed with priority.

However, this progressive increase of global energy demand that has just overcome 163000 TWh is not homogeneously distributed across the world. As highlighted by Olkuski et al., primary energy consumption in most developed European countries (e.g. Germany, France, Italy, etc.) has seen a slow but steady decrease since 2007 [6]. This decreasing trend is due to two main factors. The first is a continuous reconstruction of the energetic sector, more devoted to low-emission energy sources. The second is represented by the so-called carbon leakage i.e. the relocation of the most energy consuming factories in countries where the regulations on GHG gases are more permissive. Consequently, this share of energy consumption (and dangerous GHG gases) is simply transferred to other low-income countries whose growing quota of demand and CO_2 emissions is also related to a progressive access to energy of new shares of the population that were previously excluded. This aspect can be visualized in *Fig. 2.2*. As shown there, EU and USA are experiencing a slight reduction of carbon dioxide production which is more than offsetted by fast-developing countries such as China and India [7].
A similar inhomogeneous situation may be observed in the market of renewable energy. Currently, more than 8000 TWh yr^{-1} are produced by clean sources such as wind, solar, and hydropower. Even if accounting for $\sim$ 5% of the global production, this quota is continuously increasing year by year and is expected to gain a majority share in the next decades [4]. Interestingly, photovoltaic (PV) and wind continued their incredible growth also during the Covid-19 pandemic [1]. Anyway, as mentioned before, the renewable energy consumption per capita appears strongly localized in most developed economies (EU, USA, Australia, etc.) with some positive exception such as Brazil, whose primary energy consumption is strongly fuelled by hydropower and biomasses (*Fig. 2.3*). Just to

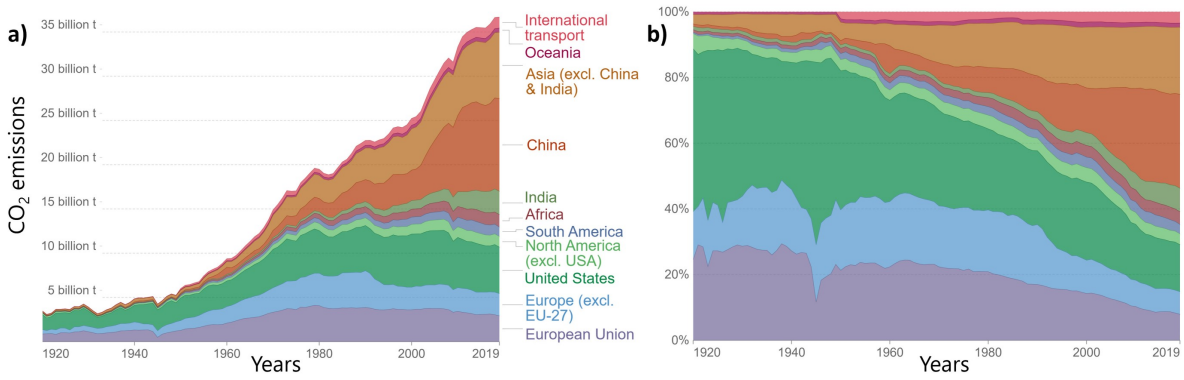

Figure 2.2: Absolute (a) and relative (b) annual CO_2 emissions from fossil fuels [7].

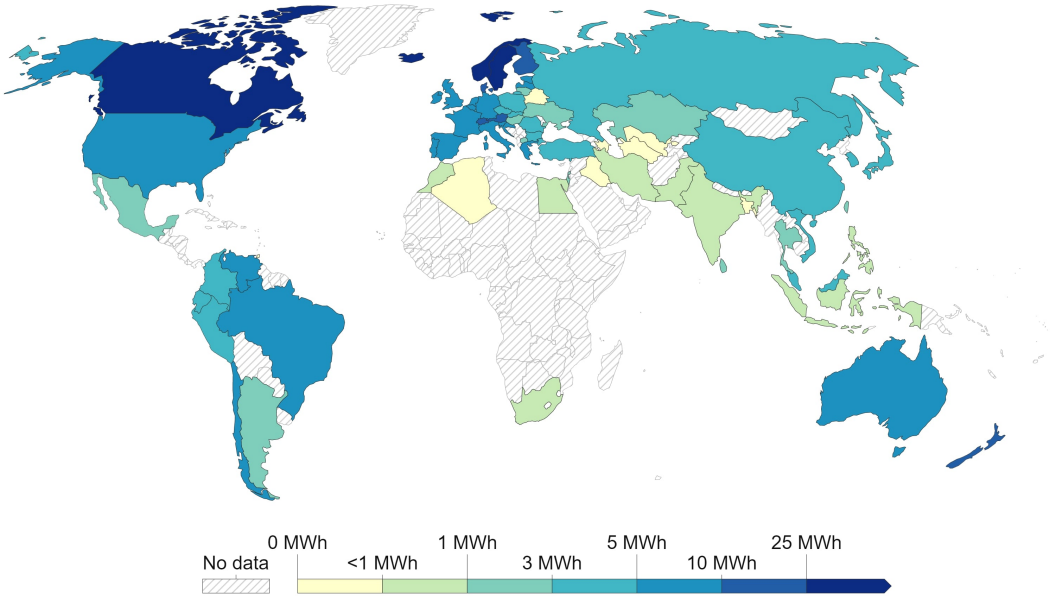

Figure 2.3: Per capita energy consumption from renewables in 2021 [4].

enumerate some data, renewables' share on the total primary energy supply goes from the 3% of the lower-middle income countries to $> 6\%$ of high-income ones. This value reaches $\approx$10% for the EU and overcomes $\geq$50% for virtuous nations like Iceland and Norway [4].

A separated discussion has to be instead devoted to electricity, often considered one of the main driving forces towards an efficient and rapid decarbonization. At 2022, $\sim$91% of the world population has access to electricity and this percentage is steadily growing yearly. Consequently, also the electricity demand is following a similar trend, having reached in 2021 28000 TWh with an yearly growth rate of $\sim$4% [8]. Therefore, it becomes of the utmost importance to provide it using clean and renewable sources. If compared to the total energy scenario, the current situation appears already a bit brighter: more than 40% of the global electricity is already produced with low-carbon sources (renewables and nuclear), with some countries such as Sweden and Uruguay getting more than 95% [4]. Focusing on 2021, wind and solar generated over a tenth of the global world electricity with a 1% increase from 2020. This 10% threshold has been surpassed by fifty countries, comprising all the world's largest economy, while Middle east and Africa still

fall short of these requirements. As example, the electricity mix of three countries that have changed most during the past years is shown in *Fig. 2.4a*. In all these cases, the growth of wind and solar electricity shares has been coupled to a decrease of the use of coal, gas and oil. Different is the case of China and India that, despite deploying new wind and solar farm devoted to electricity production, set new coal power records in 2021 (*Fig. 2.4b*) in order to meet the post-pandemic demand rise. Similar trends have been observed also in other Asian countries such as Pakistan and Mongolia [8]. These discouraging energy policies lead to record coal power in 2021 with more than 10000 TWh, equal to 36.5% of the global electricity production. Considering that Asia accounts for more than half of the global emission produced for electricity production (*Fig. 2.4c*), an immediate phasing-out of coal results mandatory for an effective decarbonisation of this critical sector [9]. Only in this way a continued electrification, coupled with clean electricity production, will be able to turn the tide on global emissions.
However, decarbonizing electricity production is only the first of three steps required to reach a low-carbon system. These improvements must be coupled to similar progresses on the other two components of primary energy demand, i.e. transport and heating, which are still strongly dependent on fossil fuels. Particular interest is therefore devoted to the replacement of internal-combustion engine (ICE) cars with electric vehicles (EVs) in order to extend the aforementioned electricity decarbonisation also to mobility sector.

In recent years EV sales, both plug-in hybrid (PHEVs) and battery-powered (BEVs) vehicles, have experienced a major surge thanks to a combination of several favourable factors such as policy support, technology improvements, and capillary expansion of charging facilities [10, 11]: the amount of EV cars sold worldwide in the whole 2012 (120000) was reached in one single week of 2021 for an annual total of 6.6 million. As shown in *Fig. 2.5a*, China and Europe currently account for more than the 85% of EVs, with the remaining quota mainly covered by USA (10%). This growth in sales has also been accompanied by a wider choice of models that reflects the interest of automakers in capturing the appeal of a broader pool of consumers [12]. *Fig. 2.5b* graphically shows this market penetration, highlighting the major changes experienced from 2016 to 2021. Anyway, some critical and unresolved issues are still hindering a complete and pervasive commercialization of EVs in place of the more polluting ICE vehicles.
The first limitation is the so called *range anxiety*, i.e. the drivers' fear that their car would not have a sufficient amount of charge to reach the final destination [13, 14]. This psychological barrier is widely considered as one of the main cons experienced by consumers where pondering the acquisition of an EV. A similar problem can be mainly tackled in two different ways. Firstly, publicly accessible charging infrastructure should be deployed more extensively in order to enable EV owners to undertake longer journeys with ease. Secondly, more performant energy storage devices able to store and deliver higher amount of energy could increase the confidence of consumers for electric mobility. In regards to this second aspect that will be thoroughly treated in the next chapter, the actual improvements achieved in the recent years can be easily understood comparing the average range for a BEV: this value passed from 211 km (2015) up to 338 km (2020), with a sharp increase of 60% in 5 years.
However, the biggest unresolved problem does not result strictly related to technological limitation but to an economical barrier: in fact, the purchase of an EV currently result $\approx$ 40% more expensive than ICE alternatives mainly due to the higher cost of the battery pack and of the whole electric powertrain [15]. Anyway, the average annual cost of owning a EV results equal to the 67.5% of petrol alternatives thanks to lower

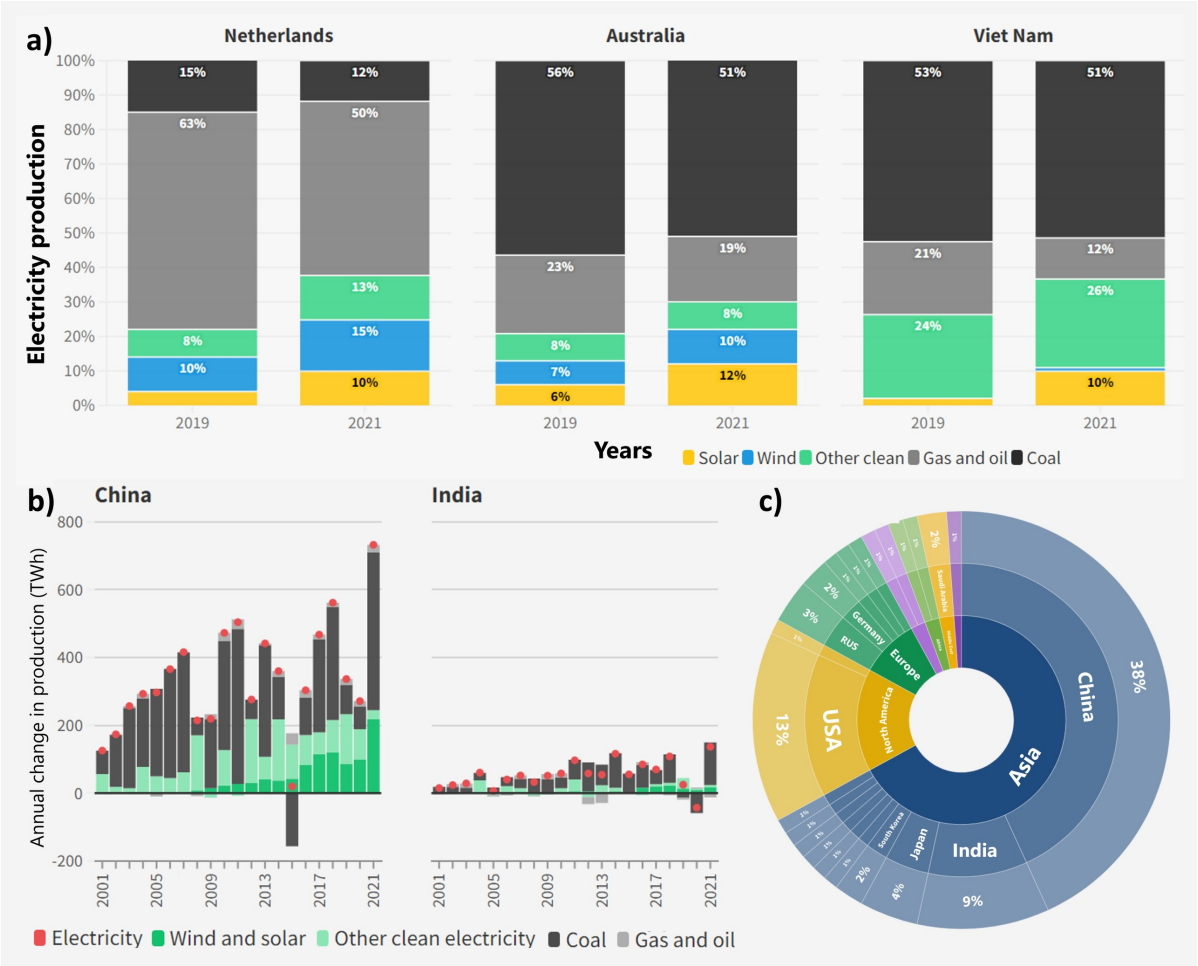

Figure 2.4: a) Electricity production mix for 2019 and 2021 in Netherlands, Australia and Viet Nam. b) Annual change in electricity production for China and India. c) Global emission distribution from electricity production in 2021 divided by region (blue: Asia; yellow: North America; dark green: Europe; light purple: South America; light green: Africa; orange: Middle East; dark purple: Oceania) [8].

maintenance and cheaper electricity price [16]. Consequently, cost parity between EVs and ICE vehicles can be currently reached in 6-7 years of ownership [17].
In conclusion, the current energy scenario appears complex, dynamic and widely fragmented. It results evident that a sharp acceleration of energy transition is required by all the different actors involved in this, both on industrial and government levels. To better understand the possible evolution of the actual energy situation, in the next section the main future outlooks will be outlined following the principal aims and pledges stated in recent years by the actors involved in this progressive decarbonisation.

2.2 Future outlooks:

Several international and intergovernmental agencies devoted to the study of energy and climate change have clearly stated the major guidelines to shape a secure and sustainable energy future. They all shared the same long-term goal set by Paris Agreement: keeping the increase in the mean world temperature below 2°C and preferably below 1.5°C [1, 2, 18]. In particular, the outlooks investigated throughout this chapter are extracted from the World Energy Transitions Outlook 2022 of IRENA [3].
Keeping in mind a 1.5°C compatible pathway, massive transformation regarding six technological avenues (*Fig. 2.6a-b*) should be undertaken promptly in order to reduce annually the CO_2 emissions of 36.9 Gt:

1. Renewables.
2. Energy conservation and efficiency.
3. Electrification of end-use sectors, such as transport.
4. Hydrogen and its derivatives.
5. Carbon capture and storage (CCS) from fossil fuels.
6. Bioenergy and other carbon removal measures.

Even if several of these topics fall outside this thesis' scope, the future evolution of the two most connected to next-generation energy storage devices will be treated thoroughly: renewable energy and electrification, particularly focusing on the roadmap to 2030.

2.2.1 Renewable energy and transport electrification:

The first step towards an effective decarbonisation during the next years is represented by the scaling up of the RE deployment undertaken in the past decades. In particular, the annual average RE addition must be tripled from today to 2030 reaching 800 GW of new capacity per year in order to reach a four-fold increase over the 2020 level. A similar trend must be maintained also for the subsequent twenty years, leading to a 2050 installed RE capacity of 27800 GW.
As shown in *Fig. 2.6c*, the biggest part of this share will be covered by solar PV with its theoretically unlimited potential and global availability. Asia and Europe are expected to remain the main actors for this technology, accounting for ≈70% of the global PV

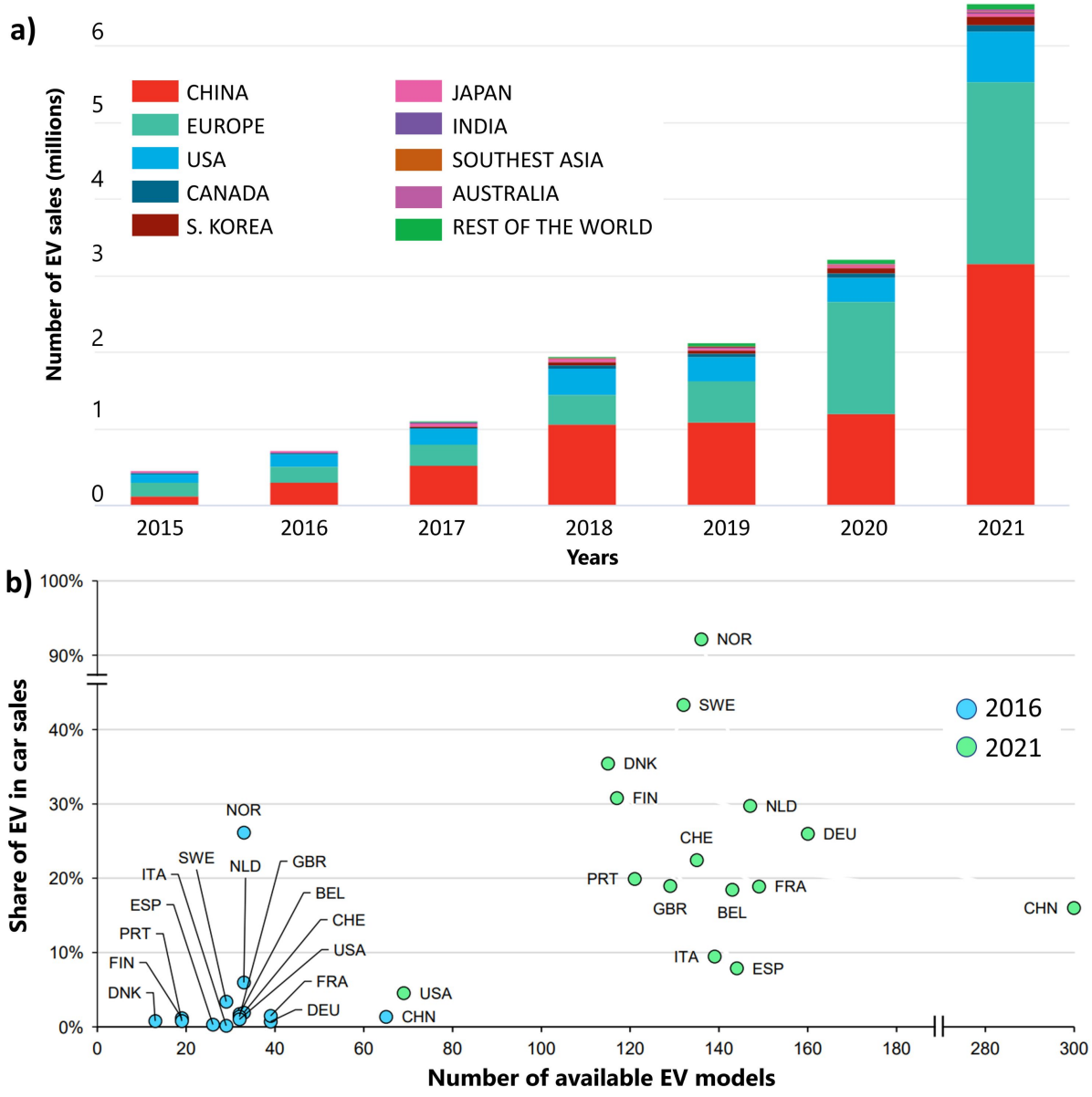

Figure 2.5: a) Global passenger EV sales by market [10]. b) Number of available EV models relative to EV sales share in selected countries [12].

installation by 2030. A critical role will be also played by Africa and Middle East, whose climate represent a key opportunity for solar power. These two regions are forecasted to experience a 44-fold increase of the installed PV capacity by 2050, enabling them to exploit this widely accessible renewable source.

Also wind power generation, both onshore and offshore, is predicted to become one of the largest energy source by 2030 (24% of global electricity). This niche will be dominated by Asia, with its immense technical potential for wind exploitation. Also Europe and North America can further expand the establishment of wind factories, with an annual growth of ≈40 GW yr^{-1} for both regions. Biggest challenges will be instead faced by Africa and Middle East, due to their lower suitability to wind power plants compared to other continents.

A more moderate growth will be instead experienced by hydroelectric generation. Anyway, even this source will have to double its generated power by 2050, reaching a deployed capacity of 2500 GW. Middle East and Africa will undergo the major relative increase, with an annual 3GW installed capacity.

Eventually, also other renewable technologies such as bioenergy, geothermal, ocean energy and concentrated solar power will fulfil a pivotal role in the energy transition, expanding six-fold their share in the renewable portfolio. In particular the latter, with massive projects already under progress in Middle East, China and Chile, is currently receiving the biggest attention from governments and energy companies [19].

However, all this renewable energy sources share an intrinsic unresolvable issue, i.e. their inherent intermittence [20]. The strong dependence on the weather conditions of wind and solar power is the most classic example carried out when dealing with this problem but also the other RE are not exempt. For instance, the severe droughts that have affected the whole world throughout 2022 summer months have had strong impacts on the hydropower productive system which is usually considered one of the most reliable RE [21, 22]. Also, this trend strongly affected the hydro power generation of the first 6 months of 2023 which experienced a global decrease of 177 TWh (-8.5% of its overall production), almost wiping out the huge additions of solar and wind in the same period (+213 TWh) [23].

Additionally, the intermittency can present not only on a seasonal but also on a daily basis. In this case, the peak of the energy demand seldom coincides with the maximum of the RE production. Considering that this unpredictability is expected to increase in the next decades as a consequence of climate change and global warming, tailored solution must be developed to address this drawback and prevent any energy shortage. Apart from a diversification of the RE portfolio, the only possible approach consists in the so-called load leveling, i.e. the storage of energy during periods of low demand and its delivery when energy demand peaks [24]. Examples of projected load leveling scenarios of selected countries are shown in *Fig. 2.7*. It is possible to easily notice the daily difference present between nations mainly based on PV (such as Italy and India) and the ones that rely on wind generation (e.g. UK and Canada). In both cases, electricity storage results the best suited instrument to address this challenge and support RE integration. It becomes therefore mandatory the development of more performant and efficient stationary energy storage devices able to store and deliver this excess of energy when required.

A major consequence of the progressive shift towards renewable energies described before is the possibility of implementing with ease zero-emission electric vehicles powered

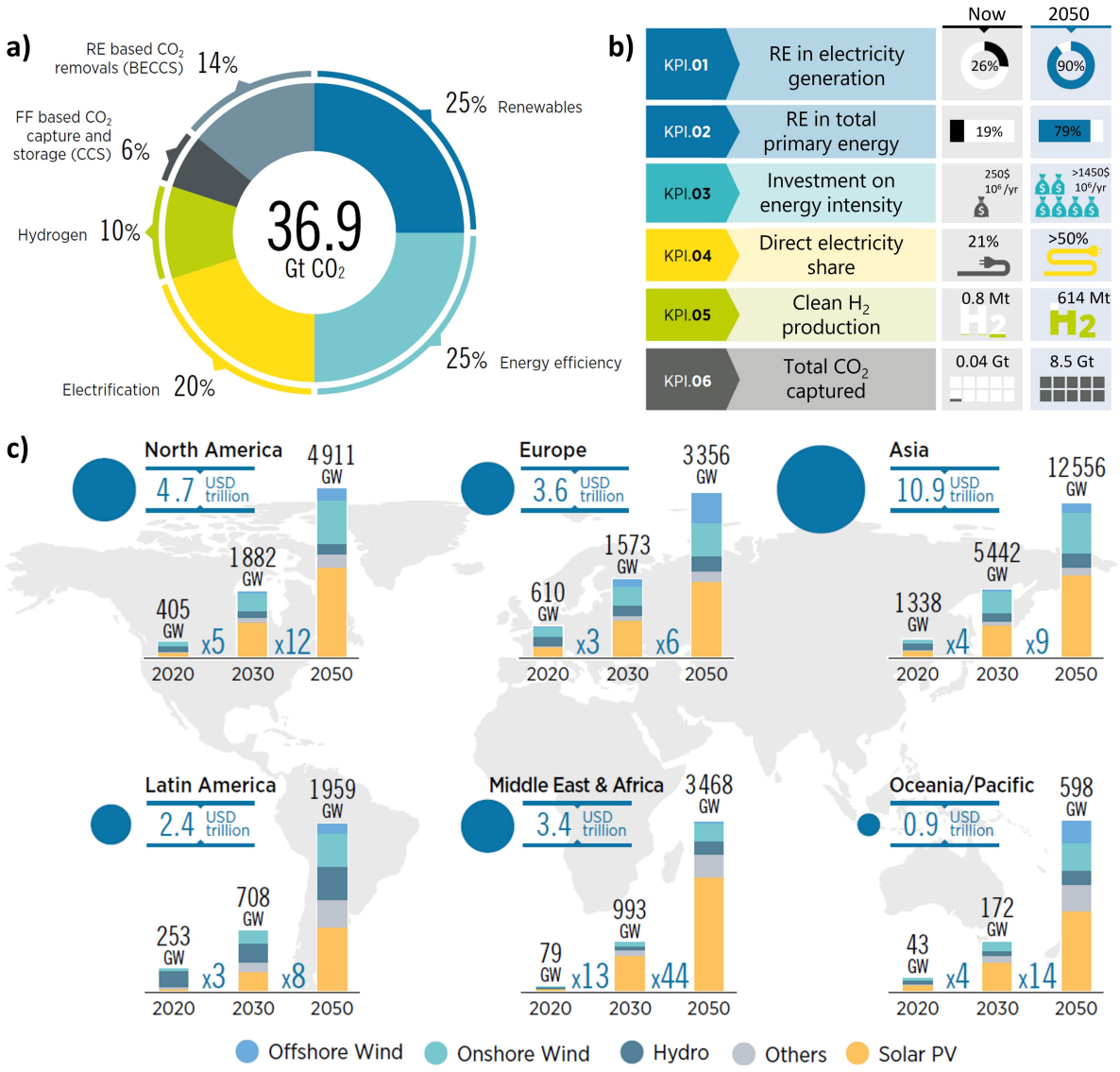

Figure 2.6: a) Six different technological avenues needed for the 1.5°C pathway with their relative share of CO_2 reduction. b) Key indicators of the 2050 energetic transition. *BECCS: bioenergy with carbon capture and storage; FF: fossil fuels.* c) Continental distribution of RE installed capacity in the 1.5°C pathway with the relative investment costs [3]. *Other: geothermal, tidal/wave, concentrated solar power, biomasses.*

Figure 2.7: Forecasted load leveling patterns of four selected countries in 2050 [3].

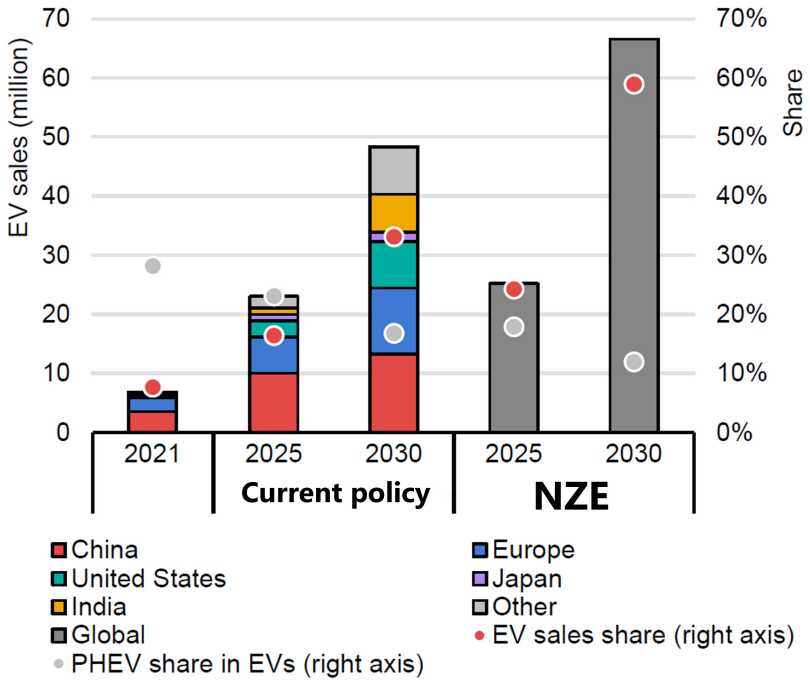

Figure 2.8: Global EV sales scenarios based on the announced government pledges and on the net-zero emission (NZE) scenario [12].

Table 2.1: Major government policies to promote electrification of low-duty vehicles (LDVs) and diffusion of zero-emission vehicles (ZEVs) [12].

Nation:	**Announced policies for EVs:**
Canada	100% ZEVs by 2035.
	1.7 billion $ for incentives for ZEVs.
Chile	100% ZEVs by 2035.
China	Progressive reduction of purchase subsidies for EVs.
France	Extension of subsidies for ZEVs .
European Union	Car fleet emissions reduction of 55% by 2030.
Germany	Increased EV purchase/lease subsidies.
India	50% increase of subsidies for electric two-wheelers.
Japan	Net zero by 2050 target.
	Supplementary budget for e-mobility.
Spain	400 million € directed to EV incentive program.
United Kingdom	Decrease of subsidies for EVs.
	Consultation to implement a ZEV mandate by 2024.
United States	Target of 50% for light-duty EVs by 2030.
	California ban on ICE vehicles sales from 2035.
	Washington state requirement to reach 100% EV sales by 2030.

by the clean electricity produced via RE.
In the wake of a more developed environmental consciousness and also thanks to renewed institutional legislations, many car manufacturers have implemented business strategies to obtain a competitive edge on this field [25]. Main national policies and companies' electrification plans and are resumed in *Tab. 2.1* and *Tab. 2.2*, respectively. Hence, under the impulse of governments' and automakers' plans, progressively more EVs are expected to be deployed on the road by 2030 and 2050. Anyway, despite this continuous progress, further improvements are still required. To achieve the net-zero emission (NZE) scenario before 2050, global EV stock has to overcome 100 million vehicles in 2025 and 350 millions five years later, surpassing the 20% of the vehicles' fleet and the 60% of the sales of 2030. These values result 80% higher than what currently predicted on the basis of the announced pledges (*Fig. 2.8*), indicating that current policies are still falling short of the final NZE aim with an excess production of 2.5 Gt CO_2 [12]. One of the main reasons behind this issue is represented by the future strong demand of vehicles by emerging markets that, despite expected to account for >40% of global sales in 2030, have not stated any decarbonisation pledges yet. Consequently, also in this case concerted actions able to involve all the different global actors are required to achieve the goals necessary for a sustainable development.

As already highlighted for RE, increased EVs production is going to necessitate an impressive scaling up of energy storage supply chain coupled to an improvement of the performance of the current lithium-based technologies [26]. Again, these aspects will be deeply investigated in *Chapter 3*.

Table 2.2: Major electrification announcements made in 2021 [12].

Automaker:	**Announced electrification plans:**
Ford	All-electric in Europe by 2030.
GM	Carbon neutrality by 2040.
Hyundai	Stop ICE vehicles sales in Europe by 2035.
Mercedes	From 2025 all newly launched vehicles will be EVs.
Stellantis	100% of Europe sales and 50% of USA sales to be BEVs by 2030.
Toyota	100% BEVs sales for Lexus by 2030.
Volkswagen	100% zero-emission vehicles by 2040.
Volvo	Fully electric by 2030.

2.2.2 Take-home messages:

In conclusion, even if a transition to cleaner energy technologies has started to be developed globally, major transformations are still necessary to align with the NZE by 2050 scenario. Nonetheless, all the outlooks show that it is not too late to reverse this trend and to achieve the goal of zero emission in the next 30 years.
Simultaneously, this green transition can also bring improvements to global stability and social equality. Currently, $\approx 80\%$ of the population lives in nations that are energy importers, therefore relying on complex and fragile geopolitical relations [3]. As highlighted by the recent Ukraine crisis, this equilibrium can be easily disrupted by national conflicts and political interests. A shift towards globally available RE would expand the energy portfolio, reducing the dependence on fossil fuels exporters and also offering an independent and easily harvestable resources to developing countries (e.g. solar power for African nations).
A pivotal role in this transition will be played by next-generation energy storage devices, lead actors in the world electrification and carefully treated in the next chapter. As stated in the Batteries Europe Strategic Research Agenda [27]:

> *"In Europe, within this decade, where it is technologically and economically viable, everything that can be electrified will be electrified, thus making battery technology one of the most important key enablers for the green energy transition facilitating existing and new technologies"*

While ensuring both high energy density and fast-charging, also other critical factors such as battery-lifetime, safety and materials availability must be considered [28, 29]. All these elements have to be successfully addressed to ensure a successful implementation of the technologies described throughout this chapter and the most promising solutions will be presented in the next sections of this elaborate.

3. Batteries: current trends and future developments

As introduced in the previous chapter, our society strongly relies on energy storage devices for many different aspects of our life: from automotive to electronics, from stationary to portable applications. Anyway, even if all these sectors use batteries, each of them requires with different characteristics.
First of all, for the sake of clarity it is better to state a definition that will be often employed throughout this work. With the term battery it will be denoted a system composed by one or more electrochemical cell able to store and deliver electric power and energy. The importance of batteries in nowadays life can be better understood watching some figures of the current market situation. The ubiquitous demand for reliable energy storage devices has brought to an incredible growth of the battery market size that passed from 62 $ billion of 2014 to the 120 $ billion of 2019 [30]. Even if many different technologies are currently exploited for energy storage, over 95% of the current market share is dominated by three chemistries, i.e lead-acid, alkaline, and lithium-based.
In particular, this last family of secondary batteries is currently experiencing a major expansion, with a double digit compound annual growth rate during the last year that is expected to reach ≈15.4% by 2026 with an overall 76 $ billion value projection starting from a <1$ billion value in 1991 [31, 32]. This incredible growth has also been accompanied by a progressive price drop: as shown in *Fig. 3.1*, the cost per kWh of lithium-ion batteries (LIBs) passed from 7500 $ to 181 $ in less than 30 years. This decrease continued until 2021 (101 $ kWh^{-1} for the cell, 132 $ kWh^{-1} for the battery pack) but has been partially hindered by the recent increase in raw material costs, linked to the Ukraine war and to the disruption of global supply chain, which has lead to a small rebound of the price in 2022 (135 $ kWh^{-1} for the whole battery pack) [33]. Nonetheless, 2023 experienced a recovery of the previous decreasing trend corresponding to a current price of 128 $ kWh^{-1} [34].

To further appreciate this incredible change it could be useful to consider a concrete example: the battery pack alone of a 2022 EV such as Nissan Leaf (a car with a 40 kWh battery and a total retail price of 29000$) would have costed more than 300000 $ in 1991.
The complete comprehension of the reasons underlying this considerable change can be completely achieved only knowing carefully the evolution of the technology behind lithium batteries. Therefore, after a short introduction about the main figures of merit related to batteries, a brief history of LIBs will be outlined in the next section particularly focusing on the most recent innovation of all the battery's components and on the still unresolved issues.

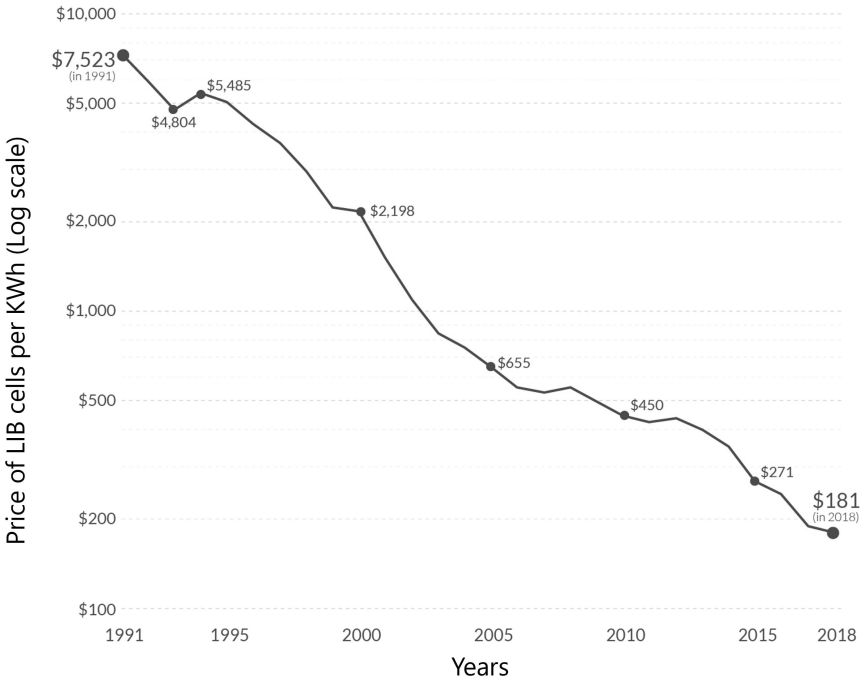

Figure 3.1: Price trend of LIBs per kWh from 1991 to 2018 [35]. All the prices have been adjusted for inflation and are expressed in 2018 US dollars ($).

3.1 The lithium-ion battery:

3.1.1 LIBs' working principle:

As every other electrochemical cell, LIBs are comprised of three main components schematically depicted in *Fig. 3.2*: two electrodes, the anode (i.e the electrode where oxidation takes place) and the cathode (i.e the electrode where reduction occurs), separated by an electrolyte, which could be solid or liquid. Purpose of the electrolyte is the conduction of Li^+ ions from one electrode to the other without allowing electron conduction. Such ions are produced by the reversible redox reactions that happens at the electrodes. During the discharge of the device, the negative electrode operates as an anode and undergoes oxidation. The released electrons and ions travel towards the positive electrode (i.e. cathode) feeding its reduction reaction following two different paths: while Li^+ cations migrate into the electrolyte medium, e^- are conducted through the external circuit where produce work. The two reactions are instead reversed during the charge, where an external applied load is required to drive the thermodynamically unfavourable process. It is worth noticing that during this second step the term anode should describe the role of the positive electrode while the negative electrode experiencing reduction operates as a cathode. However, to avoid any possible ambiguity, throughout this work the terms anode and cathode will always be used to describe the role of the electrodes during the discharge process, therefore respectively describing the negative and the positive electrode.

An example of the discharge process based on the two electrode materials shown in *Fig. 3.2* is presented below:

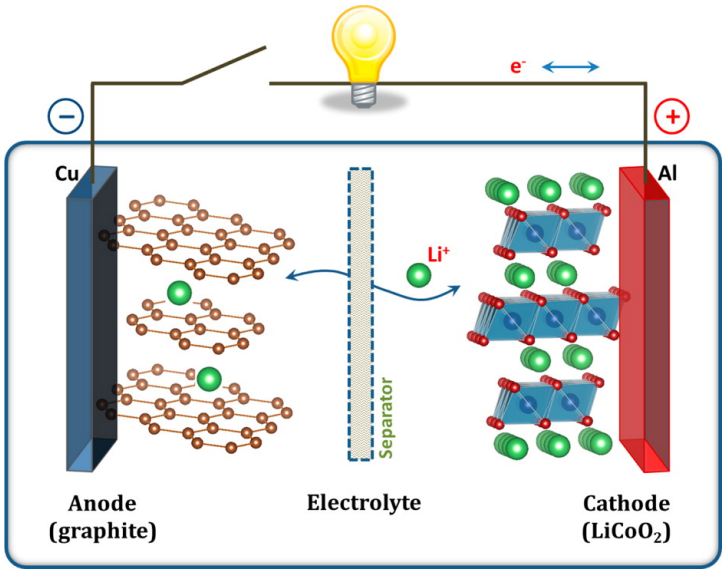

Figure 3.2: Schematic of a lithium-ion battery. Reprinted with permission from [36]. Copyright 2013 American Chemical Society.

$$anode : \mathrm{Li}_x\mathrm{C}_6 \longrightarrow \mathrm{C}_6 + \mathrm{xe}^- + \mathrm{xLi}^+$$
$$cathode : \mathrm{Li}_{1-x}\mathrm{CoO}_2 + \mathrm{xe}^- + \mathrm{xLi}^+ \longrightarrow \mathrm{LiCoO}_2$$

$$cell : \mathrm{Li}_x\mathrm{C}_6 + \mathrm{Li}_{1-x}\mathrm{CoO}_2 \longrightarrow \mathrm{C}_6 + \mathrm{LiCoO}_2$$

During these reactions, lithium ions follow the so-called *rocking-chair* mechanism upon which they are reversibly inserted into and extracted from the two electrodes.
After having understood the underlying working mechanism, it is worth highlighting some of the main figures of merit used to evaluate the performances of energy storage devices.
Aims of a battery are storing chemical energy, which can be released as electrical energy (E_e) when needed, and producing electrical power (P). These two parameters are expressed through the following formulas:

$$E_e = \int_0^{\Delta t} IV(t)dt = \int_0^{Q} V(q)dq \tag{3.1}$$

$$P = V(q) \times I \tag{3.2}$$

where

$$Q = \int_0^{\Delta t} Idt \tag{3.3}$$

is the charge stored in the battery expressed in mAh, $V(q)$ is the operating potential in V and I the delivered current. To effectively compare different systems, these values are usually normalized taking in account the mass (or the volume) of the device. Consequently, gravimetric and volumetric energy density (expressed in Wh kg^{-1} and Wh L^{-1}, respectively), gravimetric power density (W kg^{-1}), and specific capacity (mAh g^{-1}) are

commonly employed.
An additional factor of merit for energy storage devices is the Coulombic Efficiency (CE)

$$CE = \frac{Q_{dis}}{Q_{ch}} \times 100 \tag{3.4}$$

expressed as the percentage ratio between the amount of delivered and stored charge. Consequently, cycle life of a rechargeable battery is conventionally defined as the number of cycles performed before this value fades below 80%.
Among the several additional parameters that can be taken in account when dealing with this kind of devices, particular attention is devoted to safety, cost, sustainability, and the shelf life i.e. the amount of time an unused battery remains in its state of charge after being charged.
In conclusion, a battery should possess high specific capacity and high operating voltage to maximize energy density, fast kinetics to enable large output power and should be composed of safe, stable, earth-abundant materials to minimize its economic and environmental impact. Even if such *ideal* device is still non-existent, thanks to all the improvements described in the next section LIBs are currently the system which falls closer to the aforementioned requirements, particularly focusing on the performance ones.

3.1.2 LIBs' history and development:

The rechargeable batteries existing before LIBs such as lead-acid and Ni-metal hydride ones presented low values of energy density with no room for sensible improvements [37]. Despite some pioneering work in the first decades of 20th century [38], one of the biggest milestones that have characterized the energy storage world and that has been recently celebrated with the 2019 Nobel Prize in Chemistry is dated back to 1976. On that year, Stanley Whittingham proposed TiS_2 as the first example of an intercalation cathode material [39]. Coupled to a Li metal or alloy anode, this cathode able to deliver unprecedented reversibility and energy density was commercialized by Exxon in the late 1970s. Unfortunately, its low redox potential (≈2V vs Li^+/Li) and the use of reactive metallic Li anode respectively limited its performance and raised serious safety concerns. This last issue resulted particular dangerous, leading to the failure of a phone cell battery commercialization by Moli Energy Ltd in 1980 [40]. Meanwhile, in the same years at Oxford the group of another Nobel laureate John Goodenough firstly demonstrated the possibility of using a new layered oxide material ($LiCoO_2$, LCO) able to operate stably in non-aqueous electrolytes [41]. Operating above 4V vs Li^+/Li, LCO enabled open circuit voltage two times wider than TiS_2 and permitted to achieve higher energy density.
Anyway, despite the major advancements obtained through the use of oxide chemistry with deeper Fermi levels, the issue related to the anode side remained unresolved. After some unsuccessful experiments with Li alloys and insertion based oxides, carbon-based anodes were chosen as the most suitable materials [42, 43]. The major breakthrough was accomplished by the third 2019 Chemistry Nobel Prize winner Akira Yoshino that, after having also tested poly-acetylene, patented in 1985 the first LIB prototype based on a soft carbon anodic material [44, 45]. The first full cell LIB was commercialized 5 years later by Sony coupling this anode with Goodenough's LCO cathode and delivering ≈80 Wh kg^{-1} [46]. Anyway, the structure of LIBs has been continuously improved also in the subsequent years. In particular, soft carbon was substituted with hard carbon and, later, with graphite. This latter anodic material, coupled with a mixture of ethylene carbonate

(EC) and propylene carbonate (PC), enabled the formation of a stable Solid-Electrolyte Interface (SEI) which limited the irreversibility at the first discharge [47, 48]. It was this final enhancement that finally paved the path to modern LIBs, leading to the mass production and commercialization of reliable and performant energy storage devices still exploited nowadays.
Anyway, after having reached that milestone researchers have not stopped or diminished their efforts for further improvements of this device. Enhancements can be obtained on all the different components of the cell with the final aim of achieving the requirements set by the automotive sector for EVs. In particular, the current battery cost and energy density ($\approx$250 Wh kg $^{-1}$) still do not completely comply with the requirements of the industry, respectively set at $<$100 \$ kWh^{-1} and $>$350 Wh kg $^{-1}$ [49, 50].
As shown in *Tab. 3.1*, the current advancements are mainly focusing on cathode materials. Progressively, cobalt-rich electrodes (i.e. LCO) are starting to be substituted with cobalt-poor or cobalt-free (e.g. Ni-rich NMC, LFP) materials depending on the desired application. Due to its high cost and to the ethical concerns related to its mining process, cobalt replacement would impart advantages both on the social and on the economical sides [51, 52]. For instance NMC811, which contains only 6% Co by mass, imparts a raw materials cost that is less than half of the one of LCO with $\approx$60% Co by mass (54 \$ kWh^{-1} vs 135 \$ kWh^{-1}) [33].
Depending on the performance competitiveness or the cost requirements, different materials will be suited for different applications. Ni-rich NMC materials are able to deliver large values of energy densities, suitable for high-end EVs [53]. On the other side of the spectrum, thanks to its affordability and exceptional stability, LFP is expected to play a major role where cost effectiveness results more important than the lightness of the device. To provide more concrete examples, this cathodic materials is employed in the new generation of cheaper city car EVs such as Citroen eC3 which exploits a 44kWh battery pack provided by the Chinese manufacturer CATL. However, also some new Tesla cars (i.e. Model 3) are starting to employ this more stable material.
However, the sole replacement of the cathode does not endow the desired performance improvements. Consequently also the well-established intercalation chemistry of the anodic compartment, currently constituted by graphite, must be eventually replaced with more performant alternatives. The first choice, also selected and pursued by the European Commission, resides in the use of silicon or silicon-carbon composites due to the high lithiation capacity of this material (3579 mAh g^{-1} and 9786 mAh cm^{-3}) [54]. Si also relies on an appropriate discharge voltage ($\sim$0.4V vs Li^{+}/Li) and on its worldwide abundance, being environmentally friendly and low cost. However, its complete commercialization has been hampered by its poor cycling stability, mainly related to its low conductivity and to its huge volumetric deformation ($\approx$300-400%) which induces pulverization and detachment from the current collector [55]. To alleviate these issues, Si is often incorporated into carbonaceous or graphitic anodes in order to impart improved specific capacity avoiding the aforementioned problems [56]. While silicon compounds such as SiO_2 with a percentage estimated around 2-10 wt. % have already been encompassed in negative electrodes by commercial cells manufacturers (e.g. Samsung [57]) similar improved anodes based on Si are planned to be employed in the next years by some major automotive brands such as Porsche and Tesla [58, 59].
Nonetheless, the final objective of many battery manufacturers and researchers goes beyond the use of silicon. As shown in *Tab. 3.1*, from Gen 4b onwards the innovative lithium batteries are expected to be based on a different anode: metallic lithium. The

Table 3.1: Categorisation of battery generations as stated in Batteries Europe Strategic Research agenda 2020 [27]. LE: liquid electrolyte; HVS: high-voltage spinel; NCA: nickel cobalt aluminium oxide; HE-NMC: high-energy nickel manganese cobalt oxide, SSE: solid-state electrolyte.

Generation	Active materials	Cell chemistry	Market date
Gen. 1	Graphite|LE|LFP or NCA	LIB	Current
Gen. 2a	Graphite|LE|NMC 111	LIB	Current
Gen. 2b	Graphite|LE|NMC523 to 622	LIB	Current
Gen. 3a	Si-C|LE|NMC622 to 811	Optimised LIB	Current
Gen. 3b	Si-C|LE|HE-NMC or HVS	Optimised LIB	2025
Gen. 4a	Si-C|SSE|HE-NMC	Solid-state LIB	2025
Gen. 4b	Li|SSE|NMC	Solid-state LMB	>2025
Gen. 4c	Li|LE|HE-NMC or HVS	Advanced LMB	2030
Gen. 5	Li|O_2, Li|S or new ions (Na, Mg, etc.)	New chemistries	>2030

main advantages and the still unresolved obstacles associated with the use of this anode are presented in detail in the next section.

3.2 Moving to the lithium anode:

It is worth noticing that the expected evolution of LIBs somehow represents a return to the roots: as previously described, the first examples of lithium-based energy storage devices employed a Li anode [38, 39]. In fact, metallic lithium does not represent an original or recent concept but has always been considered the '*Holy Grail*' of the electrochemistry thanks to its interesting electrochemical properties. High theoretical gravimetric and volumetric capacities (3860 mAh g^{-1} and 2061 mAh cm^{-3}, respectively), low electrochemical potential (-3.04V vs SHE) and density (0.59 g cm^{-3}) make it the perfect candidate as negative electrode for high-performance secondary batteries. The advantages are clearly noticeable: passing from a LIB to a lithium-metal battery (LMB), the sole replacement of graphite with Li imparts an improvement >50% of the specific energy density of the cell (indicatively from 250 Wh kg^{-1} to 440 Wh kg^{-1}) [60]. A further boost can be achieved replacing the cathode with conversion systems such as Li-air or Li-S, not compatible with other non-lithiated anodic materials [61]. In particular, this last chemistry based on the reversible redox reaction between lithium and sulfur will be briefly introduced in a subsequent section (*Sec. 3.3*).
However, all that glitters is not gold: even if Bolloré has commercialized a Lithium Metal polymer device, the implementation of Li anodes in rechargeable devices still continues to be hindered by many serious issues related to the high reactivity of this alkaline metal and to the peculiar working mechanism of LMBs, different from the rocking chair intercalation process of graphite [62]. In fact, Li ions are not inserted into an host material, as it happens with other electrodes, but are directly plated on the surface of the anode itself. The first problem resides in the formation of a stable SEI on the surface of Li anode. Due to the strongly reductive potential, practically any feasible liquid electrolyte reacts in contact with Li. Therefore, the formation of a passivating layer results particularly critical for the stabilization of the anode. Unfortunately, the organic carbonates

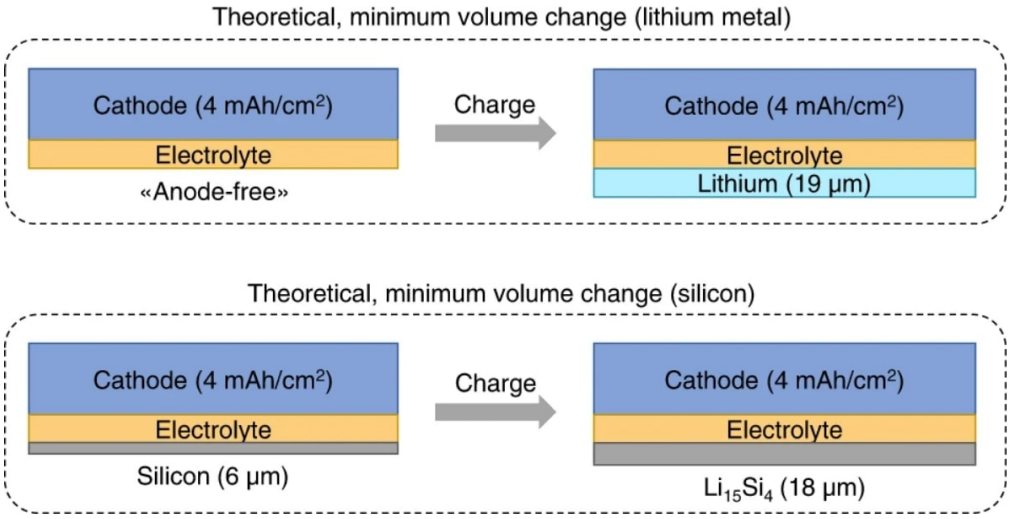

Figure 3.3: Volume change visualization of the deposition of 4 mAh cm^{-2} of Li in a LMB and in a Si-anode cell [33].

commonly employed in LIBs do not result optimal for LMBs since the resulting SEI lacks flexibility and easily breaks down during cycling. This breakage induces further reactions between electrode and electrolyte, eventually leading to continuous consumption of the freshly exposed Li surface and of the electrolytic solution. Therefore, these parasitic reactions greatly affect the efficiency and the cycling life of the cell.
Another major concern is instead related to the risk of electrical disconnection upon cycling induced by volume expansion. Even all electrodic materials share this problem, the relative volume change of a Li anode is virtually infinite due to its hostless nature. For instance, the deposition of 4 mAh cm^{-2} of Li would cause a thickness growth of 19μm, larger than what experienced in a comparable graphite-based or even Si-based cell [33] (*Fig. 3.3*). These continuous cycles of expansion and shrinking impose strong mechanical stress not only on the anode but also on the whole commercial cell which undergoes volume changes of ≈10-20%. Additionally, the great volumetric expansion plays also a major role in the breakage of the fragile SEI explained before, worsening the exposition of fresh and reactive Li surface.
The third and biggest problem that is currently hindering the development of LMBs is the growth of dendrites that are formed during the plating procedure when lithium ions are reduced and deposited on the anodic metallic surface [63]. Due to irregularity of the conduction pathways, Li^+ cations are not uniformly distributed on the surface but tends to accumulate on specific nucleation sites. The so-formed tips present a more intense electric field that will consequently attract an higher amount of plated ions. This self-enhancing phenomenon induces a continuous growth of these protrusions which, piercing through the separator, would eventually lead to the short-circuit of the device. This can lead to dangerous cell thermal runaway, usually accompanied by electrolyte combustion and/or cell explosion [64]. Such problem becomes more critical at high current densities, since the stripping/plating deposition becomes less homogenous and more localized in correspondence of defective sites.
However, short-circuiting is not the only obstacle related to dendrites. The increased surface area formed during this process induces additional degradation of the electrolyte, irreversibly consuming Li without giving any contribution to the capacity. Additionally, the breakage of these dendrites after their parasitic reactions with the electrolyte might

lead to the formation of the so called *dead lithium* i.e. electrochemically inert Li detached from the current collector, further reducing the coulombic efficiency of LMBs. Moreover, Li metal anodes with a rough dendritic surface always present an higher porosity if compared to uniform dense anodes. This uneven structure overall reduces the electronic conductivity, worsening the performances of the device [65].
Keeping in mind all this facts, it appears evident that a safe and durable LMB cannot coexist with the uncontrolled growth of Li dendrites. Consequently, several different strategies have been tested to address this undesired phenomenon. These approaches can be grouped depending on the employed mechanism under two macro-categories: dendrite prevention, if the formation of Li protrusion is totally avoided enabling an uniform Li deposition, and dendrite blocking, when the filament propagation is mechanically hindered through the presence of a physical obstacle [66]. While the principal blocking approach (i.e. the use of solid state electrolytes) will be carefully described in *Sec. 4.2*, the three main prevention concepts will be briefly outlined here just for the sake of completeness: electrolyte additives, Li-metal surface coating, and 3D current collectors [67].

3.2.1 Electrolyte additives:

The addition of specific SEI-forming agents represents one of the possible approaches apt to the stabilisation of the Li-electrolyte interface, enabling the formation of a smoother anodic surface upon plating. The resulting artificial SEI (ASEI) can be achieved through the use of many different additives. Kasse et al. added 100 ppm HF to EC/DMC electrolyte in order to induce an uniform dendrite-free morphology of Li thanks to the selective formation of ordered LiF crystals on the surface [68]. Also fluorocarbonates, borates, and dual salt systems successfully induced a stable ASEI [69–71]. A totally different concept is the one reported by Ding et al. which enabled the formation of a different kind of ASEI through the addition of selected metallic cations into the electrolyte (Cs^+ and Rb^+) [72, 73]. These ions present a redox potential below the one of Li and, therefore, will not be plated on the anodic surface but, being attracted by high negative electric fields, will segregate near any inhomogeneous tips formed upon cycling. Acting as a positively charged electrostatic shield, their presence would repel any impinging Li^+ forcing them to deposit in the neighbouring regions of the anode. This process permitted the formation of a smooth surface preventing the growth of any dendrite.

3.2.2 Li-metal surface coating:

Sometimes the use of additives alone does not result sufficient to promote the formation of a stable interface. In those cases, a proper coating layer deposited on the anode surface can work as an ASEI, playing the double role of homogenizing the impinging ion flux simultaneously reducing the formation of dendrites and dead Li. The ideal coating should possess high ionic conductivity and elasticity, in order to permit the passage of Li^+ ions while accommodating the volume change during stripping and plating, while maintaining a good electrochemical stability in the working potential range. Such coating layers can be comprised of many different materials, such as organic, inorganic or alloy compounds. For instance, Yu et al. produced a thin ZnF_2 layer to induce the formation of LiF and of an alloy coating of Li-Zn which effectively suppressed dendrites [74]. Polymers can be effective likewise: cross-linked SiO_2-reinforced polydimethylsilox-

ane provided protection to Li anode, inhibiting dendrites and promoting Li^+ migration [75]. Moreover, the high elasticity and self-healing abilities enabled the ASEI to minimize any breakage. Also ceramic ASEIs, possessing high shear modulus, can work as intrinsic barrier against dendrite short-circuiting. LiPON, LiF and Al_2O_3 are just some of the materials successfully used for this task [76].

3.2.3 3D current collectors:

An original approach to address the problem of dendrites consists in the deposition of Li anodes on three-dimensional porous current collectors. Possessing higher surface area and therefore reducing the resulting current density, they enable a more uniform plating. To achieve this peculiar structure, Pei et al. employed N-doped porous carbon nanosheets covered with Cu or Ni that simultaneously alleviated both volume expansion and dendrite formation [77]. Similar studies have been carried out on carbon nanotubes in-situ grown on the surface of Ni foam [78]. Additionally, also porous metal (as Cu) skeletons represent a viable alternative allowing a more homogenous Li deposition in the several nucleation sites present inside the framework [79]. With this system, CE was maintained ≈98.8% after 500 cycles while the efficiency using bare copper foils was reduced to 80% after less than 80 cycles.

3.3 Lithium-sulfur batteries:

Like intercalation-based LMBs, also the introduction of the Li-S battery can be traced back in the last century. It was 1962 when Herbert and Ulam first patented the concept of a sulfur cathode [80]. However, the severe capacity decay and the subsequent commercialization of the more stable LIBs have overshadowed the research on sulfur cathodes [81]. Only in the next decades the need of batteries with higher energy densities revived the attention to this technology. The final confirmation of the validity of sulfur chemistry was achieved in 2009 when Nazar's group at University of Waterloo (Ontario, Canada) reported the use of a conductive mesoporous carbon framework which enabled higher specific capacity with an unprecedented retention upon cycling [82]. Since then, the number of papers devoted to this topic has experienced an unstoppable exponential growth as shown in *Fig. 3.4a*.
The resurged interest devoted to the use of sulfur cathodes is supported by a valid rationale. Coupled with a Li anode, this cheap and abundant material offers an impressive theoretical specific capacity of 1672 mAh g^{-1} that, delivered at an average potential of 2.15V vs Li^+/Li, enables the production of Li-S battery with energy densities up to 2500 Wh Kg^{-1} [83]. All these interesting features are achieved through the exploitation of a conversion mechanism rather than the standard intercalation chemistry exploited with layered oxide cathodes. In fact, the working principle is based on the reversible multi-electron redox reactions established between Li and cyclic octasulfur S_8, one of the over 30 solid allotropes of sulfur [84]. During discharge, Li^+ ions and electrons released by the lithium anode are accepted by the sulfur cathode generating lithium sulphide Li_2S:

$$\begin{aligned} anode: &\ 16\,Li \longrightarrow 16\,Li^+ + 16\,e^- \\ cathode: &\ S_8 + 16\,Li^+ + 16\,e^- \longrightarrow 8\,Li_2S \\ cell: &\ 16\,Li + S_8 \longrightarrow 8\,Li_2S \end{aligned}$$

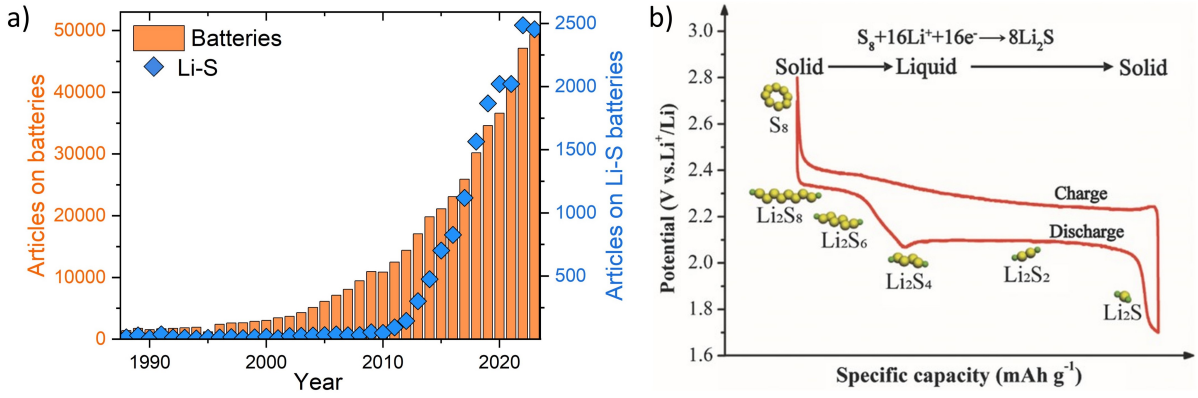

Figure 3.4: a) Publications on Li-S batteries (blu) from 1988 to 2023 compared with the overall publications on batteries (orange). Data were obtained with the search query "lithium AND sulfur OR sulfur AND battery OR batteries" and with the generic query "battery OR batteries" using Scopus website on 29th December 2023. b) Charge-discharge profile of a Li-S battery. Reproduced with permission from [85]. Copyright 2017 Wiley-VCH.

Even if the net reaction appears simple, the actual discharge process usually involves a two-step transformation that originates two different plateaus in the discharge galvanostatic profile. Cyclic octasulfur is firstly reduced to the polysulphide compounds Li_2S_8, Li_2S_6 and Li_2S_4, all of them soluble in the commonly employed organic electrolytes [85]. This first stage results in a theoretical specific capacity of 418 mAh g^{-1} at an average potential of 2.3V vs Li^+/Li. Further lithiation induces the production of Li_2S_2 and, eventually, of the solid Li_2S. This second set of reactions happening around 2.1V vs Li^+/Li produces an additional capacity of 1254 mAh g^{-1}.
Nonetheless, sulfur chemistry presents some intrinsic shortcomings that have affected its performances and prevented its wide implementation. Firstly, both S_8 and Li_2S are electronic insulators. This slows the kinetic at the cathodic side, causing a reduced sulfur utilization and therefore lowering the effective specific capacity [86]. Secondly, the significant difference between the density of S_8 (2.08 g cm^{-3}) and Li_2S (1.66 g cm^{-3}) induces a large volume expansion during lithiation (≈80%) which can result in electrode pulverization and detachment from the current collector [87]. Thirdly, the peculiar soluble nature of the intermediate polysulphides causes several undesired effects during repeated charge and discharge cycles. Driven by the concentration gradient, those compounds tend to migrate toward Li anode where they are reduced to solid Li_2S, which detrimentally passivates the anodic interface, or to long-chain polysulphides. Upon recharge, the partial reduction at the anode of those compounds and their subsequent field-driven migration to the cathode as short-chain polysulphides causes the infamous "shuttle effect": this *swinging* process with soluble polysulphides alternatively moving towards the two electrode leads to parasitic reactions and poor cycling stability [88].
Even if several approaches have demonstrated their effectiveness in reducing the aforementioned issues, a further investigation of these topics goes beyond the aim of this elaborate in which Li-S batteries will be briefly encountered in *Sec. 4.2.2* and in *Chap. 6* when dealing with sulphide solid electrolytes.

4. Electrolytes for lithium batteries:

While the electrodes usually represent the bottleneck in terms of energy density and ciclability of the cell, on the other hand the electrolyte often acts as the determining factor for the current density, therefore for the power output, and for the safety of the device [89]. As a consequence, its optimization plays a major role both on the improvements of performances and on the minimization of the safety hazards.
In general, the key features that must be considered when pondering an electrolyte can be grouped into 4 categories [90]:

i. Electrochemical stability.

ii. Temperature range of operation.

iii. Safety features.

iv. Transport properties.

Consequently, all the subsequent families of electrolytes will be analysed keeping in mind these critical aspects.
Firstly, the chosen electrolyte must be stable, thermodynamically or kinetically, with both the electrodes in order to avoid any undesired degradation or parasitic reaction. The electrochemical stability window (ESW) is commonly defined as the potential range in which an electrode can be polarized in an electrolyte without any substantial faradaic current, i.e. the voltage difference of the potential limits in which no additional oxidation or reduction reactions other than the electrodic ones are experienced [91]. It is this value which sets the maximum operating potential of the device: the higher the ESW, the wider will be the choice of feasible anodes and cathodes that can be coupled with the chosen electrolytic system. High oxidation potentials (>4.0-4.5 V vs Li^+/Li) would permit the implementation of high-voltage cathodic materials (such as HE-NMC or HVS). Conversely, electrolytes with a low reductive potential or able to form a stable anodic passivating SEI enable the use of negative electrodes with lower redox couples, pushing further the operating voltage of the device.
While the ESW is related to chemical properties, the temperature range of operation is mainly linked to the physical characteristics of the electrolyte such as boiling and freezing points for liquid electrolytes (LEs) or T_g and T_m for solid state electrolytes (SSEs). Also the presence of thermal degradation phenomena must be carefully considered when choosing the suitable electrolyte for a specific application. Even if low freezing and high boiling point are conventionally desired in LEs, these two properties are rarely found together in a single electrolyte. Consequently, binary or ternary systems are usually employed to achieve a wide temperature range of operation [92]. Analogously, the use of nanocomposite systems represents an effective way to modify the thermal properties of

polymeric SSEs playing with the crystalline/amorphous fractions of the polymer.
The third key feature of an electrolyte regards its safety, since its choice (and the one of the separator) strongly influences the safety level of the whole device [93]. Among the several issues, the main concerns are related to high flammability, risk of leakage (for LEs), and toxicity [94]. When moving to LMBs, an additional requirement resides in the prevention of dendrite growth, otherwise inducing internal short-circuit and thermal runaway of the whole cell. Since the principal safety issues strongly depend on the chemical nature of the material, additional general considerations would result naive and all these aspects will be thoroughly discussed when treating singularly the different types of electrolytes.
Eventually, the last characteristic used to evaluate the quality of an electrolyte is also the one that is conventionally considered the most important, i.e. its transport properties. First of all, an electrolyte must possess a satisfying ionic conductivity σ_{Li^+} coupled with a negligible electronic ($<10^{-10}$ S cm^{-1}) one. In this way, Li^+ will easily migrate through the electrolytic solution while the e^- will flow in the external circuit. Additionally, high solubility of lithium salt is also desired since it increases the number of charge carriers n whose value is directly proportional to σ_{Li^+} as stated in the following equation

$$\sigma \propto n \cdot u \tag{4.1}$$

where u represents the mobility of the carriers.
Unfortunately, high solubility is usually linked to high solvent polarity which induces also high viscosity for LEs. Another desired parameter is a transference number $t_{Li^+} \approx 1$, defined as the ratio between the current transported by lithium ions i_{Li^+} and the overall current i_{tot}:

$$t_{Li^+} = \frac{i_{Li^+}}{i_{tot}} \tag{4.2}$$

Avoiding an excessive accumulation of non-reactive ions on the electrodic surface, t_{Li^+} close to the unity can reduce undesired polarization phenomena at the interface between electrode and electrolyte [95]. One feasible method to determine this value is the use of the Bruce-Vincent method, named after its two main theorists [96, 97]. This approach permits an easy extrapolation of t_{Li^+} with a simple procedure. Firstly, the initial resistance of the interface R_0 is determined through Potentiostatic Electrochemical Impedance Spectroscopy (PEIS). Subsequently, a chronoamperometry measurement is performed applying a constant voltage difference ΔV ($\approx$10-20mV) until reaching the steady state. During this step, the initial current and steady state currents, I_0 and I_s respectively, are measured. Finally, an additional PEIS is used to determine the interfacial resistance R_s after the polarization. Eventually, the measured parameters are inserted into the following *Eq. 4.3*:

$$t_{Li^+} = \frac{I_s(\Delta V - I_0 R_0)}{I_0(\Delta V - I_s R_s)} \tag{4.3}$$

which takes cares of the formation of passivating layers and of the polarization established at the electrodes.

Even if a comprehensive general description of the ion conduction mechanism on the microscopic scale cannot be achieved due to the large variety of involved systems, the temperature dependence of Li^+ conductivity in electrolytes can be macroscopically modelled using two different behaviours: Arrhenius and Vogel-Tammann-Fulcher (VTF)

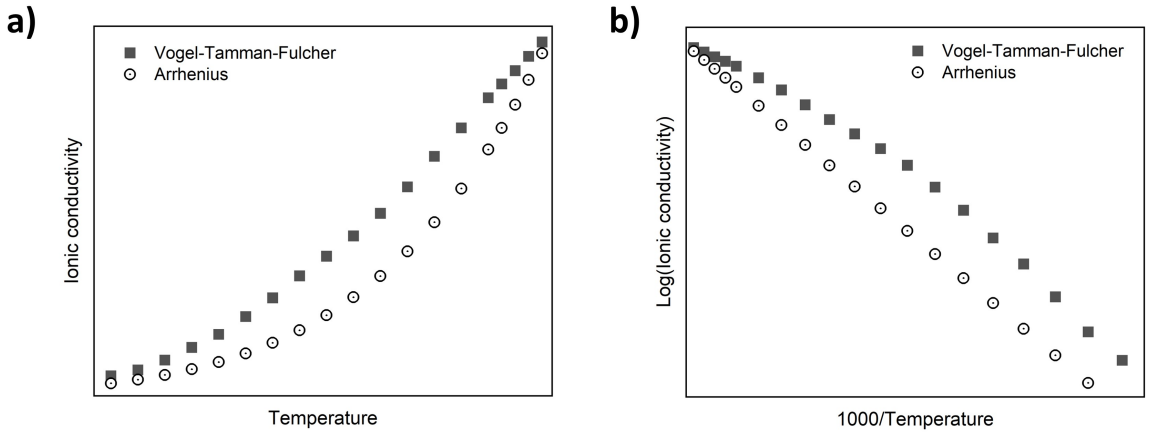

Figure 4.1: Graphs displaying the profile of VTF and Arrhenius curves in (a) ionic conductivity vs temperature and (b) logarithm of ionic conductivity vs reciprocal of the temperature. It is possible to appreciate how Arrhenius behavior appears linearized in (b) while VTF displays a 'rounded' shape.

whose profiles are presented in Fig. 4.1.

The Arrhenius behaviour, displayed in *Eq. 4.4*, is usually employed for those electrolytes where the ion-hopping is decoupled by the long-range motion of the matrix (such as ceramic-ion conductors and amorphous polymers or glasses below T_g [89, 98, 99]):

$$\sigma = \sigma_0 \exp\frac{-E_a}{(k_B\, T)} \tag{4.4}$$

In these systems, the ionic conductivity follows a simple exponential behaviour where σ_0 is a pre-exponential factor, E_a is the activation energy of the conduction expressed in eV, k_B is the Boltzmann constant ($8.617 \cdot 10^{-5}$ eV K^{-1}), and T is the temperature in K. Consequently, the values can be extrapolated by the linear fit of $log_{10}(\sigma)$ *vs.* T^{-1}:

$$log_{10}(\sigma) = log_{10}(\sigma_0) - 0.43\frac{E_a}{k_B}\, T^{-1} \tag{4.5}$$

where σ_0 is deduced by the y-intercept and E_a is obtained from the slope of the resulting line (Fig. 4.1b).

Conversely, the conductivity behaviour of those systems where the conduction mechanism is mediated by solvent molecules and/or segmental motion of polymeric chains (e.g. organic liquid electrolytes, ionic liquids, deep eutectic electrolytes, gel polymer and nanocomposite electrolytes [100–105]) follows instead a different temperature dependence, i.e. VTF one (*Eq. 4.6*) :

$$\sigma = \sigma_0 \exp\frac{-B}{(T - T_0)} = \sigma_0 \exp\frac{-E_{\mathrm{VTF}}}{K_b(T - T_0)} \tag{4.6}$$

where B is the pseudo-activation energy expressed in K and T_0 is the fitting reference temperature, usually comprised in the range [T_g-10K;T_g-50K] [89]. The optimal value of T_0 can be obtained by the best fitting of the following linearized relationship $log_{10}(\sigma)$ *vs.* $(T\text{-}T_0)^{-1}$:

$$log_{10}(\sigma) = log_{10}(\sigma_0) - 0.43B(T - T_0)^{-1} \tag{4.7}$$

Consequently, the associated values of σ_0 and B (or E_{VTF}) are extracted in accordance to the same procedure described for the Arrhenius behaviour. However it's worth highlighting that, differently from the activation barrier E_a in Arrhenius, E_{VTF} does not possess

an intrinsic physical value but just acts as a fitting parameter .
The most exploited and easy way to extrapolate experimentally these conductivity values is usually based on the use of PEIS to determine the electrolyte resistance R as the intercept on the x-axis of the Niquyst plot. Knowing the thickness l expressed in cm and the section of the electrolyte A in cm^2, it results possible to compute the electrolyte conductivity in S cm^{-1} using the following *Eq. 4.10* derived from Second Ohm's law:

$$R = \rho \frac{l}{A} \tag{4.8}$$

where ρ is the resistivity of the electrolyte equal to

$$\rho = \frac{1}{\sigma} \tag{4.9}$$

therefore

$$\sigma = R \frac{l}{A} \tag{4.10}$$

In addition to all these critical features described hitherto, another non comprehensive list of parameters that have to be considered during the choice of an electrolyte comprises cost, environmental sustainability, processability, wettability of electrodes, *etc.*.
For all the electrolytes described in the next sections, all these aspects will be carefully highlighted, particularly focusing on their advantages and weaknesses in order to present a broad contest of the possible choices for the electrolytic compartment in LIBs and LMBs.

4.1 Liquid electrolytes:

Liquid electrolytes (LEs) are undoubtedly the most applied and investigated electrolyte in LIBs [106]. They are usually composed by a polar aprotic non-aqueous solvent and by a dissolved lithium salt. Currently, the state-of-art LE consists in a mixture of specific carbonates, both cyclic (propylene carbonate, PC and ethylene carbonate, EC) and linear (such as diethyl carbonate, DEC, and dimethyl carbonate, DMC), combined with lithium hexafluorophosphate, $LiPF_6$, as conductive salt. Their chemical structures are shown in *Fig. 4.2*. While the cyclic compounds guarantee a good dissolution of Li^+, the linear alkyl carbonates are used to reduce the viscosity of the mixture, therefore enhancing the ionic conductivity in particular at low temperatures [107]. Moreover, the addition of fluorinated additives such as fluoroethylene carbonate (FEC) and vinylene carbonate (VC) enabled to push further the optimization of these cells addressing specific problems (e.g. anodic SEI formation) [108]. On the other hand, $LiPF_6$ assures a satisfying ionic conductivity (up to 10^{-2} S cm^{-1}) thanks to its low dissociation energy and compatibility with high voltage cathodes due to the high stability vs. oxidation of the perfluorinated PF_6^- anion [109]. However, the use of $LiPF_6$ also induces several disadvantages: its thermal stability appears strongly limited ($<$105°C) and its exposition to moisture yield the production of dangerous and corrosive hydrofluoric acid (HF) [110]. As a consequence, many alternative Li salts such as $LiClO_4$, lithium bis (trifluoromethanesulfonyl)imide (LiTFSI), lithium bis(fluorosulfonyl)imide (LiFSI), and lithium difluoro(oxalato)borate (LiDFOB) have been thoroughly studied to improve LEs performance [108].
Anyway, also the replacement of the conductive salt is not able to solve by itself the

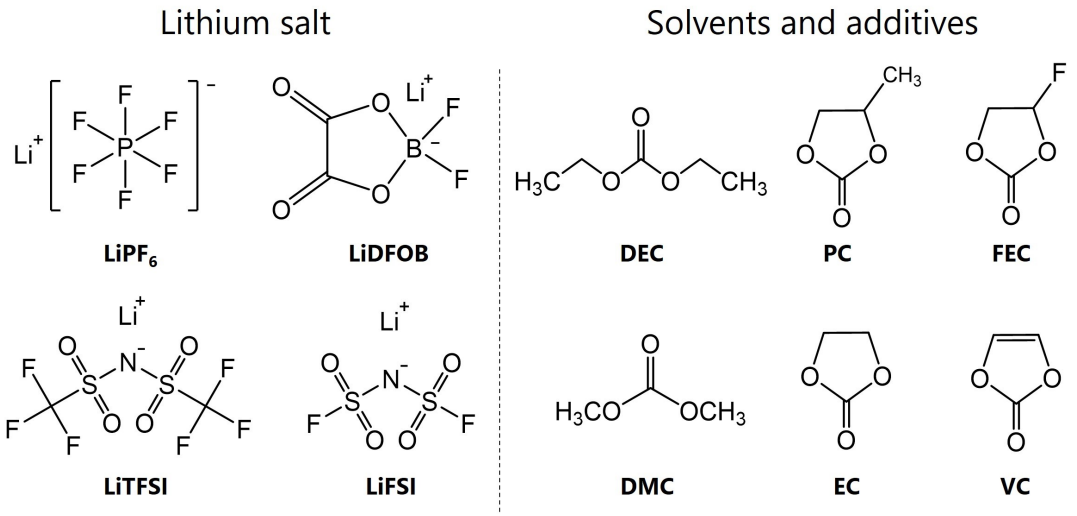

Figure 4.2: Chemical structures of commonly employed lithium salts, carbonate solvents and additives for LEs.

most critical issue inherent to linear carbonates, i.e. high flammability. As a matter of fact, while cyclic systems present a limited level of flammability, linear compounds such as DMC and DEC result highly flammable with relatively low and dangerous flashpoint (≈20°C) and autoignition temperatures (≈450°C) [111]. Mechanical, electrical and thermic abuse or intrinsic defects inducing an internal short-circuit can trigger the thermal runaway of the battery, i.e. a strongly exothermic process that leads to overheating of the cell [112]. This positive feedback failure mechanism, where the released energy causes a further increase in the temperature of the cell which in turn induces the propagation of the phenomenon [113], is obviously worsened by the presence of combustible electrolytes that can cause fire and explosions, as shown in *Tab. 4.1*. Consequently, these strict limitations have driven the investigation of safer and feasible alternatives. Even if the incorporation in common organic compounds of electronegative substituents such as fluorine able to lower the HOMO/LUMO levels has shown some beneficial effects, many researchers are shifting their efforts toward the development of new LEs beyond carbonates mixtures [114].

A first possibility is represented by the use of non-toxic and non-flammable aqueous electrolytes, whose ionic conductivity two orders of magnitude higher than organic compounds can allow high-power capabilities [116]. Even if the narrow ESW (≈1.23V) related to the acidic proton of H_2O hampers the application of these solutions, many different strategies can expand their electrochemical stability, thus enabling the production of cost-effective LIBs [117]. As a matter of principle, intercalation cathodes working in the range 3-4V vs Li^+/Li are already compatible with aqueous environment. On the other hand, hydrogen evolution strongly limits the choice of feasible anodes to those electrodes with a potential about 2-3V vs Li^+/Li [118] due to the absence of decomposition products able to form a stable SEI. An effective route for the widening of the anodic choice consists in the use of the so-called superconcentrated or water-in salt electrolytes (WiSEs), in which the use of high contents of salts induces beneficial effect to the ESW [119]. As also demonstrated for organic electrolytes [120], the dissolution of large amount of salt greatly modifies the solvation sheaths of Li^+, consequently chang-

Table 4.1: Non-comprehensive list of LIBs major fire accidents that received media coverage [113, 115]. *ISC: internal short circuit*

Application:	**Company:**	**Year:**	**Incident:**
Mobile phone	Nokia	2007	Sudden failure and fire.
	Kyocera	2004	Sudden failure and fire.
	Samsung	2016	35 sudden fires in Galaxy Note 7 due to ISCs.
Notebook	Sony	2006	Fire due to separator piercing.
	Lenovo	2007	Risk of explosion in 205000 laptops.
EVs	Chevrolet	2011	Explosion upon crash of Chevrolet Volt.
	Chevrolet	2022	18 battery-related Chevrolet Bolt fires.
	Tesla	2013	Model S took fire after hitting debris.
	Tesla	2016	Model S took fire due to improper connection.
	Tesla	2022	Model X took fire upon crash.
	Jaguar	2018	i-Pace exploded while parked.
Aerospace	UPS Airline	2010	Autoignition in the payload lead to crash.
	Boeing	2013	Fire of auxiliary units on 4 planes.
Storage	Superior Batt.	2021	Water leakage induced fire in Illinois
	Vistra Ener.	2022	Overheating and fire of California facility.

ing the electrochemical properties of water molecules. For instance, at very high LiTFSI concentration (21 mol kg^{-1}) only 2.6 H_2O are bound to each Li-cation (vs. 5 at dilute concentration), therefore permitting to the TFSI anion to form an intimate ion pair with Li^+ as $Li_2(TFSI)(H_2O)_x$. Firstly, the formation of this complex reduces water activity, thus decreasing the amount of *free water* prone to degradation [121]. Additionally, this strong interaction imbalances the stability of TFSI anion, leading to its reduction at a potential higher than water and to the formation of a LiF-based anode-protecting layer. These two factors push down the H^+/H_2 redox couple to 1.6V vs Li^+/Li and increase the oxygen evolution up to 4.9V vs. Li^+/Li, therefore enabling a 3V ESW (*Fig. 4.3*). Super-concentration can also be achieved with different types of salts, such as highly-soluble acetates [117]. Similar effects can be obtained adding a multivalent cation hydrated salt to a Li-salt system and yielding the so-called RT hydrate-melt WiSEs, i.e. a metal salt eutectic systems in which the small present amount of water is totally coordinated by the ions while retaining its fluid properties [122]. Despite these promising results, WiSEs application is still limited to the prototype level and is currently hindered by the high cost of the large amounts of fluorinated salts usually required to induce a stable SEI formation.

Another category of non-flammable LEs is instead represented by ionic liquids (ILs), i.e. ionic salts with a melting temperature conventionally set below 100°C [123]. If the liquid state is retained also at 25°C, the solution is more specifically labelled as room-temperature IL. Generally, they are composed by a weakly coordinating anion and an asymmetric and bulky organic cation (quaternary ammonium salts or cyclic amines such as imidazolium or pyrrolidinium, *Fig. 4.4*), whose dimension helps to reduce the ionic

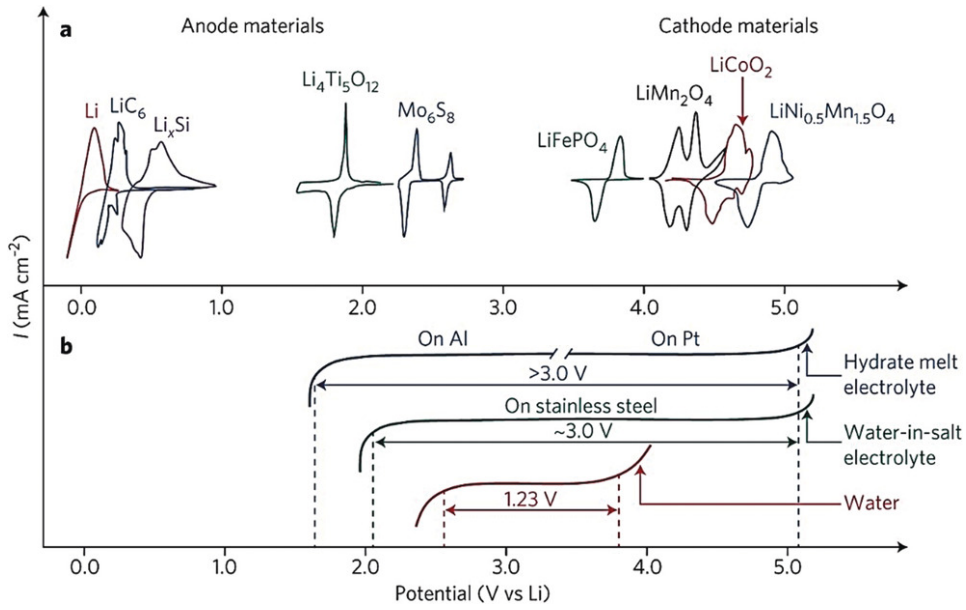

Figure 4.3: ESW of water (pH=7), WiSE and hydrate-melt WiSE compared with the redox potentials of selected LIBs' electrodes. Reproduced with permission from [116].

forces and, as a consequence, T_m [124]. Depending on the chemical nature of the cation, ILs can be further classified as aprotic or protic ionic liquids. The attractiveness of these compounds resides in the interesting properties imparted by their peculiar composition. In addition to non-flammability, ILs usually present high ionic conductivity, low volatility and enhanced thermodynamic stability [125]. These desirable features can be achieved coupling different anion-cation couples, therefore tuning Coulombic or van der Waals interactions and consequently the physico-chemical properties of the resulting ILs [126]. Even if ILs are in principle composed only by a single salt, no ILs based on Li cations are currently reported in the literature [127]. Therefore, IL-based electrolytes are usually composed by three components: a solvent, a supporting electrolyte and the electroactive species itself (i.e. Li^+ or Na^+). Apart from this complication, ILs implementation is also hindered by their high viscosity which reduces wetting and slows ion diffusion, making them less suitable for high power applications [128, 129].Nonetheless, some satisfying examples of IL able to work in contact with Li have been recently reported [130]. To overcome these limitations, ion modification or different ionic combination have enabled the production of new ILs with ESW up to 6V, consequently enabling high energy density storage devices [131]. Alternatively, also different mixtures that overcomes the original concept of employing bulky cations to achieve RT liquefaction have been recently explored. The main examples following this new approach will be reported in the next section.

4.1.1 Deep eutectic solvents as electrolytes:

A similar family of LEs that shares many properties with ILs, whose are sometimes considered a sub-class, is the one of deep eutectic solvents (DESs). As suggested by the name, DESs are liquid systems formed by the mixture of two or three solid compounds possessing an eutectic point way lower than their melting point [132]. This result is usually achieved through the mixing of Lewis or Brønsted acids/bases or of a hydrogen-bond donor (HBD) with a hydrogen-bond acceptor (HBA) [133]. It is worth noticing

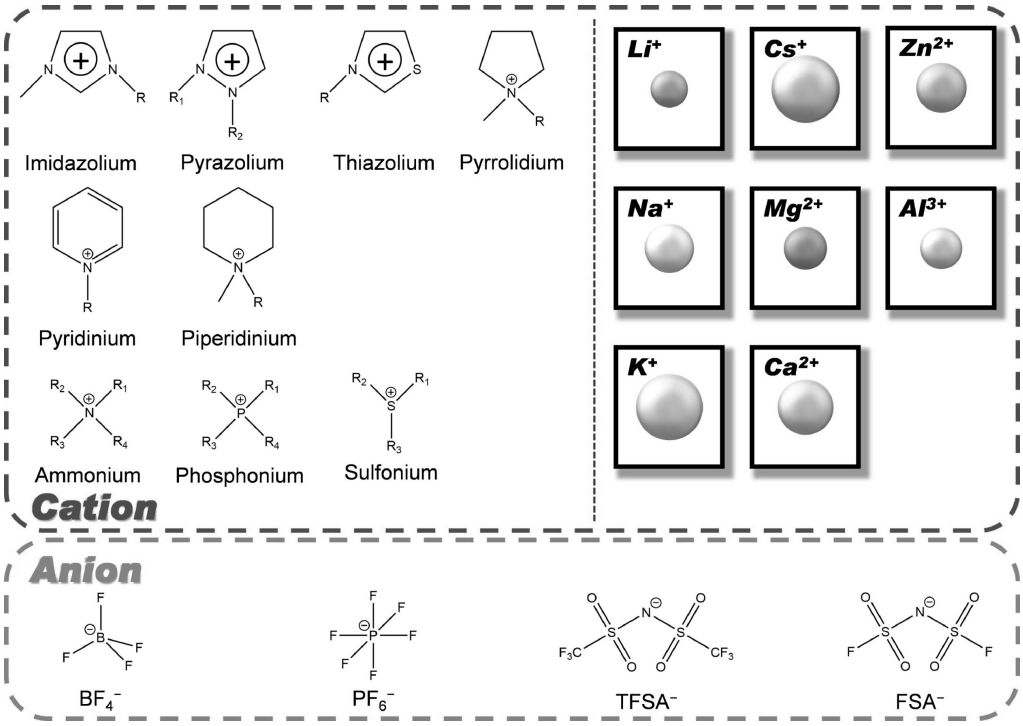

Figure 4.4: Non-comprehensive example of anions, cations and electrochemical active species employed in IL electrolytes. Reproduced with permission from [125]. Copyright 2022 Elsevier.

that this second notation is conventionally employed also in those cases when no H-bonds are effectively formed to distinguish the two compounds of the mixture.
Generally speaking, the majority of DESs can be classified under one of these five classes [134]:

- *Type I:* quaternary ammonium salt (HBA) and metal chloride (HBD).
- *Type II:* quaternary ammonium salt (HBA) and metal chloride (HBD).
- *Type III:* quaternary ammonium salt (HBA) and an amide or another HBD.
- *Type IV:* metal chloride hydrate (HBA) and an amide or another HBD.
- *Type V:* non ionic DESs.

The most famous example is represented by reline, a *Type III* DES composed by a 1:2 molar ratio mixture of two solid powders, choline chloride (T_m=302°C) and urea (T_m=133°C), which presents an eutectic point T_3=12°C and appears liquid at RT [135]. The main advantage of such systems is that they are usually comprised of non-toxic, non-flammable, environmental friendly, cheap chemicals (e.g. choline chloride is a well-known chicken feed [136]) which can be easily handled as solid and can be later processed through a simple mixing of the two powders. No additional solvents or reactions are required, therefore avoiding the need for further purification. Additionally, thanks to the wide range of feasible constituents, it has been computed that about 10^6-10^8 of different binary DESs can be investigated [137]: this allows a great tunability of the resulting properties that can further be expanded moving to the scarcely investigated ternary systems.
Thanks to these desirable features, several DESs have been successfully applied in a vast

range of applications as replacement for more pollutant and expensive solvents. These mixtures can be used to selectively separate and capture different gas species such as SO_2 and CO_2 [138, 139]. Biocatalysis represents another major application field: DESs can be used as non-conventional reaction media to facilitate alternative biocatalytic pathways [140]. Other biological applications of these solvents span from biomass processing to genomics and pharmaceutical research [141–143].
Finally, and more interestingly for the aim of this work, DESs has also been applied in the field of electrochemistry as extraction agents for electrode materials recycling or as medium for metal (Zn or Ni) plating [133]. Unfortunately, the presence of electrochemically unstable groups (-OH, -NH, -COOH) required for the establishment of the DES-forming interactions causes a major shortcoming: their ESW appears narrower than the one of the imidazolium salt-based ILs, hitherto hindering any application in lithium energy storage devices. Consequently, neoteric DESs that go beyond the utilization of easily degraded carboxyl- or hydroxil-containing materials (such as choline chloride) have to be investigated.
Even if some papers reported the dissolution of a lithium salt into a standard *type-III* DES [144], the few examples currently demonstrating successful cycling in LIBs exploit a different approach. Rather than adding a conductive salt to an already liquid eutectic solution, Boisset et al. proposed an innovative DES in which the HBA acceptor behaviour is directly carried out by the lithium salt itself (LiTFSI), coupled with N-methylacetamide (MAc) as HBD [145]. Avoiding the use of an unstable HBA, this electrolyte resulted stable in contact with a LTO anode and was able to operate for more than 60 cycles in a LTO|DES|LFP cell. The postulated mechanism behind the formation of a deep eutectic point is schematically shown in *Fig. 4.5a*: thanks to its dipolar structure, MAc is able to operate as a complexing agent for both the ions of the salt. In particular, the electronegative oxygen atom of the carbonyl group coordinates the Li^+ cation while the counteranion of the salt is attracted by the electropositive nitrogen atom of the amide. This interaction substitutes the hydrogen bonds otherwise present intramolecularly between different MAc molecules (N-H···O) that guarantee the solid state of the amide at RT (T_m=28°C). Following the success of this approach, other works have successfully improved this system encompassing the liquid electrolyte into a polymeric matrix in order to improve electrochemical stability and ionic conductivity while reducing the leakage risk [146, 147]. Dinh *et al.* substituted MAc with a different amide, 2,2,2-trifluoroacetamide (TFA, T_m≈74°C), which mixed with LiTFSI displayed a deep eutectic point below RT (≈10°C) and a satisfying ionic conductivity (1.5 mS cm^{-1} at 25°C) [148]. However, the system was overall ill characterized: despite claiming stability vs. Li anode, a LMB equipped with a LMO cathode demonstrated a CE≈80% during 10 cycles and no careful evaluation of the ESW was performed. Driven by the need for a thorough investigation of similar systems, a new deep eutectic electrolyte based on TFA, $LiPF_6$, and specific additives developed during my thesis work in the frame of the bilateral Italy-Israel ENVIRONMENTALIST project will be reported herein [149].

TFA-based deep eutectic electrolytes:

Considering its low flammability and its low cost, TFA was selected as feasible HBD for deep eutectic electrolytes. Coupled with $LiPF_6$ as HBA and exploiting the aforementioned intermolecular interaction, it resulted possible to achieve a liquid clear mixture starting from two white powders possessing a melting point clearly above RT (*Fig. 4.5b*).

As displayed in *Fig. 4.5c*, the mixture comprising a 80:20 molar ration of TFA:$LiPF_6$ presented an eutectic point of ∼4°C, therefore suitable for operation as a liquid electrolyte. The resulting DESs presented a RT ionic conductivity ∼ 3 S cm^{-1}, approximately threefold higher than the one achieved with the analogue LiTFSI electrolyte (*Fig. 4.5d*). However, despite its better conduction, this system did not offer any improved ESW: even if presenting a very high oxidative potential (∼4.5 V vs Li^+/Li) TFA:$LiPF_6$ 80:20 DES resulted strongly unstable in contact with Li metal and did not permit any stable stripping-plating behaviour. Consequently, the addition of carbonate additives was investigated to verify their effect on the stability at low potentials. EC and FEC were selected taking in account their reduced flammability and their well reported capability of forming stable SEIs in LIBs. As expected, their incorporation into the DES strongly improved the electrochemical stability of the TFA:$LiPF_6$ 80:20 +10%EC+5%FEC DES and also enabled more than 60 cycles of stable cycling in a LMB based on a LFP cathode and cycled at 0.1C (*Fig. 4.5e*). The choice of this cathodic material was motivated by the capability of this solution to extract Ni, Mn, and Co from other commercial cathodes such as NMC 622 demonstrated by inductively coupled plasma (ICP) analyses.
Additionally, the high safety standards of this system were confirmed through accelerated rate calorimetry (ARC). Compared to a commercial LP30 electrolyte, our DES displayed an increased thermal stability and a reduced tendency to thermal runaways. After these promising results, also a different lithium salt (LiFSI) has demonstrated its ability in the formation of TFA-based highly-conductive DESs: this work is still under progress as part of a master thesis work that I partially supervised during the final months of my PhD.
Additional details regarding this system and the precise methodology employed for its characterization can be found in the following scientific publication, whose complete discussion goes beyond the aim of this thesis devoted to solid state electrolytes [149].

4.2 Solid state electrolytes:

Despite the major improvements that can be still developed for LEs, it is strongly believed that next-generation energy storage devices will rely on solid-state electrolytes (SSEs) [27]. The reasons behind this choice are several and can be traced both on the aforementioned limitation connected to LEs (high flammability and/or toxicity, risk of leakage, incompatibility with lithium anodes, etc.) but also on some precise advantages typical of specific solid-state systems. Generally, almost all the SSEs share the following desirable properties: non flammability, high temperature stability, non-volatilization and higher dendrite resistance which contribute to the improvement of devices' safety while their ESW is usually sufficiently large to permit the implementation of high-voltage cathodes and, consequently, higher energy densities [150].
These features make all-solid-state batteries (ASSBs) one of the most hyped technology from the automotive industry. Additionally, some SSEs allow only Li^+ motion and this factor helps to mitigate other issues typical of LEs such as bulk polarization and self discharge, respectively thanks to a negligible anionic and electronic conductivity [151].
However, SSE implementation also presents some major obstacles that are still completely or partially unresolved both regarding the electrochemistry and the manufacturing of these electrolytes (such as low RT ionic conductivity, large interfacial resistance due to a bad adhesion with electrodes, and poor compatibility with Li metal) that will

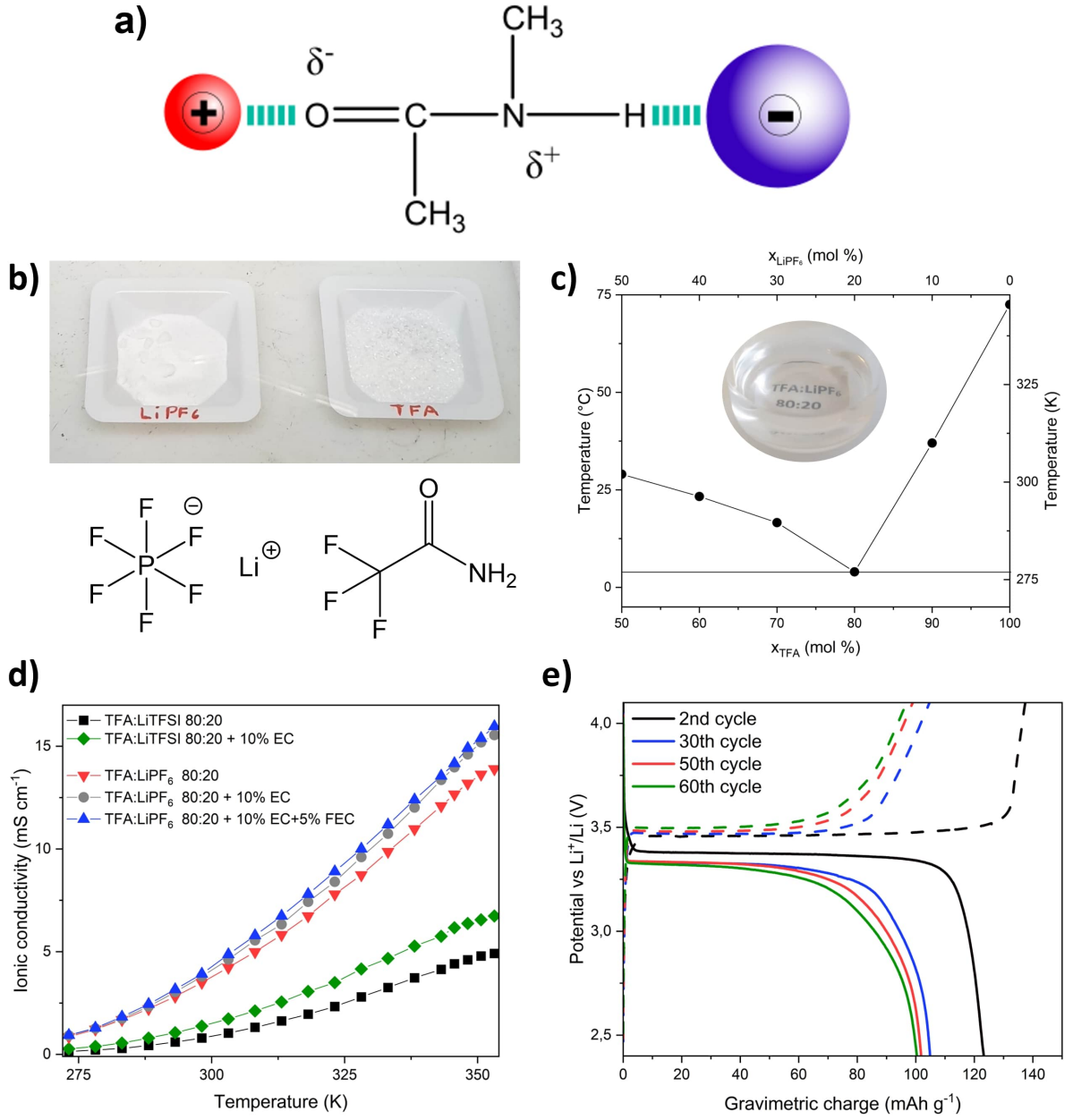

Figure 4.5: a) Schematic representation of the intermolecular interaction between a lithium salt and MAc. b) $LiPF_6$ and TFA powders with the respective chemical formula. c) Tentative phase diagram of TFA:$LiPF_6$ system with an inset showing the mixture at the eutectic point. d) Ionic conductivity of TFA:$LiPF_6$ electrolyte compared with TFA:LiTFSI. e) Discharge profile of a Li|LFP cell equipped with TFA:$LiPF_6$ 80:20 +10%EC+5%FEC electrolyte [149].

be specifically discussed afterwards [152].
Taking in account all these considerations, ASSBs emerge as a long-term and high-risk research task that can anyway enable unprecedented performances for secondary lithium batteries [153]. To better understand all the challenges related to this technology, the most important SSEs, grouped depending on their chemical nature, will be introduced in the next sections. Main peculiarities and drawbacks of every specific category will be highlighted, focusing in particular on those systems of interest for the aim of this dissertation, i.e. nanocomposite ceramic-in-polymer SSEs and sulfide electrolytes.

4.2.1 Polymer SSEs:

Polymer electrolytes have been the first solid electrolyte to be extensively investigated for lithium battery application. Their history can be traced back to 1973 when Wright *et al.* unveiled the ability of polyethylene oxide (PEO) to effectively coordinate alkali ions and to form a ionically conductive matrix into which Li^+ ions are able to move thanks to an hopping conductive mechanism aided by chain segmental motion [154]. After this first publication of Wright and the pioneering works of Armand [155], a plethora of different polymers has demonstrated a good capability of enabling ion conduction. The great variety of these systems complicates an unequivocal classification of polymer SSEs that can anyway be grouped under two main distinct classes [89]:

- Solid polymer electrolytes (SPEs): dry electrolytes in which a lithium salt is dissolved into a solid polymer.
- Gel polymer electrolytes (GPEs): systems comprising a plasticizing solvent and/or an organic electrolyte solution dispersed into a polymeric matrix.

The first category comprehends those polymers that present a polar group able to coordinate lithium ions [156]. For instance, ether-based PEO is a notable example of this family: the presence of its electron rich oxygen atoms results in a high dielectric constant and, consequently, in a excellent solubility with respect to lithium salts. Its low glass transition temperature (-60°) and its good stability with respect to Li anode have made this polymer one of the most investigated SPEs in scientific literature [157]. All these properties are also coupled to other interesting features such as excellent flexibility and processability, reduced toxicity, and relatively low cost. However, the segmental chain motion that supports the Li^+ conduction takes place only in the highly-mobile amorphous region of the polymer while it is conversely hindered by the rigid crystalline domains. Unfortunately, the semi-crystalline nature of PEO (70%-85% of crystallinity at RT) has the detrimental effect of hindering the ion conduction below its melting point ($T_m \approx 65°$). As a consequence, the ionic conductivity dramatically drops from $\sim 10^{-3}$ S cm^{-1} at 80°, where the whole crystalline phase is molten, down to $\sim 10^{-6}$ S cm^{-1}-10^{-7} S cm^{-1} at RT, totally unsuitable for any commercial application [158]. Additionally, other major issues have plagued the commercial exploitation of PEO SPEs. Firstly, its low transference number ($t_{Li^+} \sim 0.1$-0.2) involves that anionic mobility is higher than the cationic. As a consequence, undesired cell polarization can occur due to the build-up of charged non-active species at the electrode interface. Moreover, the soft and flexible PEO matrix that greatly enhances the electrolyte adhesion with the electrodes results prone to dendrite piercing and, consequently, short-circuiting [159]. As clearly demonstrated by Tikekar *et al.* [160], to prevent dendrite growth a SSE in contact with a Li

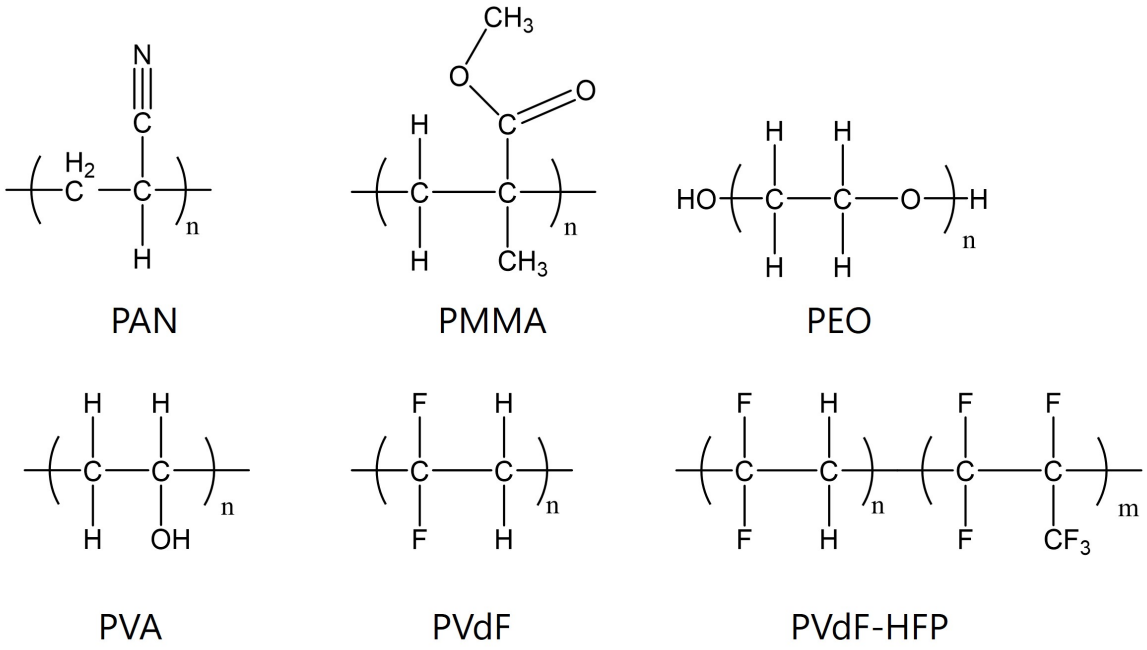

Figure 4.6: Non-comprehensive list of polymers employed for SPEs and GPEs.

anode must at least possess a shear modulus G that satisfies the following condition:

$$G > 1.8 G_{Li}(T)$$

where $G_{Li}(T)$ is the shear modulus of Li at the working temperature T. At RT, this results in a minimum SSE modulus ≈6 GPa. This requirement is completely unsatisfied by PEO-based SPEs which present G≈0.1 GPa.
Due to the aforementioned conductivity shortcomings, PEO electrolytes usually have to operate at high temperature but display anyway unsatisfying cycling stability due to poor mechanical properties of the molten phase which worsens the risk of dendrite piercing [159, 161]. For these reasons, numerous methods such as co-polymerization, cross-linking or polymer blending have been applied throughout the years as a solution to these problems. Among all of them, promising results have been achieved with the dispersion of ceramic nanoparticles into the polymer matrix. Those nanocomposite systems will be exhaustively described in the following *Sec. 4.2.3*.
Apart from polyethylene oxide, several other SPEs have demonstrated good or even better lithium conducting properties. A non-comprehensive list can include polyacrilonitrile (PAN), polyvinyl alcohol (PVA), polysiloxanes, polyurethanes, polycarbonates and the respective co-polymers (*Fig. 4.6*) [162–164] . However, their description lies outside from the scope of this work whose experimental part about SPEs will be focused on the investigation of PEO-based systems.

A separate discussion has to be addressed to GPEs. Despite being often described as solid electrolytes due to their free-standing appearance, GPEs contain a non negligible liquid content that collocates them in an intermediate situation [165]. Such liquid fraction can be represented by ILs, organic electrolytes or plasticizing solvents whose presence endow many advantages. Increased mobility, improved conduction mechanism and more homogenous electrodes' wetting are some of the usually achieved enhancements

[166]. The conduction model, in which the conductive pathways appeared disordered, is conventionally described with the use of the Site Percolation Theory which describes how a system can be considered *macroscopically connected* through the random opening of conductive pathways into its structure [167]. This model, which results well established for liquid diffusion in porous media, can be easily extended to GPEs in which a liquid conductive phase is dispersed into a polymer scaffold. In those cases, a so called percolation threshold is existent: this critical value is the point (that can be related to liquid fraction uptake, salt concentration, etc.) where a transition from a disconnected insulating system to a connected conductive network is experienced. In the frame of this model, the ionic conductivity σ is usually expressed as

$$\sigma = A(x - x_{tr})^{\alpha} \tag{4.11}$$

where A is an adjustable constant, x is a key parameter related to the conducting phases, x_{tr} is the respective percolation threshold value and α is the critical exponent that describes the dimensionality of the conductive network (i.e 1D, 2D or 3D).
The suitable polymers employable for GPEs often coincide with the ones employed for SPEs with some interesting exceptions of ionic-insulating compounds such as poly(methyl methacrylate) (PMMA) and polyvinylidene fluoride (PVdF) [168, 169]. In particular, this latter example deserves some further clarification.
Compared to other polymeric materials, PVdF possesses elevate toughness and mechanical strength thanks to a mainly crystalline nature related to the coexistence of several different phases (α, β, γ, and δ), and excellent thermal ($T_{decomp} \approx 400°$), chemical and electrochemical stability due to its fluorinated nature [170, 171]. A more amorphous polymer can be instead achieved through the random co-polymerization of PVdF with hexafluoropropylene (HFP) [172]. As a consequence, the resulting PVdF-HFP copolymer shows improved flexibility due to the presence of the dangling lateral -CF_3 chains which partially disrupt the crystalline domains. Both PVdF and PVdF-HFP have been largely investigated as polymeric scaffold for GPEs during the past years thanks to their capability of absorbing large volumes of non-aqueous electrolytes [173]. PVdF-based GPEs have been mainly prepared using two different approaches: solvent casting and phase inversion process. In the first technique, the polymer is dissolved in a proper medium such as acetone together with the desired conductive solution, usually a mixture of organic carbonates and lithium salt [174]. After the evaporation of the solvents, a quasi-solid GPE is obtained. Conversely, the phase inversion permits to produce a dry porous polymer framework that can be later soaked with the desired electrolyte [175]. This is usually achieved immersing the as-casted film, conventionally deposited from an organic mixture, in an orthogonal solvent such as water. The different surface tension between the components induces changes in the morphology and in the porosity of the resulting gel. Despite the differences between these two systems, in both of them the lithium conduction is assured by the presence of the liquid electrolyte due to the insulating behaviour of PVdF. However, more recent publications by Zhang *et. al* claimed the fabrication of dry PVdF-based SPEs displaying unprecedented RT ionic conductivities in the order of 0.1-1 mS cm^{-1} without the presence of any liquid phase [176, 177]. These electrolyte were produced with a solvent casting approach dissolving PVdF and lithium bis(fluorosulfonyl)imide (LiFSI) into a dimethylformamide:tetrahydrofuran(DMF:THF) 3:7 v:v binary solvent. As described by the authors, the resulting film were later dried at 80°C to eliminate the trapped solvent. Considering the high boiling point of DMF (T_b=153°C), it is questionable if a similar heating treatment may result sufficient for its

complete removal from the polymer matrix. As expected, TGA analysis performed on an analogous systems showed a sharp weight loss around 150°C in the order of 14% wt, attributable to the presence of residual solvent into PVdF [178]. Therefore, the excellent conductivity of the electrolyte appears strictly connected to the presence of a liquid fraction. After this observation a question remained anyway unresolved: can this system be defined as SPE, due to its totally solid appearance, or is it better to describe it as a GPE? A final clarification emerged from some subsequent analyses. After acknowledging the effective presence of a non-negligible DMF content in their systems not reported in the previous publications, Zhang's group demonstrated with the aid of Raman and FTIR spectroscopy that all the solvent molecules appear strictly bound to the Li^+ ions [179, 180]. Those $[Li(DMF)_+]^+$ complexes are transported thanks to the interaction with PVdF chains. Consequently, the conduction mechanism is described as totally different by the one experienced in classic GPEs with a major uptake of free solvents molecules where the PVdF matrix displays no active contribution towards the ionic conduction. Relying on these assumptions, the authors affirm that this polymer electrolyte can be labelled as an SPE due to the absence of free solvent molecules. Independently by the name tag that can be attributed to this electrolyte, the good performances achieved with this approach have been subsequently demonstrated also in other original works [181, 182]. Recently, also our group has decided to investigate again a similar system testing different kinds of PVdF and PVdF-HFP select the most promising candidate. The main results regarding this research will be presented in *Chap. 5.3*, where both a deep investigation on the role of residual DMF and the subsequent encompassing of functionalized fillers into the system will be reported.

4.2.2 Inorganic SSEs:

If the intrinsic softness of polymers raises serious concerns related to lithium filament propagation, ceramic or inorganic solid electrolytes (ISEs) could in principle look like a straightforward and valid alternative. Their better mechanical properties and their higher Young modulus are expected to slow or to prevent the growth of dendrites in LMBs [183]. Nonetheless, this does not result completely true since Li filaments are anyway capable of penetrating the stiff ceramic matrix of several ISEs above a certain stripping/plating critical current density (CCD) [184]. Despite their stiffness, lithium is generally able to grow along the grain boundaries, cracks or pores of the SSEs finally leading to short-circuit. Other issues usually encountered with ISEs are related to the bad contact with electrodes, due to their poor ductility, and to the unsatisfying ESW. However, their high ionic conductivity (10^{-4}-$^{-2}$ S cm^{-1} at 25°C) makes ceramic electrolytes the most suitable SSEs for performant room-temperature ASSBs. In any case, the plethora of different chemistries employed for the production of ISEs does not permit to collectively assess their pros and cons. Therefore, it results necessary to singularly describe the different types of ISEs, usually divided under two major groups: oxides and sulfides [185]. Oxide ISEs can be further divided into garnets, NASICONs (Na Super Ionic CONductors), and perovskites. While sulfide SSEs will be carefully presented later, the main properties of oxides will be briefly outlined herein and in *Tab. 4.2*.

Generally, oxide electrolyte materials present large energy gaps between the valence and the conduction band. This endows them with incredible stability at high potential,

Table 4.2: Main advantages and drawbacks of selected families of Li^+-conducting ISEs. Re-elaborated by [185].

ISE:	**Advantages:**	**Drawbacks:**
NASICONs	Good chemical stability	Low stability vs. reduction
	High thermal stability	High grain boundary resistance
	High Young modulus	Brittleness and poor adhesion
	Good σ at RT ($\sim 10^{-4}$-10^{-3} S cm^{-1})	Energy consuming synthesis
	Good stability at high potentials	
Perovskites	Good stability at high potentials	Lower σ ($\sim 10^{-4}$ S cm^{-1})
	High thermal stability	High grain boundary resistance
	High Young modulus	Poor stability vs. Li
		Sintering at high T leading to Li loss
Garnets	High thermal stability	Bad electrode contact
	Stability with Li anode	High grain boundary resistance
	High Young modulus	Difficult to process
	Good σ at RT ($\sim 10^{-4}$-10^{-3} S cm^{-1})	Energy consuming synthesis
	Good stability at high potentials	
Sulfides	High σ (up to $\sim 10^{-2}$ S cm^{-1})	High sensitivity to water
	Ductility and better adhesion	Low chemical/electrochemical stability
	Low grain boundary resistance	Lower thermal stability
	Energy-friendly synthesis	Interfacial reactions with cathodes

as shown in *Tab. 4.2* for garnets, perovskites and NASICON-type Li-ion conductors.
Going into detail, the first ISE that somehow belongs to one of these family was reported by Goodenough *et al.* in 1976. $Na_{1+x}Zr_2Si_xP_{3-x}O_{12}$, a material displaying for the first time an original NASICON-type structure, was observed to present a Na^+ ionic conductivity $\sim$5 S cm^{-1} at 300°C for x$\sim$2 [186]. As suggested by the name that hitherto described this class of compounds independently from their application, the peculiar morphology of the crystal enabled fast sodium conduction thanks to the channels present in the crystalline framework. However, this specific material displayed poor Li^+ conduction due to the unsuitability of its ion channels for lithium ions transport. Nonetheless, a careful tuning of the structural parameters has enabled to design a plethora of lithium ion conductors with a NASICON-type structure, suitable both as electrodes and electrolytes, based on the general chemical formula $AMM'(XO_4)_3$ where [187]:

- A=Li, Na, K, Mg, Ca;
- M,M'=Fe, Al, Ge, V, Ti, Zr, Sc, Mn, Nb, In, etc.;
- X=S, P, Si, As.

Focusing on NASICON-type Li^+-ion conductors, two of the most promising SSEs belonging to this family are $Li_{1+x}Al_xTi_{2-x}(PO_4)_3$ (LATP) and $Li_{1+x}Al_xGe_{2-x}(PO_4)_3$ (LAGP) [188]. Both these materials are achieved through the Al doping of a pristine phase, $LiTi_2(PO_4)_3$ and $LiGe_2(PO_4)_3$ respectively. Smaller Al^{3+} ions substituting bigger cations reduces the unit-cell of the framework and makes it better suited for Li^+ ions. The doping induces an improvement of σ_{Li^+} of about 3 order of magnitudes. Both ISEs are also air-stable and present very high oxidation stability but result prone to reduction and degradation when in contact with Li anodes [189]. This further complicates their implementation in ASSBs.
Another family of oxide SSEs with a peculiar crystalline structure is the one of perovskites. Ideal perovskite materials present a ABO_3 or $AA'BB'O_3$ composition where A/A' sites are filled by larger cations such as Li^+, Sr^{2+}, and La^{3+} while B/B' positions are occupied by cations with smaller radius such as Ti^{4+}, Zr^{4+}, and Ta^{5+} [190]. Li-ion conduction is provided by the presence of vacancies in the A-sites that enable Li^+ motion into the framework through octahedral channels [191]. The most significant example of lithium-ion conducting perovskites is $La_{0.66-x}Li_{3x}TiO_3$ (LLTO). This ISE results chemically and thermally stable also in air. In addition, LLTO presents a very large transference number and an excellent stability vs. high potentials. However, the large grain boundary resistance partially suppresses the RT ionic conductivity ($\sim 10^{-5}$ S cm^{-1}). Moreover, lithium insertion and Ti^{4+} reduction are observed below 1.5V-1.8V vs Li^+/Li, reducing the anodic compatibility of perovskites. Additionally, other major drawbacks are related to the processability: the very high sintering T required for densification (>900°C) can also promote Li evaporation while the brittleness of the final product both complicates the cell assembly and the selection of the optimal stacking pressure that should enable an intimate contact with the electrodes without inducing any crack or fracture. These several shortcomings can be partially overcome inducing some structural modification via the addition of doping elements for both A or B sites. Partial substitution of La with larger cations in the A sites such as Sr^{2+} or Ba^{2+} may improve the bulk conductivity thanks to an enlargement of the lattice and to an improved number of Li_+ required to maintain the electroneutrality of the crystal [192]. On

the other hand, Ge-doping in the B sites has demonstrated its capability to enhance the structural integrity of the densified ISE acting as a sintering aid and reducing the grain boundary resistance[193]. This enabled an improved RT σ_{Li^+}, nonetheless in the order of $\sim 10^{-4}$-10^{-5} S cm^{-1}.
Higher values of ionic conductivity can instead be achieved with the third and last category of oxide SSEs: Li^+-conducting garnets. The first report of Li^+ transport in garnets is dated back to 2003 when Thangadurai and Weppner demonstrated that $Li_5La_3M_2O_{12}$ (M=Nb, Ta) possessed $\sigma_{Li^+} \sim 10^{-6}$ S cm^{-1} [194]. This first discovery paved the path to the production of the most promising garnet thanks to the replacement of M with tetravalent Zr: $Li_7La_3Zr_2O_{12}$ (LLZO) resulted both highly conductive ($\sim 10^{-4}$ S cm^{-1}) and stable in contact with metallic Li, even if moisture and oxygen sensitive [195, 196]. Tailored synthetic procedures and doping approaches are capable to stabilise the highly conductive cubic phase of LLZO in spite of the more insulating tetragonal one [197] leading to RT σ_{Li^+} up to 10^{-3} S cm^{-1}. Its high shear modulus, about 60 GPa, can also act as an effective physical barrier against lithium dendrites. However, these promising features can be achieved only in presence of a dense structure that avoid lithium penetration and assures a limited grain boundary resistance, otherwise extremely detrimental. This processing step does not always result simple due to the very stiff nature of garnet materials and usually require elevate temperature and high pressure sintering. Those harsh conditions increase the energy consumption associated to garnets production, making them less cost effective. Another shortcoming related to the poor ductility of garnets is the scarce contact between the ISE and the electrodes, which in turn implies a large interfacial resistance [198]. The best way to overcome this issue is the application of a high-stack pressure during cell cycling. Even if effective and employed for a wide range of ISEs, this approach results mostly unpractical on the commercial scale.
Therefore, it would be desirable to find an alternative category of ISEs that can couple interesting conductive properties with an higher degree of processability. As it will be described in the next section, a good trade-off can be found employing sulfide materials.

Sulphide SSEs:

Li conductivity has been observed in sulfide systems since the pioneering work of Pradel and Ribes [199]. Generally, sulfide SSEs share many properties with oxides such as the crystal structure but the larger S^{2-} radius compared to O^{2-} implies the presence of wider conductive channels in the framework. Additionally, the binding energy of Li^+ with S^{2-} is smaller than the one established with O^{2-}, hence improving ion migration [200]. These two features impart a higher ionic conductivity when compared to oxide analogues.
At least three main subcategories can be grouped under the wide family of sulfide SSEs: glass, glass-ceramic and crystalline sulfide electrolytes. Even if sharing some major features, each single class possesses its own specific characteristics that will be described hereafter.
Glassy sulfides possess the advantages of easy film processability, no grain boundary resistance, isotropic conduction, and high compositional tunability [201]. Room-temperature σ_{Li^+} in the order of 10^{-5}- 10^{-4} S cm^{-1} can be achieved in compounds such as Li_2S-SiS_2 or Li_2S-P_2S_5. The conductivity can also be pushed up of one order of magnitude with the addition of lithium halides, such as LiI, that have the effect of increasing the lithium concentration. However, this is usually achieved at the expense of the ESW.
Heat treatment or ball-milling of different Li-P-S glassy sulfides can induce some par-

tial recrystallization, leading to the formation of glassy-ceramic SSEs [202]. Depending on the conductive or insulating nature of the crystalline phase, glass-ceramic SSEs can result more or less performant than the parent glass precursor. The advantage of this approach mainly resides in the possibility of achieving some metastable superionic phases, not directly obtainable with common synthetic routes, with a negligible electronic conductivity.
Finally, the third category is the one of crystalline sulfide SSEs. Theoretically, crystalline sulfides can display superior σ_{Li^+} thanks to the presence of well-defined conduction pathways [203]. However, for long time no satisfying results were experimentally achieved. The things changed in 2001 when Kanno et Murayama of Kobe University, Japan, reported the first thio-LiSICON (Lithium SuperIonic CONductor) [200]. Generally, thio-LiSICONs can be divided into binary systems, Li_2S-MS_n with M=P, Si, and B, or ternary systems, Li_2S-P_2S_5-MeS_n with Me=Si, Ge, and Sn. Best results are achieved with those Ge-based ternary systems like $Li_{4-x}Ge_{1-x}P_xS_4$ (LGPS) that present $\sigma_{Li^+}\sim 1.2\ 10^{-2}$ S cm^{-1} at 27°C, comparable to liquid electrolytes [204]. However, the high cost of Li_2S, the poor air stability of these compounds, and the low compatibility with cathode materials still appear as mainly unresolved problems. Additionally, Ge presence further worsens the situation due to its expensiveness and to its low stability against oxidation [201].
Some improvements regarding the electrochemical stability of crystalline sulfides can be obtained moving towards argyrodite-type SSEs. This class of electrolytes is named after the so-called mineral Ag_8GeS_6 which presents a cubic structure and the highest Ag-ions conduction [205]. The crystalline framework remains mostly unaffected when silver ions are replaced by other cations such as P^{5+}. Consequently, tetrahedrally close-packed $F\bar{4}3m$ cubic Li-argyrodite such as Li_7PS_6 can be obtained at high temperature and then stabilised at RT with the partial substitution of S^{2-} with halide X^- anions (X=Cl, Br, or I). In this conventionally ordered structure, the anions compose a cubic close-packed lattice while PS_4^{3-} and S^{2-} respectively occupy octahedral and half of the tetrahedral sites [206]. However, thanks to the similar ionic radius, small halide anions such as Cl^- and Br^- can partially exchange their positions with S^{2-} inducing the formation of a more disordered and conductive structure. As a consequence, the resulting halogen-substituted and anion-disordered Li_6PS_5X argyrodite such as Li_6PS_5Cl (LPSCl) demonstrated high ionic conductivity $\sim 10^{-3}$ S cm^{-1}. Into this particular framework, Li^+ conduction takes place as a series of ion jumps that can be classified in three types: doublet, inter-cage, and intra-cage. Doublet jumps occur between two face-sharing type 5 tetrahedra through the type 5a site. Instead, in inter-cage and intra-cage jumps lithium motion happens between two non-face sharing type 5 tetrahedra respectively belonging to the same and to different 4d Li-centered cages.
In addition to its interesting and peculiar conduction properties, LPSCl production is based on a sustainable and solid supply chain that does not present any availability constraint in the framework of current geopolitical situation [207]. This results as an interesting advantage compared to other ISEs such as LLZO or LLTO which are composed of critical rare earth elements like Zr and La.

Despite their promising ionic conductivity, argyrodites compounds nonetheless present several electrochemical limitations. First of all, LPSCl results unstable in contact with Li anode, presenting a phosphorous reduction potential of 1.08 V vs Li^+/Li. However, the compatibility is somehow ensured by an anodic SEI comprised of Li_2S and Li_3P [208].

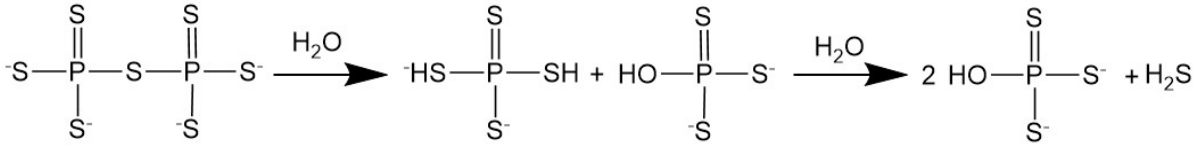

Figure 4.7: Reaction scheme of water with a sulfide ISE based on $P_2S_7^{4-}$ units.

Accordingly to this, the resistance at the interface is observed growing during the first hours of contact before reaching a plateau that confirms the formation of a stable SEI [209]. Oxidation stability appears instead more critical. LPSCl can be easily oxidized to LiCl and Li_3PS_4 above 2.5 V vs Li^+/Li. Even if the material appears somehow kinetically metastable also in contact to high-voltage cathodes due to the appearance of a cathode-electrolyte interface, the stacking up of decomposition products induces an increase of the interfacial impedance upon cycling and a continuos capacity fading [210]. Another major issue related to argyrodites is their chemical stability in air since moisture-induced hydrolysis induces the formation of poisonous H_2S gas (*Fig. 4.7*) [185]. Apart from the obvious safety concerns, this degradation strongly affects the electrochemical performances of the ISE. As a consequence, argyrodite sulfides must be handled and processed in dry rooms avoiding any contact with moisture. Unfortunately, the chemical instability of argyrodites is not limited to water but is extended to polar solutions: solvents with high polarity indexes (acetonitrile, ethanol, NMP, etc.) cause the production of degradation residues and seriously affect the ion transport [211]. This is related to their strong Lewis base behaviour: the presence of electronegative elements such as N or O with lone-pair electrons leads to the reaction with electrophilic P^{5+} of argyrodites. Only non-polar organic solvents with low dielectric constants such as p-xylene or toluene permit the retention of the crystalline structure and of the related conductive properties. From a manufacturing point of view, this generally restricts sulfide processing to dry mixing approach such as cold-pressing pelletization. Even if the lower modulus of argyrodites (and sulfides in general) when compared with stiffer oxide ISEs somehow favours their bulk processing and induces a better contact with electrodes at lower stack pressures, the use of thick pellets reduces the energy density of the resulting ASSBs [212]. Alternative dry procedures such as sputtering or physical vapour deposition may enable the production of thinner electrolytes but usually require expensive and multi-step processes unsuitable for large-scale production. Therefore, the development of solution-based roll-to-roll methodic results critical for a wider implementation of argyrodite SSEs [213]. A feasible idea consists in the production hybrid systems comprising a small quantity of polymer binder that improves the processability the ISEs. This approach, with all the related issues, will be carefully described in the next section devoted to the topic of nanocomposite electrolytes.

4.2.3 Composite SSEs:

As explained in the previous *Sec. 4.2.1*, two of the main problems encountered in PEO and shared with other polymer electrolytes are the weak mechanical properties unsuitable for stopping dendrite propagation and the low ionic conductivity below T_m due to the presence of poorly conductive crystalline domains. Conversely, the poor mechanical compliance of stiff ISEs and/or their restricted electrochemical stability have also limited the implementation of purely ceramic SSEs [214]. Taking all into consideration, bridging

the gap between SPEs and ISEs can result in the production of hybrid organic/inorganic electrolytes presenting the advantages of both classes and compensating the shortcomings of the stand-alone categories.
With this aim in mind, two similar but antithetic approaches can be employed to overcome these limitations playing with the different chemico-physical properties of organic and inorganic materials. If moderate amounts of ceramic dispersoids are blended into a polymeric matrix the nanocomposite electrolyte can be defined as "ceramic-in-polymer" [215]. Conversely, when the ceramic phase becomes preponderant or when just a small amount of polymer is added to an ISE in order to improve processability, the hybrid system can be classified as "polymer-in-ceramic". Both the techniques will be described in detail in the next paragraphs.
With respect to ceramic-in-polymer systems, interesting and original properties can be achieved with the addition of inorganic nanoparticles (NPs) into a conductive polymer without sacrificing the processability ease typical of polymers. The small size of the dispersoids is chosen to maximize the interaction also at low encompassed contents. The beneficial effects imparted to the resulting nanocomposite system can be several. Firstly, NPs act as solid-state plasticizers reducing the crystallinity of the polymer, therefore enhancing the ionic conductivity at RT. Compared to liquid plasticizers such as the one used in some GPEs, solid-state ones have the advantage of resulting non-flammable and of avoiding any leakable component in the electrolyte. Secondly, the presence of stiff nanoparticles into the soft polymeric matrix imparts improved mechanical properties and usually results in higher Young modulus and improved dendrite resistance [216]. Additionally, fillers usually act as Lewis acid site thanks to the presence of surface hydroxyl and/or oxygen vacancies [217]. This promotes the Li salt dissociation boosting again the ion conduction. One of the first examples of a successful nanocomposite system was presented by Croce in 1998 [218]. Starting from a PEO-$LiClO_4$ SPE, improved RT ionic conductivity and transference number up to 0.6 were reported upon the dispersion of 10wt% of Al_2O_3 or TiO_2 NPs. As expected, no recrystallization is observed in the DSC profiles of the nanocomposite systems thanks to the plastifying effect of NPs. The amorphous state is also retained after several days, confirming the stability of the morphology. After this publication, TiO_2 has become one of the most investigated inert nanofillers, i.e. ceramic materials that do not conduct Li^+ by themselves. Other inert NPs largely employed in PEO-based nanocomposite SSEs are SiO_2 and doped ZrO_2 [219, 220]. However, the enhancement imparted by pristine inert filler may somehow fall short of the desired improvements expected in nanocomposite SPEs. Therefore, inert fillers can be replaced with active ones, i.e. ion conductive ceramic materials. The addition of ISE particles such as LLZO, LATP, LLZTO or LPSCl can impart new conductive pathways into the electrolyte [214, 221]. This usually results in the achievement of higher ionic conductivity thanks to the formation of a fully percolating filler phase or of an enhanced filler-polymer conductive interface.
In all these cases, best results are achieved with an optimal ceramic content ($\sim$10%) while the increase of this fraction commonly induces a sharp decrease of the electrochemical performances. This is largely due to aggregation issues: large ceramic contents usually result in phase separation and agglomeration of the inorganic fillers suppressing all the advantages related to an homogeneous hybrid system [222]. This fact impedes the addition of higher loadings of NPs and consequently reduces the maximum strengthening effect achievable in SSEs with satisfying conductive properties. To solve this issue, it is critical to find original ways to improve the chemical affinity between the organic and

the inorganic phase. A feasible strategy tailored to solve this specific shortcoming will be carefully described in *Sec. 5* for PEO-based nanocomposite systems based on SiO_2 and TiO_2 and partially employed also for PVdF-HFP GPEs.
Once that the compatibility problem has been tackled, it becomes possible to produce polymer-in-ceramic SSEs where comparable amount of conductive polymer and inorganic fillers are present. This approach appears particularly suitable for those systems based on active fillers where a majoritarian ceramic content can impart interesting conductive properties. However, their dissertation would not add anything new to what already depicted for ceramic-in-polymer system and therefore will not be specifically performed in this section.
Vice versa, a totally different hybrid system that deserves to be carefully depicted is the one of the so-called thin-solid electrolyte (TSEs) or thin-solid separators. Considering that the rigidity of ISEs usually limits the manufacturing to thick and fragile pellets, a small loading of polymer binder (∼5-10 wt.%) can be encompassed into an ISE in order to facilitate its processability in a thin film and to reduce the formation of detrimental cracks. Binder addition enables new and more scalable manufacturing techniques such as tape-casting or calendering, otherwise difficultly applicable on pristine ISEs [223, 224]. But the beneficial effects of a similar approach are not limited to the processing side. First of all, the ionic conductance G_{ion} is defined as

$$G_{ion} = \sigma \cdot \frac{A}{l} \tag{4.12}$$

where σ, A and l are the ionic conductivity, the surface area, and the thickness of the SSEs respectively. Considering the inverse proportionality of G_{ion} with l, comparable conductances can be achieved using less conductive materials but with a thickness reduction. To provide a concrete example, similar values can be obtained using a 25μm thick separator soaked with a commercial liquid electrolyte or employing a 10μm thick TSE with a σ∼0.4 mS cm^{-1} (*Fig. 4.8a*) [213]. Moreover, the reduced thickness endows the ASSBs with higher volumetric and gravimetric energy densities, no more hampered by the presence of a bulky and massive electrolyte layer (*Fig. 4.8b*). This also reduces the unit cost of the resulting cell, thanks to the diminished amount of electrolyte per device and to the low cost of commonly employed polymeric binders.

But the binder encompassing may also induce some detrimental consequences. Considering the ion-insulating nature of most of the binders such as polytetrafluoroethylene (PTFE) or rubbers, the addition of high content of polymers may result in a sharp decrease of the ionic conductivity of the electrolyte that nullify the improvements achieved with thickness reduction. A further complication arises when specifically dealing with LPSCl. As mentioned before, argyrodite sulfides result extremely unstable in polar environment and this feature strongly restricts the binder choice to those soluble in apolar solutions: only polymers with a low-medium polarity can be considered while other more polar binders widely exploited in slurry production like PVdF or carboxymethyl cellulose cannot be considered. Consequently, the currently reported works are based on those few interesting materials that can be dissolved in organic aprotic and apolar solvents such as toluene, p-xylene, or heptane [185]. An illustrative list of candidates exploitable for wet-processing of LPSCl-based TSEs is shown in *Fig. 4.9*.
Taking in account these limitations, some research papers have investigated the effect of different binders-solvents and processing on TSE's performances. Riphaus *et. al* demonstrated that PMMA and SBR seem unsuitable as binders while better results can be

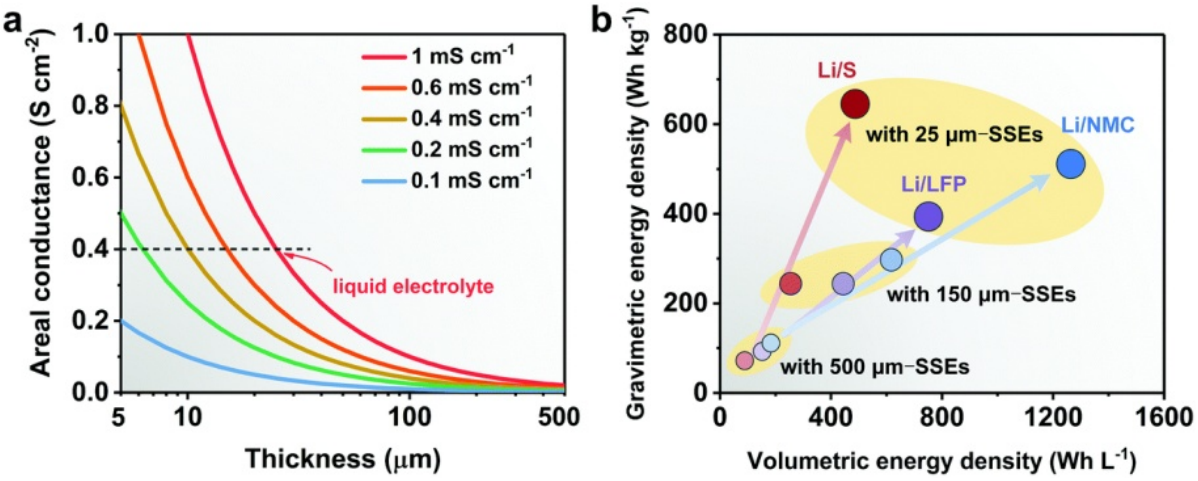

Figure 4.8: a) Comparison of the conductance normalized to the surface as a function of the thickness of electrolytes with different ionic conductivities. b) Gravimetric and volumetric energy densities of selected LMB pouch cells with decreasing separator thickness. Reproduced with permission from [213]. Copyright 2021 RSC.

achieved using hydrogenated nitrile butadiene rubber (HNBR) [225]. The same group of Technische Universität München, Germany, also reported the effect of fabrication pressure on the electrochemical properties of TSEs [226]. In fact, after the production through tape-casting, TSEs usually possess a high porosity that affects negatively the ionic conductivity. Therefore, the application of a high densification pressure in the order of hundreds of MPa is required to guarantee a more intimate contact among conductive particles. Another aspect that deserves to be highlighted is the strong dependence of cycling performances on the operating cell pressure: even if higher stack pressures result in a better adhesion between electrode and electrolyte, the use of more compliant TSEs permits to reduce the applied operating pressure compared to pellets. Finally, Lee *et. al* determined that the use of nitrile butadiene rubber (NBR) with sulfides compounds permits an homogenous distribution of the polymer in the TSE facilitated by the ion-dipole interaction between the electron rich cyanide groups of the binder and Li^+ [227]. However, subsequent work observed that the use of NBR and carboxylated nitrile butadiene rubber (XNBR) can induce an additional impedance contribute due to the presence of a thin insulating polymeric film on the surface of LPSCl particles whose formation can be attributed to the aforementioned dipolar interactions [228]. Therefore, better mechanical properties are achieved at the partial expense of ionic conductivity.

4.3 Final considerations:

To conclude, the research of an ideal electrolyte for LMBs still appears as a partially unresolved task. All the different categories presented here-above possess some interesting features coupled with pending issues that require to be solved. With respect to liquid electrolytes, the flammability and toxicity of organic carbonates have led to the investigation of safer alternatives such as super-concentrated electrolytes, ionic liquids, and deep eutectic solvents. However, the poor compatibility with metallic lithium and their inability of stopping dendrite growth are progressively shifting the researchers' attention on SSEs. Despite their promising characteristics, also these materials present

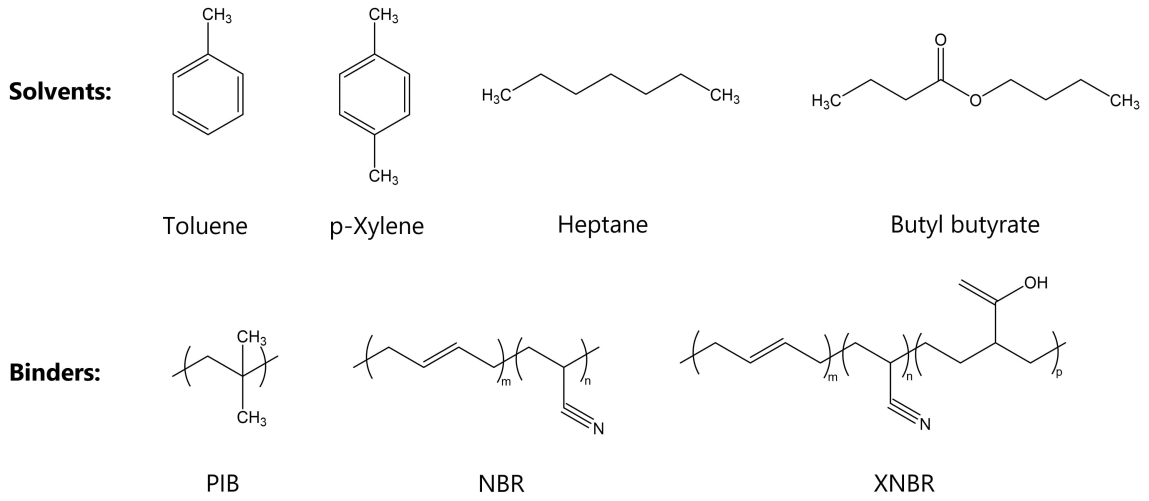

Figure 4.9: Non comprehensive list of various organic solvents and binders applicable for LPSCl-based TSEs (PIB: polyisobutilene).

some major shortcomings that must be addressed to develop performant and reliable ASSBs. In this framework, the development of hybrid polymer-ceramic electrolytes can result in a successful and feasible way to overcome several of those limitations. Overall, the main advantage related to the production of hybrid SSEs consists in the possibility of decoupling the conduction and the mechanical properties. Ceramic-in-polymer systems relies on the easy processing and on the conductive behaviour of SPEs such as PEO whose insufficient mechanical stiffness is compensated by the addition of ceramic NPs. Conversely, binder inclusion in TSEs is able to endow better flexibility to rigid but highly conductive inorganic electrolytes.
Both these approaches have been employed during my thesis work and will be described herein. Firstly, in *Chap. 5* three different nanocomposite systems will be addressed, particularly focusing on the compatibility between fillers and the polymeric matrix. The improvements imparted by the addition of PEG-capped SiO_2 and TiO_2 NPs into two different polymeric matrix, PEO and PVdF-HFP, will be characterised. In particular, the interaction of TiO_2 fillers with Li dendrites will be thoroughly described while the investigation on PVdF-HFP based SSEs will be also devoted to the evaluation of the effects of the residual solvent on the ionic conductivity.
Later, in *Chap. 6* two different manufacturing processes employed for the production of argyrodite-based TSEs comprising a moderate amount of rubbery binder will be discussed. The advantages and the issues related to calendering and tape casting will be compared, always considering the scalability and the practicality of the resulting electrolyte.

5. Hybrid fillers for nanocomposite SSEs:

As mentioned in the previous chapter, one of the main issues experienced while working with nanocomposite resides in the reduced compatibility established between the ceramic and the polymeric phases. Many detrimental effects are consequences of this problem, such as low ionic conductivity at higher inorganic content or reduced stability upon cycling. In this section, the use of hybrid organic/inorganic fillers, i.e. ceramic NPs capped with short chains of polymer that enabled an improved compatibility between the two phases, will be described and characterized in three different systems. Firstly, in *Sec. 5.1* porous PEG-capped SiO_2 fillers have been encompassed into a PEO matrix to impart an improved resistance against dendrites. Secondly, *Sec. 5.2* presents the investigation of the interactions established between PEG-capped TiO_2 NPs and Li dendrites in a nanocomposite polymer electrolyte. Finally, PVdF-based SSEs comprising non-porous PEG-capped SiO_2 fillers are described in *Sec. 5.3*, focusing both on the effect of the residual solvent and on the improvements achieved thanks to NPs dispersion.

5.1 Hybrid SiO_2 fillers for SSEs in LMBs:

Silica has been largely used as inert ceramic dispersoid in composite SSEs thanks to its ease of synthesis and to its high morphology tunability [229, 230]. SiO_2 dispersion in PEO matrix has demonstrated its effectiveness in improving the electrolyte performances thanks to a dual action of suppressing PEO crystallinity and improving the mechanical strength of the electrolyte. However, best electrochemical results are usually achieved at low inorganic loadings ($\approx$ 5-10 wt%) that usually correspond to unsatisfactory strengthening action and insufficient resistance to lithium dendrites [230, 231]. Conversely, stiffer SSEs comprising intermediate or high SiO_2 contents possess decreased ionic conductivity and worse cycling stability.
Consequently, new approaches are required to achieve an homogenous dispersion of the larger loadings of fillers necessary for a more effective hindrance of dendrite propagation. For this reason, we developed a functionalization reaction that can be employed to increase the compatibility among the dispersed fillers and the polymer matrix. These improvements can be achieved through the grafting of short chains of PEG of variable M_w (750, 2000, 5000 g mol^{-1}) on the surface of amino-functionalized spherical and porous SiO_2 NPs. The porosity of the fillers, controlled by the use of a templating agent during synthesis, was selected to maximize the effective volume of NPs that can act as a physical obstacle against Li dendrites per unit of mass.
Thanks to this functionalization, it has been possible to homogeneously encompass various ceramic content, from 10 to 23 wt%, into functional self-standing SSEs without

experiencing any extent of filler aggregation. Best performances have been achieved with an intermediate loading of 18 wt%: such nanocomposite electrolytes were able to sustain more than 300 hours of continuous operation under Li stripping/plating and to operate stably in a LFP-based LMB without any evidence of dendrite growth. The results described hereafter have also been published in the following scientific paper: *"Composite solid-state electrolyte based on hybrid poly(ethylene glycol)-silica fillers enabling long-life lithium metal batteries"*; Mezzomo L. et al; Electrochim. Acta 411 (2022) 140060 [232].

5.1.1 Materials and methods:

Materials:

Tetraethyl orthosilicate (TEOS, ≥99.0%), sodium hydroxide (NaOH, ≥98.0%), hydrochloric acid (HCl, 37 wt%), ammonium hydroxide aqueous solution (NH_4OH, 28 wt%), triethylamine (TEA, >99%), lithium bis(trifluoromethanesulfonyl)imide (LiTFSI, ≥99.0%), SuperP conductive carbon, lithium foils (99.9%) and 1-Methyl-2-pyrrolidinone (NMP, ≥99.0%) were bought from Sigma Aldrich. Acetonitrile (ACN, 99.8% anhydrous), (3-aminopropyl) triethoxysilane (APTES, 98%), dichloromethane (DCM, 99%), toluene (99%), (1-Hexadecyl) trimethylammonium bromide (CTAB, 98%), and succinic anhydride (SA, 99.0%) were provided by Alfa Aesar. Absolute ethanol (EtOH, 99.9%) was bought from Honeywell. Polyethylene glycol methyl ether (PEGx, with x=M_w) were acquired by Alfa Aesar (PEG750, M_w=750 g mol^{-1}), TCI (PEG2K, M_w=2000 g mol^{-1}), and Sigma Aldrich (PEG5K, M_w=5000 g mol^{-1}). Polyethylene oxide (PEO_{4M}, M_w=4 10^6 g mol^{-1}), polyvinylidene fluoride (PVdF, Solef^{TM} 6020), NMC 622 powders, and carbon-coated lithium iron phosphate (LFP) powders were respectively acquired by BDH Chemicals, Solvay, Sigma Aldrich and Hydro-Quebec.
It is worth noticing that, despite sharing the same chemical nature, throughout this work high-molecular weight polyether polymer will be labelled as polyethylene oxide (PEO) while the shorter chains attached to SiO_2 NPs will be defined polyethylene glycol (PEG). This diverse classification, borrowed by biology and dependant on the M_W of the compound, has been employed in order to reduce any misinterpretation between the grafted polymer and the one that composes the electrolyte matrix.

Synthesis and processing:

NPs synthesis and functionalization: The entire synthetic process is schematically depicted in *Fig. 5.1*. First of all, porous and spherical SiO_2 NPs were synthesized following a sol-gel process widely reported in the literature [233] (*Fig. 5.1a*: 4.0 g of CTAB were dispersed into 1920 ml of milli-Q H_2O under vigorous stirring at 70°C. 14 mL of a 2M NaOH solution and 14 ml of TEOS were respectively added after 20 and 40 minutes. Reaction reached completion after 2h: after this, silica NPs were filtered and washed to ensure the complete removal of residual CTAB. Finally, the washed NPs were dried at 100°C for 24 hours.
Functionalization with amine moieties was obtained dissolving 1 g of SiO_2 in 24 mL of toluene at 120°C (*Fig. 5.1b*). After their dissolution, 0.40 mL (1:3 molar ratio between APTES and available OH groups on silica surface) of APTES were injected and the whole mixture was kept under stirring for one day. After filtering, APTES@SiO_2 NPs were washed with toluene and dried at 100°C overnight.

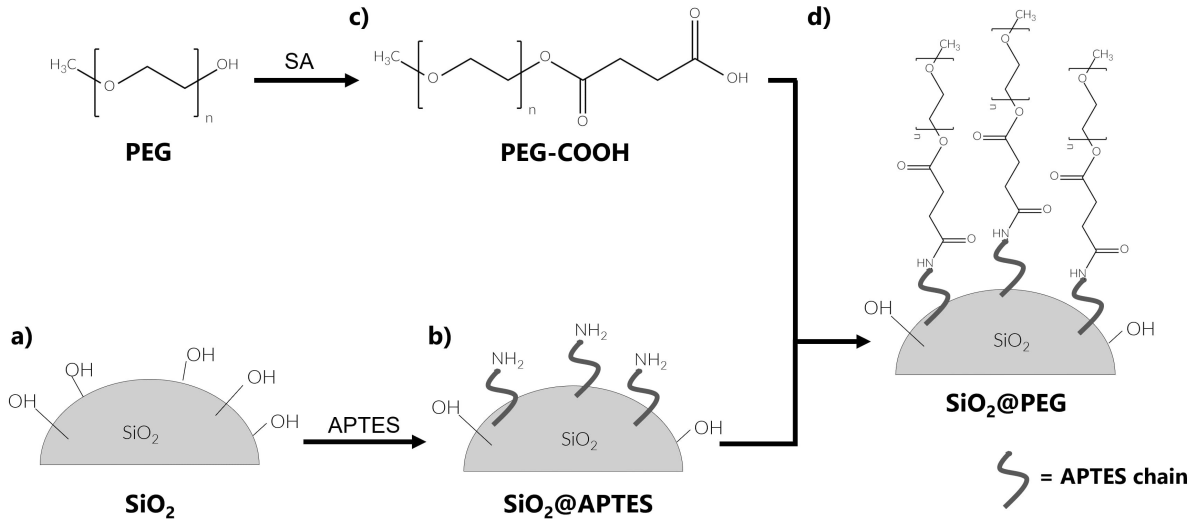

Figure 5.1: Schematic displaying the synthetic process required for the production of SiO_2@PEG hybrid NPs.

PEGx was functionalized with a terminal carboxylic moiety through the reaction with SA. To achieve this, a 1:1 molar ratio amount of PEG and SA (0.05g) was dissolved in 8.0 mL of DCM and stirred under reflux for 10h (*Fig. 5.1c*). 10 mL of TEA were also added to catalyse the reaction. The resulting PEG-COOH was extracted using a rotary evaporator.
Finally, the condensation reaction (*Fig. 5.1d*) between PEG-COOH and SiO_2@APTES was achieved mixing 0.13 g of NPs with the suitable amount of PEG-COOH (molar ratio 1:1 APTES:COOH) in 24 mL of toluene under stirring at 100°C for 20 hours. The unreacted polymer was then separated adding DCM and centrifuging at 9000 rpm for 15 minutes. After a final washing with toluene and DCM, SiO_2@PEGx NPs were dried at 100°C for 24 hours.

SSEs fabrication: SSEs were produced using a solvent casting approach pictorially depicted in *Fig. 5.2a*. First of all, a certain amount of NPs was dissolved in ACN and ultrasonically sonicated to disrupt possible aggregates. Subsequently, the desired contents of LiTFSI and PEO_{4M} were added to the mixture, always maintaining a [EO]:[LiTFSI] molar ratio equal to 10:1, and left to dissolve under vigorous stirring at 60°C overnight. The solution was then carefully poured in PTFE casting dishes (ø=5 cm) and left to evaporate at RT. The resulting film, with an average thickness ≈100μm and displayed in 5.2b-c, was then detached and dried under vacuum to remove the residual ACN. SSEs were later punched in order to obtain disks with a fixed 16mm diameter suitable for assembly in CR2032 coin cells. A complete overview of the investigated SSEs with the respective composition can be found in *Table 5.1*. All these steps were performed in Ar-filled MBraun glove box (0_2, $H_2O < 0.1$ ppm).

Electrode production: SiO_2@PEG750 electrodes were produced starting from a NMP-based ink composed of 65 wt% of active material, 20 wt% of SuperP powder and 15% of PVdF that was tape-casted on Cu foil. LFP and NMC 622 electrodes were obtained via doctor blading on Al foil using a NMP-based slurry comprising 80wt% of active material, 10 wt% of SuperP powder and 10% of PVdF as binder (LFP and NMC 622 loading ≈2.0

Table 5.1: Composition of SSEs employed in this work comprising different amount of hybrid PEG@SiO_2 fillers.

SiO_2 wt%	Filler	PEG wt%	PEO_{4M} wt%	LiTFSI wt%
0	—	0	60.5	39.5
10	SiO_2@PEG750	1.3	53.6	35.1
10	SiO_2@PEG2K	1.4	53.5	35.1
10	SiO_2@PEG5K	1.8	53.1	35.1
18	SiO_2@PEG750	2.4	48.0	31.6
18	SiO_2@PEG2K	2.5	47.9	31.6
18	SiO_2@PEG5K	3.3	47.1	31.6
23	SiO_2@PEG750	3.0	43.4	29.4
23	SiO_2@PEG2K	3.1	44.5	29.4
23	SiO_2@PEG5K	4.1	43.4	29.4

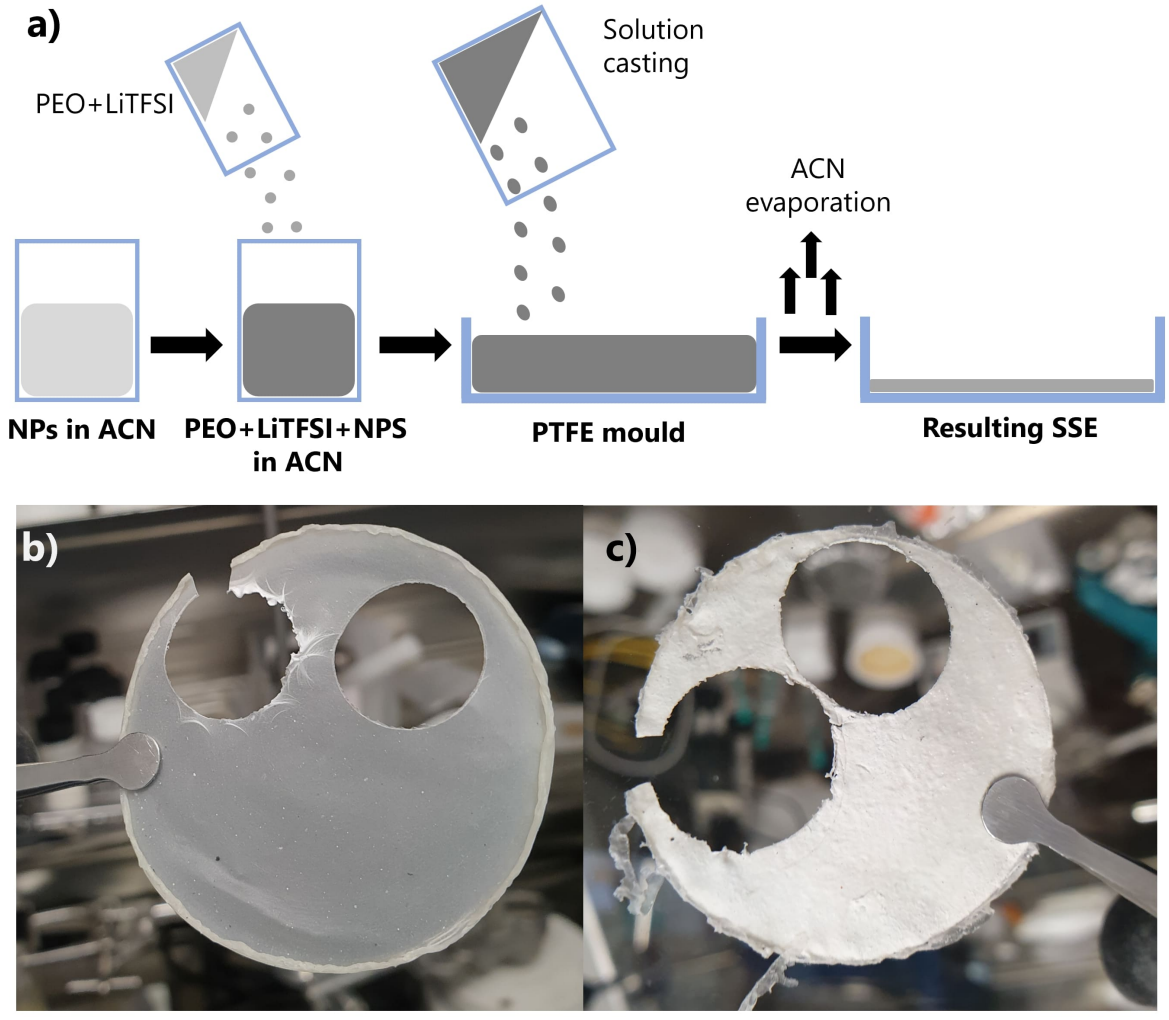

Figure 5.2: a) Schematic displaying the solvent casting approach employed for the production of SSEs. b-c) Images of nanocomposite SSEs produced employing SiO_2@PEG750 NPs and pristine SiO_2 NPs, respectively. The membrane on the right present an evident aggregation of SiO_2 on the bottom of the electrolyte while the same issue is completely avoided employing compatibilized hybrid fillers.

mg cm^{-2}). Prior to assembling, all the electrodes have been dried at 80°C overnight to ensure a complete removal of the solvent.

Instrumentation and methodology:

Chemico-physical characterization: Scanning (SEM) and Transmission (TEM) Electron Microscopy were applied to investigate the size and the morphology of NPs employing a Zeiss Gemini SEM 450 and a JEOL JEM 2110 Plus, respectively. Attenuated total reflectance Fourier transformed infrared (ATR-FTIR) spectroscopy was performed in the wavenumber range 4000-550 cm^{-1} using a Nicolet iS20 instrument fixing a 4 cm^{-1} resolution and 32 scans.
Porosity of NPs was evaluated using a Micrometrics ASAP 2020 HD analyser performing N_2 physisorption after previous degassing at 100°C. Resulting specific surface area (SSA) was evaluated using the Brunauer-Emmet-Teller (BET) model.
Amount of grafted functionalities on SiO_2 NPs was evaluated with thermogravimetric analysis (TGA) carried out on a TGA/DSC1 STAR^e system in the temperature range 30-1000°C with an heating rate of 10°C min^{-1} under a fixed air flux of 50 mL min^{-1}. The following *Eq. 5.1*, *Eq. 5.2*, and *Eq. 5.3* were respectively used to quantify silanol concentration on bare SiO_2 (n_{OH}), APTES content on SiO_2@APTES NPs (n_{APTES}), and PEGx content on SiO_2@PEGx NPs (n_{PEGx}):

$$n_{OH} = \frac{2\Delta W_{150-1000C}}{M_{\text{w } H_2O} \cdot w_{1000°C}} \tag{5.1}$$

where $\Delta W_{150\text{-}1000°C}$ is the weight loss in the temperature range 150-1000°C, $M_{w\ H_2O}$ is the molecular weight of a water molecule (18.02 g mol^{-1}), and $w_{1000°C}$ is the residual sample weight at 1000 °C. The rational behind this formula is that condensation of two silanol groups yields the production of a water molecule. Mass losses below 150°C were assumed related to the presence of residual adsorbed water or solvent molecules and therefore disregarded from the computation.

$$n_{APTES} = \frac{\Delta W_{150-1000C} - (\frac{n_{OH}}{2} \cdot w_{1000°C} \cdot M_{\text{w } H_2O})}{M_{\text{w APTES}} - \frac{M_{\text{w } H_2O}}{2}} \tag{5.2}$$

where $M_{w\ APTES}$ is the molecular weight of one APTES molecule (58 g mol^{-1}) and n_{OH} is computed using 5.1. This formula has been constructed taking in account all the three different contribution that can be observed during the heating process, i.e.:

- condensation and desorption of the residual not substituted silanol groups.
- combustion of the alkyl chains of grafted APTES covalently linked to SiO_2, assuming that on average every APTES molecule binds with two -OH sites out of its three functional groups.
- condensation and desorption of the residual not grafted -OH groups of APTES molecules.

and

$$\begin{aligned} n_{PEGx} = & \frac{1}{M_{\text{w PEGx}}}(\Delta W_{150-1000C} - n_{APTES} \cdot M_{\text{w APTES}} - \frac{1}{2}(n_{OH} \cdot w_{1000°C} - \\ & - 2n_{APTES}) \cdot M_{\text{w } H_2O} - \frac{1}{2} n_{APTES} \cdot M_{\text{w } H_2O}) \end{aligned} \tag{5.3}$$

where all the different weight loss contributions (i.e. PEGx and APTES combustion, silanol condensation, and APTES dangling -OH condensation) are taken in account.
An elemental VarioMICRO analyser (combustion column= 1150°C, reduction column= 850°C) was used to confirm the grafted amount of APTES and PEGX.
A Malvern Zetasizer Nano Series ZS90 instrument was employed to evaluate the ζ-potential on samples diluted in milli-Q H_2O (concentration∼0.1 mg mL^{-1}).
X-ray diffraction (XRD) measurements were performed using a Rigaku Miniflex equipped with a Cu source (1.54 Å) in the 2Θ range 20-80°.
Thermal properties of SSEs were characterised performing differential scanning calorimetry (DSC) on a Mettler Toledo instrument under a N_2 flux of 80 mL min^{-1} and with a scan rate of 10°C min^{-1}. After a first heating ramp up to 110°C, required to delete the previous thermal history of the polymer, SSEs were then cooled down to -80°C and then reheated up to 110°C. The resulting properties were determined during the third and final cycle. SSEs crystallinity has been quantified taking in account the endothermic melting peak observed during the final DSC cycle normalized on the mass of the polymer and then divided for the theoretical heat of fusion of PEO_{4M} (=133.65 J g^{-1} [234]).

Electrochemical measurements: Electrochemical analyses were carried out on VSP300 and VMP3 Biologic potentiostats. Ionic conductivity of SSEs was evaluated performing PEIS in the frequency range 100Hz-1MHz and in the temperature range -20°C;+75°C with a fixed wave amplitude of 10mV. Arrhenius and VTF profiles have been fitted using the *Eq. 4.4* and *Eq. 4.6*.
Transference number t_{Li^+} has been evaluated using the Bruce-Vincent method described in *Eq. 4.3* performing two impedance measurement on a symmetric Li|Li cell before and after the polarization of the cell, achieved applying a constant potential step of 20mV for 12 hours.
Galvanostatic stripping/plating measurements were performed at 70°C on Li|SSE|Li symmetric CR2032 coin cells applying alternatively positive and negative current densities spanning from 50 to 500 μA cm^{-2} plus a final step at 100 μA cm^{-2} to verify the cell integrity (50-100-200-300-400-500-100 μA cm^{-2}) for 30 minutes each for a total of 10 cycled at each current density. SiO_2 electrodes were tested in half cell comprising Li as counter electrode and Whatman® Grade GF/B Glass Microfibre Filters soaked with LP30 electrolyte and discharged to 0.01V vs Li^+/Li at a fixed current density of 200 μA cm^{-2}. GCPL analysis of full LMB was performed on Li|SSE|LFP CR2032 coin cells cycled at 70°C in the potential range 2.8-3.7 V vs Li^+/Li at different C rates (0.05C, 0.1C, 0.2C, 0.5C, 1.0C).

5.1.2 Results and discussion:

Filler characterization:

First of all, SiO_2 NPs were synthesized following the reaction described in the experimental section. Their morphology was analysed by SEM and TEM analyses which confirmed the expected spherical shape and their high porosity (*Fig. 5.3a-c*), subsequently validated by N_2 desorption-absorption isotherm that demonstrated a SSA ≈800 m^2 g^{-1}. As shown in Fig 5.3a, average NPs diameter resulted in the order of 80 nm. APTES grafting had the effect of reducing the visible porosity of APTES@SiO_2 NPs, partially filling the

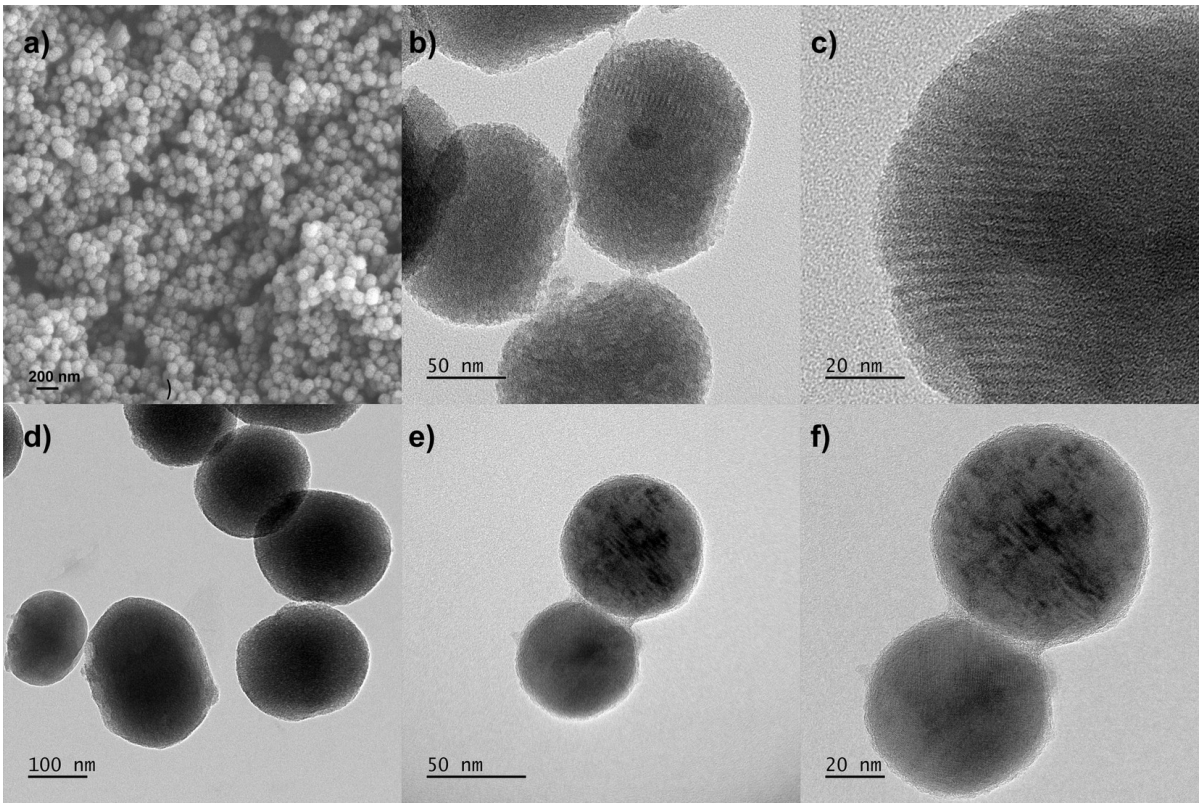

Figure 5.3: a) SEM and b-c) TEM images of SiO_2 NPs displaying their spherical shape and their elevate porosity. d) TEM image of SiO_2 APTES NPs, whose pores are partially filled by condensed APTES. e-f) TEM images at different magnifications of SiO_2@PEG2K displaying the presence of a thin polymeric layer on the surface of silica.

hollow cavities of SiO_2 and condensating as silica (*Fig. 5.3d*). The lower SSA (≈500 m^2 g^{-1}) observed during N_2 desorption-absorption further corroborated this hypothesis (*Fig. 5.4a*). APTES functionalization was also noticed through ATR-FTIR (*Fig. 5.4b*) analyses which presented the characteristic symmetric and asymmetric stretching peaks (2860 and 2940 cm^{-1}, respectively) of -CH_2 moieties of the propyl chains.

Finally, after having synthesized PEG-COOH (*Fig. 5.4c*), its grafting on NPs was verified again employing the same characterization techniques. Transmission microscopy images showed the formation of a thin polymeric layer on the surface of PEG@SiO_2 NPs (*Fig. 5.3e-f*). Also ATR-FTIR confirmed the effective grafting: the two features visible at 1646 and 1559 cm^{-1}, typical of C=O stretching and NH bending, result ascribable to the amide group formed by the condensation of -NH_2 of APTES with -COOH group of PEG-COOH, whose peak located at 1734 cm^{-1} progressively disappeared during the reaction (*Fig. 5.4d*). As expected, XRD diffractograms demonstrated no noticeable differences before and after the grafting since NPs retained their initial amorphous nature (*Fig. 5.4e*). An additional qualitative confirmation was provided by ζ-potential analyses. The negative potential observed for bare SiO_2 NPs (-35 ±4 mV) progressively became positive upon APTES (-1 ±5 mV) and PEG grafting (+25 ±6 mV), demonstrating once more the occurred functionalization.

After having qualitatively confirmed the success of the functionalization steps, APTES and PEGx contents were precisely quantified. TGA analysis on pristine SiO_2 NPs were

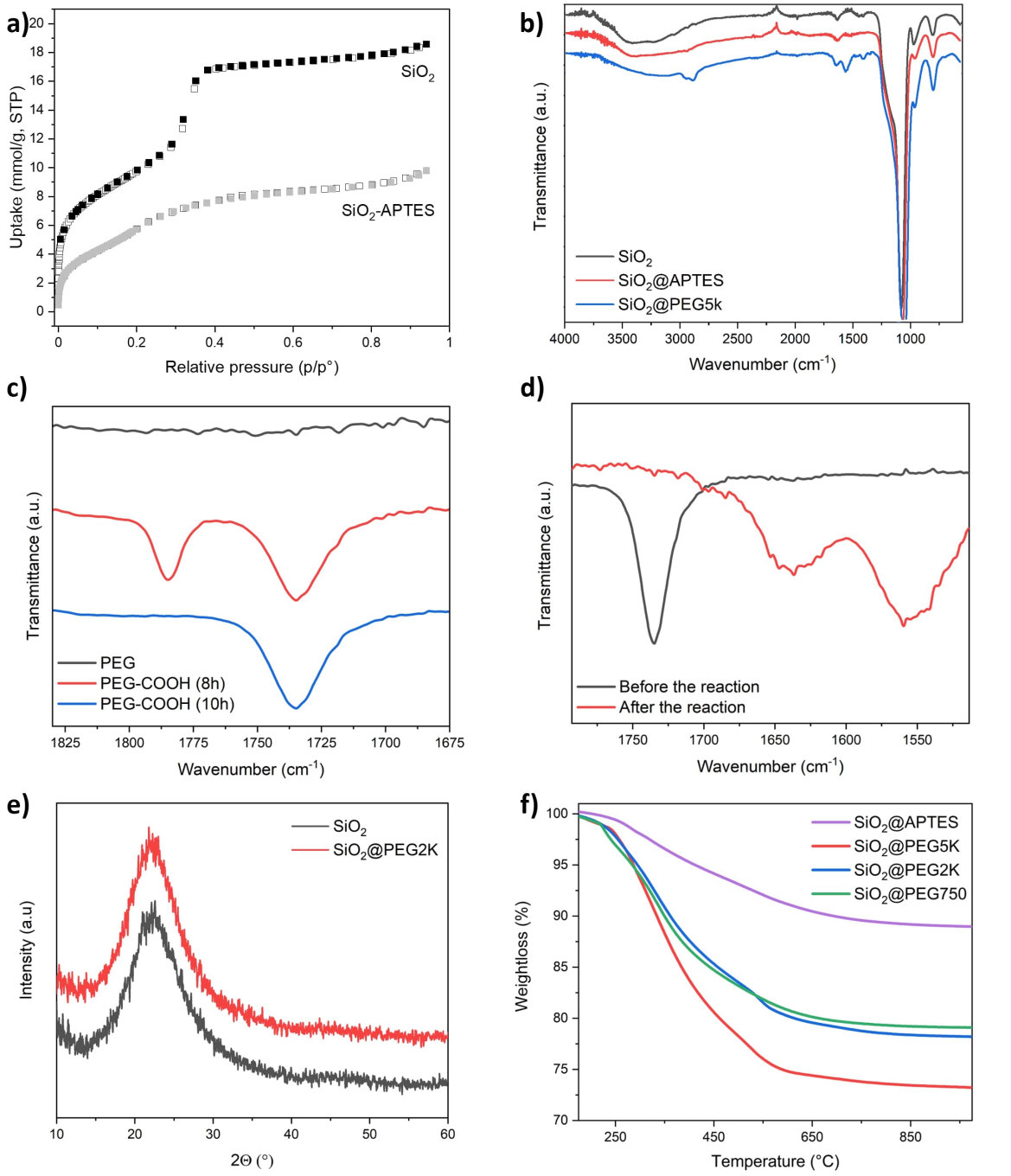

Figure 5.4: a) N_2 isotherm of absorption/desorption measured for bare SiO_2 and for SiO_2@APTES NPs displaying the different porosity of the two fillers. b) ATR-FTIR spectra of SiO_2, SiO_2@APTES and SiO_2@PEG NPs. c) ATR-FTIR image displaying the progressive consumption of the peak related to SA (1780 cm^{-1}) and the appearance at 1734 cm^{-1} of C=O stretching free carboxylic groups of PEGx-COOH after 10h during PEG functionalization. d) ATR-FTIR spectra before and after the reaction between PEG-COOH and SiO_2@APTES NPs showing the formation of the two characteristics peaks of amide group and the concurrent disappearance of C=O stretching feature. e) XRD diffractograms of SiO_2 and SiO_2@PEG2k NPs. f) TGA profiles of bare and functionalized SiO_2 NPs. Readapted with permission from [232].

Table 5.2: TGA results and respective estimation of APTES and PEGx contents grafted on silica surface. Reaction yield and ratio between the number of APTES molecules and PEG chains are also presented.

Sample	$\Delta W_{150\text{-}1000°C}$	APTES wt%	PEGx wt%	Yield	APTES/PEG
SiO_2	4.79	—	—	—	—
SiO_2@APTES	11.3	8.7	—	91%	—
SiO_2@PEG750	20.9	7.9	10	9%	11
SiO_2@PEG2K	21.9	7.3	11	4%	26
SiO_2@PEG5K	26.7	6.8	16	2%	46

Table 5.3: CHNS results and respective reaction yield for SiO_2@APTES.

Sample	N content (%)	APTES wt%	Yield
SiO_2	0.23	—	—
SiO_2@APTES	2.22	8.3	88.0%

preliminarily carried out in order to determine the amount of silanol groups n_{OH} present on unfunctionalized particles (*Fig. 5.4f*). The concentration of OH on bare SiO_2 was estimated to be 5.2 mmol g^{-1} using *Eq. 5.1*. After this quantification, it resulted possible to estimate the APTES grafted content n_{APTES} employing *Eq. 5.2*. Eventually, PEG grafted fraction was evaluated employing *Eq. 5.3*. TGA profiles, results and reaction yields are respectively displayed in *Fig. 5.4f* and *Tab. 5.2*. With respect to APTES, a satisfying reaction yield of 91% associated to a $\Delta W_{150\text{-}1000°C} \sim 11\%$ was achieved employing the previously specified 3:1 stoichiometric ratio between silanol groups and APTES molecules. Higher amounts of reactants did not significantly improve the grafted content of silane, leading to an undesired decrease of the yield that dropped below 80%. The success of PEGx grafting reaction was confirmed by the increased weight loss evidently noticeable in TGA profiles. Reaction yield resulted strongly dependent on the M_w of the polymer. PEG750, possessing a reduced steric hindrance, appeared more suitable for grafting reaction leading to a yield of 9%. This value drops down to 4% and 2% for the longer chains of PEG2K and PEG5K, even if their higher M_w accounted for a larger weight loss during TGA. Another easy way to visualize consists in the computation of the APTES/PEG ratio, i.e. the number of -NH_2 moieties available for each grafted PEG chain. Once more, shorter PEG750 enabled a more homogenous coverage of NPs leading to a ratio$\sim$11. This value appeared more than doubled when employing PEG2K and results 4 time higher for PEG5K due to the reduced capability of bulkier chains to occupy neighbouring APTES sites.

TGA results on APTES grafting were confirmed also by CHNS elemental analysis through the evaluation of nitrogen percentage content. The values, shown in *Tab. 5.3*, possessed a satisfying agreement with the one obtained with thermal analysis.

Taking in account these results it was therefore possible to confirm the composition of our three different hybrid inorganic-organic fillers, outlined herein:

- **SiO_2@PEG750**: SiO_2 82.1 wt%; APTES 7.9 wt%; PEG750 10.0 wt%.
- **SiO_2@PEG2K**: SiO_2 81.7 wt%; APTES 7.3 wt%; PEG2K 11.0 wt%.

- **SiO_2@PEG5K**: SiO_2 77.2 wt%; APTES 6.8 wt%; PEG5K 16.0 wt%.

SSEs characterization:

After having investigated the nature of our hybrid fillers, further characterization has been carried out on the SSEs composed dispersing a fixed amount of ceramic material into a conductive matrix composed by PEO_{4M} and LiTFSI in molar ratio 10:1. To facilitate the comprehension, the nanocomposite SSEs will be named in the following way: SiO_2@PEG**X** SSE **YY**% where **X** depicts the M_w of the PEG employed as grafting agent and **YY** is the wt% amount of ceramic material into the resulting electrolyte. For comparison, the polymeric membrane without NPs and containing the same molar ratio of etheric units and lithium ions 10:1 will be labelled as PEO_{4M}:LiTFSI 10:1.
DSC analyses were performed to determine the effect on thermal properties imparted by the addition of different fillers and/or growing inorganic contents. Detailed results measured in the final heating cycle are shown in *Fig. 5.5* and in *Tab. 5.4*. As expected and as already reported in the scientific literature [218, 234], LiTFSI addition had two main effects on the melting point and the glass transition of PEO_{4M} which passed from being a semi-crystalline polymer (crystalline fraction=67%) with an almost unnoticeable T_g at -65°C to a prevalently amorphous polymer with a lowered T_m preceded by a cold crystallization peak, enabled by the chain reorganization upon heating [235], and a more pronounced glass transition (T_g=-44°C) related to the passage from the rigid vitreous state to the elastic rubbery one. These phenomena are due to well known disordering action induced by the salt dissolution into PEO matrix which disrupts the long range order of the system. In addition, the strong interaction established between lithium ions and electronegative etheric units induced the formation of a transient cross-linking [236]. Moreover, the very wide endothermic peak noticed for pristine PEO_{4M} may be related to a wide distribution of the M_w of the polymer itself.
Having measured the thermal properties of these two reference systems, characterization was directed towards the nanocomposite SSEs. Considering that no evident differences were noticed when employing different types of fillers neither on the glass transition nor on the crystallinity (*Fig. 5.5c-d*), all the following consideration will be based on SSEs containing SiO_2@PEG750 NPs as most representative example (*Fig. 5.5a-b*). Low and intermediate amounts of fillers (10-18 wt%) further increased the disorder of the SSEs, progressively lowering the T_m from 46°C to 38°C and reducing the crystalline fraction, totally suppressed ah high ceramic loadings (23 wt%) when the completely amorphous electrolyte did not display any extent of endothermic peak. Considering that, as explained in *Sec. 4.2.1*, conduction in PEO takes place in the amorphous region of the polymer, the plastifying effect imparted by NPs appears strongly desired and may result beneficial for the electrochemical performance of the SSE. NPs also affected the position of the glass transition which was slightly raised upon growing ceramic addition but this effect resulted secondary if compared to the major one endowed by LiTFSI.

Electrochemical characterization and battery testing:

After having studied the thermal properties of the nanocomposite SSEs and having inferred some related beneficial effects on the electrochemical properties, ionic conductivity was measured employing impedance spectroscopy in the large temperature range [-20°C;+75°C]. Results are presented in *Fig. 5.6* and in *Tab. 5.5*. Analogously to thermal characterization, different fillers did not induce significant differences on the ionic

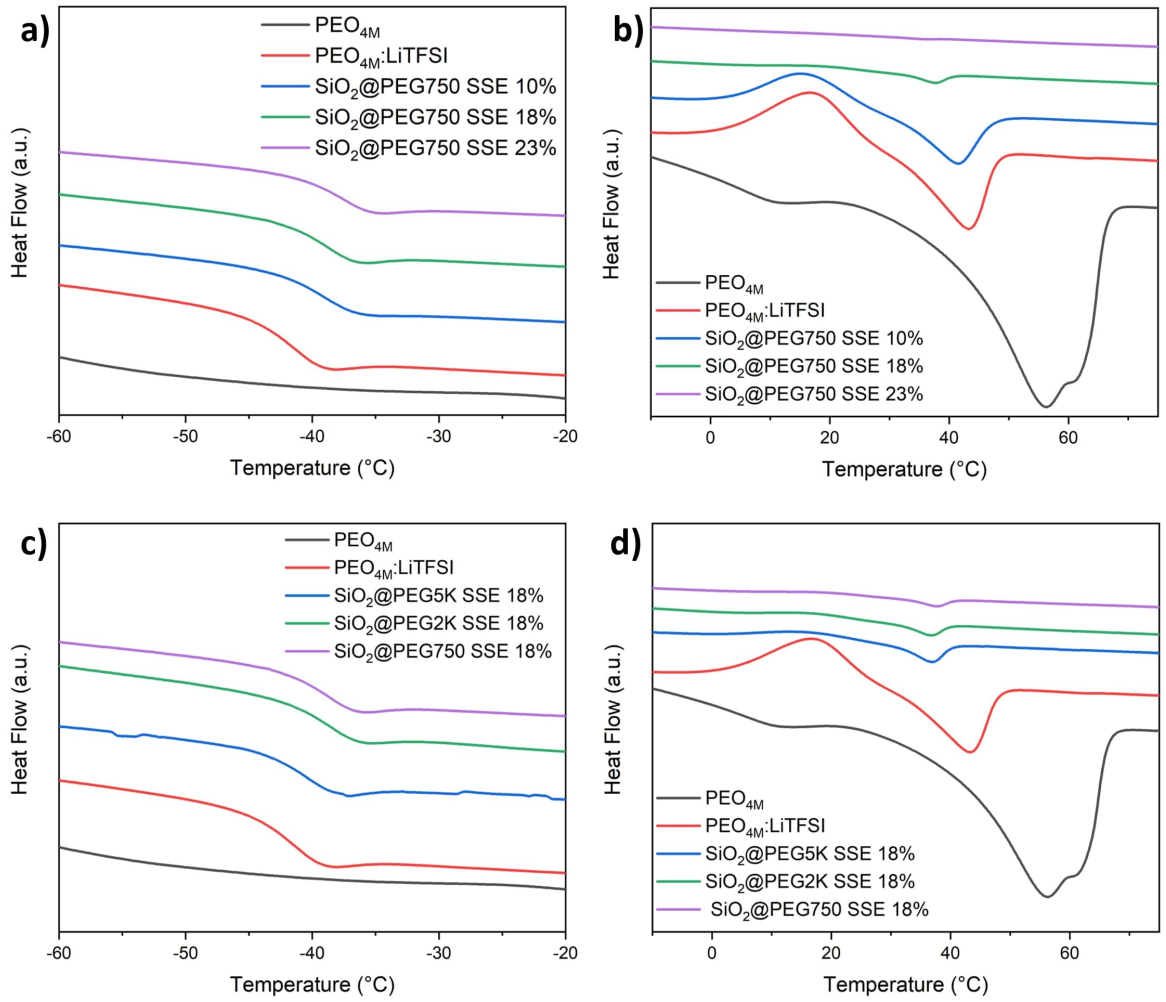

Figure 5.5: a-b) Low (from -60°C to -20°C) and high (from -10°C to +75°C) temperature regions of DSC thermograms of SSEs with different amount of SiO_2@PEG750 hybrid fillers respectively displaying glass transition and melting point. c-d) Low (from -60°C to -20°C) and high (from -10°C to +75°C) temperature regions of DSC thermograms of SSEs with different types of hybrid fillers respectively displaying glass transition and melting point. Exothermic peaks are oriented along the positive y-axis. Images have been readapted from [232].

Table 5.4: Glass transition temperature T_g, melting point T_m and crystalline fraction of SSEs shown in *Fig. 5.5*.

Sample	T_g (°C)	T_m (°C)	Crystallinity (%)
PEO_{4M}	-65	59	67
PEO_{4M}:LiTFSI 10:1	-44	46	38
SiO_2@PEG750 SSE 10%	-41	42	11
SiO_2@PEG750 SSE 18%	-40	38	5
SiO_2@PEG750 SSE 23%	-37	—	0
SiO_2@PEG2K SSE 18%	-38	37	12
SiO_2@PEG5K SSE 18%	-38	37	14

Table 5.5: Activation energy and VTF fitting parameters of SSEs shown in *Fig. 5.6.*

Sample	$\mathbf{E_{a\ T<T_m}}$ **(eV)**	$\mathbf{E_{a\ T>T_m}}$ **(eV)**	$\mathbf{T_0}$ **(K)**	$\mathbf{E_{VTF}}$ **(eV)**
PEO_{4M}:LiTFSI	1.06	0.38	—	—
SiO_2@PEG750 SSE 10%	0.87	0.44	—	—
SiO_2@PEG750 SSE 18%	—	—	173	0.13
SiO_2@PEG750 SSE 23%	—	—	162	0.17
SiO_2@PEG2K SSE 18%	—	—	166	0.15
SiO_2@PEG5K SSE 18%	—	—	161	0.17

conductivity of the nanocomposite electrolytes (*Fig. 5.6b*). As a consequence, the following discussion will focus mainly on SiO_2@PEG750-based SSEs, whose fillers contains the highest concentration of grafted PEG chains.
As widely reported in the scientific literature [157], the ionic conductivity profile of the PEO:LiTFSI system could be described by two Arrhenius curves below and above the T_m of the polymer, respectively at high and low activation energy (1.06 eV and 0.38 eV). This behaviour is easily understood considering how Li^+ conduction takes place in a PEO matrix: below the melting point, the residual crystalline domains hinder ion hopping while this obstacle is removed at $T>T_m$. A similar profile with a discontinuity around 35°C was observed for SiO_2@PEG750 SSE 10%, whose low filler content has been previously demonstrated to be incapable of totally disrupting the crystallinity of PEO_{4M}. A different curve shape was instead measured for moderate and high filler contents, i.e. 18 wt% . As clearly visible in *Fig. 5.6c*, SiO_2@PEG750 SSE 18% conductivity profile did not appear fittable by two straight lines but appears more *rounded* and therefore describable through a VTF equation whose parameter are reported in *Tab. 5.5.* The linearized curve is presented in *Fig. 5.6d.* Another aspect that deserves to be highlighted is that this SSE possessed a RT $\sigma_{Li^+}\sim 2\cdot10^{-5}$ S cm^{-1} higher than the polymeric counterpart ($\sigma_{Li^+}\sim 9\cdot10^{-6}$ S cm^{-1}) thanks to the plastifying effect imparted by NPs addition. Conversely, at high T the ionic conductivity of the nanocomposite system results slightly decreased ($2.4\cdot10^{-3}$ S cm^{-1} and $4.9\cdot10^{-3}$ S cm^{-1} respectively for SiO_2@PEG750 SSE 18% and PEO_{4M}:LiTFSI 10:1 at 70°C). Similar considerations can be extended to SiO_2@PEG750 SSE 23%. In this specific case, the increased ceramic content endowed the electrolyte with an overall decrease of the ionic conductivity that appears strongly affected by the excessive inert filler loading.

Following the investigation of the conductive properties, our SSEs have been tested to quantify the capability of these systems to sustain prolonged cycling under realistic stripping/plating conditions. It was decided to perform these tests at 70°C, in order to operate in a temperature range with satisfying ionic conductivity for all our samples ($\approx10^{-3}$ S cm^{-1}).
Li|Li symmetric cells equipped with the desired SSE were subjected to increasing values of current densities and the results are presented in *Fig. 5.7a-d.* First of all, as expected PEO_{4M}:LiTFSI 10:1 demonstrated its unsuitability for cycling in contact with a Li anode. The cell based on this electrolyte experienced a sudden voltage drop, correspondent to a dendrite induced short-circuit, at a moderate current density value of 200 μA cm^{-2} (*Fig. 5.7a*). Slightly better results were achieved using SiO_2@PEG750 SSE 10%: in that

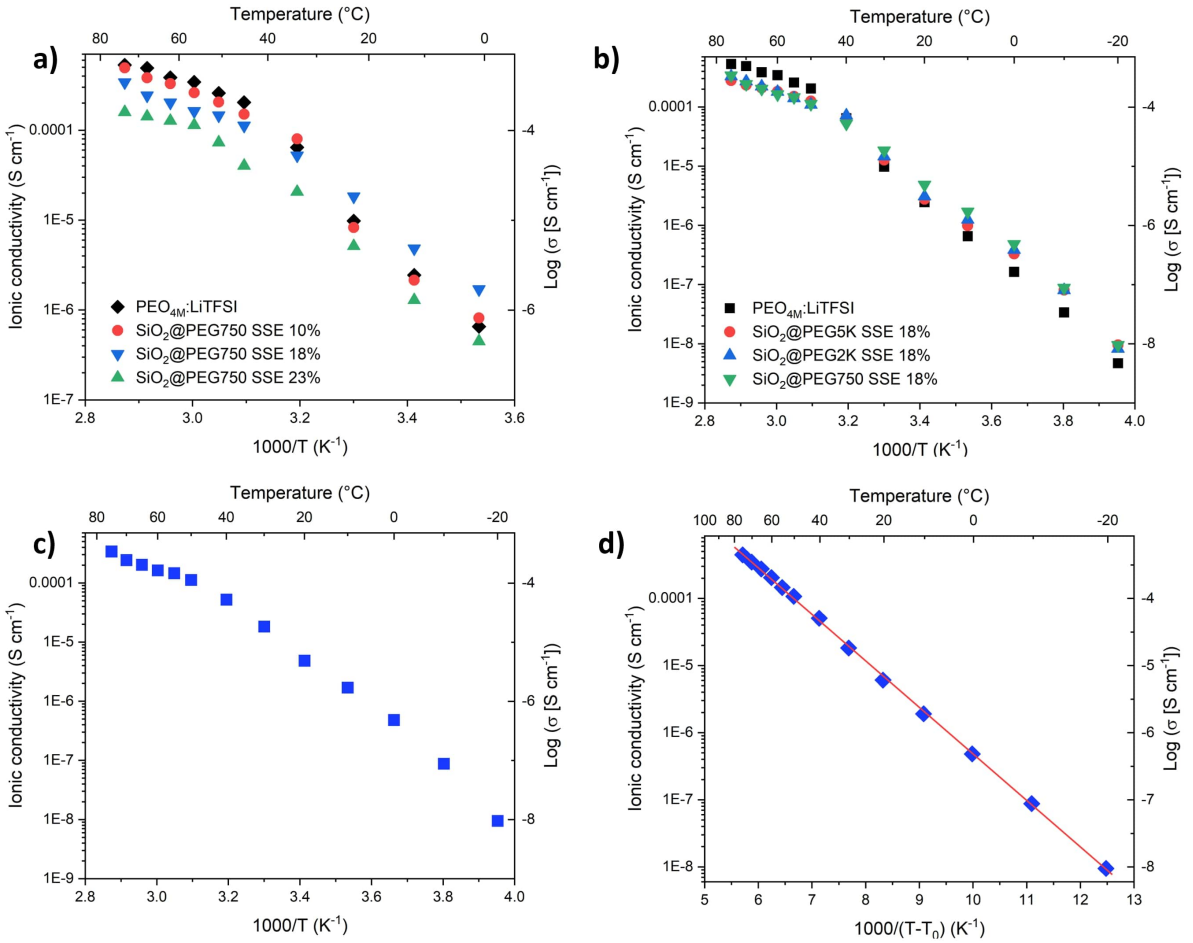

Figure 5.6: Arrhenius plots of a) SSEs with different amount of SiO_2@PEG750 hybrid fillers and b) fixed amounts different types of hybrid fillers compared with the purely polymeric PEO_{4M}:LiTFSI 10:1 system. c) Arrhenius plot and d) VTF (T_0=173 K) plot of SiO_2@PEG750 SSE 18%. All the membranes possess a [EO]:LiTFSI ratio equal to 10. Readapted with permission from [232].

systems, the value for the critical current density was increased around 300-400 μA cm^{-2}. Counterintuitively, also high ceramic content (23 wt%) led to unsatisfying cycling, probably due to the reduced ionic conductivity of the SSEs which caused less homogenous Li deposition and more pronounced dendrite growth. However, SiO_2@PEG750 SSE 18% resulted the best electrolyte due to its ability of sustaining the whole stripping-plating 70-hours long protocol with current densities up to 500 μA cm^{-2} (*Fig. 5.7b*). The temporary voltage drop observed in correspondence of the 45th hours will be later addressed and commented in the next section. Interestingly, the SSEs seemed totally unaffected by high current densities: this was demonstrated through the delivery of the final 10 stripping-plating cycles at 100μA cm^{-2} that presented the same voltage measured at the beginning of the test. To further investigate the stability of this electrolyte, the same CR2032 coin cell has been later subjected to a long-term stability analysis in which stripping-plating cycles at 200 μA cm^{-2} have been indefinitely delivered to the system until the final occurrence of short-circuit. As shown in *Fig. 5.7c*, the cell was able to sustain approximatively 200 additional hours for a total operating time of more than 350 hours. Self-healing behaviours of the cell able to autonomously reinstate its operation were again observed and will be described in the following *Sec. 5.2*. To provide a concrete comparison, an analogue cell base on PEO:LiTFSI not displayed in these graphs short-circuited after less than 5 hours of operation at the same current density. Overall, the performance of SiO_2@PEG750 SSE 18% therefore resulted more than satisfying.
The improved electrochemical performances of the SiO_2@PEG750 SSE 18% were also demonstrated by transference number measurements. As determined employing the Bruce-Vincent method, t_{Li^+} passed from 0.11 (PEO_{4M}:LiTFSI 10:1) to 0.29 (measured with SiO_2@PEG750 SSE 18%). These values, in line with what reported by previous works [237], may result in a reduced cell polarization and in a lower overpotential upon cycling, confirming once more the advantages of the nanocomposite SSEs over the PEO_{4M}:LiTFSI 10:1 pristine system.
Taking in account all these factors, full-cell tests have been later performed selecting as electrolyte SiO_2@PEG750 SSE 18%. Even if its ionic conductivity at 70°C resulted a bit lower than the one of SiO_2@PEG750 SSE 10%, its larger ceramic content enabled a largely improved stability against dendrite piercing strongly desired also in a complete LMB, otherwise prone to short-circuiting. The Li|SSE|LFP battery was initially charged and discharged at 0.05C and this value was progressively increased up to 1.0C. The following protocol was employed:

- Cycle 1-10: charging rate of 0.05C and discharging rate of 0.05C.
- Cycle 11-20: charging rate of 0.1C and discharging rate of 0.1C.
- Cycle 21-30: charging rate of 0.2C and discharging rate of 0.2C.
- Cycle 31-44: charging rate of 0.05C and discharging rate of 0.2C.
- Cycle 45-49: charging rate of 0.05C and discharging rate of 0.5C.
- Cycle 50-54: charging rate of 0.05C and discharging rate of 1.0C.
- Cycle 55-60: charging rate of 0.05C and discharging rate of 0.05C.

Taking in account the current density range explored antecedently and the relation with the C-rates for our LFP cathode shown in *Tab. 5.6*, no evidence of dendrite growth was

Table 5.6: C rates and corresponding current values in LFP LMBs.

Rate	Current (μA)	J_{curr} on Li ($\mu A\ cm^{-2}$)
0.05 C	37.3	19
0.1 C	74.6	38
0.2 C	149.2	76
0.5 C	373.0	190
1.0 C	746.0	380

expected to be experienced since all these values lie safely below the CCD. The resulting voltage profile and the efficiency vs. cycle plot are displayed in 5.7e-f. During the first 10 cycles, cell capacity progressively grew from 95 mAh g^{-1} up to 156 mAh g^{-1}. This progressive improvement was ascribed to the homogenization of the cathode/electrolyte interface upon cycling which enabled the complete delivery of LFP specific capacity. The improvement trend continued during the next 10 cycles at 0.1C until reaching a stable value of 156 mAh g^{-1} discharge capacity with a CE close to the unity. However, when moving to higher charging rate (0.2C), the battery started to display a pronounced instability related to some irreversible reaction happening upon charge. This problem resulted strongly linked to high charging rates since it was overcome from cycle 30 when the charging rate was lowered to 0.05C while leaving untouched the discharge one. Even if a small capacity fading probably related to cathode degradation was progressively observed, the LMB returned to deliver capacity values above 150 mAh g^{-1} with CE$\sim$99%. The performances were only partially affected also by higher discharge rates (0.5C and 1.0C) and the overall efficiency remained in the order of the previously reported values. Eventually, the final 5 cycles with a discharge rate of 0.05C confirmed that the battery maintained a satisfying degree of integrity even after the delivery of high C-rates since the delivered capacity resulted similar to the one measured at the beginning of the test (capacity retention=97%). Overall, no evidence of dendrite-induced short-circuit was observed during cycling. It is also worth stressing the reduced overpotential associated to Fe^{3+}/Fe^{2+} redox couple ($\approx$3.45 V vs Li^{+}/Li) which is satisfyingly maintained also at high current rates.

After the good performance of the LFP-based LMB, the use of a higher-voltage cathode such as NMC 622 was also tested in order to verify the possibility of assembling higher energy density batteries. However, the battery resulted strongly unstable and an evident capacity fading was noticeable even from the first cycles at low C-rate (*Fig. 5.8*). This issue, due to the electrochemical instability of PEO at high voltage [238], limited the use of this system with cathodes operating at more moderate working potentials. Further interfacial improvements would be needed to effectively compatibilize this system with these kind of cathodic materials.

Preliminary considerations on self-healing:

A final aspect that deserves to be highlighted concerns the peculiar phenomena observed during the stripping-plating analyses of nanocomposite SSEs (*Fig. 5.7b-d*). As previously anticipated, several of the symmetric Li|Li cells comprising our SSEs were able to restart their operation after having experienced a dendrite-induced short-circuit. Conversely, a similar behaviour was not observed when employing the PEO:LiTFSI elec-

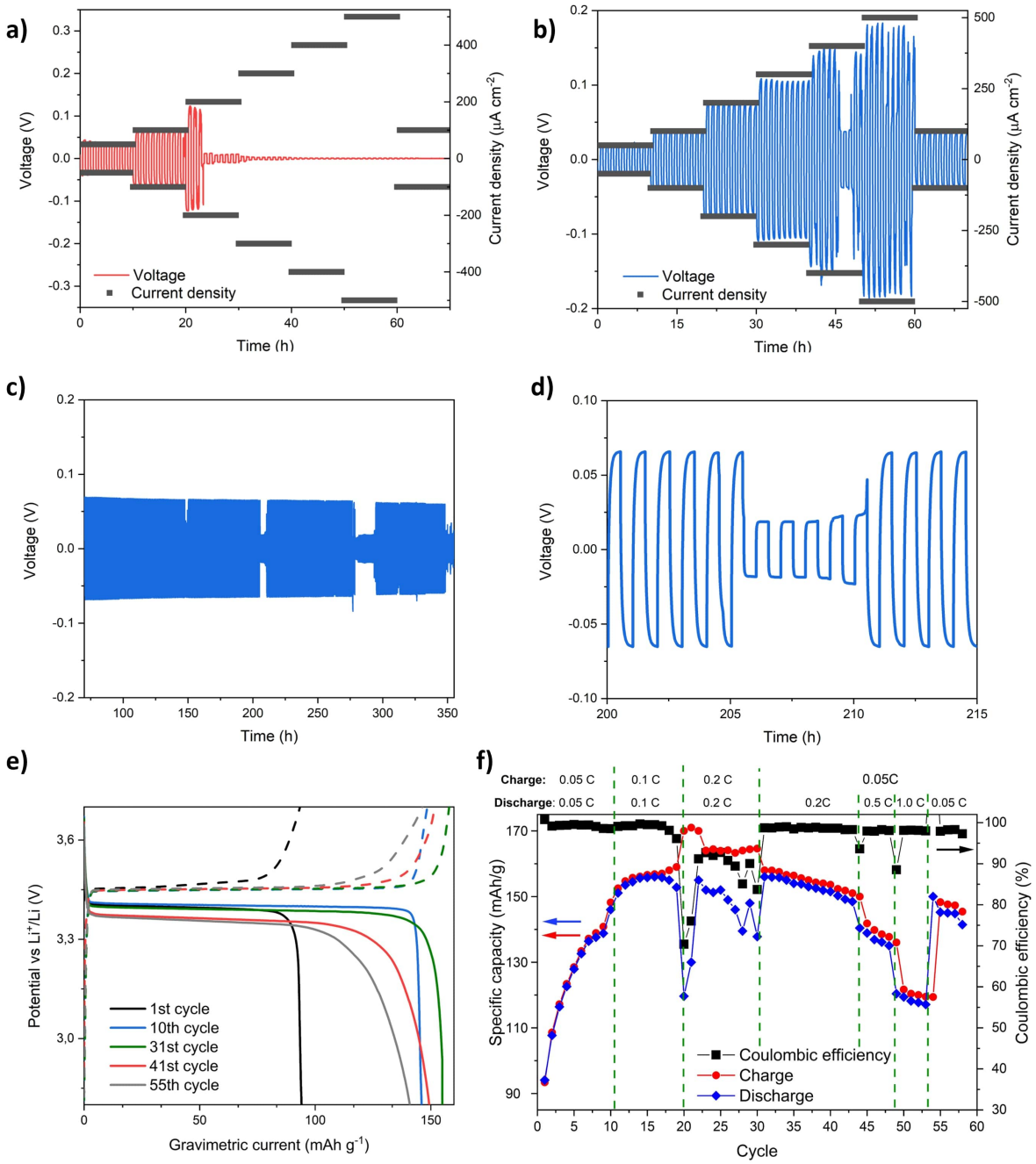

Figure 5.7: Stripping-plating profiles at growing current density (50-100-200-300-400-500-100 μA cm^{-2}) of Li|Li symmetric cells equipped with a) PEO_{4M}:LiTFSI SSE and b) SiO_2@PEG750 SSE 18%. c) Stripping-plating profile of the same Li|Li symmetric cells equipped with SiO_2@PEG750 SSE 18% operating at fixed current density of 200μA cm^{-2}. d) Magnification of one of the healed regions of image c). e) Charge-discharge profile of a LMB equipped with a LFP cathode and employing as electrolyte SiO_2@PEG750 SSE 18% operating at 70°C in galvanostatic conditions at various C rates and f) corresponding cycle performance. Images have been readapted from [232] and all tests have been performed at 70°C.

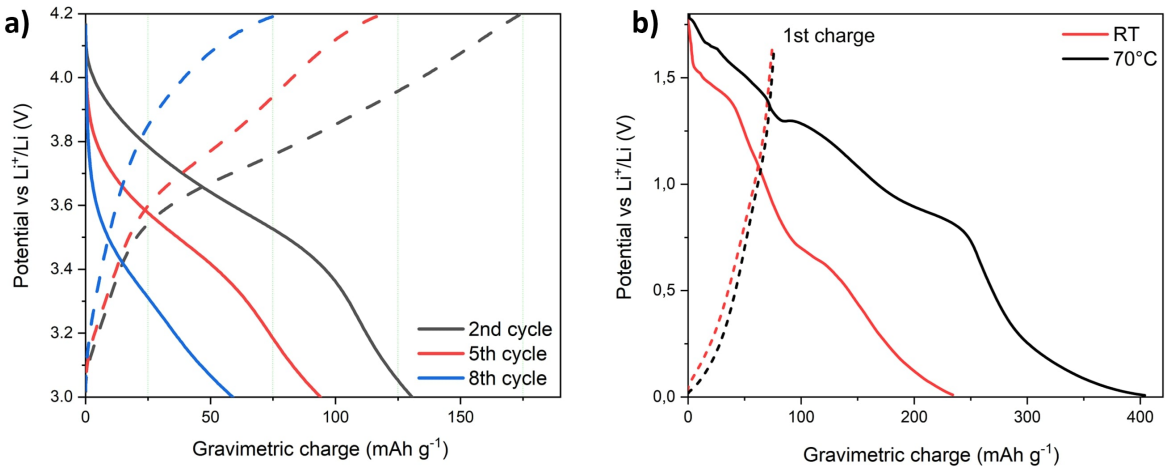

Figure 5.8: a) Charge-discharge profile of a LMB equipped with a NMC 622 cathode and employing as electrolyte SiO_2@PEG750 SSE 18% operating at 70°C in galvanostatic conditions (C rate=0.05C). b) Charge-discharge profile of a SiO_2@PEG2K based electrode vs Li at different working temperatures. Readapted with permission from [232].

trolyte. Therefore, it was postulated that a certain kind of interaction may be established between the lithium dendrites and SiO_2, whose reactivity with Li is widely known [239], consequently disrupting the metalling contact formed between the two electrodes. Example of SiO_2-functionalized reactive separators have also been described in the literature [240, 241] but a similar behaviour has never been reported for SSEs. Moreover, a recent paper addressed the issue of the so-called *dynamic soft-shorts* (i.e. non permanent short-circuiting) that resulted particularly appropriate for the description of our system [242]. Therefore, further investigation would be required for the complete understanding of this effect.
However, a deeper knowledge about the underlying 'healing' mechanism can be obtained in the next chapter, when a similar and comparable electrolyte based on PEG-functionalized TiO_2 NPs has been carefully investigated in order to clarify this aspect. As presented in the following section, the reasons behind this phenomenon appear not strictly linked to the reactivity of Li with the ceramic fillers but to the synergic effect imparted by the hybrid dispersoids which impart an improved mobility of the overall matrix coupled with an increased strength.

5.2 Unveiling the interaction of PEG-capped TiO_2 fillers with Li dendrites:

Before the study of SiO_2-based nanocomposite SSEs described in the above section, a similar system was investigated by other members of my research group and partially by myself during my master thesis work [243, 244]. Hybrid TiO_2 fillers were designed and developed to address once more the issue of poor compatibility into composite electrolytes. In particular, PEG-capped ceramic NPs containing a significant organic fraction (∼47%)were produced through the ligand exchange reaction between oleic acid and phosphate-functionalized PEG. Different loadings of these fillers were later encompassed into a PEO_{4M} matrix and the resulting SSEs were physically and electrochemically characterized to determine the beneficial effects achieved through the NPs dispersion. Overall, the electrolyte displayed satisfying performances particularly when exploiting a ceramic content of 18.8 wt% which permitted long-term stable operation in LMBs. Additionally, also this system displayed the same *healing* behaviour previously described for SiO_2 SSEs. Considering the similarities between the two electrolytes which employed the same polymeric materials (PEO_{4M}) and comparable hybrid fillers, both composed by a ceramic material chemically reactive with lithium covered with a significant amount of short polymeric chains, this additional observation further demonstrated the existence of a certain kind of unreported interaction between this category of electrolytes and Li dendrites. In fact, it was believed that an homogenous dispersion of higher contents of ceramic fillers, enabled by the compatibilizing grafted PEG chains, does not strictly act only as inert strengthener but can also endow unusual and unexplored properties to the system.
It was therefore decided to thoroughly investigate this peculiar phenomenon, keeping also in mind the great interest currently devoted to self-healing as a way to improve the operating life of energy storage devices [245, 246]. The data and the observations described in the following section have also been reported in this peer-reviewed publication: *"Unveiling the Role of PEO-Capped TiO_2 Nanofiller in Stabilizing the Anode Interface in Lithium Metal Batteries"*; Mezzomo L. et al; Nano Lett. 22 (2022) 8509-8518 [247].

5.2.1 Materials and methods:

Poly(ethylene glycol) methyl ether (M_w=5000 g mol^{-1}, PEG5K), titanium tetraisopropoxide (TTIP, 99%), triethylamine (TEA, 99%), chloroform (anhydrous, >99%), acetonitrile (ACN, anhydrous 99%), dichloromethane (DCM, 99.9%) trimethylamine N-oxide (TMAO, 99%), phosphoril chloride ($POCl_3$, 99%), lithium bis(trifluoromethanesulfonyl) imide (LiTFSI, anhydrous ≥99.0%), n-hexane (anhydrous, >99%), N-Methyl-2-pyrrolidone (NMP, 99.5%), diethyl ether ethylene carbonate (EC, anhydrous 99%), ethanol, dimethyl carbonate (DMC, anhydrous 99%), 1.0 M $LiPF_6$ solution in EC/DMC (LP30), lithium (ribbon, 99.9%), diethyl ether (>99%) and SuperP carbon were acquired by Sigma Aldrich. Polyethylene oxide (PEO_{4M}, M_w=$4{\cdot}10^6$ g mol^{-1}), polyvinylidene fluoride (PVdF, Solef™ 6020), and carbon-coated lithium iron phosphate (LFP) were respectively bought from BDH Chemicals, Solvay, and Hydro-Quebec. Celgard® H2010 separator films were kindly provided by Celgard.

Synthesis and processing:

NPs synthesis and functionalization: TiO_2@PEG NPs were produced following the three reaction steps pictorially depicted in *Fig. 5.9a*. OA was degassed performing three vacuum/N_2 cycles, during which a vigorous bubbling was observed, and then maintaining it at 120°C for 2h. Spherical oleic acid-capped anatase TiO_2 NPs (TiO_2@OA) of controlled dimension were later synthesized at 90°C under N_2 flux adding TTIP and a 2M H_2O solution of TMAO as catalysts after 5 minutes. The mixture was then left to react for 24h under stirring in order to permit the hydrolysis and the polycondensation of TTIP. The appearance of a milky solution is observed after one day. The recovery of the NPs was achieved dispersing them in hexane and then centrifuged and precipitated adding ethanol to wash the ungrafted OA. To reduce the risk of undesired aggregation, NPs were never completely dried and kept in a gel-like state.
Subsequently, PEG5K was functionalized with $PO(OH)_2$ moieties. The choice of the functionalizing group was made considering the strong affinity with titania surface [248]. After dispersing the polymer in DCM, the solution was drop-wisely added to a mixture of TEA and $POCl_3$ whose temperature was controlled with the aid of an ice bath. The solution was then slowly heated at 25°C while maintaining a constant stirring. Deionized H_2O was added and the reaction was kept under stirring for an additional hour. The resulting product was then dried with the aid of a rotary evaporator and eventually precipitated thrice using diethyl ether before drying it again at 100°C overnight.
Finally, the grafting of PEG5K on the surface of the NPs was obtained with a ligand exchange process. TiO_2@OA NPs and PEG5K-$PO(OH)_2$ were dispersed in chloroform and left to react under reflux (∼65°C) for 16 hours in order to permit the replacement of OA molecules with the polymer chains. The product was then dissolved in a DCM:diethyl ether 1:3 solution and ultracentrifuged to induce TiO_2@PEG precipitation and to ensure the removal of the non-reacted PEG5K which remains dissolved in the liquid phase. Further details on the synthetic steps can be found in the two following referenced papers [243, 248].
To produce the chemically lithiated NPs employed in the subsequent Raman and EPR characterization techniques, TiO_2@PEG5K NPs were soaked in a Li^+-rich conductive solution composed of a 50:50 (vol:vol) mixture of EC:DMC 0.5M of LiTFSI and then pressed for 72h between two foils of metallic Li. Subsequently, NPs were left to dry in order to remove the solvent and the residual salt was later washed with an excess of DMC. The whole process was carried out in an Ar-filled glove box (MBraun, O_2 and $H_2O < 0.1$ ppm) to avoid any possible oxidation of the system.

SSEs fabrication: SSEs were prepared employing a solvent casting approach. Selected contents of TiO_2@PEG5K NPs were firstly dispersed in a 50:50 (vol:vol) mixture of ACN/chloroform and vigorously stirred until the complete dissolution. The proper amounts of LiTFSI and PEO_{4M} were then added to the mixture in order to always maintain a 10:1 [EO]:[Li^+] ratio. Once homogenous, the mixture was poured in PTFE moulds and left to slowly evaporate overnight. The film was then detached with the help of tweezers and, if needed, n-heptane. SSEs were later punched in order to obtain disks with a fixed 16mm diameter suitable for subsequent assembly in CR2032 coin cells.

Electrode production: TiO_2@PEG5K electrodes were produced from a NMP-based ink containing 65 wt% of active material, 20 wt% Super P, and 15 wt% of PVdF 6020.

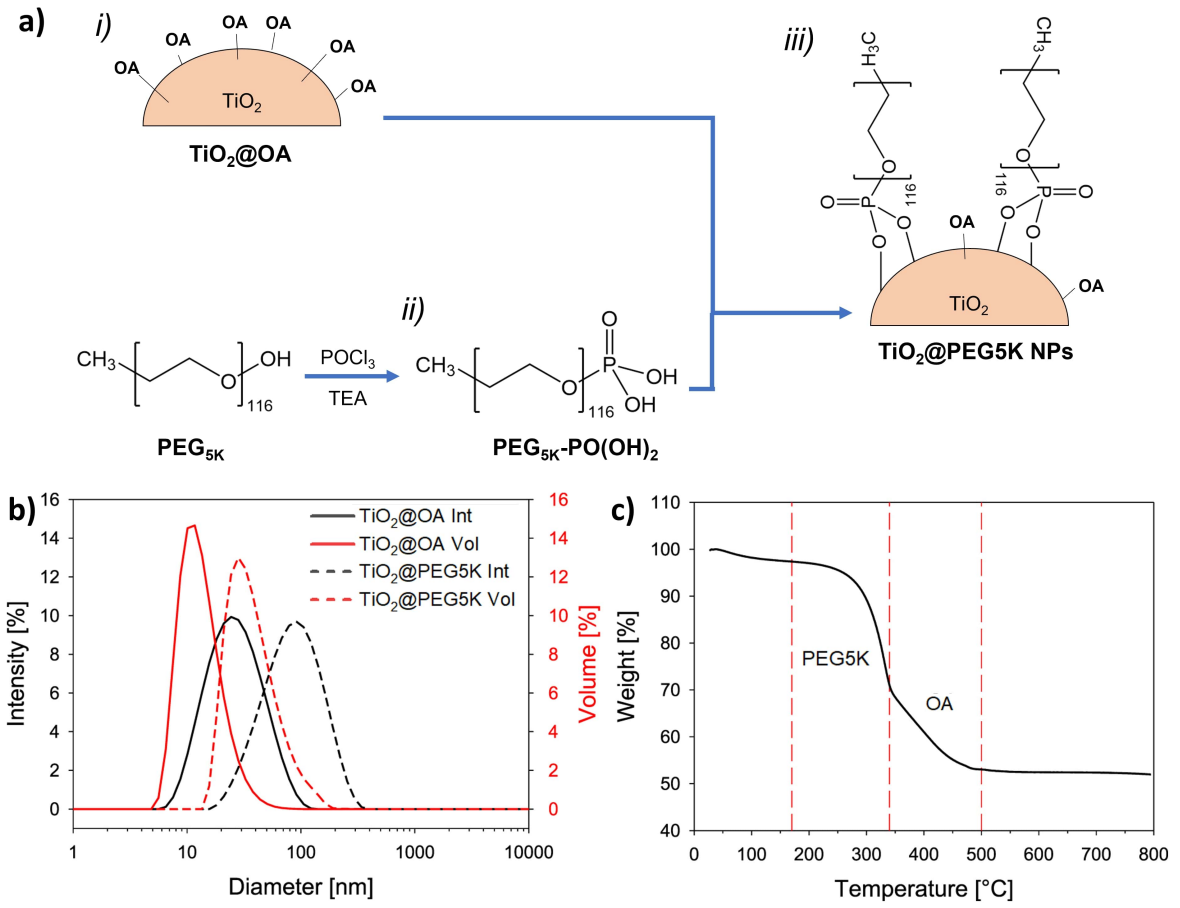

Figure 5.9: a) Schematic representation of the synthetic process of hybrid fillers: *i)* synthesis of the oleic acid capped titania NPs (TiO_2@OA); *ii)* functionalization of PEG5K with the phosphate group employing $POCl_3$ and triethylamine (TEA); *iii)* ligand exchange process that results in the production of TiO_2@PEG5K NPs. b) DLS analysis of TiO_2@OA and TiO_2@PEG5K NPs. c) TGA analysis of TiO_2@PEG5K NPs displaying the weight losses related to PEG5K and residual OA. Images have been readapted from [243] and [247].

The slurry was then casted on copper foils and dried under vacuum to ensure a complete solvent removal. LFP electrodes were prepared as described in *Sec. 5.1.1* starting from a 80:10:10 (active material:SuperP conductive carbon:PVdF) NMP-based slurry.

5.2.2 Results and discussion:

Instrumentation and methodology:

Electrochemical measurements: Electrochemical analyses were carried out on a VSP300 and on a VMP3 Biologic potentiostats. Galvanostatic stripping/plating measurements were performed at 70°C on Li|SSE|Li symmetric CR2032 coin cells applying alternatively positive and negative current for 30 minutes both at fixed (200 μA cm^{-2}) and growing current densities spanning from 50 to 500 μA cm^{-2} (50-100-200-300-400-500-100 μA cm^{-2}) each for a total of 11 cycle at every current density. TiO_2@PEG5K electrodes were tested in half cell comprising Li as counter electrode and Celgard® H2010 separator soaked with LP30 electrolyte and cycled in the potential range 0.01V-2.80V vs Li^+/Li at

a fixed current density of 200μA cm^{-2}. GCPL analysis of full LMB was performed on a Li|SSE|LFP CR2032 coin cell cycled at 70°C in the potential range 2.8-3.7 V vs Li^+/Li at fixed C rate of 0.1C.
For the ex-situ investigation of Li anodes and SSEs, Li|SSE|Li symmetric CR2032 coin cells have been assembled and galvanostatically cycled at 200 μA cm^{-2} to ensure a sufficient dendrite formation. When interested in the recollection of the SSEs, a sandwiched Celgard®|SSE|Celgard® configuration with two Celgard® H2010 separators soaked with EC/DMC 0.5M LiTFSI was employed in order to permit an easy separation of the solid electrolyte from the electrodes, otherwise undetachable one from the other. Before being analysed, Li anodes were washed with PC to remove any possible presence of residual Li salts on the surface. All the cell assembly and disassembly was performed in Ar-filled glove boxes (MBraun, O_2 and $H_2O < 0.1$ ppm).

Characterization techniques: Particle size distribution was measured using Dynamic Light Scattering (DLS) on a Malvern Zetasizer working with a 1 mW continuous wave He-Ne laser (λ=632.8 nm).
TGA analyses were carried out on a Mettler Toledo TGA/DSC1 STARe System in the temperature range from 30°C to 800°C with a fixed heating rate of 10°C min^{-1} and a constant air flow of 50 mL min^{-1}.
After having determined both the NPs size and their composition, the average number of grafted PEG chains per NP n_{PEG5K} was determined employing *Eq. 5.4*:

$$n_{PEG5K} = \frac{\%_{\mathrm{PEG5K}}}{MW_{\mathrm{PEG5K}}} \cdot \frac{V_{\mathrm{NP}} \cdot \rho_{\mathrm{TiO_2}}}{\%_{\mathrm{TiO_2}}} \tag{5.4}$$

where $\%_{PEG5K}$ and $\%_{\mathrm{TiO_2}}$ are respectively the mass fractions of PEG5K and TiO_2in TiO_2@PEG NPs; MW_{PEG5K} is the molecular weight of the grafted PEG5K chains after condensation expressed in grams (8.4·10^{-21} g), V_{NP} is the geometrical volume of a NP in cm^3 (6.1·10^{-19} cm^3), and $\rho_{\mathrm{TiO_2}}$ is the density of anatase TiO_2 in g cm^{-3} (3.8 g cm^{-3}).
It resulted then possible to quantify both the grafting density of PEG5K chains σ_{PEG5K} and the mean distance between PEO5K chains D_m using *Eq. 5.5* and *Eq. 5.6*, respectively:

$$\sigma_{\mathrm{PEG5K}} = \frac{n_{PEG5K}}{A_{\mathrm{NP}}} \tag{5.5}$$

$$D_{\mathrm{m}} = \sqrt{\frac{4\Sigma_{\mathrm{PEG5K}}}{\pi}} \tag{5.6}$$

where A_{NP} is the geometrical surface of a single NP expressed in cm^2 (3.46·10^{-12} cm^2), and Σ_{PEG5K} is the footprint of a single PEG5K chains on the surface of TiO^2 computed as $(\sigma_{\mathrm{PEG5K}})^{-1}$ [248].
High resolution TEM and energy dispersive X-ray spectroscopy (EDX) have been performed on a JEM-2100F TEM of JEOL. *In-situ* TEM measurements were conducted using a Dual-Probe STM-TEM in situ sample holder of Nanofactory Instruments composed by a TiO_2@PEG5K on Cu tip as working electrode (WE) and by a lithium oxide-lithium metal on a tungsten tip as a counter and reference electrode (CE/RE). A positive bias of 1.5V applied for 300s induced Li^+ migration towards the WE overcoming the thin Li_2O layer formed by the rapid exposure of Li to the atmosphere during the loading of the cell into the TEM.
Electron paramagnetic resonance (EPR) was carried out on a Bruker EMX instrument

equipped with an Oxford cryostat (temperature range: 4-298K) and working at the X-band frequency. All the spectra were acquired at 130K under vacuum condition (pressure$<10^{-8}$ bar). For the analyses both pristine and chemically lithiated NPs were loaded in quartz glass tubes.
Micro-Raman measurements were carried out at RT with a confocal LABRAM spectrometer of JobinYvon working in a backscattering configuration. Spectrograph was calibrated prior to every analysis using the 521 cm^{-1} reference peak of silicon. An helium-neon laser (wavelength=632.8 nm, nominal power=17 mW) and a Peltier-cooled CCD (Sincerity-JobinYvon) were respectively chosen as excitation source and detector. The laser was focused using an Olympus BX40 optical microscope equipped with a 50x objective. *In-situ* Raman characterization was performed employing an ECC Opto-STD optical cell equipped with an optical glass window and constituted using a Li|SSE|Li vertical configuration. Analysis of the sandwiched SSE was carried out through the use of a Li top electrode with a small hole (diameter=1mm) that enabled the study of the electrolyte during cycling.
X-ray photoelectron spectroscopy (XPS) analyses were completed using a ultra high-vacuum chamber (pressure $<10^{-13}$ bar) equipped with an hemispherical electron/ion 16-channel energy analyser of the VSW and with a non-monochromatized Al radiation (1486.6 eV). The C*1s* low component of the Celgard® H2010 separator was setted at 284.0 eV to calibrate the binding energy of the system. X-ray source operated at 15 kV and 10 mA, for a resulting operating power of 150W. Photoelectrons were collected in the normal direction with respect to the sample surface and maintaining fixed at 54.5° the angle between the analyser and the X-ray emitter.
A Zeiss Gemini 500 SEM operating at 5kV was used to evaluate the morphology of lithium anodes after cycling. Li electrodes were mounted on conductive stubs employing double side carbon tape into an Ar-filled glove box and transferred to the SEM chamber minimizing the contact with air to reduce any possible side reaction of lithium with oxygen.
Tensile testing analyses on rectangular shaped SSE samples (ca. 6cm x 1cm) have been carried out at room temperature using a Zwick Universal Testing Machine equipped with a 100N load cell. Experiments were completed applying a preloading of 0.1N and monotonically loading in tension the samples with an extension rate of 500 mm min^{-1}. Tensile modulus (TM), maximum elongation at break (ε_b), and ultimate tensile strength (UTS) were determined by the analysis of resulting graphs.
Time dependant nuclear magnetic resonance (TD-NMR) have been completed on a Minispec mg20 ND series presenting a ^1H resonance frequency close to 19.9 MHz. A BVT300 cooling unit employing a N_2 flow of 935 L h^{-1} ensured the temperature control in the system. Magic sandwich echo (MSE) experiments with 128 scans and a delay of 1s to permit the full recovery of the system were carried out in the temperature range from -25°C to 70°C, with increasing temperature steps of 5°C. Finally, Baum-Pines (BP) experiments were instead carried out at the fixed temperature of 70°C with 128 scans. The detailed BP and MSE sequences are described elsewhere in selected references [249].

For the sake of clarity, a brief recap of the main characteristics of the hybrid fillers and of the results previously obtained with this system will be outlined here. As demonstrated by DLS analysis, the average TiO_2@OA NPs size resulted of 10.5 nm (*Fig. 5.9b*). This value was slightly increased up to 13 nm after the PEG5K grafting, confirming the success of the functionalization reaction. This grafted amount was later quantified with the use of TGA that demonstrated two weight losses at ∼170°C and ∼340°C, respec-

Table 5.7: Fillers composition as determined by TGA and main characteristics of TiO_2@PEG NPs.

TiO_2 (wt%)	OA (wt%)	PEG5K (wt%)	n_{PEG5K}	σ_{PEG5K} (nm^{-2})	D_m (nm)
53.4	16.6	30.0	154	0.44	1.7

tively attributed to PEG5K and OA (*Fig. 5.9c*). Consequently, TiO_2@PEG5K NPs were demonstrated to be composed of 53.4 wt% of TiO_2, 16.6 wt% of unexchanged OA, and a 30.0 wt% of PEG5K. The main properties of TiO_2@OA NPs are recapped in *Tab. 5.7*, where the results computed using *Eq. 5.4*, Eq. *5.5*, and*Eq.5.6* are also displayed. It is possible to notice that these fillers present an high polymer coverage (0.44 chain nm^{-2}) which, in turn, results in a very short mean distance between neighbouring chains (1.7 nm). These values would be also increased when considering the high content of OA also present on the surface of TiO_2.
Considering that the Flory radius R_F for PEG5K-$PO(OH)_2$ is equal to 6.0 [248], the R_F/D_m ratio results equal to 3.5. Therefore, our system can be described as a conformational regime of a dense brush, possessing a R_F/D_m ratio >2. Such a dense conformation was not observed in analogous systems when the grafting was performed after a previous ligand stripping of OA and not exploiting a direct exchange process [248]. In those cases, the low R_F/D_m ratio <1 induced the formation of a mushroom morphology. Therefore, the residual OA counterintuitively plays a beneficial role for PEG5K grafting, working as a spacer between neighbouring chains and permitting the formation of a *double brush* system. These consideration on the surface morphology of the hybrid fillers will result of great significance at the end of the section when dealing with NMR data.

Additionally, three different YY:ZZ w/w SSEs with variable ceramic contents but fixed EO:LiTFSI ratio (10:1) were investigated in the referenced paper [243]:

- 50:50 w/w SSE: 18.8 wt% TiO_2, 51.4 wt% organic, 29.8 wt% LiTFSI;
- 70:30 w/w SSE: 28.1 wt% TiO_2, 46.9 wt% organic, 25.0 wt% LiTFSI;
- 90:10 w/w SSE: 38.7 wt% TiO_2, 41.8 wt% organic, 19.5 wt% LiTFSI;

where YY:ZZ is referred to the mass ratio between the TiO_2@PEG5K filler and the PEO_{4M}.
However, to investigate the effect of TiO_2-based hybrid fillers, it was decided to select only a single ceramic composition among the ones reported in the previous reference [243], i. e. 50:50 w/w SSE. This specific electrolyte displayed the best electrochemical performance and resulted the most suitable for application in LMBs. Therefore, to reduce an excessive long nomenclature, the 50:50 w/w SSE electrolyte will be from now on generically labelled also as nanocomposite SSE or SSE throughout this chapter.

Electrochemical results:

To further confirm the satisfying electrochemical properties of this nanocomposite SSE, several cells were assembled and tested at 70°C, temperature at which the ionic conductivity is satisfying. As shown in 5.10a-b, 50:50 w/w SSE was able to operate stably in a LMB equipped with a LFP cathode. The CE resulted always in the order of ∼99%

with a delivered discharge capacity close to 125 mAh g^{-1}. The same electrolyte was able to sustain more than 700 hours of stripping/plating at fixed current density of 200 μA cm^{-2} (*Fig. 5.10c*) or values up to 500 μA cm^{-2} (*Fig. 5.10d*) in Li|Li symmetric cells. Apart from this satisfying stability upon cycling, the interesting feature resides in the phenomenon visible after 70 hours in *Fig. 5.10d* and clearly highlighted in *Fig. 5.10e*. The sharp decrease in the voltage profile at the 61^{st} hour with a current density of 500 μA cm^{-2} was attributed to a dendrite-induced short-circuit which caused an abrupt reduction of the cell impedance. In the absence of any healing capability, the low voltage would remain proportional to the delivered current density with a proportionality factor equal to the new low resistance of the system with the current flowing in the metallic contact established by the dendrites. This ohmic proportionality, maintained after the 66^{th} hour when the current density was lowered to 100μA cm^{-2}, appeared suddenly interrupted when the voltage returned to the value observed before the short-circuiting (11^{th}-22^{nd} hours). A similar behaviour can only be attributed to the disruption of the metallic contact formed between the two symmetric Li electrodes. The first hypothesis which can justify such an effect may reside in the well-known reactivity of anatase TiO^2 with lithium [250, 251]. Therefore, the reaction of the fillers with Li dendrites might induce the disruption of the low-resistance metallic conductive path established through dendrite growth. Such reactivity was also improved by two of the features of our systems, i.e. small NPs size and high operating temperature [252, 253].
However, the reactivity of polymer-grafted TiO_2 NPs cannot be given for granted since the presence of PEG5K can hinder the lithiation of anatase. To verify this feature, an electrode containing TiO_2@PEG5K NPs as active material was tested vs. Li. As shown in *Fig. 5.10f*, a specific capacity >400 mAh g^{-1} was delivered during the first discharge. Even if of reduced entity, it was possible to notice the presence of a plateau at 1.75V vs Li^+/Li, related to the coexistence of the orthorhombic lithium-rich $Li_{0.5}TiO_2$ with lithium-poor tetragonal Li_xTiO_2. However, the capacity appeared greatly irreversible and the discharge in the 2nd cycle was limited to 100 mAh g^{-1}. Further insights were also obtained by the study of the profile of differential capacity in *Fig. 5.12a*. Even if clearly visible and pronounced, the integration of the feature at ~1.75V yielded a result attributable to the insertion of 0.1 Li per TiO_2. Therefore, even if not completely hindered, anatase lithiation resulted somehow limited by the simultaneous presence of the dense double brush morphology of PEG5K and of the residual OA which did not permit a facile and effective transit of Li^+ ions into the NPs. As previously reported, a deeper lithiation of the system could only be gained after a complete stripping of the capping ligand agents [254].

TiO_2@PEG5K characterization:

After having demonstrated electrochemically that our hybrid TiO_2@PEG5K NPs can experience a certain degree of lithiation, it was decided to verify the same aspect exploiting other characterization techniques.
Firstly, the fillers were shipped to the Ulsan National Institute of Science and Technology, South Korea, where a thoroughly microscopy characterization was performed. Preliminarily, HR-TEM confirmed the polycrystalline nature of anatase TiO_2 (*Fig. 5.11a*), who was further proved also by selected area electron diffraction (SAED) shown in the inset of the same figure. Additionally, EDX analyses verified an homogenous distribu-

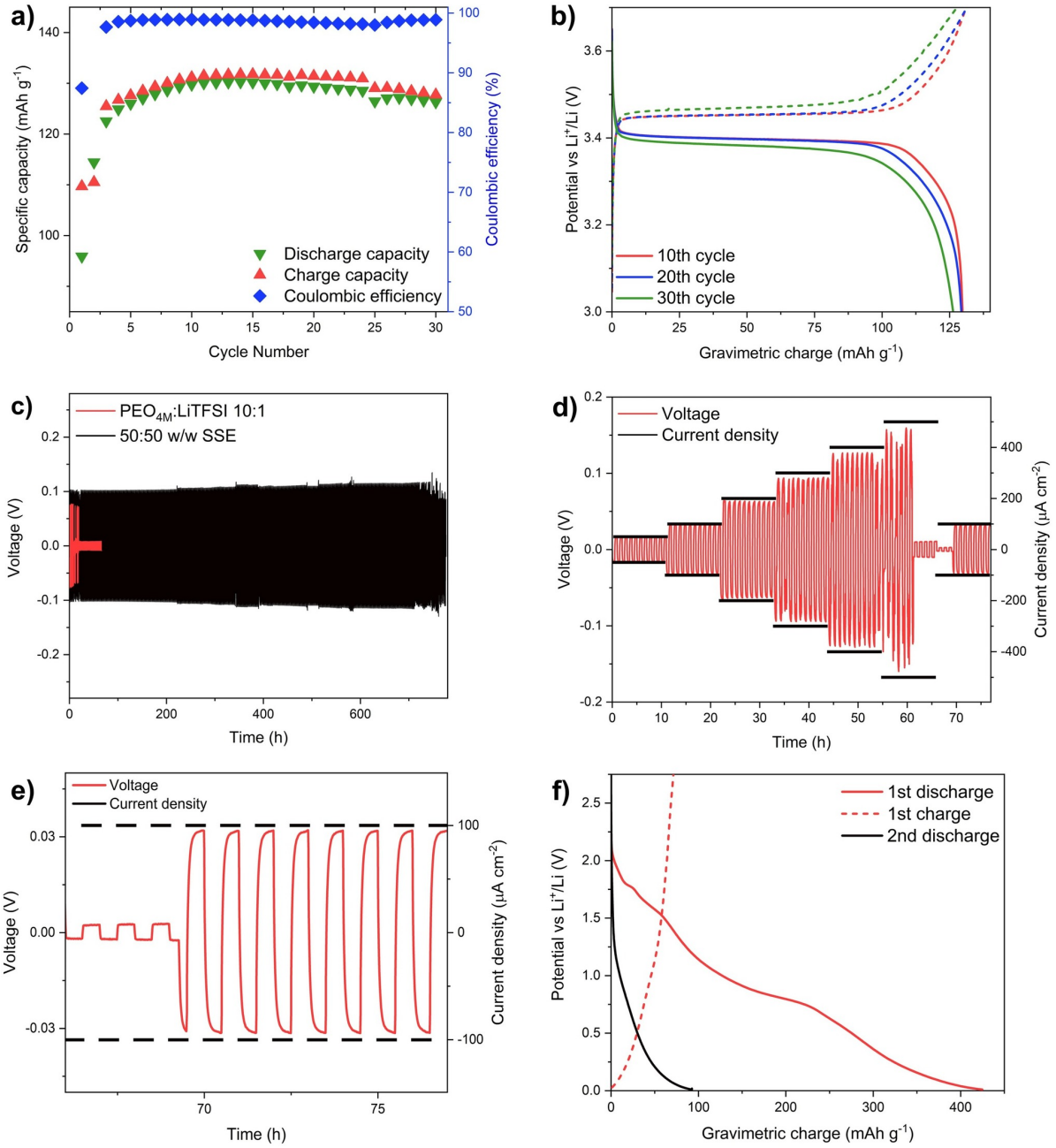

Figure 5.10: a-b) Charge-discharge profile of a LMB equipped with a LFP cathode and employing as electrolyte 50:50 w/w SSE operating at 70°C in galvanostatic conditions at various 0.1C and corresponding cycle performance. c-e) Stripping/plating profiles of c) 50:50 w/w SSE and PEO_{4M}:LiTFSI 10:1 at fixed current density of 200 μ cm^{-2} and of d) 50:50 w/w SSE at increasing current density with e) the magnification of the region experiencing self-healing. f) Charge-discharge profile of a TiO_2@PEG5K electrode vs. Li metal using LP30 as electrolyte. All electrochemical tests have been performed at 70°C. Readapted with permission from [247].

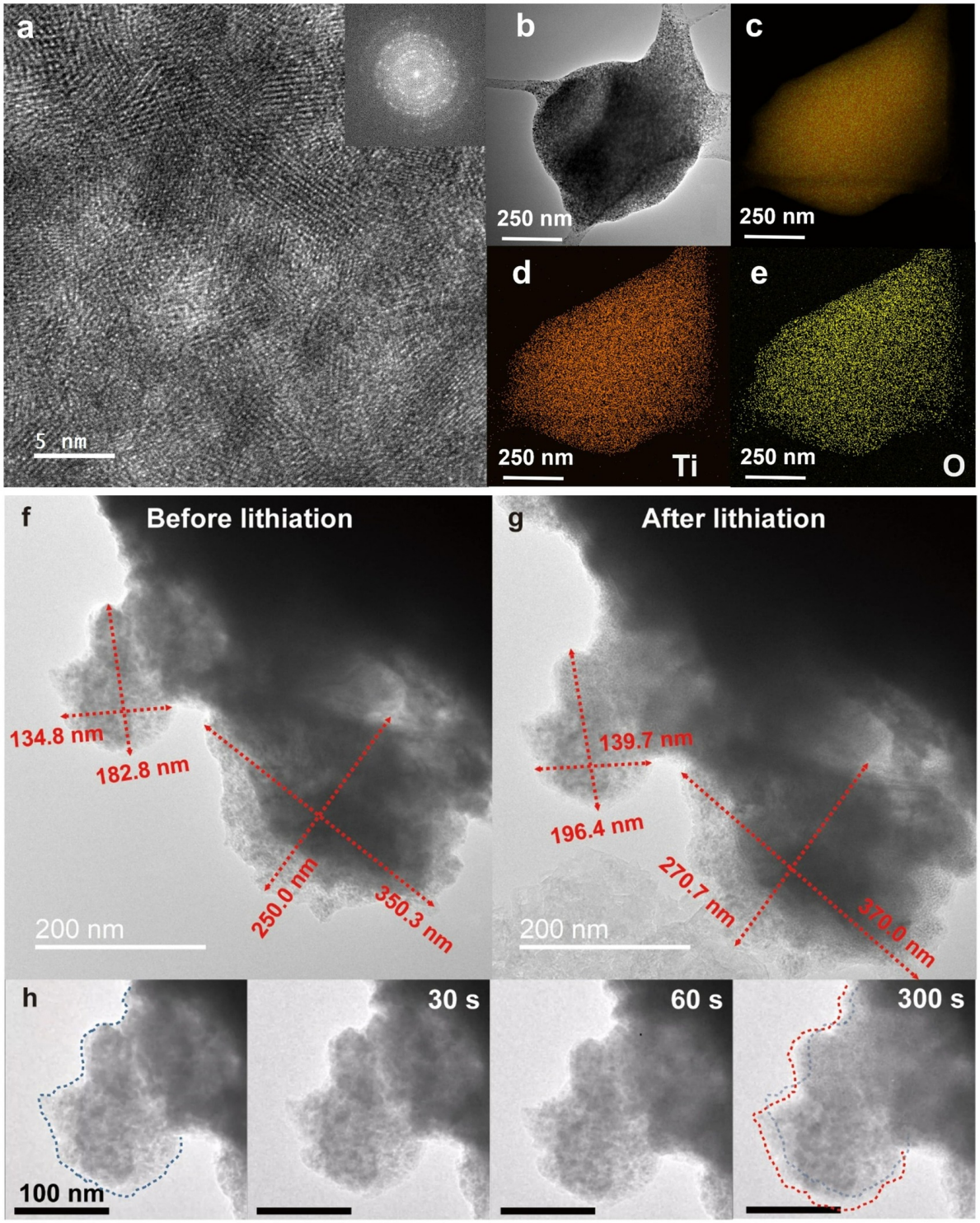

Figure 5.11: a) High resolution TEM images of TiO_2@PEG5K NPs with an inset displaying the respective selected area diffraction pattern. b-e) SEM (b) and EDX (c) images of an aggregate of TiO_2@PEG5K NPs showing the homogenous distribution of Ti (d, orange) and O (e, yellow). f-h) TEM images of TiO_2@PEG5K NPs before (f) and after (g) the *in-situ* lithiation highlighting the size modification with h) the associated magnified time-lapse of the upper particle. Blue and red dotted lines respectively mark the profile of the selected NP at the beginning and at the end of the lithiation process. Readapted with permission from [247].

tion of Titanium and Oxygen elements into the NPs (*Fig. 5.11b-e*, Ti in orange and O in yellow). After this preliminary investigation, it was possible to perform some *in-situ* TEM imaging of the NPs under lithiation with the aid of a W tip covered with Li metal and a voltage bias of 1.5V. As visible comparing the two images displayed in *Fig. 5.11f-g*, small TiO_2@PEG5K NPs or agglomerates (<200nm) experienced a significant volumetric expansion in the order of ≈11%. The similar behaviour was also appreciated in the time-lapse progression displayed in *Fig. 5.11h* where the blue and the red dotted lines represent the particle contour before and after 5 minutes of continuous lithiation, respectively. Conversely, a comparable volumetric expansion was not experienced by bigger NPs agglomerates (>500nm) which displayed a reduced growth ≤1% (*Fig. 5.12d*). These results confirmed the strongly dependence of volume increase on the TiO_2 particle size [255] and demonstrated the existence of a certain interaction between TiO_2@PEG5K fillers and lithium. However, TEM analyses could not completely clarify if the observed expansion resulted related only to the direct lithiation of anatase or also to the unfolding of the grafted PEG chains.

Consequently, the physicochemical nature of the hybrid fillers was further investigated employing other techniques able to provide deeper insights on the extent of the lithiation of NPs. Considering the magnetic properties of titania, EPR was employed to observe any measurable extent of lithiation chemically induced in TiO_2@PEG5K fillers with the protocol described in the experimental section. As shown in *Fig. 5.12b*, pristine NPs displayed a spectra composed of two resonance lines typical of oxygen poor nanometric titania and assignable to $O^{-\bullet}$ and $O_2^{-\bullet}$ centres [256]. Chemical lithiation induced limited modification to the spectra, such as the appearance of the resonance correspondent to $Ti^{3+\bullet}$ defects due to a partial reduction of Ti^{4+} [255, 257]. Differences were noticed performing the subtraction between the two curves which highlighted the presence of an additional resonance attributable to paramagnetic oxygen vacancies [258]. Overall, EPR analyses proved only a partial deprivation of surface oxygen species upon Li contact with a concurrent reduction pf Ti but did not confirm any extensive lithiation of the fillers.
Similar results were provided by *ex-situ* Raman measurements, analogously performed on pristine and chemically lithiated TiO_2@PEG5K NPs. No relevant differences were noticed in the Raman spectra before and after lithiation since all the major peaks were ascribable to anatase TiO_2 and remained unaffected upon lithiation (*Fig. 5.12c*, red and blue curve respectively) [259]. The main contribution at 155 cm^{-1} corresponded to $E_g(1)$ mode while the secondary features pf $B_{1g}(1)$, $B_{1g}(2)$, and $E_g(3)$ are respectively observable at 404 cm^{-1}, 520 cm^{-1}, and 643 cm^{-1} [260, 261]. Small additional features visible at 364 cm^{-1} and 584 cm^{-1} were ascribed to the presence of a minoritarian brookite phase [262]. Additionally, the main feature at 155 cm^{-1} appeared enlarged, presenting a full width at half maximum of 24 cm^{-1}, and partially shifted of 11 cm^{-1}. Both these observations were consistent with the previous results. In fact, peak shift and broadening can be explained taking in account the small crystallite size of TiO^2, which induces phonon confinement in crystalline domains of ∼8 nm as deduced with TEM analyses, and/or assuming a partial oxygen deficiency of TiO_x (x∼1.9) as demonstrated by EPR measurements [263, 264].

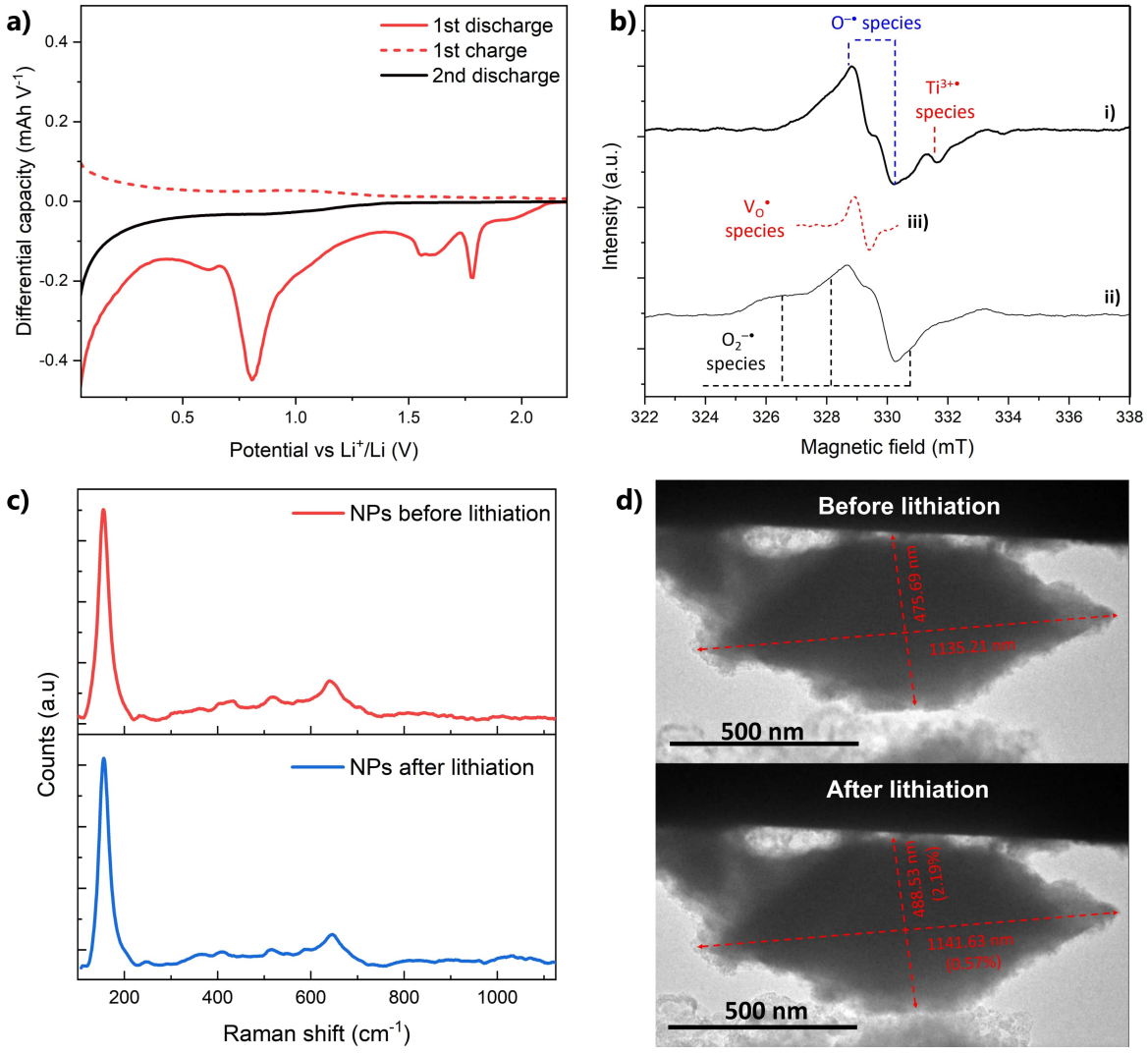

Figure 5.12: a) Differential capacity profile of *Fig. 5.10f* highlighting the redox potential of the reaction observed during lithiation of TiO_2@PEG5K electrode. b) EPR spectra of pristine (ii) and chemically lithiated (i) TiO_2@PEG5K NPs with (iii) the associated subtraction curve. c) Raman spectra of pristine (top) and chemically lithiated (bottom) TiO_2@PEG5K NPs. d) TEM images of a big TiO_2@PEG5K NPs before (top) and after (bottom) the *in-situ* lithiation process. Images have been readapted from [247]

Solid-state electrolyte characterization:

Overall, all the characterization performed on stand-alone TiO_2@PEG5K fillers offered some useful insights on the interaction with Li. Electrochemical testing and TEM displayed that NPs can react with Li, demonstrating an important irreversible specific capacity and a non-negligible volume expansion. However, Raman and EPR disproved any significant formation of $LiTiO_x$ species, partially disproving the extent of any major interaction between lithium and TiO_2. Therefore, to gain a deeper comprehension of our system, additional analyses were carried out on the real complete system, i.e. 50:50 w/w SSE composed by a PEO_{4M} matrix containing LiTFSI as conductive salt and an homogenous dispersion of the aforementioned fillers.
Firstly, *in-situ* Raman measurements were performed exploiting an optical cell in order to monitor the evolution of the SSE spectra upon cycling. As visible in 5.13a, the electrolyte did not experience any modification during stripping/plating and all the major features remains untouched. Apart from the presence of the peaks related to anatase TiO_2 described before and labelled with an orange square in the picture, all the other bands were attributed to PEO (green circle) or LiTFSI (black diamond) [265]. Therefore, no evidence of the formation of any lithium titanate species, otherwise clearly visible in the Raman spectra and associated to the appearance of specific distinct features [266], was reported: any modification of the peak intensity could be naively justified by a slight modification of the focus of laser upon the long-term cycling.
Similar considerations were deduced from the XPS measurements, performed on the pristine and on the post-mortem SSEs to investigate the possible presence of reduced form of titanium atoms such as Ti^{3+} formed by the interaction of Li with Ti^{4+}. *Fig. 5.13b* presents the comparison of the spectra on Ti *2p* region before and after cycling and no visible differences between them are detectable. The spectrum was fitted with a main contribution at 457.9 eV which was attributed to Ti^{4+} and with the relative spin-orbit coupling component shifted of 5.7 eV in accordance with the literature [267, 268]. Both of them are plotted using a burgundy line. Moreover, all the other peaks were fitted considering shake-up components (blue, 459.5-465.2 eV) and additional satellite feature (green, 471.4-477.6 eV) [267, 268]. No supplementary contribution at lower energy attributable to Ti^{3+} were observed [269]. This final consideration does not automatically contradict what previously described with EPR measurements, which reported the presence of an oxygen deficiency and a partial reduction of Ti^{4+} to Ti^{3+}. In fact, EPR possesses a sensitivity way higher than the one of XPS, respectively <1 ppm vs 1000 ppm, and resulted therefore capable to detect the minimal amount of defect centres present in NPs. As shown in Fig 5.13c-d, also the other regions of the XPS spectrum remained unaffected. The S *2p* portion, linked to the sulfonyl group of LiTFSI, did not display any evident difference before and after cycling. The same considerations can be extended to the O *1s* region whose peak was fitted by three components: the main feature at 531.3 eV is related to oxygen atoms linked to carbon and sulfur, as in PEO or LiTFSI, or in Ti-OH groups (blue) while the lower one was attributed to the O of the bulk of TiO_2 (burgundy) [270–272]. Finally, the only detectable difference resided in the Li *1s* region (Fig 5.13e) where a small shoulder at 55.1 eV is observed upon cycling due to the migration of Li^+ ions or to the partial oxidation of dendrites. However, this peak resulted too small and negligible to act as a proof of our proposed healing mechanism.

Considering that all the characterization techniques performed on SSEs have dis-

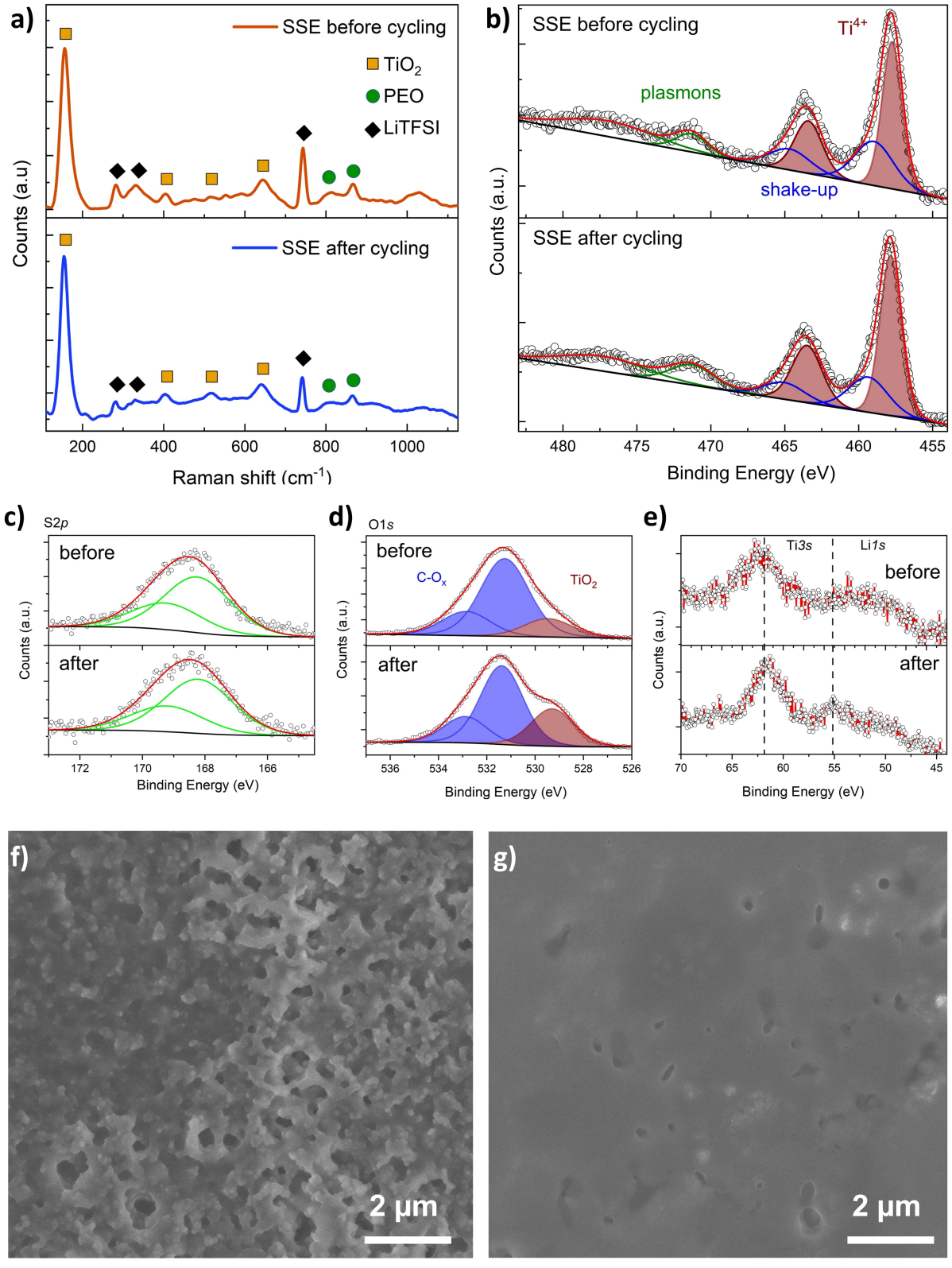

Figure 5.13: a) Raman spectra of 50:50 w/w SSE before and after cycling in a Li|Li symmetric cell under stripping plating at constant current density (j_{curr}=200 μA cm^{-2}). All the present peaks can be ascribed to TiO_2 (orange squares), PEO (green circles) or LiTFSI (black diamonds). b-e) XPS spectra of 50:50 w/w SSE before and after cycling in a Li|Li symmetric cell under stripping plating at constant current density (j_{curr}=200 μA cm^{-2}). Ti*2p* (b), S*2p* (c), O*1s* (d), Ti*3s* and Li*1s* (e) regions are respectively highlighted. f-g) *Ex-situ* SEM images showing the morphology of Li electrodes after cycling in a Li|Li symmetric cell under stripping plating at constant current density (j_{curr}=200 μA cm^{-2}) respectively equipped with f) PEO_{4M}:LiTFSI 10:1 and g) 50:50 w/w SSE. Readapted with permission from [247]

Table 5.8: Tensile modulus TM, maximum elongation at break ε_b, and ultimate tensile strength UTS of pristine PEO_{4M} film, PEO_{4M}:LiTFSI 10:1 polymer electrolyte, and our nanocomposite 50:50 w/w SSE.

Sample	**TM (MPa)**	ε_b **(%)**	**UTS (MPa)**
PEO_{4M}	200	40	6.1
PEO_{4M}:LiTFSI 10:1	0.9	364	0.1
50:50 w/w SSE	5.3	356	0.5

proved any significant chemical interaction between Li dendrites and NPs, it was therefore decided to investigate other possible explanations behind the interesting performances of this system. First if all, we quantified the effective strengthening effect imparted by the filler addition performing tensile testing experiments on thin strips of three different samples: pristine PEO_{4M} film, PEO_{4M}:LiTFSI 10:1 polymer electrolyte, and our nanocomposite 50:50 w/w SSE. For all these specimens, the averaged value of three different properties was measured: tensile modulus TM, maximum elongation at break ε_b, and the ultimate tensile strength UTS i.e. the maximum stress experienced by a materials before fracture. As shown in *Tab. 5.8*, PEO_{4M} presented very high TM and UTS, respectively equal to 200 MPa and 6.1 MPa, compatible with its stiff crystalline nature. Conversely, a limited ε_b of 41% was observed confirming its brittleness when compared to other polymers. The situation resulted greatly changed when moving to PEO_{4M}:LiTFSI 10:1, in which the salt addition was expected to greatly suppress the rigid crystalline domain as already proved by DSC analyses presented in *Sec. 5.1* [157, 232]. As predicted, the plasticizing effect of LiTFSI led to a sharp decrease of TM and UTS (0.9 e 0.1 MPa, respectively) coupled with a greatly improved elongation thanks to the increased amorphous content. However, the most interesting results were obtained when testing the nanocomposite SSE. In fact, the five-folds improvements achieved on TM (5.3 MPa) and UTS (0.9 MPa) with respect to the polymeric analogue are accompanied by a quasi-total retention of the elasticity with a maximum elongation of 356%, almost equal to the one of PEO_{4M}:LiTFSI 10:1 (361%). This confirmed once more the great homogeneity of the system achieved with the hybrid fillers since similar electrolytes experienced a great reduction of the maximum strain upon the encompassing of comparable contents of non-functionalized fillers [273, 274]. However, it's worth highlighting that the modulus of the nanocomposite system still remained below the threshold necessary to completely stop the dendrite propagation [160].
To verify if this greatly improved mechanical strength induced some major effects on the cycling properties of the systems, identical Li|Li coin cells were assembled employing both PEO_{4M}:LiTFSI 10:1 and 50:50 w/w SSE. After several stripping/plating cycles, Li electrodes were recollected and analysed with the aid of a SEM. Due to its poor mechanical properties, the morphology of the electrode cycled in contact with the polymer electrolyte resulted mossy and presented the evidence of dendrite growth (5.13f), with a surface similar to the one formed in presence of liquid electrolytes [275]. Conversely, the nanocomposite SSE enabled a more homogenous deposition of Li_+ and its improved strength acted as a physical barrier against any evident formation of dendrites. Consequently, the lithium surface displayed in *Fig. 5.13g* resulted flatter and less rough.

Nonetheless, even if the strengthening can effectively explain the improved stability

of the SSE against dendrites, no satisfactory explanations have been so far provided with respect to the healing mechanism. Consequently, time-dependant nuclear magnetic resonance (TD-NMR) analyses were carried out with the aim of clarifying furthermore the effect imparted by the filler dispersion on the polymer matrix. To do that, two different experimental protocols were exploited. Firstly, a magic sandwich echo (MSE) refocusing block was applied to evaluate the rigid fraction of the system as a function of the temperature [276]. Such fraction, defined by the mobility of the polymer chains and not strictly by the structure, can be both crystalline or glassy. From the results presented in *Fig. 5.14a* it is possible to clearly notice the differences showed by the different samples. PEO_{4M} and PEO_{4M}:LiTFSI 10:1 presented a similar behaviour: their rigid fraction, linked to the crystalline domains still present in the polymer, progressively decreased with the increasing temperature until sharply falling down to zero in correspondence of the melting of the system, lowered in presence of the lithium salt. Both T_m appeared in accordance with the values previously observed in *Sec. 5.1* and the profile of the curve follows the ones experienced for standard polymeric melts. Instead, the curve relative to 50:50 w/w SSE resulted totally diverse. In particular, due to its completely amorphous nature, the rigid polymer fraction was reduced also at lower temperature: the nanocomposite SSE retained a certain mobile fraction also at -20°C. However, the system maintained a non-negligible rigid fraction in the order of 10% even at 70°C confirming once more the strengthening action imparted by TiO_2@PEG5K NPs. It is worth stressing that this rigidity did not result directly connected to the ceramic nature of the NPs but appeared linked to a particular interaction of the PEO_{4M} chains with the brush-like grafted PEG5K and OA chains on the surface of the fillers. In turn, this interaction induced a different motional chain regime responsible for the improved polymer mechanical properties. Interestingly, also the subsequent MQ-NMR measurements, performed with a modified Baum-Pines sequence adapted to low-field environment to evaluate the effect of the NPs on a less local level, confirmed this hypothesis. Here, we recall that a normalized intensity of the MQ signal >0.5 corresponds to the presence of a fully developed polymer network [249]. As visible in *Fig. 5.14b*, neither PEO_{4M} nor PEO_{4M}:LiTFSI 10:1 presented any significant interchain interaction since their values fell largely short of the 0.5 threshold, as expected for polymer melts. Conversely, the nanocomposite SSE displayed a completely different profile with a clearly defined build-up curve that reaches the aforementioned threshold further confirming the existence of a physicochemical interaction between PEO_{4M} strands and grafted PEG5K chains. This induced an increase of the stiffness of the system, without sacrificing its elastomeric nature. These two features, coupled with the strengthening effect imparted by the high-modulus ceramic dispersoids, enabled the absence of dendrite growth observed upon cycling and with SEM. Moreover, Tichonov regularization of 50:50 w/w SSE curve permitted to extract the underlying distribution of the dipolar couplings as a function of the frequency (*Fig. 5.14g*) [277]. Two distinct distributions were distinguishable: the sharp peak located at low values corresponds to the free motion of the majority of PEO_{4M} chains which virtually experience no cross-linking while the final build-up at high coupling frequencies (∼3 kHz) results associated to the constrained polymer strands in proximity of TiO_2@PEG5K NPs, therefore interacting with the brush-covered hybrid fillers.
It is also worth noticing that the MQ-NMR tests were performed at 70°C in order to completely mimic the SSE at the working temperature of the electrochemical cells and in a situation where no residual crystallites are present for any of the specimens.

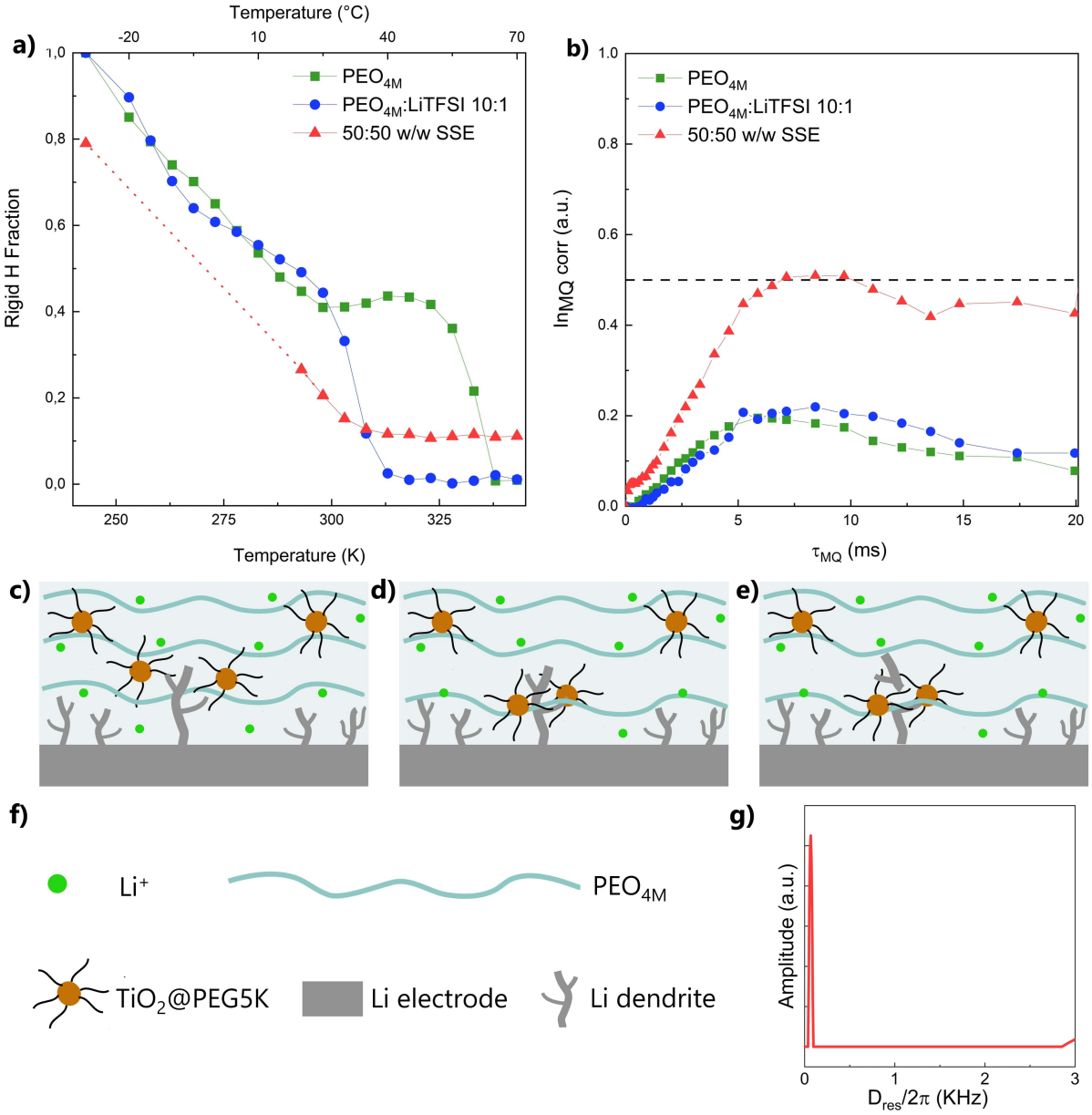

Figure 5.14: a) Rigid fraction of different systems as a function of temperature obtained from MSE-NMR analyses performed in the range [-25°C:+70°C]. The dotted line represents a region in which two component fitting resulted unreliable. b) Normalized MQ-NMR build-up graphs plotted vs. excitation time τ_{MQ} performed at 70°C. The black dashed line marks the 0.5 threshold, usually associated to the presence of cross-linked networks. c-e)Naive representation of the proposed *razor effect* established in our nanocomposite SSE thanks to the presence of the hybrid fillers and to the high mobility of PEO_{4M} and PEG5K chains with f) the relative legend. g) Distribution of dipolar moments D_{res} obtained by Tichonov regularization of the build-up of 50:50 w/w SSE MQ NMR. Error bars resulted in the order of the dot size. Readapted with permission from [247].

Final considerations on the healing mechanism:

In summary, both stand-alone TiO_2@PEG5K NPs and the final SSE have been investigated in order to clarify the peculiar healing mechanism observed in this nanocomposite electrolyte. Even if electrochemical testing and *in-situ* TEM of NPs displayed a certain degree of lithiation, all the subsequent characterization highlighted that no significant interaction was established between NPs and Li, in particular when the fillers are encompassed into the PEO_{4M} matrix (or, at least, below the sensitivity of XPS $\approx$ 0.1-1%). Consequently, the healing of the Li|Li symmetric cells can only be justified taking in account the very distinctive mechanical properties of the system which endows a synergic action, both preventing and disrupting Li protrusions. The filler dispersion greatly improved the strength of the electrolyte without reducing its elasticity, therefore leading to a reduced growth of dendrites due to the higher modulus of the matrix. Moreover, the cross-linked mobile network, observed with TD-NMR and established between PEO_{4M} and grafted PEG5K, imparted additional stiffness to the SSE while locally enhancing its mobility. It was therefore possible to postulate that the healing can be achieved through the interplay between the highly mobile but stiff polymer matrix and the fillers. This interaction permitted a physical breakage of Li dendrites able to disrupt the metallic contact formed between the electrodes. The fractured dendrites were therefore detached from the electrode and displaced into the SSE as dead lithium, inducing the healing of the cell at the expense of an irreversible loss of capacity. It must be considered that this effect was also permitted by partial softening of Li dendrites cycled at 70°C. A naive representation of this proposed *razor effect* is presented in *Fig. 5.14c-f*. Conversely, PEO_{4M}:LiTFSI 10:1 did not permit a similar intrinsic self-healing due to its lack of mechanical strength.
Considering that such a behaviour result chiefly independent from the chemical nature of the ceramic filler whose lithiation is negligible, this effect can also be used to explain the analogue phenomenon observed in *Sec. 5.1* for similar PEG-capped SiO_2 hybrid fillers. Additionally, subsequent publications reported a similar behaviour in a comparable system based on PEO and LLZO [242, 278], further confirming the possibility of this peculiar phenomenon in the presence of dynamic soft shorts.

5.3 PVdF-based SSEs: preliminary investigation and filler encompassing

The third project devoted to the investigation of polymer nanocomposite electrolytes was addressed to the study of PVdF-based lithium-conductive systems. As described in *Sec. 4.2.1*, conduction into PVdF matrices is assured thanks to the presence of residual solvents that permits Li^+ motion upon the application of an external electric field. However, their properties required further investigation in order to clarify their behaviours and to better understand their categorization as SPEs or GPEs. Consequently, it was decided to test 6 different PVdF-based polymers, three homopolymers and three PVdF-HFP copolymers, in order to select the one with the most interesting electrochemical properties. After having chosen the most suitable candidate, the first part of the work was devoted to understanding the effect of residual solvent on the electrolyte properties. Subsequently, after having acknowledged the solvent impacts and after having standardised the drying procedure for these electrolytes, two different functionalized hybrid SiO_2 fillers were encompassed into a nanocomposite SSE (or, as it will be defined quasi-solid electrolyte) in order to verify the beneficial effects imparted by the addition of tailored ceramic NPs. In particular, two different fillers were investigated. Firstly, PEG-grafted silica NPs (SiO_2@PEG NPs) were tested to prove if the presence of a Li^+ conductive polymer chains can induce a second conduction pathway into the PVdF matrix. Secondly, a perfluoroalkyl silane (PFOTES) was preliminarly produced as grafting agent in order to enhance the compatibility between the functionalized NPs (SiO_2@PFOTES NPs) and the fluorine-rich polymer matrix. The results described in the following sections have been collected in the following scientific papers: *"Host-guest interactions and transport in poly(vinylidene fluoride)-based quasi solid electrolytes for lithium batteries"* and *"PVdF-HFP-based quasi-solid nanocomposite electrolytes for lithium metal batteries"* [279, 280].

5.3.1 Materials and methods:

For the production of SSEs, N-N Dimethylformamide (DMF, 99.8% anhydrous) and tetrahydrofuran (THF, 99.8% anhydrous) were acquired from Alfa Aesar and stored in a glove box (O_2, H_2O<0.1 ppm). Lithium bis(fluorosulfonyl)imide (LiFSI, 99.9%) was provided by Solvionic while LiTFSI was bought from Sigma Aldrich. PVdF Solef® 6020, PVdF-HFP Solef® 21510 and PVdF-HFP Tecnoflon® NH have been kindly provided by Solvay. PVdF Kynar® 761, PVdF-HFP Kynar® 2751 and PVdF-HFP Kynar® 2801 were generously obtained from Arkema. All the polymer powders have been dried at 80°C under vacuum prior using and were then transferred into the glove box.
For the synthesis and functionalization of SiO_2 NPs, absolute EtOH (99.97%), milliQ H_2O, and toluene (99.0%) have been acquired from VWR Chemicals. 1H,1H,2H,2H-perfluorooctyltriethoxysilane (PFOTES, 97%), succinic anhydride (99%), and APTES (98%) were bought from Alfa Aesar. TEOS, triethylamine (99%), dichloromethane (DCM, 99%) and a 25% w/w aqueous solution of NH_4OH have been provided by Sigma Aldrich. Polyethylene glycol methyl ether of different molecular weight (PEGx, with X=M_w) were acquired by Alfa Aesar (PEG750, M_w=750 g mol^{-1}) and Sigma Aldrich (PEG5K, M_w=5000 g mol^{-1}). All the materials have been used as received and without any further purification.

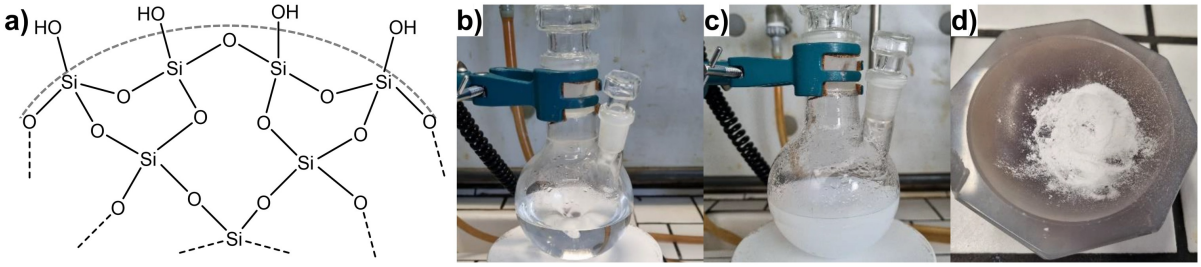

Figure 5.15: a) Schematic representation of the chemical bond present into SiO_2. Silica surface is represented by the grey dashed line. b-c) Reaction mixture at the beginning (b) and after 23 hours (c). d)SiO_2 powder after drying and grinding

Carbon-coated LFP powder was obtained from Hydro-Quebec while Li ribbons (99.9%) were provided by Sigma Aldrich.

Synthesis and processing:

NPs synthesis and functionalization: SiO_2 NPs have been synthesized exploiting a Stöber approach which enables an easy control of the particle size with an elevate dimensional homogeneity [281]. In fact, the reaction exploits the hydrolysis of alkyl silicates, such as TEOS, to mono-hydrolysed monomers which eventually leads to their final condensation in alcoholic solutions and in presence of a catalyst such as ammonia (*Fig. 5.15a*). The tuning of parameters such as temperature, stirring, and reactants/catalyst concentration strongly influences the reaction speed hence anticipating or postponing the reaching of the over-saturation condition, responsible for the nucleation of new NPs. A careful control of these aspects can therefore produce a simultaneous nucleation and a narrow distribution of particles' size.
In our case, spherical non-porous SiO_2 NPs were produced with the following synthetic approach. 10.8 mL of MilliQ H_2O (6.00 mol L^{-1}) and 1.53 mL of NH_4OH solution (0.04 mol L^{-1}) were dispersed in 100 mL of EtOH and sonicated at RT for 10 minutes. 6.25 mL of TEOS (0.28 mol L^{-1}) were then added into the flask and left under controlled stirring at 550 rpm for 23 hours. During the reaction it was possible to appreciate a colour change of the mixture that pass from transparent to milky due to the formation of SiO_2 suspension (*Fig. 5.15b-c*). To recollect the solid product, the solution was centrifuged at 9000 rpm for 30 minutes and the supernatant was removed. The residue was then washed with EtOH and the procedure is repeated for two additional times. Finally, the resulting white powder was washed with MilliQ water and left to dry overnight at 75°C in a oven. Before using, the powder was carefully crushed with the aid of an agate mortar and pestle (*Fig. 5.15d*).
For the production of the SiO_2@PEGX NPs, a two-steps reaction path similar to the one shown in *Fig. 5.2a* has been followed. Even if the overall process resembles the one presented previously in *Sec. 5.1.1*, some small experimental modifications described herein have been implemented. 1.0 g of pristine SiO_2 NPs were dispersed into 24mL di EtOH (instead of toluene, as done before). The different solvent has been selected to reduce both the cost and the environmental impact of the process. 100 μL of NH_4OH solution (25% w/w) were then injected and the mixture was left to homogenize for 15 minutes while stirring at 600 rpm and heating at 80°C. Then, 24 μL of APTES (1:2 molar ratio between APTES and OH on the surface of SiO_2) were added and left to react for one day under the same conditions. The SiO_2@APTES solid residue was then recollected

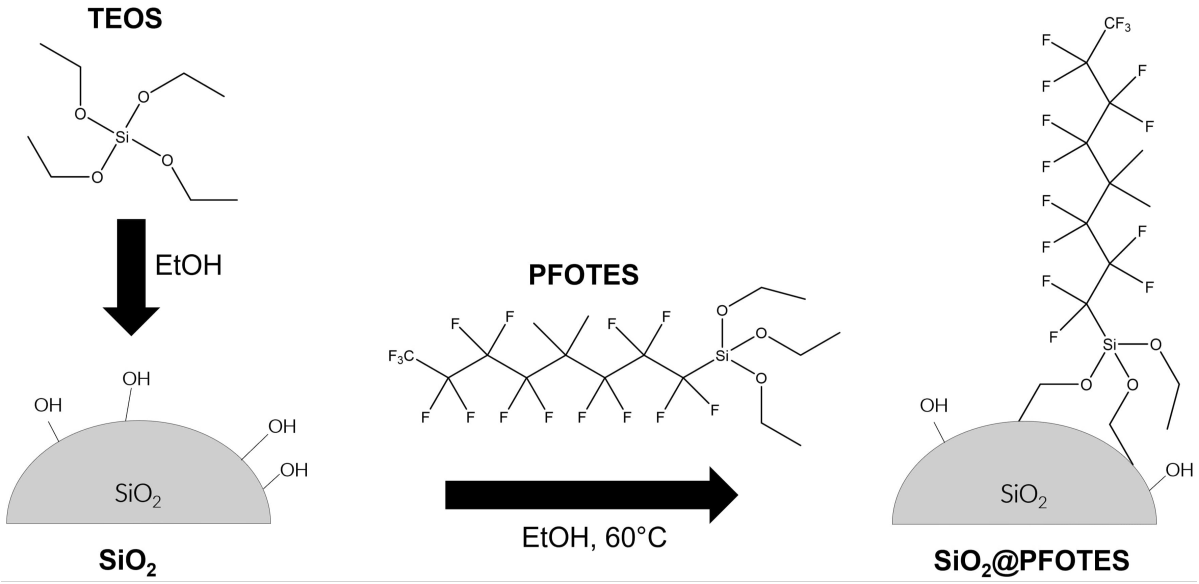

Figure 5.16: Schematic representation of the reaction process for the synthesis of SiO_2@PFOTES NPs.

through sequential centrifugation and washing with EtOH, as described previously with bare SiO_2 NPs, and dried. Finally, SiO_2@APTES was made to react with PEGX-COOH (X=750 and 5K g mol_{-1}, produced as described in *Sec. 5.1.1*) using a APTES:PEG molar ratio equal to 1:1 (for PEG5K) and 1:2 (for PEG750) using the same reaction conditions reported in *Sec. 5.1.1*. After centrifugation and washing, the SiO_2@PEGX product was ground in a mortar and dried at 100°C overnight.
To produce fluorosilane-functionalized silica NPs, i.e. SiO_2@PFOTES, the simple reaction showed in *Fig. 5.16* was exploited. 1.0 g of SiO_2 were dispersed into 20 ml of solvent (EtOh or toluene) and dispersed under stirring at 300 rpm under heating (60°C for EtOh, 120°C for toluene) using a Liebig reflux condenser. When reflux conditions were achieved, 1.05 mL of PFOTES (1:2 molar ratio between PFOTES and OH on the surface of SiO_2) and 0.1mL of NH_4OH solution were added to the mixture. After 24 hours, the reaction was completed and the product (SiO_2@PFOTES) was recollected, centrifuged and washed with the same procedure previously described before being ground and dried.

SSEs fabrication: PVdF and PvDF-HFP-based SSEs have been fabricated exploiting a solvent casting approach already reported in literature [177]. Polymer, lithium salt and the eventual filler were dispersed in a THF:DMF mixture (7:3 v/v) and the solution was stirred at RT until complete dissolution. These two solvents have been chosen in accordance to literature for their good capability of dissolving both the polymer and the salt. Purely polymeric SSEs were produced using five different PVdF and PVdF powders (PVdF Solef® 6020, PVdF-HFP Solef® 21510, PVdF Kynar® 761, PVdF-HFP Kynar® 2751 and PVdF-HFP Kynar® 2801) while all the nanocomposite SSEs employed PVdF-HFP Kynar® 2751. When an homogenous dispersion was achieved, the mixture was poured into PTFE moulds and left to gently dry for a fixed amount of time. This value was set to 72 hours for the nanocomposite SSEs while different drying procedures (24, 72, and 168 hours with or without a vacuum treatment) have been tested for the purely polymeric electrolytes. In order to standardise the solvent intake of the membranes, all the systems were produced starting from a solution containing a 3 wt% of the selected

Table 5.9: Composition of the different SSEs containing bare SiO_2 and SiO_2@PEGX fillers.

SSE sample	SiO_2 wt%	LiFSI wt%	PVdF-HFP wt%	PEGX wt%
SiO_2_5	5	38.2	56.8	0
SiO_2_10	10	36.1	53.9	0
SiO_2_15	15	34.1	50.9	0
PEG750_5	5	37.9	56.5	0.3
PEG750_10	10	35.5	53.4	0.6
PEG750_15	15	33.4	49.9	0.9
PEG5K_5	5	37.9	56.8	0.2
PEG5K_10	10	35.8	53.8	0.3
PEG5K_15	15	33.7	50.4	0.5

Table 5.10: Composition of the different SSEs containing SiO_2@PFOTES fillers.

SSE sample	SiO_2 wt%	LiFSI wt%	PVdF-HFP wt%	PFOTES wt%
PFOTES_8%	8	52.1	34.7	5.2
PFOTES_10%	10	50.1	33.4	6.5
PFOTES_16%	16	44.2	29.4	10.4
PFOTES_24%	24	36.2	24.2	15.6
PFOTES_30%	30	30.3	20.2	19.5

polymer. When needed, the fillers and the lithium salts were added accordingly to the polymer mass and in order to achieve the desired w/w ratio. PVdF:LiFSI content has been kept constant to a 3:2 ratio while different ceramic contents, spanning from 5 to 15 wt% for SiO_2@PEGX and from 8 to 30 wt% for SiO_2@PFOTES, have been tried for SiO_2-based fillers. To avoid any misinterpretation with the nanocomposite SSEs based on similar fillers previously described in *Sec. 5.1*, electrolytes will be depicted with the following label: **XXX_Y** SSE (or QSE) where **XXX** is related to the functionalization of the specific kind of filler (SiO_2 for bare silica NPs; PEG750, PEG5K, PFOTES for functionalized SiO_2 NPs) employed in the membrane while **Y** is the wt% of ceramic material into the electrolyte. All the different investigated compositions are displayed in *Tab. 5.9* and *Tab. 5.10*.

All the procedures have been performed in an Ar-filled glove box to prevent any water intake from the hygroscopic lithium salt.

Electrode production: Electrode production followed the same specifications described in the previous experimental sections *5.1.1* and *5.2.1*.

Instrumentation and methodology:

Physicochemical characterization: ATR-FTIR spectra were collected on a Thermo Fisher Scientific Nicolet iS20 spectrometer, measuring 32 scans with a resolution of 4 cm^{-1}. All the spectra have been acquired in the wavenumber range 4000-500 cm^{-1} in order to identify the vibrational features associated to the different moieties of our

compounds.
DLS evaluation of the particle size distribution was carried out on a Malvern Zetasizer Nano Series ZS90 at RT dispersing SiO_2 fillers into deionized H_2O in a quartz optical cuvette (concentration$\sim$0.1 mg mL^{-1}). The instrument operated with a 663 nm laser. The same device was also utilised to quantify the ζ-potential of bare and functionalized SiO_2 NPs in analogue diluted solutions.
TGA analyses were performed on a Star^{e}System of Mettler Toledo employing alumina crucibles. Measurements on fillers have been carried out with an air flux of 50 mL min^{-1} and an heating rate of 10 °C min^{-1} employing the following protocol:

- heating from 30°C to 150°C;
- 10 minutes isotherm at 150°C to induce evaporation of residual solvent and absorbed H_2O;
- heating from 150°C to 1000°C.

TGA measurements on SSE were instead conducted on the same instrument in nitrogen atmosphere with a single heating ramp (5°C min^{-1}) in the temperature range [+30°C;+250°C] or with a 9h isotherm at 150°C to evaluate weight losses related to DMF removal.
To evaluate the shape and the average size of SiO_2 NPs, TEM analysis have been carried out on a JEOL JEM 2100 PLUS transmission electron microscope equipped with a LaB_6 source operating at 200 kV. EDX mapping and SEM images have been acquired using a Zeiss Gemini 500 microscope with a Bruker QUANTAX EDX micro-analyser. Samples have been mounted on conductive stubs with the aid of double-sided conductive carbon tape and then gold-coated to improve their electronic conductivity. Cross section images have been instead obtained mounting the SSEs on conductive silicon pieces. All the tests were performed with a tension of 5 kV.
To investigate the crystalline or amorphous nature both of SiO_2 fillers and of PVdF powders and films, XRD analyses have been performed on a Rigaku MiniFlex 600 diffractometer equipped with a Cu source (λ=1.54 Å) in the 2Θ range from 10° to 60° at a scan speed of 1°C min^{-1}.
Thermograms of different PVdF and PVdF-HFP powders and films were acquired with DSC measurements on a Mettler Toledo instrument. Specimens were loaded into 40 μL aluminium crucible and sealed in a Ar-filled glove box to avoid any possible contamination. Analyses were performed in the temperature range [-60°C;+195°C], in order to be able to detect both T_g and T_m, with an heating rate of 5°C min^{-1} under a N_2 flux of 80 mL min^{-1} applying the following experimental method:

- heating from RT to 195°C;
- 2 minutes of isotherm at 195°C;
- cooling from 195°C to -60°C;
- 2 minutes of isotherm at -60°C;
- second heating cycle from -60°C to 195°C.

^{13}C and ^{7}Li solid-state NMR spectra have been collected on a Bruker Avance III equipped with a 9.4 T magnet and 4mm probe with a 10 KHz spinning speed. The results were obtained performing the average over 1000 scans with delay of 50 seconds and 90° pulse duration of 2.5 μs using as a reference adamantane and LiCl aqueous 1M, respectively. A 7mm MAS probe with a rotation frequency of 5 kHz has instead been employed for ^{29}Si acquisitions and referenced to tetramethylsilane.
A Bruker Minispec mq20 instrument equipped with a BVT3000 N_2-fed temperature controller was employed to collect the TD-NMR spectra.
Micro-Raman measurement have been carried out on a LabRAM confocal spectrometer using a He-Ne laser (λ=632.8 nm) in backscattering mode. The signal was collected by a CCD-Sincerity mounted on an Olympus BX40 microscope head. The system was calibrated using a crystalline silicon standard. Spectra of SSEs have been collected in open air while the DMF:THF:LiFSI solutions were tested in glass vials sealed in an MBraun Glove Box.
Interactions between Li^+, FSI^-, DMF and PVdF were computed with the aid of Density Functional Theory (DFT) using Gaussian16 suite [282]. To account for solvation, a conductor-like polarisable continuum model with a dielectric constant of 10.1 was employed [283]. For the sake of simplicity, PVdF oligomers ($C_{15}F_{14}H_{18}$) in α phase were employed instead of PVdF-HFP copolymers considering the reduced HFP fraction (<6% mol) in the sample. Simulated Raman spectra were computed with Molden using a Lorentzian with bandwidth of 10 cm^{-1} [284]. DFT in conjunction with ab-initio molecular dynamic (AIMD) simulations were instead employed to investigate the motion and the diffusion of Li/DMF complexes into PVdF electrolyte. Tryglyme was employed as a model system for PEG and its interaction with Li^+ has been computed using Gaussian16 theory [282].
Mechanical testing was performed on a ZwickRoell RetroLineTesting Machine employing n≥5 rectangular specimens (1x5cm) per each composition with preloading of 0.01 N and extension rate of 100 mm $min^{-1.}$

Electrochemical characterization: Ionic conductivity of SSEs has been evaluated employing PEIS on symmetric coin cells with two stainless steel (SS) blocking electrodes. Frequency range from 100 Hz to 1 MHz and temperature range from 20°C to 80°C have been investigated to determine the resistance of the selected electrolytes and, consequently, the ionic conductivity of the systems using *Eq. 4.10*.
Electrical conductivity of the electrolytes has been quantified using the Hebb-Wagner polarization method on Li|SSE|SS CR2032 cells [285]. A constant potential U was applied for an amount of time sufficient to reach the steady current $i_{e,h}$ related to the electron and holes motion. Consequently, the electronic conductivity σ_e+σ_h attributable to electron and holes was determined with the following *Eq. 5.7* and *Eq. 5.8*:

$$i_{e,h} = \frac{kT}{eL}[\sigma_e(exp\Big(-\frac{Ue}{kT} - 1\Big) + \sigma_{\mathrm{h}}(1 - exp\Big(\frac{Ue}{kT}\Big)))] \tag{5.7}$$

$$\sigma_e + \sigma_h = \frac{L}{A} \cdot \frac{d|i_{\mathrm{e,h}}|}{dU} \tag{5.8}$$

where L is the thickness of the electrolyte, A the contact surface, and e the electronic charge.
Cronopotentiometric tests at selected current densities have been employed to verify the

stability of our SSEs during stripping and plating of Li in symmetric Li|SSE|Li CR2032 coin cells. Two different experiments were performed:

- six steps composed by 10 stripping-plating cycles at increasing current densities (50-100-200-300-400-500-10 μA cm^{-2}) of 1 h each (alternatively 30 minutes of positive and negative current density) followed by a final step at 100 μA cm^{-2} to verify the final integrity of the cell;

- continuous stripping-plating cycling at fixed current density of 100 μA cm^{-2} until the final cell failure.

Linear sweep voltammetry (LSV) and cyclic voltammetry (CV) were used to evaluate the ESW of different SSEs both at positive and negative potentials. Cells comprising SS as WE and Li as RE and CE were assembled and tested at a scan rate of with a scan rate of 0.1 mV s^{-1}. Linear oxidation stability tests were performed in the potential range from OCV to 5.5 V vs Li^+/Li while reduction stability was investigated performing 3 cycles from -0.125 V vs Li^+/Li to 1.0 V vs Li^+/Li.
GCPL measurements were performed on Li|SSE|LFP CR2032 coin cells thermalized at 30°C and cycled at 0.1C in the potential range 2.7 V-3.9 V vs Li^+/Li.
ARC tests were applied in the standard *wait and seek* mode to Li|LFP cells in the temperature range from 35°C to 300°C with a heating step of 5°C on a THT instrument.

5.3.2 Results and discussion:

Evaluation and investigation of PVdF and PVdF-HFP SSEs:

The first part of the project was devoted to a preliminary investigation of the different homopolymers and copolymers. Of the six candidates received by the two manufacturers (Arkema and Solvay), PVdF-HFP Tecnoflon® NH was discarded prior to testing due to its very peculiar nature. Its very high HFP content (whose specific value cannot be disclosed publicly) rendered this material completely amorphous but also imparted a totally different consistence. As a consequence, Tecnoflon® NH appeared as a rubbery material difficult to process rather than as a white powder like all the other polymers. Therefore, after a preliminary DSC analysis performed for the sake of completeness, the further investigation will be carried out only on the remaining five powdery materials.

For every material, three different samples have been tested: pristine powder, polymer membrane obtained with solvent casting, and polymer electrolyte containing LiFSI and produced with solvent casting. For the sake of clarity, the following nomenclature approach will be employed: **XXXX-Y**, where **XXXX** is related to the specific commercial numeric name of the polymer (761 and 6020 for the homopolymers, 2751, 2801, and 21510 for the copolymers) and **Y** describes the kind of sample (P for powder, M for the casted membrane without Li salt, S for the complete SSE).
Firstly, all the received PVdF and PVdF-polymers were tested with a DSC instrument to verify their thermal property. Results are displayed in *Fig. 5.17* and *Fig. 5.18*. Thermograms of pristine powders (5.17a-b) confirmed the expected differences between strongly crystalline PVdF materials and partially amorphous PVdF-HFP ones, whose lateral hexafluoropropylene chains disrupt the ordered packing of the systems. As expected, 6020-P and 761-P possessed an higher T_m and a more evident crystallization

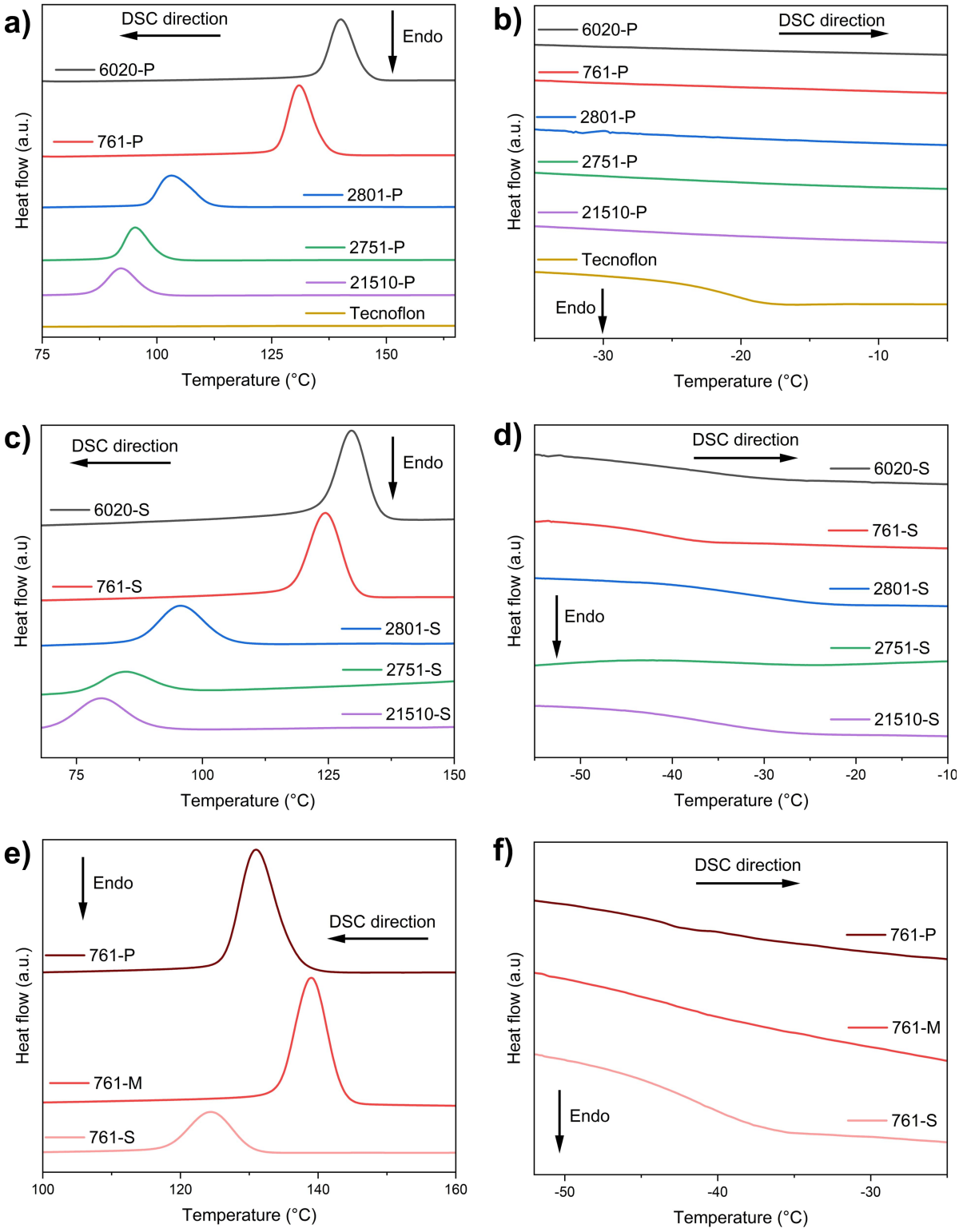

Figure 5.17: a-b) DSC profile of PVdF and PVdF-HFP powders in the region of crystallization (a, cooling) and glass transition (b, 2nd heating). c-d) DSC profile of PVdF and PVdF-HFP SSEs in the region of crystallization (c, cooling) and glass transition (d, 2nd heating). e-f) Comparison of DSC profiles of Kynar 761 PVdF powders, membranes and SSEs in the region of crystallization (e, cooling) and glass transition (f, 2nd heating).

peaks related to a more pronounced crystalline fraction. Conversely, the endothermic features of three copolymers (2801-P, 2751-P, and 21510-P) appeared less intense and located at lower temperatures. Complete amorphicity is instead observed for Tecnoflon specimen. Due to its prevalent amorphous fraction, Tecnoflon was also the only polymer to display a visible glass transition, unnoticeable in the other polymers and copolymers. Upon the addition of the lithium salt, a progressive amorphization was induced into the polymer. This fact was highlighted both by a lowering of the intensity of the peak (*Fig. 5.17e*) and by the appearance of the glass transition in all the 5 SSEs (*Fig. 5.17d*). Interestingly, additional insights can be obtained when comparing the thermograms of the powders, the membrane and the SSEs of a single polymer as Kynar 761 which was selected as exemplificative sample. When passing from 761-P to 761-M, a noticeable positive shift of the crystallization temperature (≈5°C) is visible. This feature is compatible with the transition from the low-melting α phase to the high-melting β one [171]. The additional incorporation of LiFSI instead induced a plastifying effect in the system, which corresponds to a pronounced T_g and a way less intense crystallization peak.
A further aspect, whose comprehension would result pivotal for the subsequent thermal analyses, deserves to be highlighted here. During the 1st heating cycle, all the LiFSI based SSEs displayed a strong irreversible exothermic peak occurring around 140°C, i.e. overlapping with the melting of the PVdF and the evaporation of DMF (*Fig. 5.18a*). This degradation phenomena were attributed to LiFSI salt, whose thermal instability is reported in specialistic articles in correspondence of its melting [286]. A similar behaviour was not observed for SSEs exploiting a more stable salt such as LiTFSI: their thermograms, reported in *Fig. 5.18b*, only presented a distinct and reversible endothermic peak attributable to PVdF melting. Consequently, all the aforementioned consideration on the crystallinity of LiFSI based SSEs were made taking in account the crystallization peak recorded upon cooling where no degradation was observed.
Similar considerations on the crystallinity were also provided by XRD analysis. *Fig. 5.18c-d* displays the diffractograms of all the PVdF and PVdF-HFP powders. All the system displayed a crystalline or semi-crystalline morphology with two sharp peaks located around 20° and an additional feature at 26° related to the presence of α phase. Further insights on the effect of solvent addition can be achieved comparing the curve of 761-P and 761-M (Fig. 5.18e): it can be clearly noticed that the casted membrane present a reduced crystallinity. Additionally, it results possible to appreciate the disappearance of the peak located at 26°, associated to α phase, and the simultaneous increase of the feature at 36° [287]. In fact, it is well known that the β phase can be produced with casting from various solvents such as DMF and THF [288]. Therefore, this measurement confirmed the previous consideration postulated after thermal analysis.
Finally, we also performed some ATR-FTIR spectroscopy on all the powders. Considering the small differences present among different samples, just two selected examples, 761-P and 2751-P, are presented in *Fig. 5.18d*. Vibrational spectra confirmed the coexistence of different phases both in pristine PVdF and PVdF-HFP. Peaks located at 986 and 761 cm^{-1} are assigned to α phase while the feature at 842 cm^{-1} is attributed to β one. Finally, the amorphous band is detected at 873 cm^{-1} and the characteristic peaks observed at 1402, 1179 and 1069 cm^{-1} are respectively assigned to CH_2 wagging, asymmetric CF_2 stretching and out-of-plane CF_3 deformation [289].

After having physically characterized the different materials, all the SSEs were electrochemically tested in order to select the desired material for the subsequent investi-

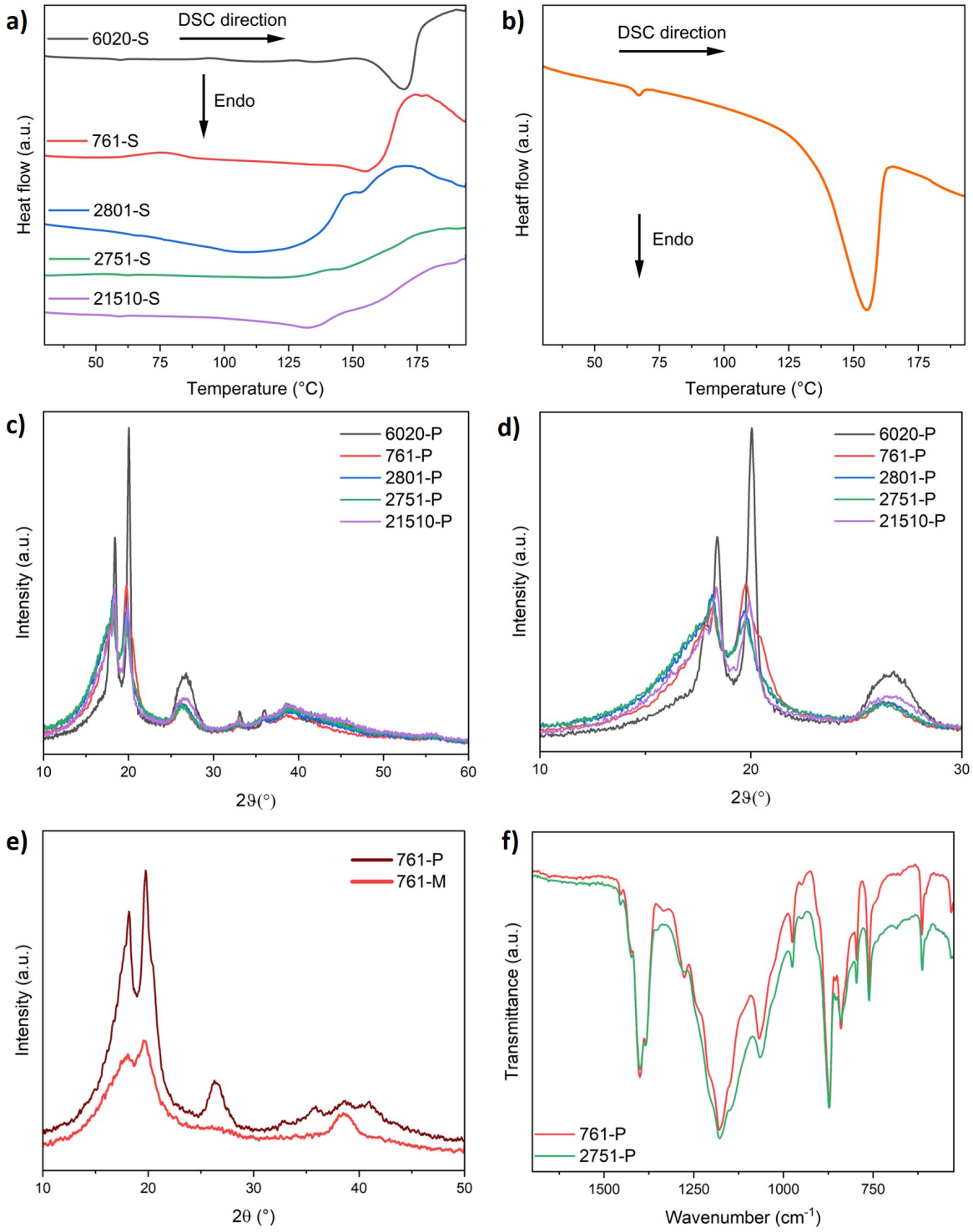

Figure 5.18: Comparison between the DSC thermogram of the 1st heating of (a) all LiFSI based SSEs (b) and of Kynar 761 SSE containing LiTFSI salt. c) XRD diffractograms of PVdF and PVdF-HFP powders with a magnification (d) on the region of interest. e) XRD diffractograms of 761-P and 761-M in the angular range 10°-50°. d) Magnification of ATR-FTIR of two selected powders, 761-P and 2751-P, in the wavenumber range 1700-500 cm^{-1}.

gations. For this preliminar characterization, it was decided to standardise the drying procedure in order to avoid fluctations in the ionic conductivity related to the presence of different residual solvent. Consequently, all the casted membranes were left to dry for 72 hours under inert atmosphere and were then detached from the PTFE mould and punched into 16mm disks. As shown in *Fig. 5.19a-b*, the electrolytes ionic conductivities spanned into an order of magnitude from 10^{-4} S cm^{-1} to 10^{-3} S cm^{-1} at RT up to 10^{-3} S cm^{-1} to 10^{-2} S cm^{-1} at 90°C. Higher σ_{Li^+} were obtained with 761-S but all the samples presented an activation energy in the order of 0.20 eV. All these data were in line with the results previously reported in literature [176, 180]. LSV measurements also demonstrated no sharp differences on the ESW of different systems (*Fig. 5.19c*). As expected, a strong oxidative peak, associated to PVdF dehydrofluorination [290], was detected in proximity of 4.5 V vs Li^+/Li. At that potential, C=C double bonds are formed leading to the unsaturation of the main polymer chain at the expense of fluorine loss. More pronounced differences were instead observed when comparing the processability of these electrolyte. As displayed in *Fig. 5.19d*, the use of highly crystalline PVdF homopolymers led to diffused cracking upon drying of 761-S and 6020-S. Therefore, achieving homogenous and free-standing electrolyte disks suitable for cell testing resulted a complex and time-consuming task due to their brittleness. Conversely, PVdF-HFP systems presented an improved flexibility to the resulting SSEs which appeared more compliant and easy to produce thanks to the presence of HFP lateral chains which endowed increased amorphous content.

Taking in account all the aforementioned features, it was decided to carry on the following study on the solvent effect exploiting the PVdF-HFP Kynar 2751, the material that presented the most satisfying trade-off between electrochemical performances and ease of processability.

Evaluation of the effect of the residual solvent:

After having selected the most suitable polymer for the production of the SSE, it was possible to start investigating the effect of the residual solvent on the conductive properties of the electrolyte. Preliminarily, the evaporation rate of the two solvents employed for solvent casting, i.e. THF and DMF and their 7:3 v/v (68.6:31.4 w/w) mixture, was tested monitoring the weight loss of the solutions left to evaporate at RT in a vial. For the two pristine solvents the evaporation followed a perfectly linear behaviour (R^2>0.998): the rate was then extracted from the slope of the linear curve and normalized on the exposed area of the vials (5.93 cm^2). As displayed in *Fig. 5.19e*, THF presented a evaporation rate 30-folds higher than DMF (1.23 10^{-2} % min^{-1} cm^{-2} and 3.2 10^{-4} % min^{-1} cm^{-2} respectively.) These results appeared in good agreement with the boiling point of the liquids, which are 66°C for the fast evaporating THF and 153°C for the slower DMF. As expected, the mixture displayed an intermediate behavior with a fast evaporating region at the beginning of the curve, associated to THF, and a progressive reduction of the rate when DMF content becomes preponderant.To verify if the salt presence imparted any difference to the evaporation behaviour of the solvents, also THF:LiFSI and DMF-LiFSI solutions were tested. No major differences were noticed for THF-LiFSI and the evaporation rate appeared mostly unaffected by salt presence (*Fig. 5.19f*) disproving any major interaction between the two compounds. Instead, considering the reduced weight losses associated to DMF, inconclusive results were obtained for the other solution and more precise analyses will be required to quantify the associate effect of salt presence on

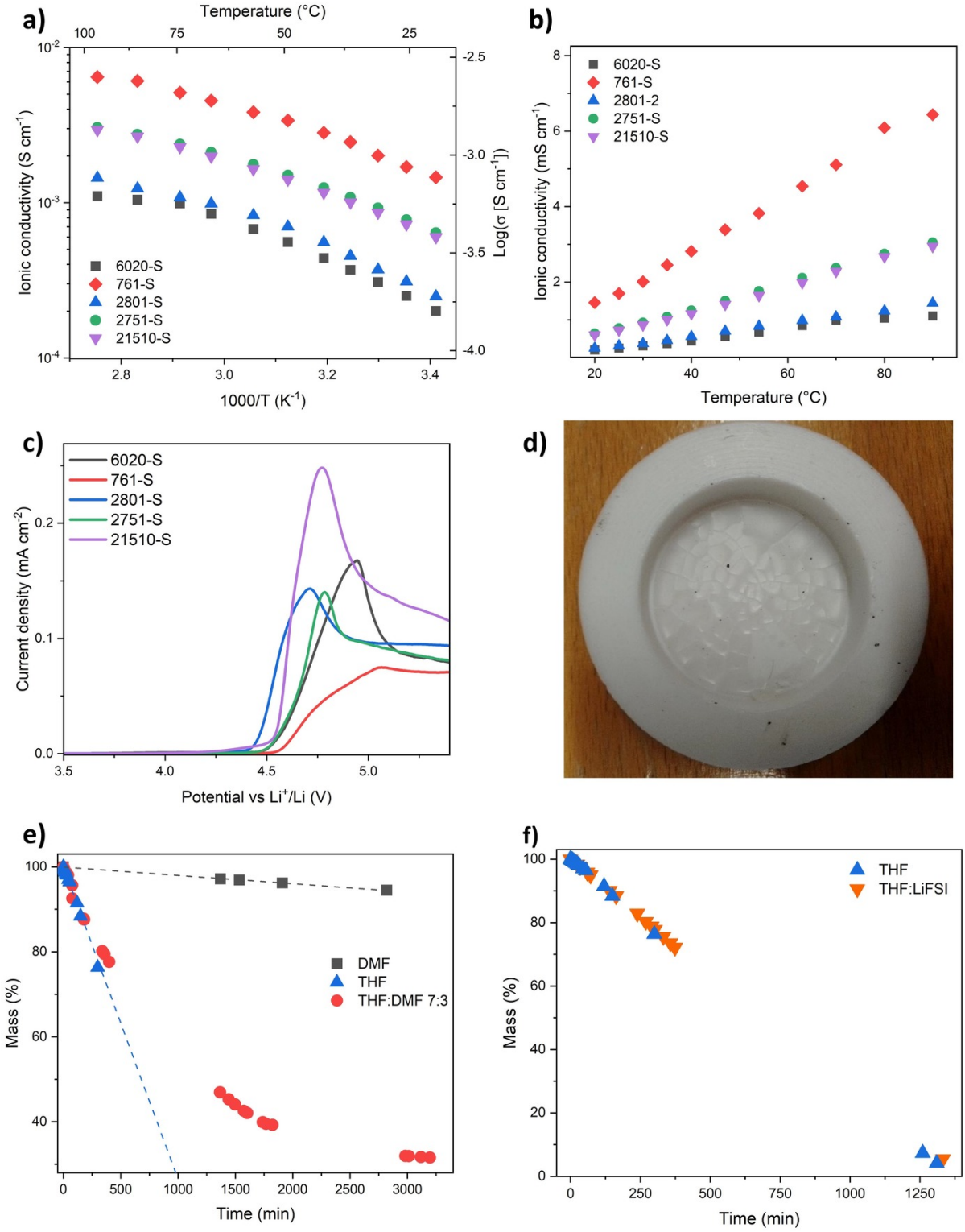

Figure 5.19: a-b) Arrhenius plot (a) and linear plot as a function of temperature (b) of ionic conductivity of different PVdF-based SSEs after 3 days of drying. c) LSV profiles of of different PVdF-based SSEs after 3 days of drying. d) 6020-S electrolyte into a PTFE mould displaying pronounced cracking after drying procedure. e) Comparison of the evaporation weight losses of DMF, THF and THF:DMF 7:3 mixture at RT and in an inter atmosphere. Linear fitting lines are represented as dashed lines. f) Comparison of the evaporation weight losses of THF and THF:LiFSI mixture. For the solution containing the salt, the weight loss is computed taking in account the solvent alone.

this solvent.
Considering our interest in understanding the interaction between DMF with the polymer, two different drying procedures were selected to induce the complete removal of the undesired THF while modifying the amount of residual DMF. Firstly, the electrolytes were left to dry at RT in an Ar-filled glove box for 72, 168 or 336 hours. Additionally, some of the samples have also been treated under vacuum (≈10 mbar) overnight to further induce the DMF evaporation. Instead, no heat treatments were employed to avoid any possible degradation of the LiFSI salt [286].
Taking in account that all the following analyses were performed on a single PVdF-HFP material, i.e. Kynar 2751, this part of the nomenclature will be disregarded from now on. However, the labels will be extended in the way described hereon in order to highlight the different drying procedures and/or the solvent employed for the SSEs production: **Y-BBB CC** where

- **Y** describes if the specimen is a Kynar 2751 powder (**P**), a polymer membrane with no Li salt (**M**), or a SSEs comprising LiFSI (**S**).

- **BBB** is related to the solution employed for the solvent casting of **M** and **S** samples. Apart from **THF**, **DMF**, and **THF:DMF** (i.e. THF:DMF 7:3 v/v), also a 4th mixture labelled as $\mathbf{DMF_{st}}$ has been employed. This solution is composed by THF:DMF 97.4:2.6 v/v and contains the exact stoichiometric amount of DMF molecules necessary for the formation of $Li^{+}{}_{3.29}$:DMF complexes reported in the literature [179] and accounted for the outstanding performances of the electrolyte.

- **CC** describes the drying procedure, depicting the hours of drying (**72h**, **168h**, **336h**) and, when applicable, the number of overnight vacuum treatments (+**V**, +**Vx2**, and so on.)

The first estimation of the residual DMF content was directly performed weighting the SSEs after the different drying procedures and comparing it with the mass of the dry solute (PVdF-HFP and LiFSI). The results are presented in *Tab. 5.11*. It is worth noticing that all the electrolytes produced from DMF containing solutions presented a large excess mass (≈15-25%) even after 72 and 168 hours of drying in inert atmosphere. These values corresponded to [DMF]/[Li^{+}] molar ratios that spanned from 0.90 to 2.58. A great reduction of the excess mass was only experienced after vacuum drying, confirming that harsh conditions are required to effectively remove the DMF to Li^{+}.
Conversely, the solution casted from THF yielded reduced excess mass (≈2%) confirming that no significant THF retention is present in this system.

After this rough estimations based on the consideration previously reported in the scientific literature, it was decided to better verify the nature of the residual DMF in our polymer matrix.
IR spectroscopy was preliminarily selected as a practical way to confirm the effective presence of DMF (or THF) in our electrolytes and the results, zoomed in the region of the peaks of interest and compared with the profile of the pristine Kynar 2751 powder as a reference, are shown in *Fig. 5.20a*. Firstly, no THF was detected in any of the investigate samples due to its higher volatility and its incapability of interacting with Li^{+}. The spectrum of M-THF:DMF 72h (i.e. PVdF-HFP membrane with no lithium salt casted from THF:DMF 7:3 and dried for 72 hours) did not present any evident peak

Table 5.11: Mass of the different membranes after drying procedures.

Sample	Solute mass (g)	SSE mass (g)	Excess (%)	[DMF][Li^+]
S-THF:DMF 72h	0.333±0.002	0.452±0.010	26.4±2.2	2.29±0.09
S-DMF 72h	0.333±0.002	0.467±0.007	28.7±1.6	2.58±0.06
S-DMF_{st} 72h	0.333±0.002	0.435±0.011	23.5±2.4	1.96±0.12
S-THF 72h	0.333±0.002	0.343±0.002	2.9±0.4	—
S-THF:DMF 168h	0.333±0.002	0.383±0.007	15.0±1.6	0.96±0.06
S-DMF 168h	0.333±0.002	0.392±0.005	17.7±1.2	1.13±0.04
S-DMF_{st} 168h	0.333±0.002	0.380±0.008	14.1±1.8	0.90±0.08
S-THF 168h	0.333±0.002	0.341±0.002	2.4±0.4	—
S-THF:DMF 72h+V	0.333±0.002	0.350±0.003	5.1±0.8	0.33±0.04
S-DMF 72h+V	0.333±0.002	0.351±0.002	5.4±0.6	0.35±0.03
S-DMF_{st} 72h+V	0.333±0.002	0.349±0.003	4.8±0.8	0.31±0.04
S-THF 72h+V	0.333±0.002	0.339±0.002	1.8±0.6	—

in the range 680-650 cm^{-1}, proving that no relevant DMF amount was retained inside the polymer in absence of LiFSI. On the other hand, E-THF:DMF 72h i.e. PVdF-HFP membrane with LiFSI casted from THF:DMF 7:3 and dried for 72 hours) displayed two overlapping peaks: bound DMF at 685-670 cm^{-1}, when the solvent is complexed by the lithium salt, and *free* DMF at 665-655 cm^{-1} [179]. The effect of different drying protocols are presented in *Fig. 5.20b*. It is worth noticing that vacuum treatment induced a bigger fraction of *free* DMF than bound, probably related to a modification of the morphology that will be discussed later in the section about SEM.
Similar consideration were deduced by ^{13}C MAS NMR measurements that confirmed both the absence of residual THF and the presence of DMF in LiFSI-containing samples (*Fig. 5.20c*).
Fig. 5.20d presents instead the morphological characterization of three SSEs that underwent different drying protocols: S-THF:DMF 72h, S-THF:DMF 168h and S-THF:DMF 72h+V. S-THF:DMF 72h and S-THF:DMF 168h possess a similar structure with compact and dense layers in the order of the micron scale visible at 1000x magnification (*Fig. 5.20d, top line*). However, the more prolonged drying experienced by S-THF:DMF 168h induced a less uniform and more rough surface, as visible comparing the images acquired at 5000x (*Fig. 5.20d, bottom line).* Conversely, the morphology of S-THF:DMF 72h+V appears totally different, presenting a defined porous structure ($\approx$ few μm) caused by the forced removal of DMF under vacuum.
A more quantitative evaluation of the residual content of solvent into the polymeric membrane was instead carried out with the aid of TGA. As visible in *Fig. 5.20e*, both PVdF-HFP and M-THF:DMF 72h displayed no weight losses in the whole temperature range, confirming once more the high thermal stability of the polymer (thermal decomposition$\approx$375°C [291]) and the zero retention of both solvents in absence of LiFSI. Two distinct significant mass losses were instead noticed for salt-containing samples such as S-THF:DMF 72h and S-THF:DMF 168h which experienced a weight reduction of 14% and 22%, respectively. This two distinct phenomena, roughly below 100°C and 150°C, were previously attributed in the literature to THF and DMF [178]. However, even in

the case of a single solvent (S-THF 72h and S-DMF 72h, *Fig. 5.20f*) a similar two-steps loss was detected therefore disproving the former assumption. Taking also in account the high hygroscopicity of LiFSI and its possible degradation at T>150°C [286], we later addressed the two peaks visible in S-THF 72h to H_2O and LiFSI, respectively. In the presence of DMF, its evaporation appeared superimposed to the salt degradation, therefore hindering any precise estimation from the thermogravimetric profiles.
Nonetheless, to further investigate the relation between thermal properties, the employed solvents, and the drying protocols we carried out additional thermogravimetric measurements whose profiles are displayed in *Fig. 5.20g-h*. Firstly, we tested the effect of different drying procedures (*Fig. 5.20g*). It may be easily noticed the great difference between the vacuum-dried and non vacuum-dried samples. Both S-THF:DMF 72h+V and S-THF:DMF 168h+V presented a monotonous slope after 150°C never encountered in other specimens. The thermal behavior of vacuum dried samples was therefore attributed to the different morphology described in the previous paragraph about SEM: the open porous structure, together with a forced removal upon vacuum treatment of the bound DMF otherwise complexed to salt ions, facilitates the degradation of LiFSI above that temperature. Further information were obtained by TGA isotherm at 150°C. Once more, the major weight loss (25%) experienced by S-THF 72h (which, we recall, do not contain any significant amount of THF as demonstrated by NMR) must be attributed to the degradation of the *free* salt, not bound to any molecule of DMF, while values determined for the electrolytes casted from DMF containing solutions (THF:DMF, DMF and DMF_{st}) are a superimposition of DMF evaporation and of a milder LiFSI decomposition.

Considering the unsuitability of TGA for the determination of the precise amount of residual solvent, it was decided to employ Raman spectroscopy as a way to better characterise the Li^+ environment and its ratio with bound DMF molecules. To carefully evaluate these quantities, we firstly calibrated our system preparing five solutions with different DMF/LiFSI molar ratio i.e. 2.1, 3.1, 10:1, 20:1 and pure DMF. The resulting spectra are displayed in *Fig. 5.21a*, together with the profile of S-THF:DMF 72h, while the calibration line computed taking in account the ratio between the areas of FSI (720-740 cm^{-1}, S-N-S symmetric stretching [292]) and DMF (865 cm^{-1}, C-N-C symmetric stretching [293]) characteristic peaks is presented in Fig. *Fig. 5.21b*. Calculating the I_{DMF}/I_{FSI} value for S-THF:DMF 72h, a ratio [DMF]/[LiFSI] of 2.1±0.2 was obtained.
After having determined the concentration of residual DMF into our main SSE, also the solvating effect imparted by DMF on Li salt was investigated. The free DMF peak, located at 600 cm^{-1} progressively shifted at higher wavenumber upon increase of solute concentration due to the high sensitivity of O=C-N vibration mode to solvation [294]. This effect is due to the appearance of a new spectral component related to the *bound* DMF fraction. Considering the complexity of a precise fitting, complicated by several possible solvating geometries, it was decided to evaluate the evolution of DMF/LiFSI solvation as a function of the barycentre of that peak (*Fig. 5.21c*). The data collected for S-THF:DMF 72h, with a barycentre∼670 cm^{-1}, corresponded to [DMF]/[LiFSI] ratio ∼3, compatible with the previous estimation.
An analogue approach was employed to investigate the coordination of the anion FSI^-. Its population can be divided in three different contributes, easily distinguishable studying the S-N-S stretching mode previously mentioned. Free FSI^- anions resonate at 719 cm^{-1}, contact-ion pairs (CIP, one anion interacting with one Li^+ cation) present a signal at 731 cm^{-1} while aggregate configurations (AGG, one anion interacting with more Li^+ cations)

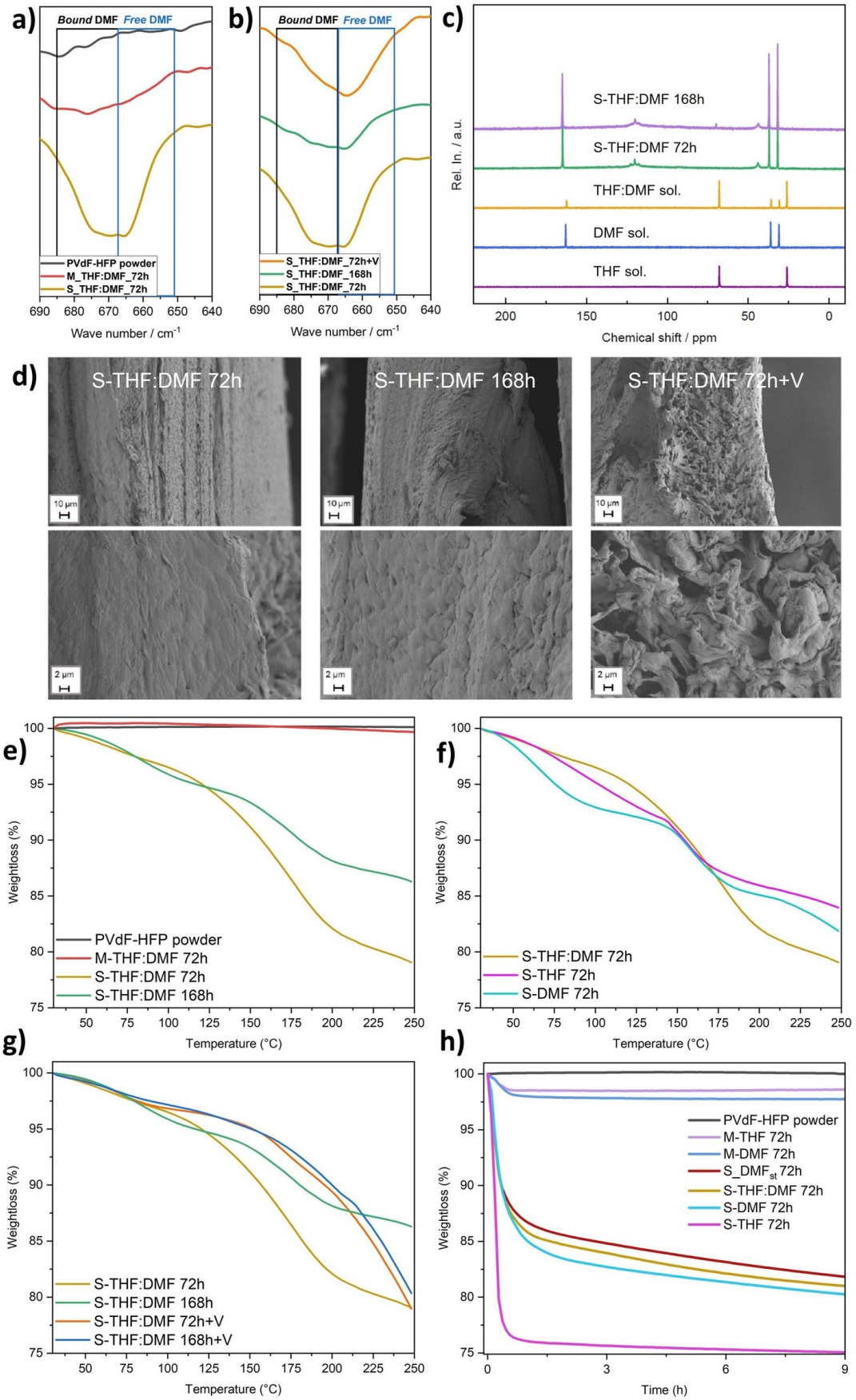

Figure 5.20: a-b) ATR-FTIR spectra of different PVdF systems enlarged in the zone of interest. c) $1^{13}C$-^{1}H CPMAS NMR spectra of employed solvents and selected electrolytes. d) Cross-section SEM images of three SSEs at dried with different protocols. e-h) TGA profiles of selected SSEs in the T range 30-250 °C (e-g) and with an isotherm at 150°C for 9h (h).

are detected at 739 cm^{-1} [295]. Considering that their areas result directly proportional to the respective populations, a precise deconvolution of the peak located around 730 cm^{-1} may provide an accurate quantification of these three distinct geometries [102]. As shown in *Fig. 5.21d-e*, the variation of the concentration of LiFSI greatly modified the proportion between these three populations. When working at low concentration of salt ([DMF]/[LiFSI]>3), FSI^- was mostly present as free while more concentrated solutions resulted in a complete bound population of the anion, either as CIP or AGG. Interestingly, the same analysis performed on S-THF:DMF 72h, that we recall to possess a [DMF]/[LiFSI]∼2.1, yielded a 67% amount of CIP, slightly higher than the values reported for the liquid solution with the highest concentration [DMF]/[LiFSI]=2, and 33% of AGG. These discrepancies can be attributed to the presence of the polymer matrix that, possessing an higher percentage of Li^+ strictly interacting with FSI^- anions, somehow reduces the amount of Li^+ cations able to sustain charge migration.

A possible explanation to the aforementioned effect on the Raman results may be provided by DFT calculations performed on this electrolytic system by the group of Prof. Livia Giordano of University of Milano-Bicocca. It was firstly decided to simulate a Li^+ ion surrounded by a variable number of PVdF oligomers and DMF molecules. The binding energy of the resulting $Li(DMF)_n(PVDF)_m{}^+$ complexes are presented in *Fig. 5.21f*. Disregarding the negligible interaction of PVdF with DMF, it was possible to notice how the Li^+ cation appeared way more stable when complexed with DMF rather than with PVdF. This difference, initially equal to 0.3 eV, was also maintained for a ligand number n≥4. However, when increasing this ligand number to 5, the two complexes $Li(DMF)_3(PVDF)_2{}^+$ and $Li(DMF)_4(PVDF)^+$ became more stable than $Li(DMF)_5{}^+$. These results pointed out to the fact that Li^+-DMF interaction is significantly more intense than Li^+-PVDF one even if the polymer plays a role in the stabilization of complexes with an higher amount of ligands.
Including also FSI^- anion in the analysis, $Li(FSI^-)_p(DMF)_n(PVDF)_m{}^+$ complexes were later investigated (*Fig. 5.21g*). It is worth noticing that $Li(FSI^-)(DMF)^+$ complex resulted 0.25 eV more stable than the two-ligand complex without the presence of the anion. However, increasing the number of ligands, the interaction of the anion with DMF became competitive and the energy difference between $Li(FSI^-)_p(DMF)_n(PVDF)_m{}^+$ with or without the anion was lower than 0.1 eV when dealing with four ligands (p=0-2, n=1-3, m=0-1). This hinted to the fact that DMF presence helps to reduce the coordination of Li^+ with FSI^-, increase the effective number of charge carrier. Conversely, in absence of residual solvent, the negligible interaction of PVdF with the cation did not suffice to break the intimate pair with its anion.
Also theoretical simulations of Raman spectra were performed (*Fig. 5.21h*). No evident difference can be noticed when comparing the spectra of PVdF and Li^+(PVdF) in the top panel, confirming once more the reduced interaction among them. On the opposite, the simulated vibrational spectra of free and bound DMF (bottom panel) presented all the features previously described in the experimental Raman section, such as the increase of the C-N-C stretching at 871 cm^{-1} and a progressive separation of DMF characteristic peak at 660 cm^{-1} into the bound feature at 691 cm^{-1} typical of Li^+(DMF) (*Fig. 5.21i-j*). As shown in (*Fig. 5.21k-l*), considerable modifications were also visible in the region of CH_3 deformation (1000-1200 cm^{-1}) and in correspondence of C=O stretching (1700-1760 cm^{-1}) which experienced a redshift of approximately 40 cm^{-1}. The middle panel displays instead the effect imparted by the presence of residual DMF on anion's features. As expected, $Li^+(FSI^-)DMF$ and $Li^+(FSI^-)DMF_2$ spectra present all the feature of LiFSI and

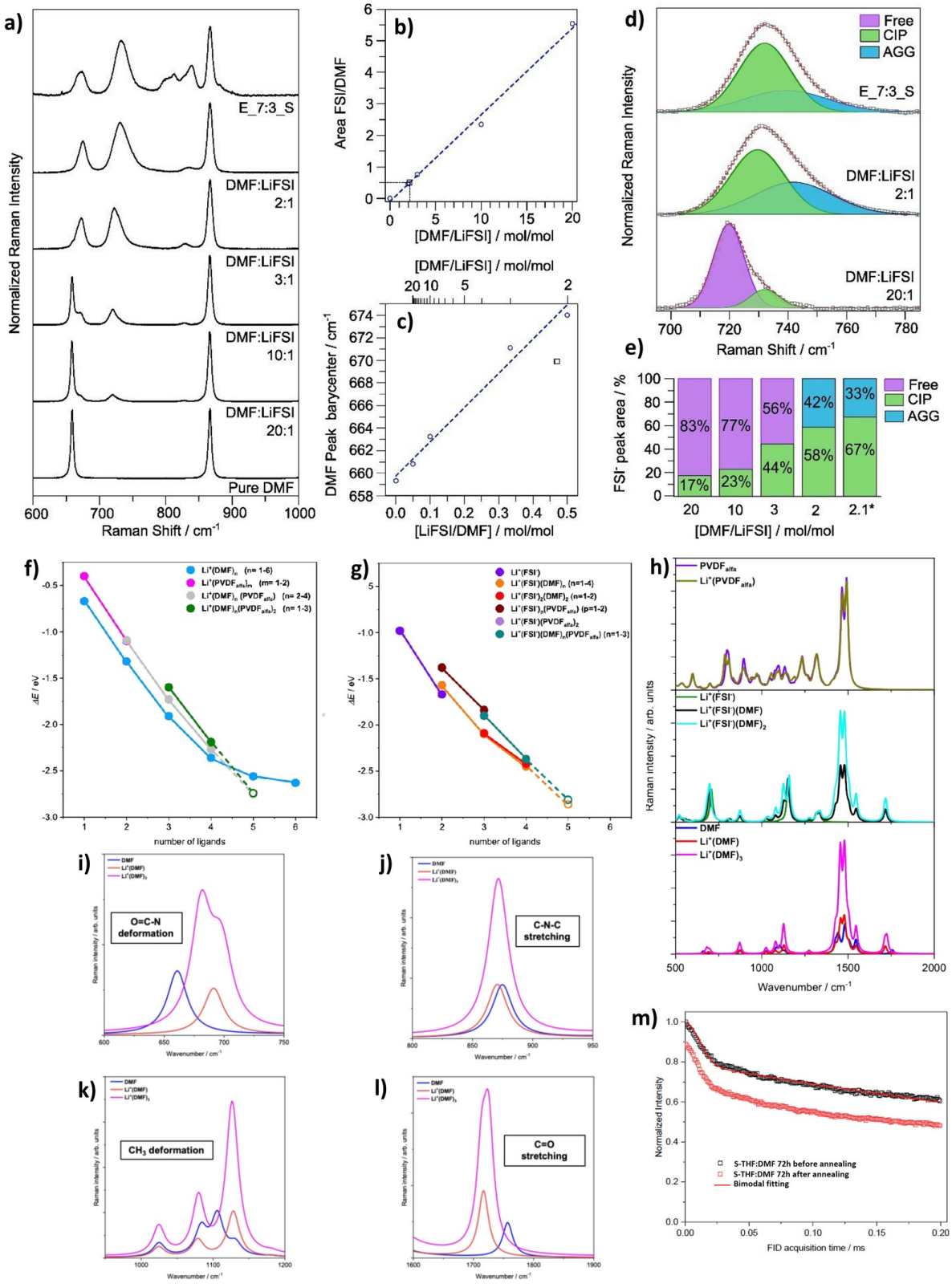

Figure 5.21: a) Raman spectra of S-THF:DMF 72h and of DMF:LiFSI solutions. b) Calibration curve obtained from reference DMF:LiFSI solutions. c) Barycentre of DMF peak as a function of Li^+/DMF ratio. d) Deconvolution of main FSI^- peak in the three contributes attributed to free, bound and aggregate anion. e) Percentage of the FSI^- population achieved from the deconvolution shown in f-l) Binding energy vs. number of ligands for (f) $Li(DMF)_n(PVDF)_m^+$ and (g) $Li(FSI^-)_p(DMF)_n(PVDF)_m^+$ with (h) the relative simulated Raman spectra and (i-l) the magnification on the zone of interest. m) TD-NMR FID recorded at 60°C for S-THF:DMF 72h before and after annealing at 80°C. Readapted from [279].

Li^+DMF. Overall, these results confirmed the experimental observations and proved that DMF interaction is possible and relevant even in the presence of the FSI^-. Consequently, competitive solvation of Li^+ with residual solvent and/or counterion will strongly depend also on the amount of DMF present into the polymer matrix.
Additional insights on the effect of DMF into the PVdF-HFP matrix have been provided by ^1H TD-NMR analysis performed on S-THF:DMF 72h before and after an overnight annealing at 80°C. This technique was selected for its ability of investigating the rigid fractions of polymers and because the seven hydrogen atoms present in DMF render this molecule easily measurable. As shown in *Fig. 5.21m*, an 11% intensity loss was experienced between the two measurements. Considering that the signal is proportional to the number of ^1H nuclei in the specimen, such variation can only attributed to a reduction in the order of 4% of the amount of residual DMF. However, this small DMF removal led to a modification of the rigid fraction quantified through a bimodal fitting that passed from 12% to 17.5%. These results further confirmed the major plasticizing effect imparted by the residual solvent which increases the mobility of the matrix.
Eventually, ionic conductivity of several SSEs was then measured to correlate the physico-chemical characterization of the system with its electrochemical features. *Fig. 5.22a* presents the values obtained for the same electrolyte S-THF-DMF submitted to different drying methods. As expected, more prolonged evaporation times led to less conductive electrolytes due to the progressive DMF removal previously explained. Additionally, vacuum treatment strongly affected the ionic conductivity, particularly at RT where σ_{Li^+} passed from $\sim 3 \cdot 10^{-4}$ S cm^{-1} to $\sim 10^{-5}$ S cm^{-1}. Also the activation energy E_a, extrapolated by the linear fitting of Arrhenius equation (*Eq. 4.4* and *Eq. 4.5*), resulted strongly influenced. As shown in *Tab. 5.12*, E_a values are more than doubled (from 0.25 eV to 0.57 eV) after two vacuum treatments, due to massive removal of the DMF solvent which enabled Li^+ conduction and probably due to the different morphology of these samples.
A more complete understanding can be achieved considering *Fig. 5.22b* which depicts the ionic conductivity of SSEs that underwent the same drying treatment after having been casted from different solutions. First of all, it was possible to notice that S-THF 72h appeared ionically insulating, presenting a room temperature resistivity of $6.7 \cdot 10^6$ Ω cm which is two-three orders of magnitudes larger than the counterparts produced from a DMF-based solution coupled to an activation energy close to 1 eV. For comparison, less noticeable differences were instead observable between S-DMF, S-THF:DMF, and S-DMF_{st}. Therefore, even the presence of a small amount of DMF resulted critical for the conductive properties of this system. The higher values of σ_{Li^+} associated to S-DMF and S-THF:DMF appeared related to the presence of excess DMF whose effect was partially reduced increasing the drying time to 168 hours (*Fig. 5.22c*). After this prolonged treatment, ionic conductivity of both systems was depressed and such reduction was accompanied by an increase of the associated energy barrier E_a (*Tab. 5.12*). On the other hand, both these values remained most unaffected in S-DMF_{st}, confirming the presence of a *permanent* residual DMF content necessary for lithium conduction that cannot be removed by RT evaporation. The same considerations are also presented in *Fig. 5.22e-f*, where a different representation facilitates the comparison of the two systems after 72 and 168 hours. In these plots, it is possible to appreciate better how upon drying the conductivity of S-DMF and S-THF:DMF is progressively approaching the values measured for S-DMF_{st}.
Exploiting the Site Percolation Theory and *Eq. 4.11*, it was possible to determine the value of the percolation threshold $x_{tr} \approx 0$ and of the critical exponent $\alpha = 1.26$ (with coef-

Table 5.12: Ionic conductivity σ_{Li^+} at 25°C and 80°C, and Arrhenius fitting parameters E_a and σ_0 of different SSEs based on PVdF-HFP Kynar 2751.

SSE sample	$\sigma_{25°C}$ **(S cm^{-1})**	$\sigma_{80°C}$ **(S cm^{-1})**	E_a **(eV)**	σ_0 **(S cm^{-1})**
S-THF:DMF 72h	4.3 10^{-4}	2.0 10^{-3}	0.25	8.9
S-THF:DMF 168h	2.6 10^{-4}	1.4 10^{-3}	0.28	12.5
S-THF:DMF 72h+V	8.6 10^{-5}	9.6 10^{-4}	0.39	316
S-THF:DMF 72h+Vx2	2.6 10^{-5}	7.8 10^{-4}	0.57	$7.9 \cdot 10^4$
S-THF 72h	1.5 10^{-7}	4.7 10^{-5}	0.96	$3.1 \cdot 10^9$
S-DMF 72h	5.6 10^{-4}	2.5 10^{-3}	0.25	9.8
S-DMF 168h	3.6 10^{-4}	1.8 10^{-3}	0.27	11.5
S-DMF$_{st}$ 72h	2.0 10^{-4}	1.2 10^{-3}	0.29	24.5
S-DMF$_{st}$ 168h	1.9 10^{-4}	1.1 10^{-3}	0.29	12.8

ficient of determination $R^2 > 0.99$). A α value close to the unity hints to a 1D transport mechanism which suggests an uniform distribution of the DMF along the strands of the PVdF-HFP matrix. The resulting power-law behavior is displayed in *Fig. 5.22d* where the RT ionic conductivity is plotted vs. the DMF content of different SSEs. Additionally, the percolation threshold very close to zero suggests that very small DMF amounts are able to greatly improve the transport mechanism of Li ions in this SSE imparting great enhancement of the conductivity when passing from S-THF to S-DMF$_{st}$ as predicted by Eq. 4.1 thanks to an increase of the number of charge carriers n.
Finally, also the use of an alternative salt has been tested. Unfortunately, as already reported for similar electrolytes [177] and as shown in *Fig. 5.22f* for an exemplificative SSE, the replacement of LiFSI with LiTFSI induced a sharp decrease of the conductivity confirming once more the key role played by the anion in this system. Further investigation will be later required to better clarify this peculiar aspect.
In conclusion, this project has investigated the effect of residual DMF solvents on the phisico-chemical and electrochemical properties of solvent casted PVdF-HFP based SSEs containing LiFSI as conductive salt. Even if the macroscopic appearance of these systems resembles the one of dry solid systems, all the analyses pointed out that a significant amount of DMF, entrapped into the polymer matrix due to its strong and unavoidable interaction with Li cations, resulted critical for the ion transport mechanism. A careful tuning of DMF content can therefore lead to an optimization of both the mechanical and the conductive properties of these systems that could be better named as quasi-solid electrolytes (QSEs) due to the impossibility of a complete removal of residual solvent.

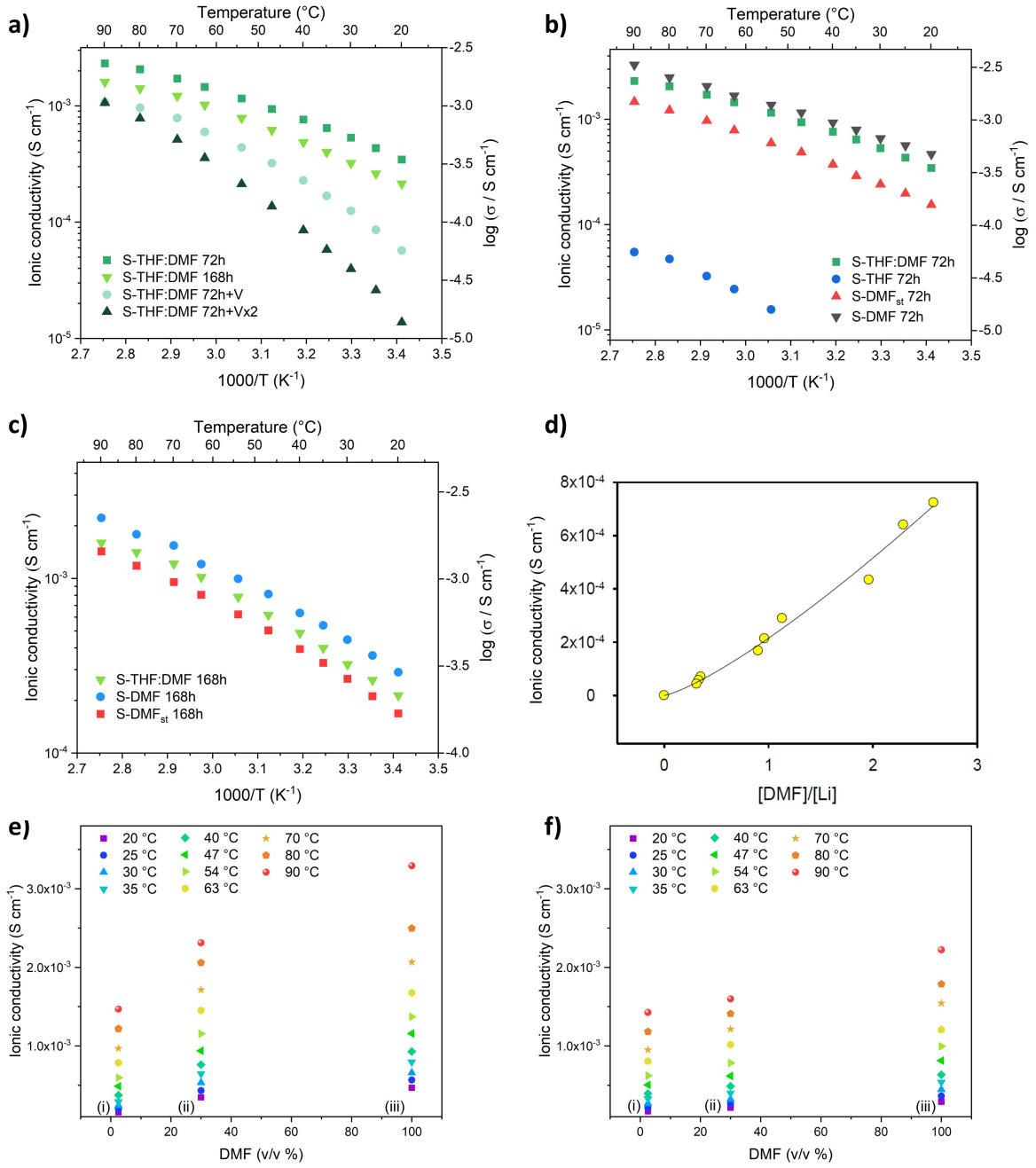

Figure 5.22: a) Arrhenius plot of SSEs produced from a THF:DMF 7:3 v/v solution and dried with different procedures. b) Arrhenius plot of SSEs produced from different solution and dried for 72 hours at room temperature. c) Arrhenius plot of SSEs produced from different solution and dried for 168 hours at room temperature. d) Relation of the RT ionic conductivity of SSEs containing different amount of DMF. e-f) Ionic conductivity at different temperatures as a function of DMF content in the solvent casting solutions [(i) S-DMF$_{st}$, (ii) S-THF:DMF, (iii) S-DMF] after (e) 72 hours and (f) 168 hours of drying at RT. Readapted from [279].

SiO_2-based nanocomposite QSEs:

After having thoroughly characterized the effect of residual DMF on the properties of the electrolyte, it was decided to test filler addition as a suitable way to improve the performances of our QSEs.
Both hybrid fillers, i. e. SiO_2@PEG and SiO_2@PFOTES, have been successfully implemented into PVdF-HFP matrices with the composition listed in *Tab. 5.9* and *Tab. 5.10*. However, due to the poor preliminary results currently achieved with the use SiO_2@PFOTES that are still under investigation, the following discussion will be focused on SiO_2@PEG based SSEs.

Filler characterization: Pristine SiO_2 NPs and surface functionalized SiO_2@APTES, SiO_2@PEG5K and SiO_2@PEG750 NPs were produced following the synthetic procedure explained in the experimental section. Similarly to what already described for *Sec. 5.1*, the positive outcome of SiO_2 synthesis and of the subsequent functionalization steps was validated by several characterization analyses.
All the ATR-FTIR spectra *(Fig. 5.23a)* displayed the classic fingerprint of silica with its several features in the region around 1000 cm^{-1} such as Si-O-H and Si-O-Si stretching (949 cm^{-1} and 1053 cm^{-1}, respectively). However, both SiO_2@APTES and SiO_2@PEG showed two additional peaks at 2983 and 2834 cm^{-1} ascribable to C-H stretching of APTES propyl groups and PEG alkyl chains. Additionally, a low-intensity feature at 1560 cm^{-1} was detectable for SiO_2@PEG, possibly attributable to the N-H bending of the amide formed during the final functionalization step (*Fig. 5.23b*).
XRD diffractogram, with its broad peak located at $2\Theta \sim 23°$, also confirmed the expected amorphous morphology of our pristine NPs (*(Fig. 5.23c)*). This amorphicity was maintained upon APTES and PEG grafting, proving that the functionalization steps did not alter the core of silica.
A quantification of the APTES and PEG content was performed with TGA. While the weight loss for SiO_2 is due to OH decomposition ($n_{OH} \sim 6.0$ mmol g^{-1}), the other phenomena were related to the degradation of APTES and PEG chains grafted on the surface. Employing *Eq. 5.1*, *Eq. 5.2*, and *Eq. 5.3* it resulted possible to precisely quantify the organic amount successfully attached to SiO_2. The values are reported in *Tab. 5.13* and, as already noticed in *Sec. 5.1*, shorter PEG substituent led to an higher ratio of PEG/APTES chains thanks to the reduced steric hindrance of PEG750. However, both PEG and APTES values resulted lower if compared to the analogue quantities reported in *Sec. 5.1*: these discrepancies are justified taking in account the higher porosity of those fillers which, in turn, led to a reduced NP mass and, therefore, to an higher w/w ratio between the organic grafted components and the silica. Moreover, the higher SSA also caused a larger number of feasible grafting sites that induced the possibility of APTES grafting not only on the external surface but also into the pores of NPs.

These results were later confirmed by ^{29}Si MAS NMR that demonstrated a content of Q3 and Q4 of 35% and 65%, respectively (*Fig. 5.23d*), compatible with a APTES functionalization in the order of 2% wt% with a consequent reduction of the n_{OH} content. It is worth remembering that the notation Q_n is referred to $[Si(OSi)_n(OH)_{n-x}]$ with $n \geq 0$, $x \leq 4$. Therefore, Q4 peaks are ascribable to bulk Si atoms while Q3 ones corresponds to Si-OH surface groups.
Dimensional analysis was then performed employing TEM and DLS. As displayed in

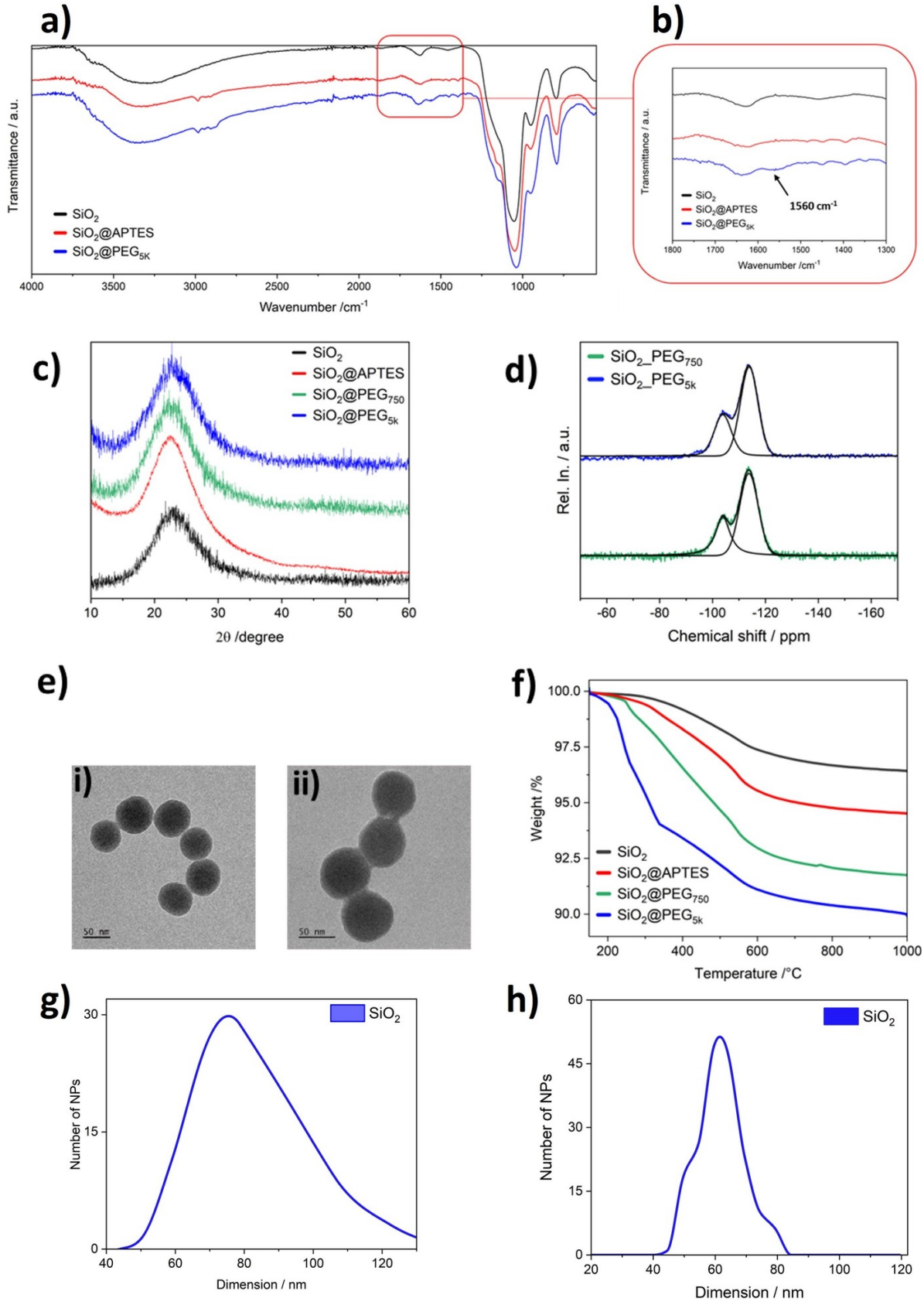

Figure 5.23: a) ATR-FTIR of SiO_2, SiO_2@APTES, and SiO_2@PEG with b) magnification on the range 1800-1300 cm^{-1}. c) XRD of different SiO_2 fillers. d) ^{29}Si NMR spectra of the two hybrid fillers. e) TEM images of (i) pristine SiO_2 and (ii) SiO_2@PEG5K. f) TGA of different SiO_2 fillers. g-h) Particle size distribution of pristine SiO_2 determined by g) DLS and h) TEM. Readapted from [280].

Table 5.13: TGA results and respective estimation of APTES and PEGx contents grafted on silica surface. Reaction yield and ratio between the number of APTES molecules and PEG chains are also presented.

Sample	$\Delta W_{150\text{-}1000°C}$	APTES wt%	PEGx wt%	Yield	APTES/PEG
SiO_2	2.79	—	—	—	—
SiO_2@APTES	5.48	2.3	—	15	—
SiO_2@PEG750	8.25	2.2	3.2	11	9
SiO_2@PEG5K	8.83	2.2	4.4	2	40

Fig. 5.23e, the procedure led to the formation of spherical NPs with an average size of 60±7 nm (*Fig. 5.23h*). After the functionalization with PEG, the edges of NPs appeared more smoothed and the appearance of an *halo* around the particles hinted to an effective formation of PEG layer on the silica surface. DLS measurements were in accordance with what observed with TEM: this analysis provided a mean diameter of 75±16 nm. The small discrepancy between the two result can be explained taking in account that DLS measures the hydrodynamic radius, therefore also considering the solvated water molecules in the final value. Concurrent ζ-potential measurements also confirmed the effective grafting of APTES and PEG. The negative potential (-25±5 mV) measured for pristine SiO_2 NPs and compatible to the presence of hydroxide group and the surface progressively grew for SiO_2@APTES (0±4 mV) and SiO_2@PEG (21±4 and 9±2 for PEG750 and PEG5K, respectively) due to the functionalization that reduced the negative charge observed for pure silica.
Another figure of merit that can be used to evaluate the effectiveness of PEG grafting was provided by the study of the spacial occupation of PEG chains around the NPs. As already described in *Sec. 5.2*, it resulted easily possible to evaluate the grafting morphology of a system exploiting *Eq. 5.4*, *Eq. 5.5*, and *Eq. 5.6*. Thus, after having determined the Flory's radius R_F as

$$R_F = \alpha \cdot N^{0.6} \tag{5.9}$$

where α is the length of PEG monomer (0.358 nm) and N is the number of monomeric units per grafted chains, it was possible to calculate the ratio between R_F and D (*Eq. 5.6*) that both for PEG750 and PEG5K resulted comprised in the range $1<x<2$ (1.3 and 1.8, respectively). Consequently, both fillers displayed a brush regime with a dense and satisfying polymer coverage.

QSEs characterization: After having produced with a solvent casting approach the several electrolytes presenting the composition illustrated in *Tab. 5.9*, the self-standing membranes were characterised with a plethora of experimental techniques. Filler based on PEG750 were selected as the representative system due to their improved number of grafted chains.
First of all, ^{13}C-MAS NMR was employed to investigate any possible interaction between fillers, polymer and the residual solvent that we recall being in the order of 20% w/w. As displayed in *Fig. 5.24a*, no major differences seemed to be detectable when comparing the polymeric electrolyte (i.e. S-THF:DMF 72h of the previous section) and PEG750_5 (i.e. S-THF:DMF 72h containing a 5% of SiO_2@PEG750 fillers) since the

two curves appeared almost superimposable. However, even if this results completely true for the polymer peaks, DMF signals were altered by filler addition into PVdF-HFP. As highlighted in the insets of the same figure, in the presence of SiO_2@PEG750 two distinct contributions were observed for each solvent peak that can be in first approximation attributed to two different DMF populations, one of which partially interacting with NPs. Additionally, quantitative estimation of DMF amount was also performed on the basis of NMR spectra. Polymer-solvent ratio was estimated as 77:23 w/w for the polymeric system and 74:26 for PEG750_5. Considering the identical drying protocol, fillers seemed somehow able to induce a major retention of DMF into the otherwise insulating PVdF-HFP scaffold.
As already done in the previous section, also TGA analyses were carried out to obtain a rough estimation of the residual DMF amount with and without the presence of functionalized fillers and to corroborate the hypothesis formulated on the basis of NMR data. Even if the aforementioned LiFSI degradation made impossible a precise quantification with this experimental techniques, a major weight loss in correspondence of DMF boiling point (153°C) was noticed when employing SiO_2@PEG rather than bare SiO_2 or no fillers.
TD-NMR experiments were later performed to gain useful insights on the rigidity and on the mobility of polymer chains in absence or presence of hybrid fillers (Fig. 5.24a). As predictable, the PVdF-HFP membrane containing no salt (labelled as NoLiFSI) displayed an high stiffness showing a very fast Gaussian decay of the intensity. Upon salt addition but in the absence of filler, the resulting QSEs presented instead a much increased softness probably due to the plastifying effect of LiFSI and to the simultaneous retention of DMF. Addition of 5 wt% of bare SiO_2 did not significantly modify the free induction decay (FID) while a more evident difference, indicating a pronounced interaction between the grafted chains and the polymer matrix, was noticeable for PEG750_5. Interestingly, the FID of PEG750_10 resulted almost coincident to the one of PEG750_5 while the addition of 10% of unfunctionalized SiO_2 NPs led to a massive suppression of chain mobility, displayed as a faster decay of the normalized intensity. Therefore, larger amount of hybrid fillers are tolerated inside the polymer matrix while the addition of bare silica acting as a non-interacting inclusion disrupted most of the chain mobility demonstrating a limited capacity of being homogeneously distributed into the PVdF-HFP system.
To better characterise the mechanical properties of the electrolytes, tensile tests were carried out on the same samples previously investigated with TD-NMR. Tensile modulus *TM* and ultimate tensile strength *UTS* of all the tested specimens are reported in *Tab. 5.14*. As expected, the pure PVdF-HFP displayed the larger values of TM and UTS thanks to its higher degree of crystallinity that is instead suppressed by LiFSI addition and DMF retention in the other QSEs. Interestingly, SiO_2 addition, both bare and functionalized, induced a general decrease of the mechanical properties when compared to S-THF:DMF 72h. However, the implementation of hybrid SiO_2@PEG750 fillers led to better performance for both parameters when compared to pristine silica, demonstrating once more the beneficial effect of grafted polymer chains.

To further investigate the effect induced by the addition of SiO_2, Raman spectroscopy was performed on two samples: the purely polymeric electrolyte and PEG750_5. All the results are presented in *Fig. 5.25b-f*. Even if the full spectra were collected in a wider wavenumber range (200-1200 cm^{-1}, *Fig. 5.25c-d*), most of the significant peaks fall in a narrower region, roughly between 650 and 900 cm^{-1}, magnified for greater clarity in

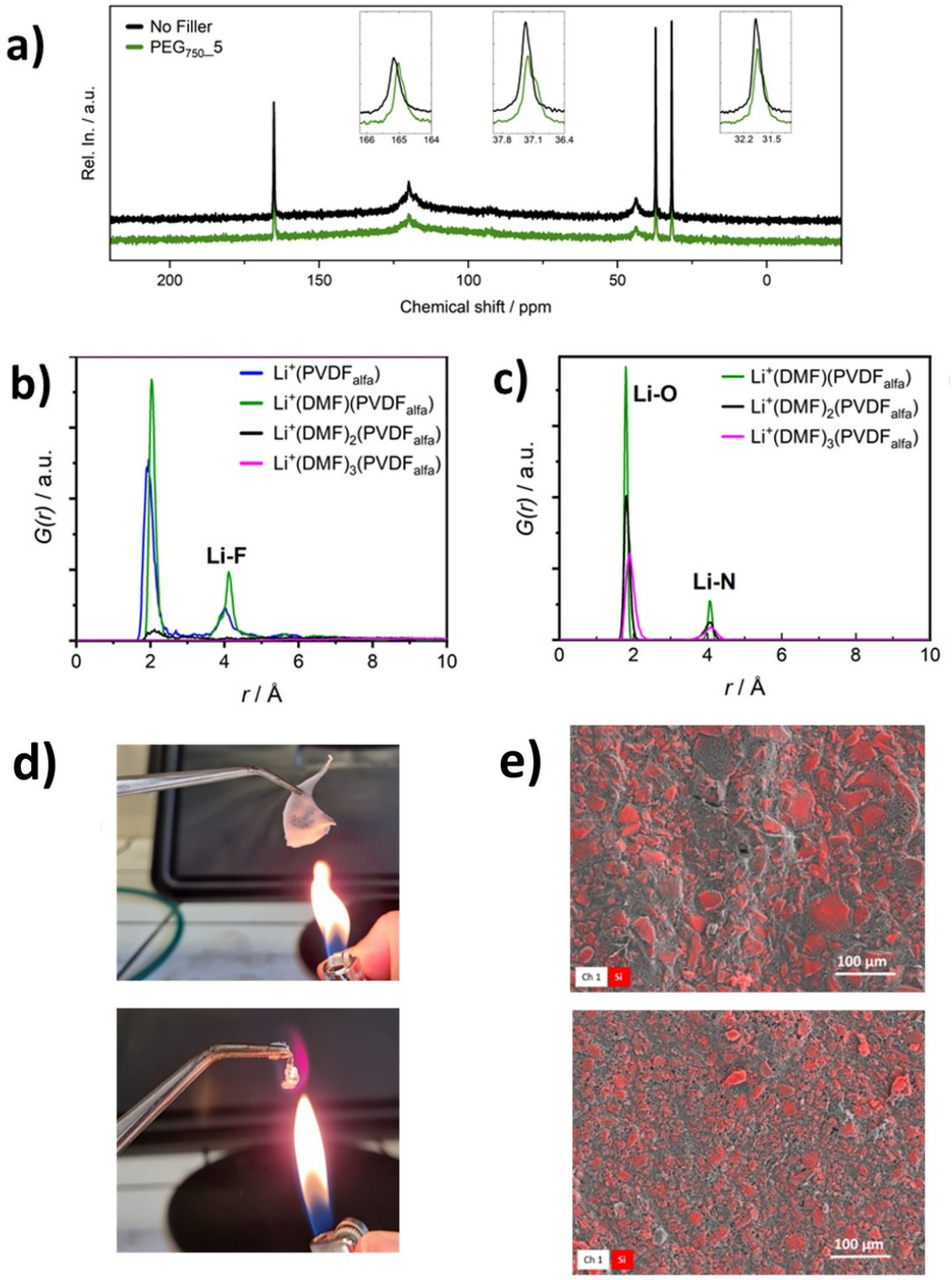

Figure 5.24: a) ^{13}C-MAS NMR of PVdF-HFP QSEs with and without 5 wt.% PEG750 fillers with magnifications on the zones of interest. b-c) PDF plots of $Li(DMF)_n(PVdF)^+$ between (b) Li and F with n=0-3 and (c) Li and O/N with n=1-3. d) Flammability test of PEG750_5 (top) compared with a Celgard 21510 film soaked with LP30 (bottom). e) EDX images acquired for PVdF-HFP QSEs encompassing 5% of bare SiO_2 (top) compared with 5% of bare SiO_2@PEG750 (bottom). Readapted from [280].

Table 5.14: Mechanical properties of selected samples. TM: tensile modulus; UTS: ultimate tensile strength.

Sample	**TM (MPa)**	**UTS (MPa)**
PVdF-HFP	271±30	13.4±0.7
S-THF:DMF 72h	19±4	2.7±0.3
SiO_2_5	12±4	2.3±0.2
SiO_2_10	13±3	2.4±0.6
PEG750_5	14±2	2.6±0.4
PEG750_10	16±2	2.7±0.6

Fig. 5.25b. All those feature are respectively ascribable to DMF (O=C-N bending at 672 cm^{-1} and N-CH_3 at 865 cm^{-1}) [293], LiFSI (S-N-S symmetric stretching at 730 cm^{-1}) [292], and PVdF-HFP (C-F stretching of side chains in the range 780-820 cm^{-1}) [296]. Considering that both spectra have been normalized with respect to the N-CH_3 peaks, the lower intensity detected for LiFSI and PVdF-HFP signals of PEG750_5 hinted, in agreement to NMR and TGA, to the fact that filler containing systems are capable of retaining more solvent. Apart from this difference, no significant modification on DMF and polymer Raman spectra were detectable upon filler addition. For both systems, DMF peaks appeared slightly shifted (13 cm^{-1}) in accordance to the presence of *bound* solvent with a less numerous population of *free* DMF. Instead, significant differences between samples can be appreciated comparing the shape of S-N-S signal. As previously described, this FSI^- peak in the convolution of three distinct mode of the anion in free (719 cm^{-1}), contact-ion pair (CIP, 731 cm^{-1}), and aggregate (AGG, 739 cm^{-1}) geometry. As displayed in *Fig. 5.25e-f*, no free anion geometry was detected either with and without fillers since all the anion solvation appeared as CIP or AGG. From the deconvolution, it resulted possible to quantify the relative percentage of CIP/AGG species that for S-THF:DMF 72h and PEG750_5 resulted equal to 60/40 and 70:30, respectively.
Another major improvement imparted by the use of hybrid fillers was observed with EDX. As visible in *Fig. 5.24e*, the use of bare silica led to the formation of big aggregates and poor homogeneity. Conversely, functionalized SiO_2@PEG750 induced a more homogenous distribution of the fillers and smaller agglomeration.
Additionally, our PVdF-HFP based electrolytes also demonstrated satisfying safety standards when compared to the two solvents supported on a different substrate. *Fig. 5.24d* presents the result of the flammability test exposing the two systems to a free flame for 10 seconds. While the Celgard soaked with THF:DMF was completely burned, the PVdF-HFP resisted in a satisfying way to the test and did not develop any flame thanks to the absence of any free combustible solvent.
Finally, also in this case DFT calculations were employed to better clarify the interaction of Li^+ ions in these systems. In particular, after propagating the trajectory of Li^+ and $Li(DMF)_n^+$ (n=1-3) in the proximity of PVdF polymer chain for 30s at 350K, the resulting Pair Distribution Functions (PDF) were reported. *Fig. 5.24b* displays the calculated PDF for lithium and fluorine atoms to firstly understand the relation between Li^+ cation and polymer strands. In the absence of DMF, Li^+ interacts on average with three F atoms at a distance of 1.93 Å. Upon the addition of one solvent molecule, $Li(PVdF)(DMF)^+$ presents an extension of the average bond length (2.03 Å) but no

modification of the coordination number which remains equal to three. Conversely, the global picture results greatly modified when considering $Li(DMF)_2(PVdF)^+$. In this case, the interaction with the polymer is strongly weakened and the coordination number of Li and F falls to 0.3, with a more elongated length of 2.21 Å. Further addition of DMF with n=3 caused no interaction at all with PVdF since the cation results coordinated only by DMF molecules. The great intensity of the bonding between cation and residual solvent is also confirmed by *Fig. 5.24c* which depicts the evolution of the Li-O and Li-N bonding, i.e. the coordination of the cation with respect to DMF. The coordination number changes almost linearly with n, since growing from 1 (for n=1) to 2.98 (for n=3), while the average bond length remains almost unaffected. Shorter Li-O distances also highlights the preferential binding of the cation with oxygen atoms, rather than with N ones. A more detailed description of the computational part performed by the group of Prof. Livia Giordano can be found in the referenced publication [280].

Electrochemical testing: After having completed our phisico-chemical characterization, we started to test the electrochemical properties of the QSEs.
First of all, we determined the electronic conductivity using the Hebb-Wagner method as explained in *Eq. 5.7* and *Eq. 5.8*. This value was estimated equal to $9\pm1\ 10^{-12}$ S cm^{-1} at RT, demonstrating the predicted negligible contribution of holes and electrons to the total conductivity of this system.
Ionic conductivity was later measured to verify the effects of different fillers and loadings. The results are shown in *Fig. 5.26a-b*. Firstly,*Fig. 5.26a* displays the Arrhenius plots of QSEs possessing 5 wt% of different fillers compared the the purely polymeric analogue. All the samples presented a VTF like behaviour, as expected for GPEs that possess a certain amount of free volume [175]. However, filler addition reduced the available free volume, transforming the profile in more Arrhenius-like. It is possible to notice that fillers' addition, with the only exception of SiO_2@PEG5K, led to an improvement of ionic conductivity. Overall, best results were obtained with the addition of 5 wt% of SiO_2@PEG750 even if its RT σ_{Li^+} was slightly lower than the one achieved with bare SiO_2. *Fig. 5.26b* presents instead the ionic conductivity for growing amounts of SiO_2@PEG750 collected at different temperatures. It is easy to appreciate that higher loadings of filler carried to a reduction of σ_{Li^+} in the whole T range. However, this decrease was not as marked as the one experienced with bare SiO^2: for example, PEG750_15 and PEG5K_15 demonstrated a three timed higher ionic conductivity ($\sim3\cdot10^{-4}$ S cm^{-1}) when compared to SiO_2_15 ($1\cdot10^{-4}$ S cm^{-1}). This confirmed the expected compatibility enhancement imparted by the surficial grafting of ceramic fillers. The better results achieved using SiO_2@PEG750 rather than SiO_2@PEG5K can be attributed to higher grafting density achieved with the shorter PEG chains. Taking in account all of these considerations, it was decided to focus our attention on the QSEs containing 5% wt of ceramic fillers.
Voltammetric measurements were then performed to verify the electrochemical compatibility of our QSEs with commonly employed cathodic and anodic materials. LSV analysis was firstly performed to verify its stability at high potential. As visible in *Fig. 5.26c*, filler addition enlarged the oxidative ESW of the electrolyte which resulted electrochemically stable up to 4.8 V vs Li^+/Li. A strong oxidative peak, related to polymer decomposition, was observed for higher values. CV was then carried out using Cu as working electrode to verify the suitability of the QSEs in contact with a Li anode. The

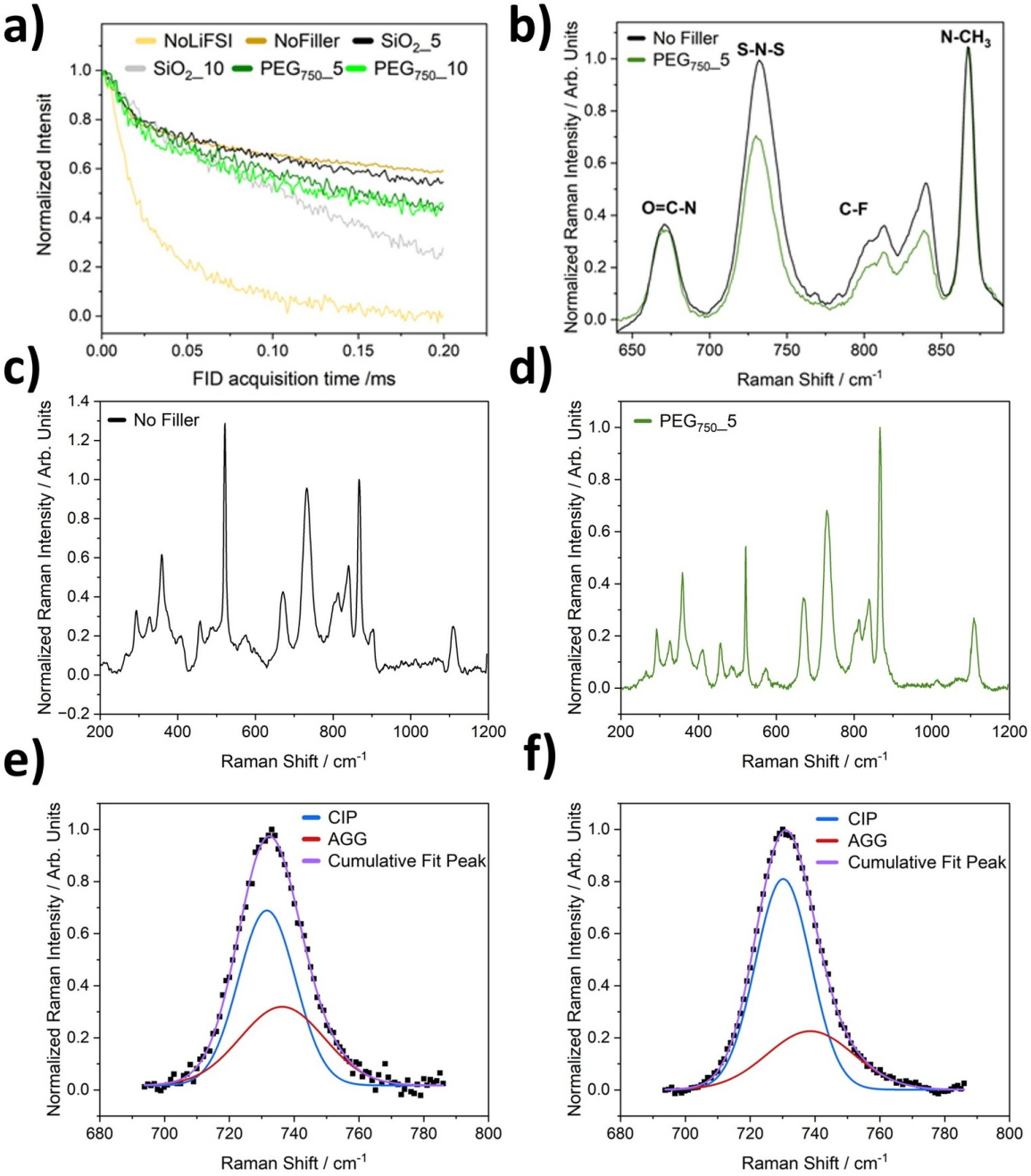

Figure 5.25: a) TD-NMR FIDs of different membranes and QSEs. b-d) Raman spectra of QSEs with and without 5 wt.% PEG750 fillers with magnifications on the zones of interest. e-f) Band fitting of S-N-S symmetric stretching mode for QSEs without (e) and with (f) 5 wt.% PEG750 fillers Readapted from [280].

profile, presented in *Fig. 5.26d*, confirmed the capability of PEG750_5 QSEs to permit reversible stripping and plating on a Li anode.
Therefore, to better evaluate this final aspect, Li|Li symmetric cells were then assembled and tested with the same two protocols described in the previous chapters. *Fig. 5.26e* shows the voltage profile at growing current densities, from 50 to 500 μA cm^{-2}, of three different samples. Both S-THF:DMF 72h with no filler and SiO_2_5 were not able to sustain current densities larger than 200 μA cm^{-2}: as already reported in other works [177], PVdF-based electrolytes commonly experiences large voltage polarization due to the unconstrained build-up of insulating species at the interface. Conversely, PEG750_5 resulted stable even at the highest current value (500 μA cm^{-2}), only experiencing a reduced overpotential. Interestingly, the same cell also sustained more than 150 additional hours of cycling at 100 μA cm^{-2} before the appearance of a detrimental open-circuiting behaviour related to the aforementioned build-up (*Fig. 5.26f*).
Eventually, the most performing QSEs (i.e. PEG750_5) was implemented in a LMB equipped with a LFP cathode. The CR2032 coin cells demonstrated an incredible stability, delivering approximately 100 mAh g^{1} at 0.1C for more than 100 cycles with a CE≈99.2% and a reduced overpotential (*Fig. 5.26g*). Similar results were not obtained with the polymeric analogue: S-THF:DMF 72h resulted incapable of providing stable cycling, with discharge capacity value below 40 mAh ^{g} after the first 10 cycles.
To finally evaluate the possible safety advantages related to the use of this QSEs in place of the flammable and dangerous liquid carbonates, ARC measurements were carried out on two LFP LMBs, one employing our PEG750_5 electrolyte and one commercial LP30. As observable in *Fig. 5.26h*, the carbonate-based battery experienced a thermal runaway around 175°C, noticeable by a continuous temperature increase detected in the cell. Conversely, the nanocomposite system did not present any extent of thermal runaway up to 300°C: external heating was always required to reach that temperature threshold and no spontaneous heating was ever revealed.

In conclusion, PEG grafting on SiO_2 NPs resulted a valid approach to improve the performances of PVdF-HFP based QSEs. Firstly, more homogenous dispersion were achieved when employing these hybrid fillers rather than bare silica nanoparticles. Additionally, higher ionic conductivity (∼10^{-3} S cm^{-1} at RT) and better electrochemical properties were measured when exploiting nanocomposite electrolyte based on our SiO_2@PEG750 fillers, probably due to a major DMF retention and to addition of a second Li^+ conductive mechanism such as the one mediated by PEG chains. Overall, these nanocomposite electrolytes also demonstrated satisfying safety features due to their non-flammability, their elevate dendrite resistance, and to the absence of thermal runaway when employed in full LMB. Additionally, their solid appearance facilitated handling and reduced any risk of leakage, otherwise possible with liquid electrolytes.

Acknowledgments:

The work on SiO_2 hybrid fillers was part of the Master Thesis of Stefano Bonato, who I supervised during his work. I would like to thank him and the group of Prof. Roberto Scotti, in particular Dr. Silvia Mostoni, that assisted us for the synthetic part of this project.
TiO_2 characterization was carried out in collaboration with Dr. Roberto Lorenzi, Dr. Michele Mauri, and Prof. Massimiliano D'Arienzo from Milano-Bicocca-University and

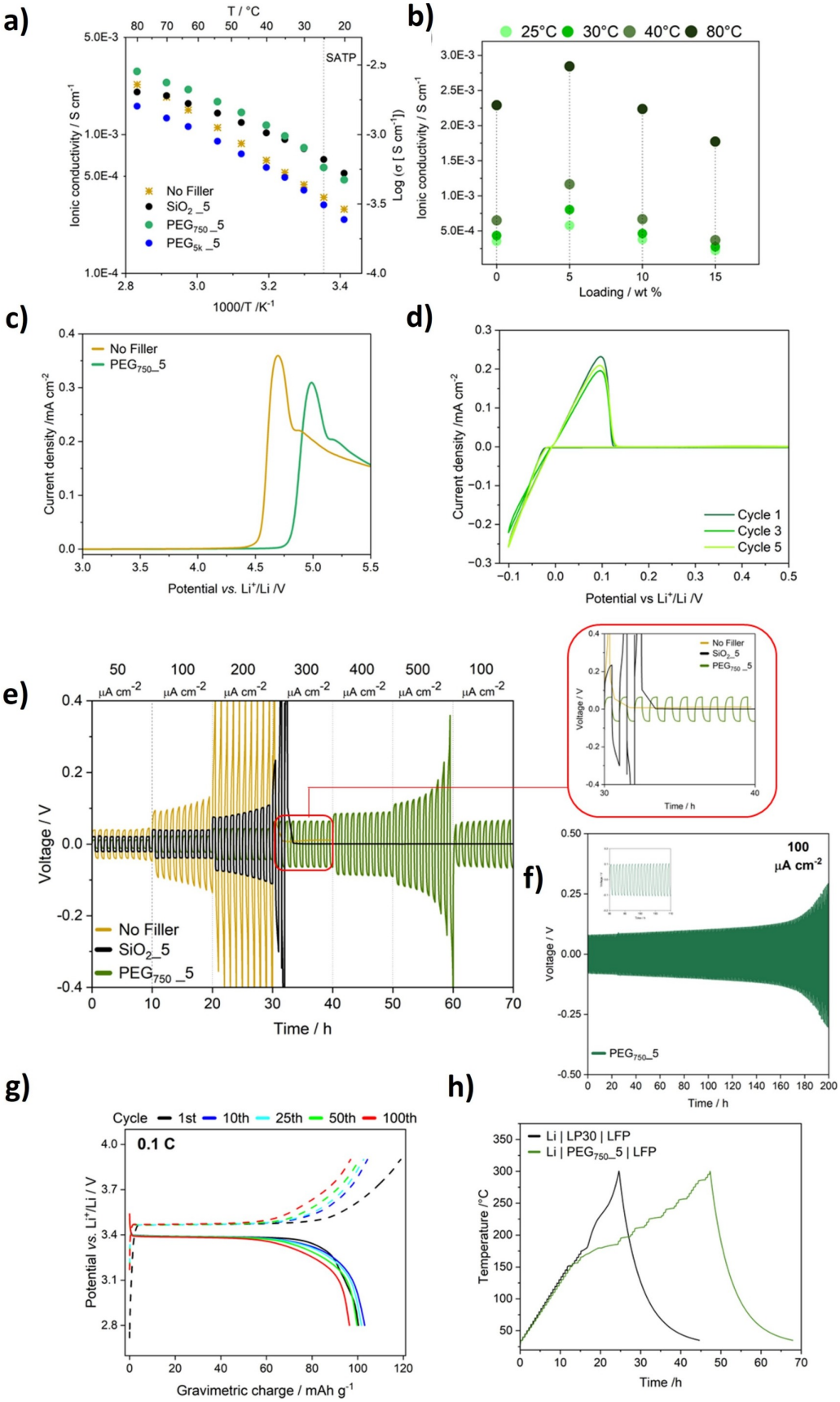

Figure 5.26: a) Arrhenius plots of different QSEs. b) Ionic conductivity vs. loading of SiO^2@PEG750 fillers at different temperatures. c) LSV curves of QSEs without and with 5 wt.% PEG750 fillers. d) CV of PEG750_5. e-f) CP profiles at e) increasing and f) constant current densities. g) Voltage profile of a Li|LFP employing PEG750_5 as electrolyte. h) ARC measurements of a cell employing PEG750_5 and a reference cell with LP30. Readapted from [280].

with Prof. H. W. Lee of Ulsan Institute of Technology, South Korea.
Finally, the investigation of PVdF-HFP SSEs was performed together with Eleonora Carena and Nicholas Vallana during their Master Thesis period and, unfortunately for them, also during their PhD at University of Milano-Bicocca. Therefore, I have to deeply thank them for all the time spent together trying to figure out these peculiar system. Additionally, PFOTES investigation has been carried out during the Bachelor Thesis of Siro Saronni and computational studies on PVdF-HFP electrolytes have been performed by the group of Dr. Giovanni Di Liberto and Prof. Livia Giordano of my same university.

6. Argyrodite-based thin separators:

As already mentioned, the implementation of SSEs into LMBs plays a pivotal role for the development of safer secondary energy storage devices with improved performance (gravimetric energy > 500 Wh kg^{-1} [297]. Considering that the not always satisfying ionic conductivity of polymer electrolyte usually prevents their application for room temperature applications, inorganic ionic conductors appear as a more feasible SSEs able to permit the production of performant all-solid state batteries (ASSBs).
As described in Sec, 4.2.2, among the possible ceramic SSEs argyrodite sulfides (Li_6PS_5Cl) offer the notable advantages of high ionic conductivity at room temperature with processable mechanical deformability, enabling ASSBs for practical application. However, a poor chemical stability of sulfides in the air and polar environments, detrimental interfacial electrochemical and electrochemo-mechanical effects, and limited SSE fabricating process are still hindering their effective employment [298].
To mitigate such problems, the addition of an elastic component which improves flexibility is usually considered propitious for the fabrication of more compliant thin solid electrolytes (TSEs) with reduced thickness and cost, lower resistance, and better adhesion to the electrodes. Ceramic/polymer ratio must be optimized in order to individuate the optimal trade-off between the ionic conductivity, reduced by the addition of the insulating binder, and mechanical flexibility, vice versa facilitated by polymer inclusion [225]. Another benefit of these systems resides in their improved processability: similar separators can be manufactured exploiting scalable and industrially feasible techniques that go beyond the use of thick SSE pellets often employed in the lab scale but not suitable for industrial applications. In this perspective, tape casting, a straightforwardly scalable and well-established technique widely reported in the production of solid-state electrolytes, emerges as one of the best candidates for TSE production. However, the chemical instability of Li_6PS_5Cl (LPSCl) restricts the selection of solvent to non-polar systems such as toluene and p-xylene, limiting the binder choice accordingly [185]. Additionally, it has been recently reported that the use of nitrile-butadiene rubber (NBR), one of the most studied binders for tape-casted TSE, can induce the formation of a thin insulating layer on the surface of the sulfide particles that reduces the overall ionic conductivity [228]. Conversely, novel processing techniques such as calendering can permit the implementation of alternative polymeric binders like carboxylated nitrile-butadiene rubber (XNBR), otherwise not soluble and processable into apolar solvents. The transition to a roll-to-roll manufacturing approach can entail a whole set of original improvements but also requires a careful evaluation of its effect on the TSEs' characteristics.
Herein, we investigated the impact of processing on LPSCl based TSEs for ASSBs with mechanical, structural, and electrochemical perspectives based on the intrinsic differences between these two systems; NBR-based tape-casting and XNBR-based calendering. Depending on the process, the binding of the polymer to LPSCl appeared in different

morphologies, which greatly affected the mechanical properties and ionic conductivity of the TSEs. The investigation of the process-dependent characteristics of SSEs may provide useful insights and new directions on which processes will be the optimized model in the various designs of ASSBs. This part of my thesis project was developed in collaboration with the University of Oxford, where I spent an abroad research period of 9 months during 2022 and 2023 while contributing to this project whose results are currently under review in the following scientific article: *"Processing-Structure-Property Relationships in Practical Thin Solid-Electrolyte Separators for All-Solid-State Batteries"* [299].

6.0.1 Materials and methods:

Materials:

Li_6PS_5Cl powder (99.9 %, average size ≈10 μm, density ρ_{LPSCl}=1.64 g cm^{-3}) was acquired by Ampcera Inc., USA. Arlanxeo kindly provided both nitrile butadiene rubber (NBR, Krynac 3345F, density ρ_{NBR}=0.97 g cm^{-3}) and carboxylated nitrile butadiene rubber (XNBR, Krynac X750, density ρ_{XNBR}=0.98 g cm^{-3}). Anhydrous toluene (99.8%, T_b=110.6°C) was acquired from Sigma Aldrich.
Lithium bis(fluorosulfonyl)imide (LiFSI, 99.0%, Fluorochem Ltd) was obtained from Fluorochem Ltd. Lithium bis(trifluoromethanesulfonyl) imide (LiTFSI), 1,3-dioxolane (DOL, anhydrous 99.8%), and 1,2-dimethoxyethane (DME, anhydrous 99.8%) were bought from Sigma Aldrich. Commercial tape-casted sulfur cathode (3.54 mg cm^{-2} of S loading, 70 wt.% S, 20wt.% of carbon black, 10 wt.% PVdF) was provided by NEI Corp.

Electrolytes and cells production:

For the tape casting of TSEs (T-TSEs), 500 mg of NBR are dissolved in 10 mL of anhydrous toluene. Slurries with three different weight concentration (95:5, 90:10, 80:20) are prepared adding the desired amount of LPSCl into the NBR solution and ball-milling for 40 min at 900 rpm in a Fritsch Pulverisette 7 planetary ball mill using jar and spheres of ZrO_2. The ink is later doctor-bladed on a silicone-coated polyethylene terephthalate (PET, thickness=50 μm) film used as substrate for the TSEs. After an overnight drying at room temperature, the T-TSE is carefully peeled off the PET substrate.
Calendered TSEs (C-TSEs) were prepared following the procedure reported in a previous scientific paper [300]. Different ratios of LPSCl and XNBR (95:5, 90:10, 80:20 w/w) are dissolved into anhydrous toluene and combined using agate mortar and pestle. The so-produced composite materials is then sandwiched into two silicone-coated PET films and calendered, using a MSK-2150 instrument (MTI Corp.) to produce a free-standing electrolyte. The thickness of the C-TSE was controlled modifying the distance between the rolls.
Densification of TSEs is ensured exploiting stainless steel plungers (10 mm diameter) with an uniaxial press (100-200 MPa) for 3 minutes.
LPSCl pellet were produced pressing LPSCl powders at 370 MPa employing a a polyether ether ketone (PEEK) die and the same SS plungers.
Composite cathodes were prepared infiltrating a 2M solution of LiTFSI in DOL into sulfur cathode (10 μL per mg of S). A solid-polymer catholite (P-DOL) is formed through the polymerization induced by LiFSI which acts as initiator.
Liquid comparison electrolytes were composed of a 1.0 M LiTFSI/0.8M $LiNO_3$ 1/1 v/v

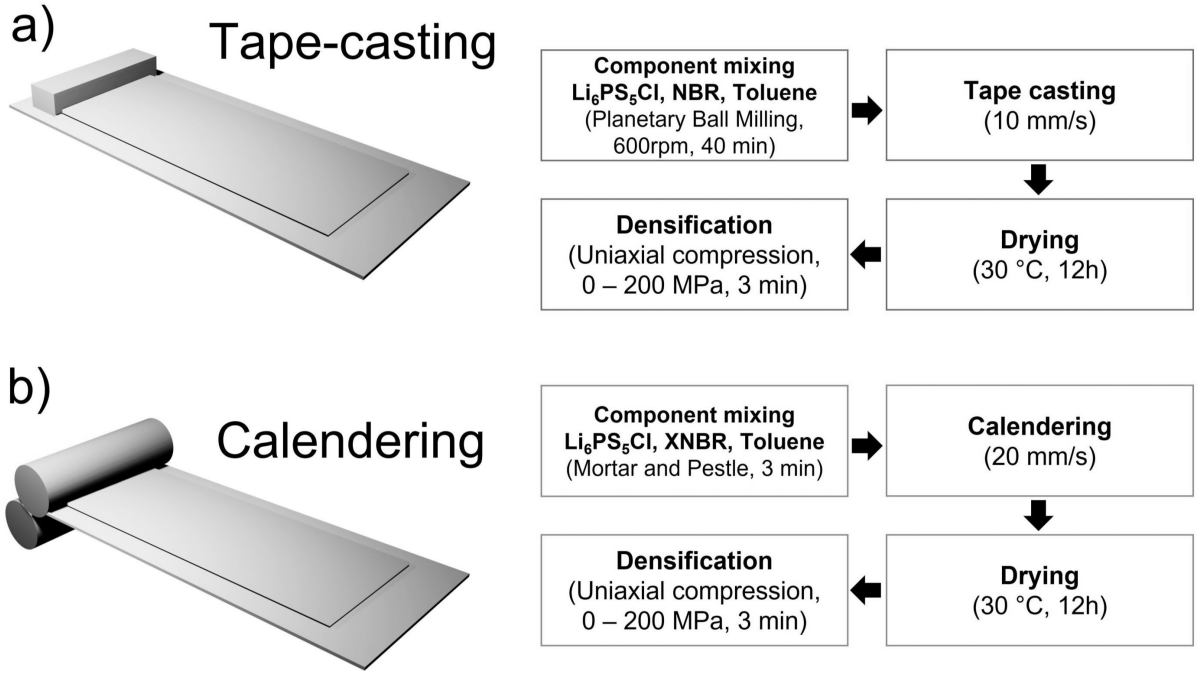

Figure 6.1: Schematic representation of the two processes employed for the fabrication of TSEs: a) tape-casting and b) calendering.

solution of DOL and DME.
All the aforementioned processes have been carried out in a MBraun Ar-filled glove box (O_2, H_2O<0.1ppm) to avoid LPSCl degradation in contact with moisture.

Instrumentation and methodology:

Physico-chemical characterization: Archimede's porosity p_{Arch} expressed as a percentage of the total volume was computed taking in account the geometric parameters of the electrolyte and using the following equation:

$$p_{Arch} = [1 - \frac{W_{TSE}}{V_{TSE}} \cdot \left(\frac{X_{LPSCl}}{\rho_{LPSCl}} + \frac{X_{pol}}{\rho_{pol}}\right)] \cdot 100 \tag{6.1}$$

where W_{TSE} and V_{TSE} are the weight and the volume of the TSE while ρ_a and X_a are the density and the weight fraction of a generic phase a. To determine W_{TSE} and V_{TSE}, several TSE specimens for each composition (n>5) were punched and their weight and thickness were measured, respectively using a Sartorius Cubis micro-balance and a Mitutoyo 293-344 screw gauge micrometer.
Tensile testing analyses were carried out on a DEBEN Microtest MT5000 Dual Leadscrew Tensile Tester H-550 Controller tensile, compression and horizontal bending stage equipped with a digital extensometer (travel length=20mm) and a 1000N load cell operating at 50x gain to maximize the sensitivity. To visually monitor and record the experiments, a ThorCam digital camera was employed. Rectangular specimens of constant length (3.0 cm) and width (0.8 cm) were punched using a die cutter and then transferred to the tensile stage. The thickness of each specimen was individually quantified using a digital screw micrometer (sensitivity=0.001 mm) and the mean value was obtained averaging from 3 different points of the TSE. After a careful alignment of TSEs

with the clamps of the stage, tensile tests were performed monotonically loading in tension the TSEs with a fixed extension rate of 1.0 mm min^{-1}. The resulting force was recorded by the instrument until the breakage of the TSE. At least 5 samples for each combination of parameters (C-TSE and T-TSE; 5%-10%-20% wt.; 0-100-200 MPa) were characterized in order to determine average values and standard deviation. To avoid any possible side reaction of the argyrodite with environmental water, all the tests were performed in an MBRaun Ar-filled glove box (O_2, H_2O < 0.1 ppm). Error bars of the stress/strain plots were added taking in account the average oscillations in the force detected by the instrument when monotonically loaded in force.
Plasma focused ion beam (PFIB) SEM sectioning was carried out on a Thermo Fisher Helios G4-CXe Plasma FIB in order to characterize microstructurally the TSEs. To avoid their degradation, TSEs were transferred to the PFIB-SEM exploiting a Gatan airless transfer vessel. Samples were then polished and sectioned applying a fixed voltage (30 kV) and a current of 15 nA. ImageJ software was employed to evaluate the microstructural porosity p_{PFIB}.

Electrochemical characterization: After having punched TSEs disks (10mm diameter), ionic conductivity was determined by A Biologic VMP-3 potentiostat with PEIS applying a 10 mV voltage sinusoidal input with a frequency in the range 0.01Hz-1MHz. All the measurements were carried out at RT on a custom-made test cell with two electrodes of carbon-coated aluminium and a stack pressure of 2.5 MPa.
For the assembly of the full lithium-sulfur cell, a composite cathode was prepared with the following methodic. A 2M solution of LiFSI in DOL was injected into a commercial sulfur cathod with a loading of 10 μL per mg of S. The presence of LiFSI which acts as a polymerization initiator for DOL enables the formation of a solid polymer catholite. Li metal foil was used as anode material and applied to the TSE pressing at 5 MPa. All these steps were performed in an Ar-filled MBraun glove box (O_2, H_2O <0.1 ppm). The cell was then galvanostatically cycled at 0.05C in the potential range 1.5V-2.8V vs Li^+/Li using a Biologic BCS-800 battery tester.
An analogue Li-S cell comprising a liquid electrolyte (1M LiTFSI and 0.8M $LiNO_3$ in DOL and DME) was also tested in the same operating conditions.

6.0.2 Results and discussion:

For the sake of clarity and to avoid misleading long names for the samples, all the TSEs will be labelled with the following form **AX-YYY** where:

- **A** describes the technique employed for the fabrication of the electrolyte (**T** for tape-casting, **C** for calendering).
- **X** refers to the binder wt% into the TSE (**5**, **10**, or **20**).
- **YYY** indicates the densification pressure expressed in MPa, when applicable (**100** or **200**; 0 MPa if unspecified).

TSE fabrication and morphology evaluation:

As previously described, different manufacturing processes can be exploited for the production of TSEs. Even if dry-processed TSEs based on PTFE binder have been recently

reported in the literature [301], the reactivity of this polymer with metallic lithium [302] and the reduced scalability of this approach forced us to focus on other two different solution-based techniques that permits the use of more electrochemically stable binders. Consequently, also the binder selection appeared limited to those soluble in solvents with a reduced dielectric constant able to preserve the chemical nature of LPSCl.
Firstly, a NBR-based slurry was produced dissolving LPSCl and the polymer binder in toluene. The resulting ink was tape-casted in order to produce thin sheets of electrolyte upon evaporation of toluene. Improved film homogeneity was obtained when using ball-milled argyrodite while the use of untreated powder lead to visible aggregation and poor film quality.
Instead, the use of a more polar binder like XNBR enabled the implementation of a different and original approach based on calendering. After having obtained a rubbery-like toluene-based mixture, the roll-to-roll processing permitted the production of self-standing homogenous TSEs without the need of previous ball-milling of the argyrodite powder.
The two binders did not result interchangeable: the presence of -COOH moieties of XNBR reduced its solubility into toluene, preventing the production of an ink suitable for tape-casting. Conversely, the limited polarity of NBR did not permit the formation of a rubbery quasi-solid mixture with toluene and argyrodite, required for the calendering treatment. Overall, for each processing techniques three different binder loadings (5-10-20 wt%) and three different densification pressures (0-100-200 MPa), required to ensure an intimate contact between particles into the TSE, have been tested. Full experimental details of both methods can be found in Sec. 6.0.1.
After having produced TSEs with various compositions, the geometrical porosity p_{Arch} of the film was evaluated using *Eq. 6.1*. As shown in *Fig. 6.2a*, significant porosity (≈35-45 %) was observed in non-densified samples with the lowest binder content (T5 and C5). These values resulted decreased upon densification and with the increasing rubber content but always remained in the order of 10%-20% with the only exception of T20-100 and T20-200. No clear trend were however observed, with the obvious exception of porosity reduction upon densification

To further investigate the morphology of TSEs and the effects of growing densification pressured and/or polymer contents on the resulting structure, plasma focused ion beam (PFIB) SEM sectioning was performed on selected specimens (*Fig. 6.3*). From the digital elaboration of the images using ImageJ software (*Fig. 6.2d-e* it resulted possible to evaluate the porosity p_{PFIB} of our electrolytes. All the porosity values are presented also in *Tab. 6.1* and *Tab. 6.2*. Even if the values obtained from PFIB appeared lower than the one obtained from geometrical calculations, a good agreement between the two trends was observed (*Fig. 6.2b-c*). The discrepancies can be justified considering that our digital analysis of the images only permitted a 2D evaluation porosity, therefore disregarding the volumetric extension of the pores. More precise techniques, such as PFIB tomography, would be required to achieve a complete quantification of the 3D porosity.

Apart from this numerical evaluation of the pores, PFIB images also permitted a more qualitative evaluation of TSE's morphology. From the side-to-side comparison of T-TSEs and C-TSEs in *Fig. 6.3* it results possible to appreciate the intrinsic differences present between the two systems. Smaller particle size, compatible with ball-milling,

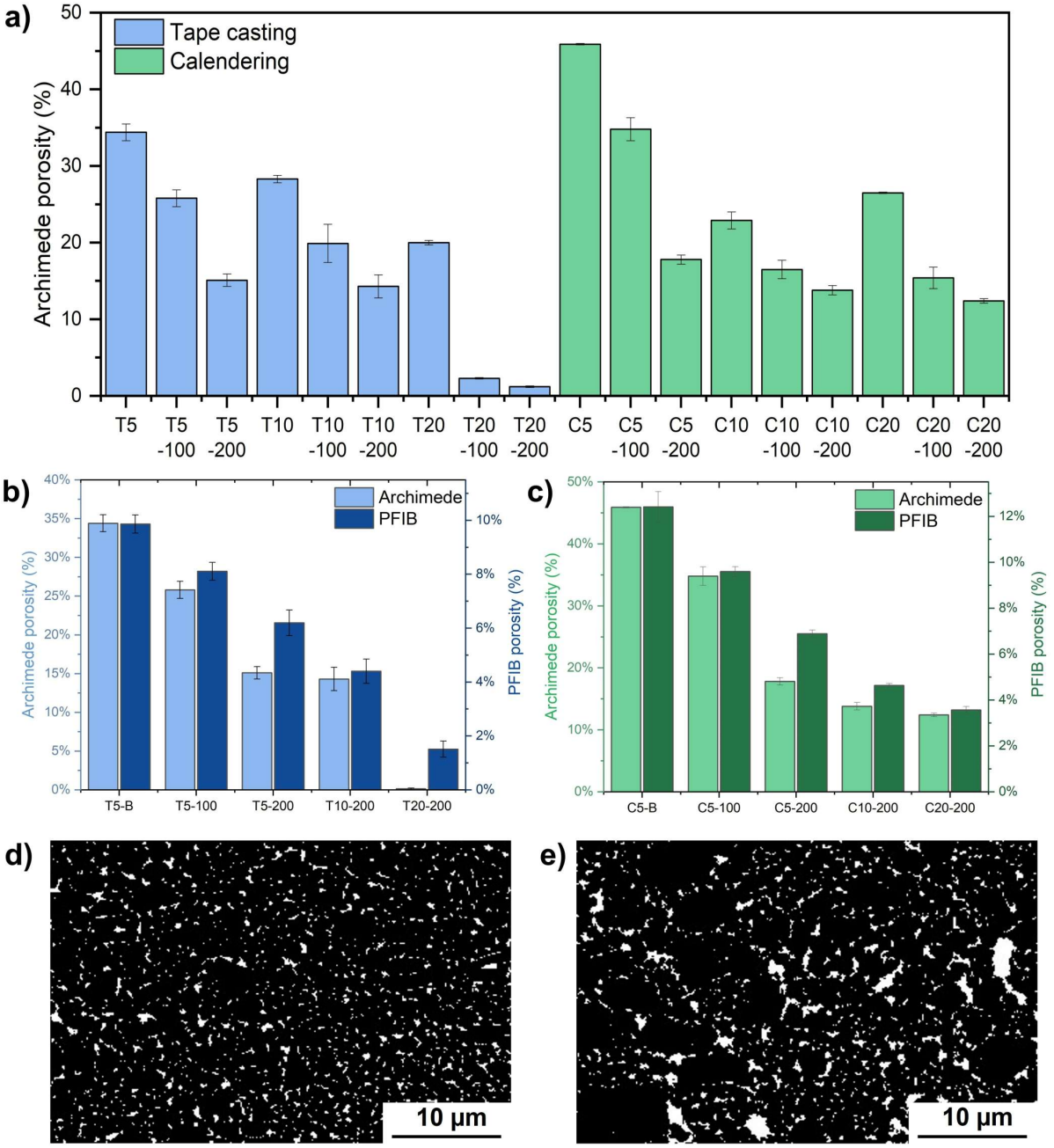

Figure 6.2: a) Archimede's porosity of all the produced TSEs samples. b-c) Comparison between Archimede's porosity and the porosity values obtained from PFIB images for selected b)T-TSEs and c)C-TSEs. d-e) PFIB cross-section image of T5 (d) and C5 (e) TSEs elaborated with ImageJ software in order to highlight the porosity of the system in white.

Table 6.1: Composition of tape-casted TSEs employed in this work comprising different amount of binder and with the respective porosity determined with geometric calculation (p_{Arch}) and from PFIB images (p_{PFIB}).

Name	**NBR (wt.%)**	**Densification**	p_{Arch} (%)	p_{PFIB} (%)
T5	5%	0 MPa	34.4 (±1.1)	9.9 (±0.3)
T5-100	5%	100 MPa	25.8 (±1.1)	8.1 (±0.3)
T5-200	5%	200 MPa	15.1 (±0.8)	6.2 (±0.5)
T10	10%	0 MPa	28.3 (±0.5)	—
T10-100	10%	100 MPa	19.9 (±2.5)	—
T10-200	10%	200 MPa	14.3 (±1.5)	4.4 (±0.5)
T20	20%	0 MPa	20.0 (±0.3)	—
T20-100	20%	100 MPa	2.3 (±0.1)	—
T20-200	20%	200 MPa	1.2 (±0.1)	1.5 (±0.3)

Table 6.2: Composition of calendered TSEs employed in this work comprising different amount of binder and with the respective porosity determined with geometric calculation (p_{Arch}) and from PFIB images (p_{PFIB}).

Name	**XNBR (wt.%)**	**Densification**	p_{Arch} (%)	p_{PFIB} (%)
C5	5%	0 MPa	45.9 (±0.1)	12.4 (±0.6)
C5-100	5%	100 MPa	34.8 (±1.5)	9.6 (±0.2)
C5-200	5%	200 MPa	17.8 (±0.6)	6.9 (±0.2)
C10	10%	0 MPa	22.9 (±1.1)	—
C10-100	10%	100 MPa	16.5 (±1.2)	—
C10-200	10%	200 MPa	13.8 (±0.6)	4.6 (±0.1)
C20	20%	0 MPa	26.5 (±0.1)	—
C20-100	20%	100 MPa	15.4 (±1.4)	—
C20-200	20%	200 MPa	12.4 (±0.3)	3.6 (±0.2)

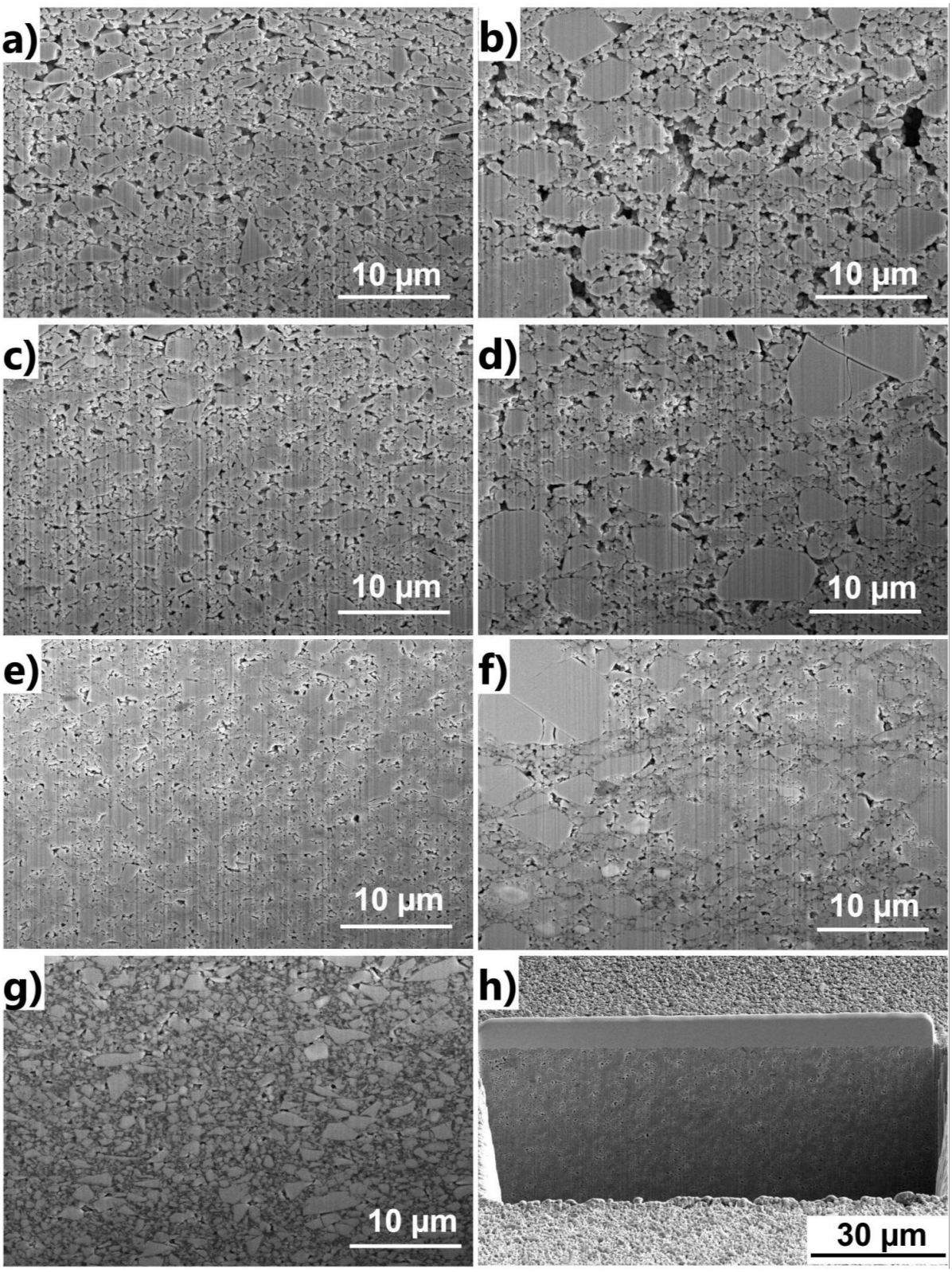

Figure 6.3: Cross-section PFIB images of a) T5, b) C5, c) T5-100, d) C5-100, e) T5-200, f) C5-200, and g) T20-200 TSEs. h) Exemplificative image of a cross-sectioned region obtained using PFIB milling.

and improved homogeneity can be seen for tape-casted specimens while calendered ones presented a more elongated particles, due to the rolling step. Overall, T-TSEs also possessed a more distributed polymer network throughout the whole electrolyte. This feature can be particularly noticed in those specimens with high binder content such as T20-200 (*Fig. 6.3*g) where the high NBR content coupled with a technique able to ensure an homogenous dispersion of the binder lead to a morphology composed of a polymeric matrix which encompass distributed LPSCl particles. This particular structure is responsible of the peculiar mechanical properties discussed in the next section.

Mechanical characterization:

After having estimated the porosity and having understood the different morphologies of the two TSEs, all the electrolytes were tested in order to quantify their mechanical properties. In place of other more time-consuming techniques such as nano-indentation, it was decided to characterize mechanically our TSEs employing tensile testing. To the best of my knowledge, only a few research papers have reported the use of tensile testing in SSEs with a significant or predominant inorganic content due to the difficulty encountered in the specimen preparation at increasing ceramic loading [247, 301, 303, 304]. Even if tensile analysis appears obviously not suitable for electrolytes prepared as monolithic pellets, the technique can be easily applied to TSEs thanks to their high degree of processability, enabling a rapid and facile evaluation of the most important mechanical properties such as tensile modulus (TM), ultimate tensile strength (UTS, i.e. the maximum stress a system can withstand before fracturing) and elongation at break. First of all, useful insights can be obtained from the systematic comparison of TSEs produced with the two different processing approaches. Going into detail, higher modulus and more pronounced elongation are measured for T-TSEs (*Fig. 6.4a-b*). Such discrepancies were not completely attributable to the slightly different chemical nature of the two binders, which possess a very similar TM (2.15 and 1.55 MPa, respectively for NBR and XNBR [305, 306]). Also the different LPSCl size does not justify on its own these variations because composites' TM results independent on the dimension of the particles when a good adhesion between the two phases is present [307, 308]. These results were therefore attributed to the more homogenous distribution of polymer into the T-TSEs, clearly visible in PFIB images, in which the coupling of ball-milling and tape-casting from solution lead to a better distribution of NBR throughout the electrolyte. This morphology enabled a more efficient transfer of the local stresses between LPSCl and the polymer, favoured by the high adhesion between NBR and sulfide particles [228], which accounted for the higher elongation at break of these systems. As visible in *Fig. 6.5a-c*, tensile testing profiles of T-TSEs present a first steep elastic region then followed by a plateau in which the elongation of the elastomeric matrix takes place. As expected, this second feature appears more pronounced for undensified specimens and at higher binder contents. Also necking phenomena observed in tape casted specimens become more evident at growing rubber loadings, when TSEs are more deformable and less brittle (*Fig. 6.5e*) Conversely, stress-strain curves of C-TSEs show a totally different shape with no clear yield strength points or elongation plateaux (*Fig. 6.5b-d-e*). Bigger LPSCl particles and less dispersed XNBR induced by calendering process lead to an easier fracturing of TSEs upon tensile loading that, therefore, present a reduced elongation at break and a lower modulus.

Focusing on the effect of the applied pressure, as shown in *Fig. 6.4a* both tape-casted

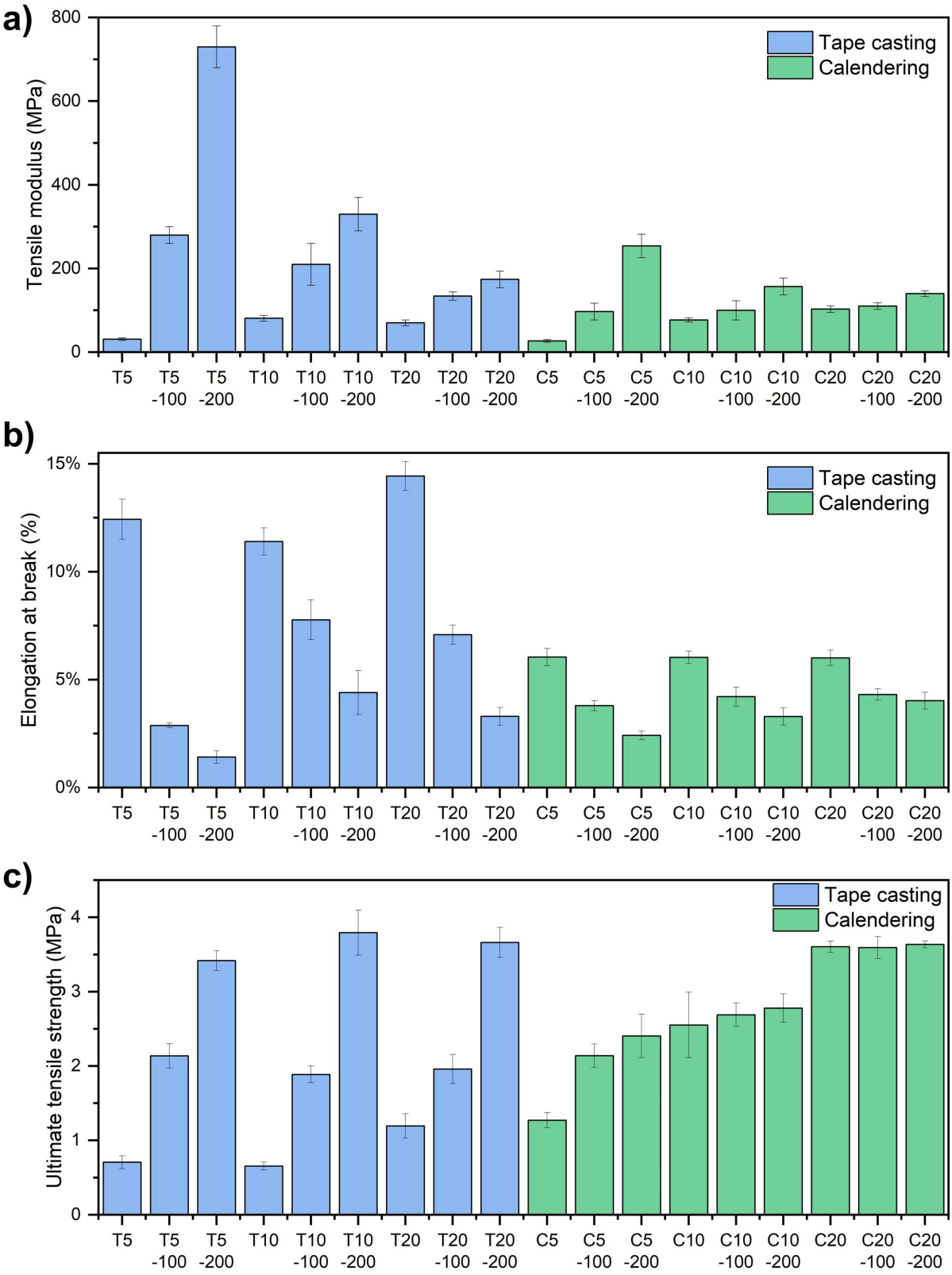

Figure 6.4: a) Tensile modulus, b) elongation at break, and c) ultimate tensile strength of T-TSEs and C-TSEs.

and calendered specimens displayed an obvious increment of TM upon densification, coupled to a decrease of the elongation at break (*Fig. 6.4b*). This tendency was observed for all the three binder contents, confirming that the applied pressure greatly modifies the mechanical properties of the composites making them stiffer and less deformable. This feature can also be visually appreciated when comparing different TSEs before and after tensile testing (*Fig. 6.6*). An increasing trend was also noticed for UTS (*Fig. 6.4c*). Interestingly, these values resulted comparable or higher than the one reported for dry-processed LPSCl SSEs based on a binder, PTFE, which intrinsically possesses a tensile strength distinctly larger than NBR or XNBR [301, 309–311]. The high UTS values hint to a good particle/matrix adhesion into the composite, since in multi-phases systems an effective stress transfer between the two phases results as one of the most important factors contributing to the resulting strength [312].
Additional observations can also be made comparing the effects of densification on the UTS of T-TSEs and C-TSEs. Confronted with tape casted analogues, calendered separators experienced less pronounced variations after being pressed at increasing load. A first reason can be found considering the different particle size of the two systems. Upon densification, the adhesion between binder and LPSCl in T-TSEs, which possess smaller particles with higher surface area, is improved more than in C-TSEs with bigger particle and less-distributed polymer. Additionally, even if not densified, blank C-TSEs experienced a certain pressure upon rolling during the calendering process which can contribute to a stiffening of the undensified separators, therefore leading to lower differences with the densified samples. Similar considerations will be later recalled when dealing with the ionic conductivity of C-TSEs and T-TSEs at different pressures.

Finally, focusing on variable binder contents, higher modulus values for non-densified specimens were curiously observed at increasing polymer loading. Despite the reduced modulus of the binder, this phenomenon can be justified taking in account the high porosity fraction present in the pristine TSEs (>20%)). In this case, larger binder amounts act as a strengthening agent, forming a polymer network which increases the cohesion among separate LPSCl particles and improves the mechanics of the systems. This effect is reversed after densification, when porosities of 5 wt% and 10 wt% TSEs are commensurable and the contact among LPSCl grains becomes more intimate. As expected, T5-200 and C5-200 TSEs possess respectively a roughly three-fold and two-fold increased TM when compared to 10 wt% analogues. A longer elongation is instead achieved for systems comprising larger amounts of rubbery binder: for instance, this can be noticed comparing T5-200 with T10-200 or C5-200 with C10-200. However, samples with the highest polymer content (20 wt%) generally displayed a reduced homogeneity and a higher amount of flaws that induced localized breakage throughout the specimens' section before the final fracture, therefore affecting their maximum elongation.
All the values of TM, elongation at break, and UTS are also displayed in *Tab. 6.3* and *Tab. 6.4*. Overall, tensile testing demonstrated its validity as a rapid and facile way to characterize the macroscopic mechanical properties of our TSEs.

Electrochemical testing:

After having measured their mechanical features, our thin solid electrolytes were electrochemically characterised in order to determine the optimal composition for the im-

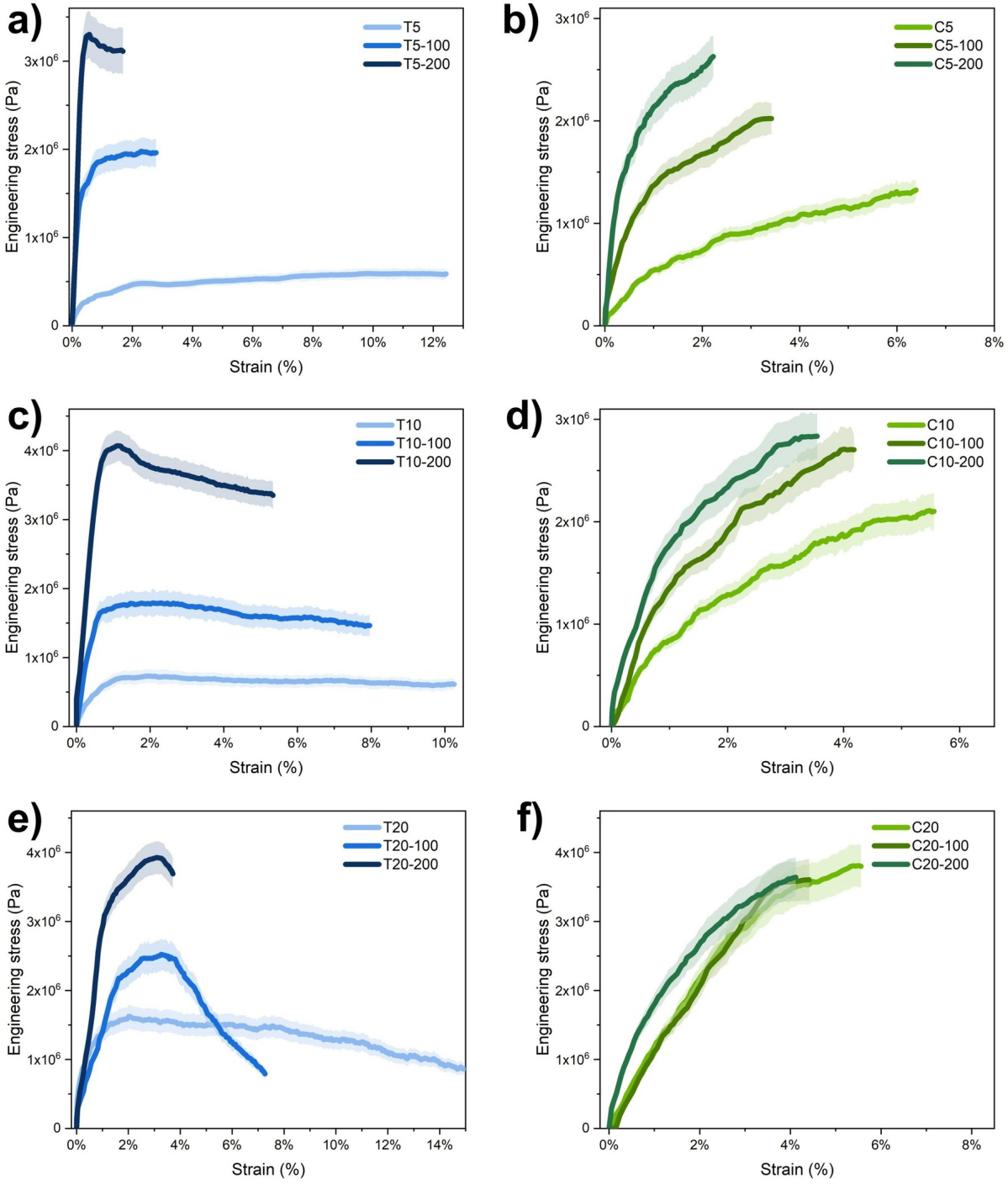

Figure 6.5: Exemplificative stress-strain plots of tape-casted (a-c-e) and calendered (b-d-f) TSEs with different binder contents. Error bars are represented as light-coloured areas surrounding the curves.

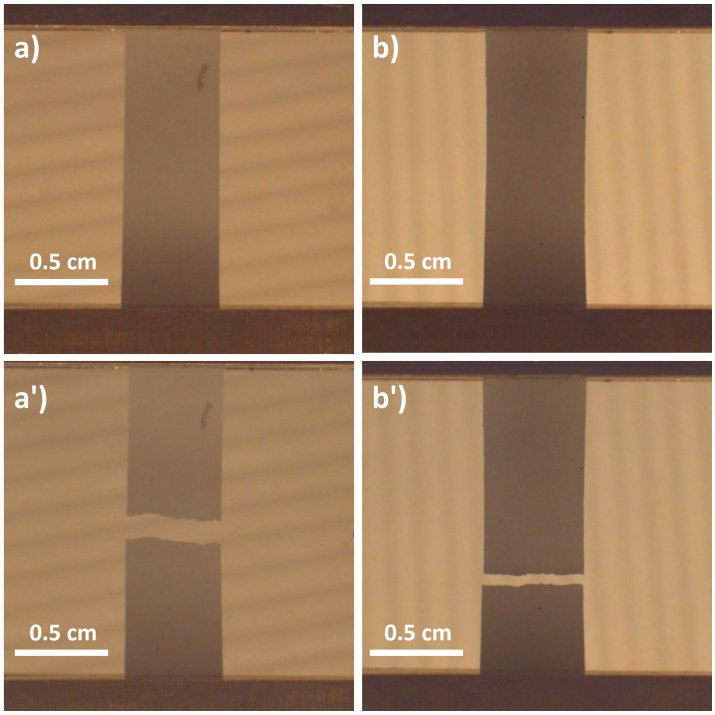

Figure 6.6: Digital images of C5 (left) and C5-200 (right) TSEs before (a-b) and after (a'-b') the tensile testing. It is possible to appreciate the larger displacement of the clamps experienced with the more deformable C5 TSE.

Table 6.3: Recap of the mechanical properties (tensile modulus TM, maximum elongation at break, and ultimate tensile strength UTS) of tape-casted TSEs.

Sample	TM (MPa)	Max. elongation (%)	UTS (MPa)
T5	31 (±3)	12.4 (±0.9)	0.71 (±0.08)
T5-100	280(±20)	2.9 (±0.1)	2.1 (±0.2)
T5-200	730 (±50)	1.4 (±0.3)	3.4 (±0.1)
T10	81 (±7)	11.4 (±0.6)	0.65 (±0.5)
T10-100	210 (±50)	7.8 (±0.9)	1.9 (±0.1)
T10-200	330 (±40)	4.4 (±1.0)	3.8 (±0.3)
T20	70 (±7)	14.4 (±0.7)	1.2 (±0.1)
T20-100	134 (±10)	7.1 (±0.4)	2.0 (±0.2)
T20-200	174 (±20)	3.3 (±0.4)	3.7 (±0.2)

Table 6.4: Recap of the mechanical properties (tensile modulus TM, maximum elongation at break, and ultimate tensile strength UTS) of calendered TSEs.

Sample	TM (MPa)	Max. elongation (%)	UTS (MPa)
C5	27 (±3)	6.1 (±0.4)	1.3 (±0.1)
C5-100	97 (±20)	3.8 (±0.2)	2.1 (±0.2)
C5-200	254 (±28)	2.4 (±0.2)	2.4 (±0.3)
C10	77 (±5)	6.0 (±0.3)	2.6 (±0.4)
C10-100	100 (±23)	4.2 (±0.4)	2.7 (±0.2)
C10-200	157 (±20)	3.3 (±0.4)	2.8 (±0.2)
C20	103 (±8)	6.0 (±0.4)	3.6 (±0.1)
C20-100	110 (±8)	4.3 (±0.3)	3.6 (±0.2)
C20-200	140 (±7)	4.0 (±0.4)	3.6 (±0.1)

plementation in Li-metal and Li-S devices.
First of all, the ionic conductivity of all the TSEs was determined at a fixed stack pressure employing a custom made conductivity cell. This parameter usually results a critical factor both for ionic conductivity and ciclability of solid-state batteries [313]. In particular, low conductivity due to a poor electrode-electrolyte contact usually arises when reduced pressures are applied. On the other hand, increased short-circuit likelihood is experienced at high stack pressures due to the extrusion of the malleable Li into the pores of the ceramic electrolyte [314]. Considering the improved softness imparted by the polymer addition which can partially improve the adhesion of the electrodes even at low pressure and the desire of investigating a scalable system, it was decided to fix the stack pressure at 2.5 MPa, well below the values usually employed for LPSCl pellets [314]. Additionally, considering the reduced thickness of or TSEs, an elevate stack pressure would enormously increase the risk of dangerous Li extrusion throughout the whole separator.
The results, presented in *Fig. 6.7*, displays the strong dependence of ionic conductivity both on binder content and on densification pressure. As expected, higher amounts of insulating binder reduced the ionic conductivity of TSEs both for tape-casted and calendered separators. Consequently, the values related to samples containing 20 wt% of polymer (as T20 and C20) have been omitted due to their unsatisfying performances. Also densification pressure resulted to play a major role for the conductive properties since an improved inter-particle contact enabled higher ionic conductivity up to $\sim 2 \cdot 10^{-4}$ S cm^{-1} for C5-200 TSE.
Finally, it is also worth noticing the enormous difference between the values measured for tape-casted and calendered TSEs, with the latter demonstrating a greatly larger σ_{Li^+}. The reasons behind this phenomenon can be found in the different preparation methodology needed for the fabrication of the two electrolytes. High-energy ball milling was required as a mixing step for the production of T-TSE in order to achieve homogeneous separators without LPSCl aggregates in the resulting casted film. Conversely, this step could be omitted during the fabrication of C-TSE when a simple mortar and pestle mixing process was enough to produce an homogenous rubbery mixture. As previously shown in PFIB-SEM images (*Fig. 6.3*), this manufacturing difference resulted in a different particle size: as expected, ball-milled LPSCl possessed a reduced particle size

compared to the one employed for calendered separators. This endowed two different consequences. Firstly, considering the large bulk conductivity of LPSCl, smaller particles lead to an increased inter-particle resistance which accounts for the majority of the impedance contribution of the electrolyte. Additionally, it has been demonstrated that rubber binders such as NBR can effectively coat LPSCl particles when deposited from a tape-casted solution [228]. Apart from imparting great flexibility and cohesion to the TSEs as previously described, this thin insulating polymer layer might also introduce an additional impedance contribution which depresses the overall conductivity. Upon increase of the binder content, this film lead to the formation of an insulating polymer matrix which encompass the LPSCl as visible for T20-200 TSE in *Fig. 6.3g*. Conversely, the negative influence of this film in the XNBR-based calendered TSEs appears strongly mitigated due to the different manufacturing approach that, employing reduced amounts of solvent during the mixing step, did not permit the detrimental formation of the insulating coating layer of rubber.

Also, CCD measurements were carried out in order to verify the existence of a dependence of the critical current on the modulus of our electrolytes (*Fig. 6.7c-d*). To do that, current density was continuously increased from 0.01 mA cm^{-2} to 0.4 mA cm^{-2} until cell failure. Firstly, a reference analysis was performed on a thick (∼600 μm) LPSCl pellet: a sudden voltage drop experienced at 0.325 mA cm^{-2} confirmed the formation of Li filaments. Interestingly, despite the enormously reduced thinness of TSEs (∼ 50 μm), their CCD values resulted comparable and equal to 0.300 mA cm^{-2} for the best performing C5-200 specimen. However, no clear relation between tensile modulus and CCD was discovered, confirming once more that short-circuiting in this kind of electrolyte appears mainly related to an inter-particle lithium filaments growth rather than to a piercing if the TSE [315]. Therefore, the addition of a pore-filling polymer binder enabled satisfying CCDs also for TSEs with a thickness of $\sim \frac{1}{12}$ of the pellet and a tensile modulus of 2 orders of magnitude lower than pure LPSCl (21 GPa vs 200 MPa).

Taking in account the consideration on the conductivity and CCD mentioned above, subsequent analyses have been carried out only on the most performing TSE, i.e. C5-200. This electrolyte also displayed a satisfying electrochemical stability when contacted with Li anode. As shown in *Fig. 6.7e*, PEIS analyses applied on a symmetric Li cell comprising our C5-200 TSE demonstrated a negligible growth of the impedance after 24 hours of direct contact with metallic lithium thus proving the formation of a stable SEI favoured by XNBR presence. Conversely, similar analysis carried out on LPSCl pellets displayed a continuous increase of the interfacial resistance due to the intense reactivity between the sulfide and Li.

Li|Li cells were also employed to furthermore test the stability of our TSE upon long-term stripping-plating. As reported in *Fig. 6.8a*, C5-200 resulted able to sustain over 500 hours of continuous cycling at a current of 0.1 mA cm^{-2} experiencing a reduced overpotential (∼7mV). No evidence of Li filament growth was detected during the analysis.

After this promising results, it was decided to verify the performance of this system in a full Li-S cell under a mild stack pressure of 1 MPa. To overcome the serious limitation related to the poor interfacial contact between the cathode in solid-state cell architecture, a LiFSI-PDOL catholite was added to a commercial sulfur cathode. This lead to the establishment of improved conductive pathways into the cell, enabling cycling at our desired practically relevant working condition (RT, 1 MPa). To better evaluate the performance of our system, an analogue cell based on a liquid electrolyte LE was also assembled and tested. Fig. 6.8b shows the discharge profiles of both cells: while the LE

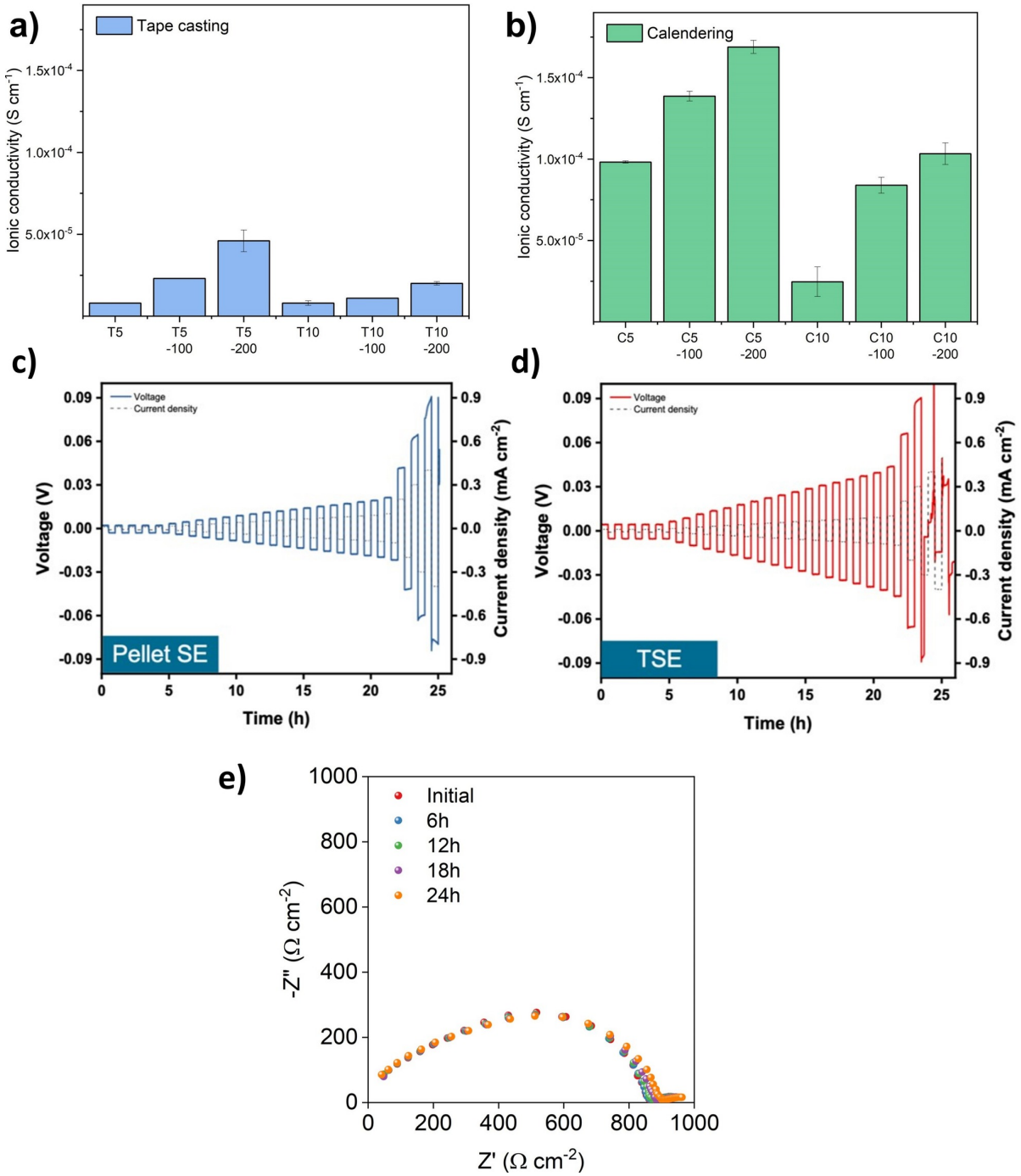

Figure 6.7: a-b) Ionic conductivity of a) tape-casted and b) calendered TSEs. c-d) Comparison of CCD analysis performed on Li|Li symmetric coin cells employing a pellet of LPSCl and a C5 TSE [300]. e) Nyquist plot showing the evolution of the impedance profile of Li|TSE|Li cell employing a C5-200 TSE demonstrating a good electrochemical stability in contact with lithium. Readapted with permission [300] and [299].

presented two distinct plateaux, associated to the subsequent conversion S_8 to Li_2S_4 and from Li_2S_4 to Li_2S, the TSE enabled a direct reaction with a single discharge plateau at ~2.15V.
Eventually, both the Li-S cells have been cycled at a current density of 0.3 mA cm^{-2}, equal to the CCD value previously determined. The solid-state battery delivered more than 50 cycles with a satisfying coulombic efficiency ~99%. In addition, the delivered specific capacity of 410 mAh g^{-1} resulted similar to the one obtained using LE (433 mAh g^{-1}).
However, none of these systems achieved performances comparable with the theoretical capacity of sulfur, i.e. 1675 mAh g^{-1}. The reasons behind this issue can be found in the partial dissolution of poly-sulfides into the catholite, leading to the undesired detrimental shuttle effect. A more efficient and optimized cathode architecture with encapsulated sulfur particles will be required to partially mitigate this problem that goes beyond the topic of my thesis.

Conclusion:

In conclusion, both tape-casting and calendering demonstrated their potentiality for the production of thin, free-standing, and flexible argyrodite-based electrolytes thanks to the addition of moderate amounts of binder. Best results were achieved with higher densification pressures, which lead to a pronounced reduction of TSEs porosity.
Thanks to the embedding polymer matrix formed during the deposition from the toluene ink, T-TSEs displayed satisfying mechanical properties with high elongation and tensile modulus. However, the insulating nature of the rubber lead to an undesired suppression of the ionic conductivity. Additionally, despite the promising scalability of this manufacturing approach, the use of toluene in large excess and the need of a ball-milling step affected the sustainability and the affordability of the process.
Conversely, the use of a more polar binder such as XNBR enabled the use of roll-to-roll calendering. The use of reduced amount of toluene, only employed as a lubricant, did not lead to the formation of the insulating polymer matrix previously noticed and also improved the sustainability of this technique. Consequently, a more satisfying ionic conductivity, up to $2 \cdot 10^{-4}$ S cm^{-1} for the densified C5-200 TSE, was measured. This was achieved at a partial expense of mechanics: C-TSEs presented lower stiffness and worse elongation at break due to the less homogenous binder dispersion.
All these considerations are schematically recapped in the radar plots presented in Fig. 6.8c where the two different fabrication approaches are evaluated with respect to their main features.

Acknowledgments:

As previously mentioned, this part of my PhD research was carried out during my abroad period at the University of Oxford, United Kingdom, in the group of Prof. Mauro Pasta that hosted me during this period. I also have to thanks Dr. Junhao Li, Dr. Soochan Kim, Jack Aspinall, and Yvonne Chart that assisted me during my research and all the members of the Pasta Group (Giulia, Shoban, Max, ...) that greeted and helped me during this awesome experience.

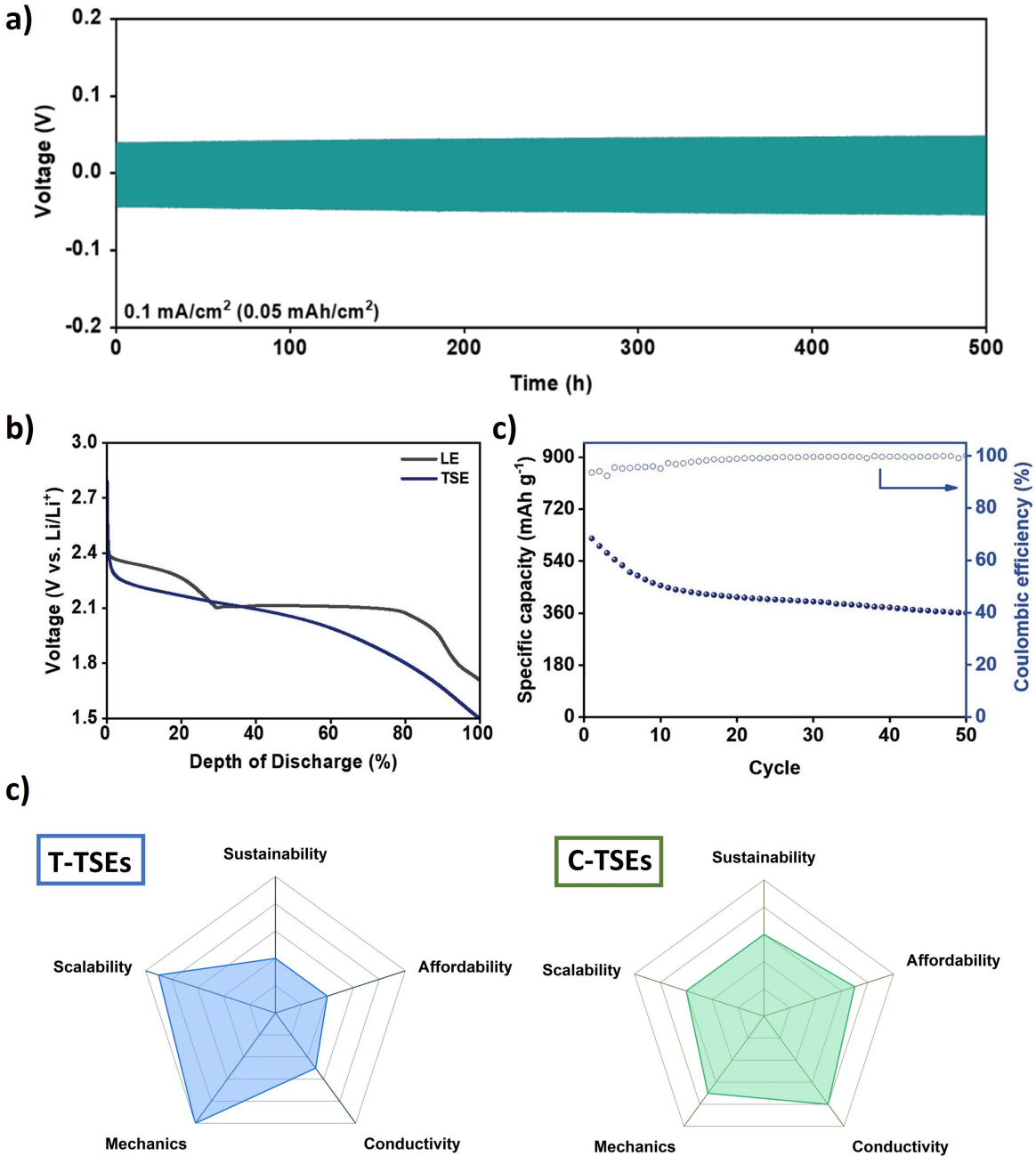

Figure 6.8: a) Cycling of a symmetric Li|Li cell at 0.1 mA cm^{-2} at 30°C. b) First cycle discharge curve of Li-S cell employing a liquid electrolyte and our C5-200 TSE. c) Discharge specific capacity and CE of Li-S cell employing C5-200 TSE. c) Comparison of the main characteristics of tape-casted and calendered TSEs. Readapted with permission from [300].

7. Final remarks:

Throughout this work, two different categories of electrolytes have been presented: nanocomposite polymer electrolytes, composed by a polymer matrix encompassing specifically designed inorganic fillers, and TSEs based on argyrodites sulfide electrolytes in which a small content of polymer binder is introduced in order to facilitate processability. Both approaches have demonstrated their capability of improving the properties of solid state electrolytes, enabling stable cycling in LMBs.
In particular, the first part of my thesis project was devoted to the development of tailored fillers for the fabrication of nanocomposite SSEs. Hybrid NPs formed by silicon dioxide covered with short chains of PEG greatly improved the compatibility of our fillers with the polymer matrix composed of PEO (*Sec. 5.1*). In this way, it resulted possible to encompass higher amounts of ceramic materials (up to 23 wt%) without experiencing any extent filler aggregation. When compared to the PEO electrolyte with no filler, the SSE containing an 18 wt% of NPs demonstrated a higher ionic conductivity at RT and a comparable one at 70°C. Additionally, this nanocomposite SSEs resulted able to deliver specific capacity in the order of 150 mAh g_{-1} in a LFP LMB and to sustain more than 350 hours of continuous stripping/plating operation at 70°C confirming the ability of the hybrid fillers in slowing down the dendrite growth. Interestingly, a peculiar behavior was also observed: after having experienced a dendrite-induced short-circuit, some of the cells were able to autonomously restart their cycling unaffected.
Considering that an analogue phenomenon was also detected in similar systems based on hybrid TiO_2-PEG fillers, in *Sec. 5.2* it was decided to deeply characterize this latter SSE in order to clarify the self-healing behaviour. The reactivity of fillers with lithium was preliminarily investigated in order to understand if a chemical reaction between the high loadings of titania present in the nanocomposite SSEs and dendrites could be responsible for the disruption of the short-circuit. The extent of lithiation appeared negligible into the SSE, therefore disproving any chemical interaction between fillers and dendrites. Tensile testing and subsequent TD-NMR analyses proved instead that the presence of the grafted PEG on the surface of NPs greatly improved the mechanical properties of the SSEs and induced the formation of a physically crosslinked network established between grafted chains and polymer matrix. Consequently, the electrolyte possessed both a satisfying stiffness and an elevated chain mobility also on the microscopic scale, otherwise not achieved in purely polymeric systems. The synergic action of these two features caused the breakage of the dendrites, relocated as dead lithium into the electrolyte, therefore leading to the restart of the cell. Even if a similar self-healing approach appears difficultly applicable on larger scale due to a continuous lithium consumption, these results confirmed the major improvements that can be achieved in homogenous nanocomposite SSEs based on hybrid fillers.
However, even if the addition of fillers improved the performances of SSEs, the room tem-

perature ionic conductivity of PEO-based electrolyte still remained way below the one of liquid electrolytes. For this reason, it was decided to include in my project also other polymers able to ensure a faster ionic conduction such as PVdF (*Sec. 5.3*). After having selected the best performing polymer, a PVdF-HFP copolymer presenting satisfying ionic conductivity and good casting properties, different drying procedures were tested in order to understand better the effect of the solvent on the electrochemical properties. As already reported in similar systems, the presence of residual DMF resulted critical for the ionic conduction: mild drying conditions endowed high RT ionic conductivity larger than 10^{-4} S cm^{-1}). The presence of residual DMF, strongly interacting with Li+ cations and present in a bound state rather than as free solvent, was also confirmed with the help of other characterization techniques such as NMR, Raman, DFT, and IR spectroscopy. Despite containing non negligible amounts of solvents, all the SSEs (or QSEs) resulted self-standing, easy to handle and possessed a solid appearance. Subsequently, also hybrid fillers were encompassed into the previously studied PVdF-HFP electrolytes. SiO_2@PEG fillers similar to the one described before were encompassed with the hope to add a second conductive path, assisted by PEG chains, in addition to the one enabled by the presence of residual DMF. SiO_2@PEG750 demonstrated a capability of increasing the DMF retention which induced better cycling properties and improved ionic conductivity of the resulting QSEs, that additionally proved to be safe and stable.
Finally, the last project included in my PhD thesis partially reversed the previous paradigm. Rather than including moderate loadings of ceramic materials into a polymer SSE to improve its otherwise mediocre mechanical and electrochemical properties at RT, an antipodal approach can be employed adding a small amount of polymer in an inorganic solid electrolyte (ISE). During the exchange period spent at the University of Oxford I had the opportunity to study TSEs based on Li_6PS_5Cl, a sulfide material well known for its appealingly high RT ionic conductivity. Two different industrially relevant processes were selected and investigated in *Chap. 6*: tape-casting and roll-to-roll calendering. Variable densification pressures were applied to reduce the porosity of the resulting electrolytes and their effect on the TSEs' morphological, mechanical, and electrochemical properties was determined. Different binder loading (5-10-20 wt%) were also tested in order to determine the optimal trade off between electrochemical and mechanical properties. Higher elasticity, coupled with an improved tensile modulus, was achieved for the sample produced with tape casting while calendered TSEs displayed higher RT ionic conductivity (10^{-4} S cm^{-1}) also at low stack pressure (2.5 MPa).
In conclusion, several different approaches have been investigated as feasible techniques to improve the performance of SSEs. Particular attention has been devoted to the possibility of decoupling the mechanical and the electrochemical properties of the electrolyte, in order to be able to effectively combine stiff ceramic materials with flexible polymers. For nanocomposite SSEs, the dispersion of inert hybrid fillers into a conductive polymer matrix has enabled the fabrication of more stable electrolytes demonstrating a satisfying stability against lithium dendrites due to an improved tensile modulus and an improved chain mobility. On the other hand, small contents of rubbery binder rendered feasible the fabrication of more processable and compliant TSEs base on sulfide electrolytes, overcoming the limitations related to highly conductive but brittle ISEs. Hopefully, similar systems will be able to favour a rapid implementation of safe and performant all-solid-state batteries in key sectors of our nowadays lives.

Ringraziamenti:

I am sorry to all the non-native Italian speakers since I am about to write the personal acknowledgments in my mother tongue in order to be able to express better my feelings. Don't worry, you are not losing anything as interesting as the previous 134 pages of battery science.
Prima di tutto, vorrei ringraziare sinceramente il Prof. Ruffo per avermi fatto da supervisor nel corse di questi tre anni (e tre mesi) oltre che nel corso della mia laurea triennale e magistrale. In tutto questo periodo ho avuto l'opportunità non affatto scontata di svolgere il mio lavoro in maniera stimolante ed indipendente ma con la possibilità di confrontarmi sempre in casi di dubbi o problemi.
Vorrei poi ringraziare anche il Prof. Mustarelli, con cui ho spesso collaborato nella stesura di lavori nel corso del mio dottorato, e il Prof. Pasta, che mi ha ospitato nel suo gruppo di ricerca durante il mio periodo ad Oxford.
Questi tre anni non sarebbero stati altrettanto produttivi (?) e piacevoli (!) senza la compagnia del gruppo di elettrochimica. Tra aperitivi, collaborazioni, sfide a Geotastic e tanta, troppa manutenzione alle glove box avete reso tutto questo lavoro meno pesante e più divertente. Devo anche ringraziare tutti i tesisti che ho seguito nel corso di questi anni e che hanno contribuito al mio progetto con il loro lavoro. Un ringraziamento particolare tocca a Nicholas ed Eleonora (messi in quest'ordine in modo da compensare la prolungata assenza di una scatola personale per uno dei due soggetti) che hanno avuto la doppia sfortuna di lavorare con me non solo nel corso del loro progetto di tesi ma anche durante il dottorato. Dopo essere sopravvissuti a polimeri arancioni, test di fiamma, rapidissime analisi TD-NMR e al PVdF nella sua interezza mi auguro che riusciranno a portare avanti certe inestinguibili tradizioni anche dopo la mia sparizione.
Devo poi anche ringraziare tutti i membri del gruppo di ricerca di Oxford, che mi hanno accolto con amicizia nei nove mesi trascorsi in Regno Unito. Il modo in cui Giulia, Shoban, Max, Yvonne, Lorenz e gli altri mi hanno invitato alle lore feste e reso parte del loro gruppo è stato davvero importante in quel periodo trascorso in un ambiente nuovo e differente quindi thank you all guys!
Anche se non direttamente coinvolti nelle dinamiche del dottorato, devo sicuramente ringraziare anche tutti i miei amici e la mia famiglia che mi hanno dato compagnia e supporto nel corso di questi tre anni abbondanti.
Infine un ringraziamento va anche a Giulia che si è sorbita i miei resoconti giornalieri giorno per giorno sull'attività di laboratorio, le prove delle mie presentazioni e tutti i miei dubbi sulla grafica dei Powerpoint. Senza di lei le mie slide, così come le mie giornate, sarebbero state molto più brutte.

A. Appendix A: abbreviation list:

- ACN: acetonitrile
- AGG: aggregate
- AIMD: ab-initio molecular dynamics
- APTES: (3-aminopropyl) triethoxysilane
- ARC: accelerated rate calorimetry
- ASEI: artificial SEI
- ASSB: all solid-state battery
- ATR: attenuated total reflectance
- BET: Brunauer-Emmett-Teller
- BEV: battery-powered EV
- CIP: contact-ion pair
- CCD: critical current density
- CE: coulombic efficiency
- CV: cyclic voltammetry
- DES: deep eutectic solvent
- DFT: density functional theory
- DLS: dynamic light scattering
- DMF: N,N-Dimethylformamide
- DSC: differential scanning calorimetry
- EC: ethylene carbonate
- EDX: energy dispersive X-ray spectroscopy
- EPR: electron paramagnetic resonance
- ESW: electrochemical stability window
- EtOH: ethanol
- EV: electric vehicle
- FEC: fluoroethylene carbonate
- FID: free induction decay
- FTIR: Fourier transform infrared spectroscopy
- GCPL: galvanostatic cycling with potential limitations
- GHG: greenhouse gases
- GPE: gel polymer electrolyte
- HBA: hydrogen-bond acceptor
- HBD; hydrogen-bond donor
- HFP: hexafluoropropylene
- HVS: high-voltage spinel
- ICE: internal-combustion engine
- IEA: International Energy Agency
- IL: ionic liquids
- IRENA: International Renewable Energy Agency
- ISE: inorganic solid electrolyte
- LE: liquid electrolyte
- LFP: lithium iron phosphate
- LIB: lithium-ion battery
- LMB: lithium-metal battery
- LPSCl: Li_6PS_5Cl
- LSV: linear sweep voltammetry
- MAc: N-methylacetamide
- MQ-NMR: multiple quantum NMR
- NBR: nitrile butadiene rubber
- NMC: Li-Ni-Mn-Co oxide
- NMP: N-methyl-2-pyrrolidone
- NMR: nuclear magnetic resonance
- NP: nanoparticle
- NZE: net zero emission
- PC: propylene carbonate
- PDF: pair distribution function
- PEIS: potentiostatic electrochemical impedance spectroscopy
- PEG: polyethylene glycol
- PEO: polyethylene oxide
- PFIB: plasma focused ion beam
- PHEV: plug-in hybrid EV

- PTFE: poly tetrafluoroethylene
- PV: photovoltaic
- PVdF: polyvinylidene fluoride
- QSE: quasi-solid electrolyte
- RE: renewable energies
- RT: room temperature
- SA: succinic anhydride
- SEI: solid-electrolyte interface
- SEM: scanning electron microscopy
- SHE: standard hydrogen electrode
- SPE: solid polymer electrolyte
- SS: stainless steel
- SSA: specific surface area
- SSE: solid state electrolyte
- TD-NMR: time dependant NMR
- TEM: transmission electron microscopy
- TEA: triethylamine
- TEOS: tetraethyl orthosilicate
- TFA: 2,2,2-trifluoroacetamide
- TGA: thermogravimetric analysis
- THF: tetrahydrofuran
- TM: tensile modulus
- TSE: thin-solid electrolyte
- UTS: ultimate tensile strength
- VTF: Vogel-Tamman-Fulcher
- WiSE: water-in-salt electrolyte
- XNBR: carboxylated NBR
- XPS: X-ray photoelectron spectroscopy
- XRD: x-ray diffraction

Bibliography

1. IEA. *World Energy Outlook 2021* (International Energy Agency, Paris, 2021).
2. Shukla, P. R. *et al. Climate Change 2022: Mitigation of Climate Change. Contribution of Working Group III to the Sixth Assessment Report of the Intergovernmental Panel on Climate Change* (Intergovernmental Panel on Climate Change, Cambridge, 2022).
3. IRENA. *World Energy Transitions Outlook 2022: 1.5°C Pathway* (Internationl Renewable Energy Agency, Abu Dhabi, 2022).
4. BP. *BP Energy Outlook - 2022 edition* (BP p.l.c., London, 2022).
5. Ritchie, H., Roser, M. & Rosado, P. Energy. *Our World in Data*. https://ourworldindata.org/energy (2020).
6. Olkuski, T. *et al.* Primary energy consumption in selected EU Countries compared to global trends. *Open Chemistry* **24,** 503–510 (2021).
7. Global Carbon Project. *Global Carbon Atlas 2022* `https://www.globalcarbonproject.org/index.htm`. Dec. 2022.
8. Jones, D. *et al. Global electricity review 2022* (Ember, 2022).
9. Mo, J. *et al.* The role of national carbon pricing in phasing out China's coal power. *iScience* **24,** 102655 (2021).
10. McKerracher, C. *et al. Electric Vehicle Outlook 2022* (Bloomberg, New York, 2022).
11. Mo, T. *et al.* Trends and Emerging Technologies for the Development of Electric Vehicles. *Energies* **15,** 6271 (2022).
12. Dhir, S. *et al. Global EV Outlook 2022: securing supplies for an electric future* (IEA, Paris, 2022).
13. Dimitropoulos, A., Rietveld, P. & Van Ommeren, J. N. Consumer valuation of changes in driving range: A meta-analysis. *Transportation Research Part A* **55,** 27–45 (2013).
14. Neubauer, J. & Wood, E. The impact of range anxiety and home, workplace, and public chying infrastructure on simulated battery electric vehicle lifetime utility. *J. Power Sources* **257,** 12–20 (2014).
15. Konig, A. *et al.* An Overview of Parameter and Cost for Battery Electric Vehicles. *World Electr. Veh. J* **12,** 21 (2021).
16. Borlaug, B. *et al.* Levelized Cost of Charging Electric Vehicles in the United States. *Joule* **4,** 1470–1485 (2020).
17. Liu, Z. *et al.* Comparing total cost of ownership of battery electric vehicles and internal combustion engine vehicles. *Energy Policy* **158,** 112564 (2021).
18. United Nations. *Paris Agreement* (United Nations Climate Change Conference, Paris, 2015).

19. Shahabuddin, M. *et al.* A critical review on the development and challenges of concentrated solar power technologies. *Sustain. Energy Technol. Assess.* **47,** 101434 (2021).

20. Chen, C., Yang, Z. & Hu, G. Signalling the cost of intermittency: What is the value of curtailed renewable power? *J. Cleaner Prod.* **302,** 126998 (2021).

21. Outcalt, C. *"Hydropower production down 20% as the Upper Colorado River system finished water year 2022."* The Colorado Sun. Oct. 2022.

22. Weiss, S. *"Swiss hydropower prepares for future energy shortage."* SwissInfo.ch. Sept. 2022.

23. Wiatros-Motyka, M. *et al. Global Electricity Mid-Year Insights 2023* (Ember, 2023).

24. Tae, D.-H. *et al.* Estimation Method of Greenhouse Gas Reduction for Electrical Energy Storage Based on Load-Leveling Application. *Energies* **14,** 5492 (2021).

25. Siebenhofer, M., Ajanovic, A. & Haas, R. How Policies Affect the Dissemination of Electric Passenger Cars Worldwide. *Energies* **14,** 2093 (2021).

26. Eftekhari, A. Lithium Batteries for Electric Vehicles: From Economy to Research Strategy. *ACS Sustainable Chem. Eng.* **7,** 5602–5613 (2019).

27. European Commission. *Batteries Europe: Strategic Research Agenda for Batteries 2020* (European Technology and Innovation Platform on Batteries – Batteries Europe, 2020).

28. Kwade, A. *et al.* Current status and challenges for automotive battery production technologies. *Nat. Energy* **3,** 290–300 (2018).

29. Yu, X. & Manthiram, A. Sustainable Battery Materials for Next-Generation Electrical Energy Storage. *Adv. Energy Sustainability Res.* **2,** 2000102 (2021).

30. Zhao, Y. *et al.* A Review on Battery Market Trends, Second-Life Reuse, and Recycling. *Sustain. Chem.* **2,** 167–205 (2021).

31. Global Market Insights. *Lithium-Ion Battery Market Size by Chemistry, by Component , by Application.* (Global Market Insights, 2020).

32. Pillot, C. *EU battery demand and supply (2019-2030) in a global context* (Avicenne Energy, Paris, 2020).

33. Frith, J. T. *et al.* A non-academic perspective on the future of lithium-based batteries. *Nat. Comm.* **14,** 420 (2023).

34. IEA. *Global EV Outlook 2023* (IEA, Paris, 2023).

35. Ziegler, M. S. & Trancik, J. E. Re-examining rates of lithium-ion battery technology improvement and cost decline. *Energy Environ. Sci.* **14,** 1635–1651 (2021).

36. Goodenough, J. B. & Park, K. S. The Li-Ion Rechargeable Battery: A Perspective. *J. Am. Chem. Soc.* **135,** 1167–1176 (2013).

37. Li, M. *et al.* 30 Years of Lithium-Ion Batteries. *Adv. Mater.* **30,** 1800561 (2018).

38. Lewis, G. N. & Keyes, F. G. The potential of lithium electrode. *J. Am. Chem. Soc.* **4,** 340–344 (1913).

39. Whittingham, M. S. Electrical Energy Storage and Intercalation Chemistry. *Science* **192,** 1126–1127 (1976).

40. Laman, F. C. Effect of discharge current on cycle life of a rechargeable lithium battery. *J. Power Sources* **24,** 195 (1988).

41. Mizushima, K. *et al.* LixCoO2 (0<x<1): A new cathode material for batteries of high energy density. *Solid State Ion.* **3/4,** 171–174 (1981).

42. Lazzari, M. & Scrosati, B. A Cyclable Lithium Organic Electrolyte Cell Based on Two Intercalation Electrodes. *J. Electrochem. Soc.* **127,** 773 (1980).

43. Besenhard, J. O. The electrochemical preparation and properties of ionic alkali metal-and NR4-graphite intercalation compounds in organic electrolytes. *Carbon* **14,** 2 (1976).

44. Yoshino, A. The Birth of the Lithium-Ion Battery. *Angew. Chem. Int. Ed.* **51,** 5798 (2012).

45. Yoshino, A *et al. pat.* USP4,668,595 (1985).

46. Xie, J. & Lu, Y.-C. A retrospective on lithium-ion batteries. *Nat. Comm.* **11,** 2499 (2020).

47. Xu, K. Nonaqueous Liquid Electrolytes for Lithium-Based Rechargeable Batteries. *Chem. Rev.* **104,** 4303–4418 (2004).

48. Peled, E. *et al.* Advanced model for solid electrolyte interphase electrodes in liquid and polymer electrolytes. *J. Electrochem. Soc.* **144,** L208 (1997).

49. Deng, J. *et al.* Electric Vehicles Batteries: Requirements and Challenges. *Joule* **4,** 509–515 (2020).

50. Yang, C. Running battery electric vehicles with extended range: Coupling cost and energy analysis. *Appl. Energy* **306,** 118116 (2022).

51. Li, M. & Lu, J. Cobalt in lithium-ion batteries. *Science* **367,** 979–980 (2020).

52. Sovacool, B. K. The precarious political economy of cobalt. *Extr. Ind. Soc.* **6,** 915–939 (2019).

53. Ryu, H.-H. *et al.* Reducing cobalt from lithium-ion batteries for the electric vehicle era. *Energy Environ. Sci.* **14,** 844 (2021).

54. Zuo, X. *et al.* Silicon based lithium-ion battery anodes: A chronicle perspective review. *Nano Energy* **31,** 113–143 (2017).

55. Gonzales, A. F. *et al.* Silicon Anode Design for Lithium-Ion Batteries: Progress and Perspectives. *J. Phys. Chem. C* **121,** 27775–27787 (2017).

56. Li, P. *et al.* Diverting Exploration of Silicon Anode into Practical Way: A Review Focused on Silicon-Graphite Composite for Lithium Ion Batteries. *Energy Storage Mater.* **35,** 550–576 (2021).

57. Lain, J. M. *et al.* Design strategies for high power vs. High energy lithium ion cells. *Batteries* **5,** 64 (2019).

58. Gardner, G. *"Group14 Technologies Raises $400 From Porsche-Led Investor Group"* Forbes. June 2022.

59. TeslaInc. *2020 Annual Meeting of Stockholders* (Tesla Inc, Fremont, CA, 2020).

60. Lin, D., Liu, Y. & Cui, Y. Reviving the lithium metal anode for high-energy batteries. *Nat. Nanotechnol.* **12,** 194–206 (2017).

61. Li, B., Wang, Y. & Yang, S. A Material Perspective of Rechargeable Metallic Lithium Anodes. *Adv. Energy Mater.* **8,** 1702296 (2018).

62. Guo, Y. *et al.* Reviving Lithium-Metal Anodes for Next-Generation High-Energy Batteries. *Adv. Mater.* **29,** 1700007 (2017).

63. Yuan, H. *et al.* A review of concepts and contributions in lithium metal anode development. *Materials Today* **53,** 173–196 (2022).

64. Wang, Q. *et al.* Thermal runaway caused fire and explosion of lithium ion battery. *Journal of Power Sources* **208,** 210–224 (2012).

65. Cheng, X. B. *et al.* Toward Safe Lithium Metal Anode in Rechargeable Batteries: A Review. *Chem. Rev.* **117,** 10403–10473 (2017).

66. Dienemann, L. L. *et al.* Understanding Lithium Dendrite Suppression by Hybrid Composite Separators: Indentation Measurements Informed by Operando X-ray Computed Tomography. *ACS Appl. Mater. Interfaces* **15,** 8492–8501 (2023).

67. Zhang, X. & Sun, C. Recent advances in dendrite-free lithium metal anodes for high-performance batteries. *Phys. Chem. Chem. Phys.* **24,** 19996 (2022).

68. Kasse, R. M. *et al.* Understanding additive controlled lithium morphology in lithium metal batteries. *J. Mater. Chem. A* **8,** 16960–16971 (2020).

69. Kasse, R. M. *et al.* Lithium cyano Tris (2, 2, 2-trifluoroethyl) borate as a multifunctional electrolyte additive for high-performance lithium metal batteries. *ACS Energy Lett.* **6,** 3851–3857 (2021).

70. Surace, Y. *et al.* Evidence for stepwise formation of solid electrolyte interphase in a Li-ion battery. *Energy Storage Mater.* **44,** 156–167 (2022).

71. Phiri, I. *et al.* Synergistic Effect of a Dual-Salt Liquid Electrolyte with a LiNO3 Functional Additive toward Stabilizing Thin-Film Li Metal Electrodes for Li Secondary Batteries. *ACS Appl. Mater. Interfaces* **13,** 31605–31613 (2021).

72. Ding, F. *et al.* Dendrite-Free Lithium Deposition via Self-Healing Electrostatic Shield Mechanism. *J. Am. Chem. Soc.* **135,** 4450–4456 (2013).

73. Ding, F. *et al.* Effects of Cesium Cations in Lithium Deposition via Self-Healing Electrostatic Shield Mechanism. *J. Phys. Chem. C* **118,** 4043–4049 (2014).

74. Yu, J. *et al.* Smart construction of multifunctional Li1.5Al0.5Ge1.5(PO4)3|Li intermediate interfaces for solid-state batteries. *Energy Storage Mater.* **46,** 68–75 (2022).

75. Chang, C. *et al.* Self-healing single-ion-conductive artificial polymeric solid electrolyte interphases for stable lithium metal anodes. *Nano Energy* **93,** 106871 (2022).

76. Zhou, H. *et al.* Protective coatings for lithium metal anodes: Recent progress and future perspectives. *J. Power Sources* **450,** 227632 (2020).

77. Pei, F. *et al.* Robust lithium metal anodes realized by lithiophilic 3D porous current collectors for constructing high energy density lithium-sulfur batteries. *ACS Nano* **13,** 8337–8346 (2019).

78. Zhang, Z. *et al.* In-situ growth of hierarchical N-doped CNTs/Ni Foam scaffold for dendrite-free lithium metal anode. *Energy Storage Mater.* **29,** 332–340 (2020).

79. Liu, Y. *et al.* A scalable slurry process to fabricate a 3D lithiophilic and conductive framework for a high performance lithium metal anode. *J. Mater. Chem. A* **7,** 13225–13233 (2019).

80. Herbert, D & Ulam, J. *pat.* US3043896A (1962).

81. Chen, Y. *et al.* Advances in Lithium–Sulfur Batteries: From Academic Research to Commercial Viability. *Adv. Mater.* **33,** 2003666 (2021).

82. Ji, X. *et al.* A highly ordered nanostructured carbon–sulphur cathode for lithium–sulphur batteries. *Nat. Mater.* **8,** 500–506 (2009).

83. Chen, R. *et al.* From a historic review to horizons beyond: lithium–sulphur batteries run on the wheels. *Chem. Comm.* **51,** 18–33 (2015).

84. Meyer, B. Solid allotropes of sulfur. *Chem. Rev.* **64,** 429–451 (1964).

85. Fang, R. *et al.* More Reliable Lithium-Sulfur Batteries: Status, Solutions and Prospects. *Adv. Mater.* **29,** 1606823 (2017).

86. Moon, S *et al.* Encapsulated Monoclinic Sulfur for Stable Cycling of Li–S Rechargeable Batteries. *Adv. Mater.* **25,** 6547–6553 (2013).

87. Seh, Z. W. *et al.* Sulphur–TiO2 yolk–shell nanoarchitecture with internal void space for long-cycle lithium–sulphur batteries. *Nat. Comm.* **4,** 1–6 (2013).

88. Zhang, S. Liquid electrolyte lithium/sulfur battery: Fundamental chemistry, problems, and solutions. *J. Power Sources* **231,** 153–162 (2013).

89. Quartarone, E. & Mustarelli, P. Electrolytes for solid-state lithium rechargeable batteries: recent advances and perspectives. *Chem. Soc. Rev.* **40,** 2525–2540 (2011).

90. Aurbach, D. *et al.* Design of electrolyte solutions for Li and Li-ion batteries: A review. *Electrochim. Acta* **50,** 247–254 (2004).

91. Xu, K. *et al.* Toward Reliable Values of Electrochemical Stability Limits for Electrolytes. *J. Electrochem. Soc.* **146,** 4172–4178 (1999).

92. Smart, M. C. *et al.* Electrolytes for Low-Temperature Lithium Batteries Based on Ternary Mixtures of Aliphatic Carbonates. *J. Electrochem. Soc.* **146,** 486 (1999).

93. Yuan, M. & Liu, K. Rational design on separators and liquid electrolytes for safer lithium-ion batteries. *J. Energy Chem.* **43,** 58–70 (2020).

94. Kalhoff, J. *et al.* Safer electrolytes for lithium-ion batteries: State of the art and perspectives. *ChemSusChem* **8,** 2154–2175 (2015).

95. Goodenough, J. B. & Kim, Y. Challenges for Rechargeable Li Batteries. *Chem. Mater.* **22,** 587–603 (2010).

96. Evans, J. *et al.* Electrochemical measurement of transference numbers in polymer electrolytes. *Polymer* **28,** 2324–2328 (1987).

97. Bruce, P. G. *et al.* Conductivity and transference number measurements on polymer electrolytes. *Solid State Ion.* **28-30,** 918–922 (1988).

98. Peng, L. *et al.* Unraveling the crystallinity on battery performances of chlorine-rich argyrodite electrolytes. *J. Power Sources* **520,** 230890 (2022).

99. Agrawal, R. C. & Pandey, G. P. Solid polymer electrolytes: materials designing and all-solid-state battery applications: an overview. *J. Phys. D: Appl. Phys* **41,** 223001 (2008).

100. Dehghani, E. *et al.* In Situ Dendrimer-Crosslinked Gel Polymer Electrolytes for Lithium-Ion Batteries with High Ionic Conductivity and Excellent Electrochemical Performance. *CS Appl. Polym. Mater.* **4,** 4154–4165 (2022).

101. Ratner, M. A. *et al.* Polymer Electrolytes: Ionic Transport Mechanisms and Relaxation Coupling. *MRS Bull.* **25,** 31–37 (2000).

102. Stigliano, P *et al.* Physicochemical properties of Pyr13TFSI-NaTFSI electrolyte for sodium batteries. *Electrochim. Acta* **412,** 140123 (2022).

103. Morina, R. *et al.* Nanocomposite Janus Gel Polymer Electrolytes for Lithium Metal Batteries. *Batteries* **8,** 8 (2022).

104. Qu, W. *et al.* A novel nanocomposite electrolyte with ultrastable interface boosts long life solid-state lithium metal batteries. *J. Power Sources* **484,** 229195 (2021).

105. Gu, G. Y. *et al.* Conductivity-Temperature Behavior of Organic Electrolytes. *Electrochem. Solid-State Lett.* **2,** 486 (1999).

106. Xu, K. Electrolytes and Interphases in Li-Ion Batteries and Beyond. *Chem. Rev.* **114,** 11503–11618 (2014).

107. Horowitz, Y. *et al.* Between Liquid and All Solid: A Prospect on Electrolyte Future in Lithium-Ion Batteries for Electric Vehicles. *Energy Technol.* **8,** 20000580 (2020).

108. Armand, M. *et al.* Lithium-ion batteries – Current state of the art and anticipated developments. *J. Power Sources* **479,** 228708 (2020).

109. Tarascon, J. M. & Guyomard, D. New electrolyte compositions stable over the 0 to 5 V voltage range and compatible with the Li1+xMn2O4/carbon Li-ion cells. *Solid State Ion.* **69,** 293–305 (1994).

110. Zinigrad, E. *et al.* On the thermal stability of LiPF6. *Thermochim. Acta* **438,** 184–191 (2005).

111. Eshetu, G. G. *et al.* In-depth safety-focused analysis of solvents used in electrolytes for large scale lithium ion batteries. *Phys. Chem. Chem. Phys.* **15,** 9145–9155 (2013).

112. Wang, Q. *et al.* Thermal runaway caused fire and explosion of lithium ion battery. *J. Power Sources* **208,** 210–224 (2012).

113. Diaz, L. B. *et al.* Meta-Review of Fire Safety of Lithium-Ion Batteries: Industry Challenges and Research Contributions. *J. Electrochem. Soc.* **167,** 090559 (2020).

114. Quartarone, E. & Mustarelli, P. Emerging Trends in the Design of Electrolytes for Lithium and Post-Lithium Batteries. *J. Electrochem. Soc.* **167,** 050508 (2020).

115. Recycling, E. & IT. *"The 5 Biggest Lithium Ion Battery Fires To Date"* eridirect.ch. Mar. 2022.

116. Zhang, H. *et al.* Challenges and Strategies for High-Energy Aqueous Electrolyte Rechargeable Batteries. *Angew. Chem. Int. Ed.* **60,** 598–616 (2021).

117. Khalid, S. *et al.* Use of Water-In-Salt Concentrated Liquid Electrolytes in Electrochemical Energy Storage: State of the Art and Perspectives. *Batteries* **9,** 47 (2023).

118. Wang, Y. *et al.* Recent Progress in Aqueous Lithium-Ion Batteries. *Adv. Energy Mater.* **2,** 830–840 (2012).

119. Forero-Saboya, J. *et al.* Water-in-Bisalt Electrolyte with Record Salt Concentration and Widened Electrochemical Stability Window. *J. Phys. Chem. Lett.* **10,** 4942–4946 (2019).

120. Nilsson, V. *et al.* Critical evaluation of the stability of highly concentrated LiTFSI - Acetonitrile electrolytes vs. graphite, lithium metal and LiFePO4 electrodes. *J. Power Sources* **384,** 334–341 (2018).

121. Suo, L. *et al.* "Water-in-salt"electrolyte enables high-voltage aqueous lithium-ion chemistries. *Science* **350,** 938–943 (2015).

122. Yamada, Y. *et al.* Hydrate-melt electrolytes for high-energy-density aqueous batteries. *Nat. Energy* **1,** 16129 (2016).

123. Balducci, A. *et al.* in. Chap. 1, Ionic Liquids II (Springer, 2018).

124. Montanino, M. *et al.* Physical and electrochemical properties of binary ionic liquid mixtures: (1-x) PYR14TFSI-(x) PYR14IM14. *Electrochim. Acta* **60,** 163–169 (2012).

125. Zheng, Y. *et al.* Ionic Liquid Electrolytes for Next-generation Electrochemical Energy Devices. *EnergyChem* **4,** 100075 (2022).

126. Tang, X. *et al.* Recent development of ionic liquid-based electrolytes in lithium-ion batteries. *J. Power Sources* **542,** 231792 (2022).

127. Ethekari, A. *et al.* Different roles of ionic liquids in lithium batteries. *J. Power Sources* **334,** 221–239 (2016).

128. Ma, D. *et al.* Synergistic effect of functionalized ionic liquid and alkanolamines mixed solution on enhancing the mass transfer of CO2 absorption in microchannel. *Chem. Eng. J.* **417,** 129302 (2021).

129. Galinski, M. *et al.* Ionic liquids as electrolytes. *Electrochim. Acta* **51,** 5567–5580 (2006).

130. Bhowmick, S. *et al.* Ambient temperature liquid salt electrolytes. *Chem. Comm.* **59,** 2620 (2023).

131. Eshetu, G. G. *et al.* Ionic liquids as tailored media for the synthesis and processing of energy conversion materials. *Energy Environ. Sci.* **9,** 49 (2016).

132. Smith, E. L. *et al.* Deep Eutectic Solvents (DESs) and Their Applications. *Chem. Rev.* **114,** 11060–11082 (2014).

133. Wu, J. *et al.* Deep Eutectic Solvents for Boosting Electrochemical Energy Storage and Conversion: A Review and Perspective. *Adv. Funct. Mater.* **31,** 2011102 (2021).

134. Abranches, D. O. *et al.* Phenolic hydrogen bond donors in the formation of non-ionic deep eutectic solvents: the quest for type V DES. *Chem. Commun.* **55,** 10253–10256 (2019).

135. Abbott, A. P. *et al.* Novel solvent properties of choline chloride/urea mixtures. *Chem. Commun.* **1,** 70–71 (2003).

136. Gregg, C. R. *et al.* Impacts of Increasing Additions of Choline Chloride on Growth Performance and Carcass Characteristics of Broiler Chickens Reared to 66 Days of Age. *Animals* **12,** 1808 (2022).

137. Hansen, B. B. *et al.* Deep Eutectic Solvents: A Review of Fundamentals and Applications. *Chem. Rev.* **121,** 1232–1285 (2021).

138. Yang, D. *et al.* Efficient Absorption of SO2 by EmimCl-EG Deep Eutectic Solvents. *ACS Sustainable Chem. Eng.* **5,** 6382–6386 (2017).

139. Song, Z. *et al.* Systematic Screening of Deep Eutectic Solvents as Sustainable Separation Media Exemplified by the CO2 Capture Process. *ACS Sustainable Chem. Eng.* **81,** 8741–8751 (2020).

140. Pätzold, M. *et al.* Deep Eutectic Solvents as Efficient Solvents in Biocatalysis. *Trends Biotechnol.* **37,** 943–959 (2019).

141. Morrison, H. G. *et al.* Characterization of Thermal Behavior of deep eutectic Solvents and their Potential as Drug Solubilization Vehicles. *Int. J. Pharm.* **378,** 136–139 (2019).

142. Mamajanov, I. *et al.* DNA and RNA in Anhydrous Media: Duplex, Triplex, and G-Quadruplex Secondary Structures in a Deep Eutectic Solvent. *Angew. Chem. Int. Ed.* **49,** 6310–6314 (2010).

143. Kumar, A. K. *et al.* Natural deep eutectic solvent mediated pretreatment of rice straw: bioanalytical characterization of lignin extract and enzymatic hydrolysis of pretreated biomass residue. *Environ. Sci. Pollut. Res.* **23,** 9265–9275 (2016).

144. Millia, L. *et al.* Bio-inspired choline chloride-based deep eutectic solvents as electrolytes for lithium-ion batteries. *Solid State Ion.* **323,** 44–48 (2018).

145. Boisset, A. *et al.* Deep eutectic solvents based on N-methylacetamide and a lithium salt as suitable electrolytes for lithium-ion batteries. *Phys. Chem. Chem. Phys.* **15** (2013).

146. Jaumaux, P. *et al.* Deep-Eutectic-Solvent-Based Self-Healing Polymer Electrolyte for Safe and Long-Life Lithium-Metal Batteries. *Angew. Chem. Int. Ed.* **59,** 9134–9142 (2020).

147. Li, Z. *et al.* Deep eutectic solvent-immobilized PVDF-HFP eutectogel as solid electrolyte for safe lithium metal battery. *Mater. Chem. Phys.* **267** (2021).

148. Dinh, T. T. A. *et al.* Deep Eutectic Solvent Based on Lithium Bis[(trifluoromethyl)sulfonyl] Imide (LiTFSI) and 2,2,2-Trifluoroacetamide (TFA) as a Promising Electrolyte for a High Voltage Lithium-Ion Battery with a LiMn2O4Cathode. *ACS Omega* **5,** 23843–23853 (2020).

149. Mezzomo, L. *et al.* Deep eutectic solvent electrolytes based on trifluoroacetamide and LiPF6 for Li-metal batteries. *J. Power Sources* **561,** 232746 (2023).

150. Lv, F. *et al.* Challenges and development of composite solid-state electrolytes for high-performance lithium ion batteries. *J. Power Sources* **441,** 227175 (2019).

151. Janek, J. & Zeier, W. G. A solid future for battery development. *Nat. Energy* **1,** 16141 (2016).

152. Xia, S. *et al.* Practical Challenges and Future Perspectives of All-Solid-State Lithium-Metal Batteries. *Chem* **5,** 753–785 (2019).

153. Pasta, M. *et al.* 2020 roadmap on solid-state batteries. *J. Phys. Energy* **2,** 032008 (2020).

154. Wright, P. V. *et al.* Complexes of alkali metal ions with poly (ethylene oxide). *Polymers* **14,** 589 (1973).

155. Armand, M. B. *et al. Fast Ion Transport in Solids* (Elsevier, New York, USA, 1979).

156. Sashmitha, K. & Rani, M. U. A comprehensive review of polymer electrolyte for lithium-ion battery. *Polym. Bull.* **80,** 89–135 (2022).

157. Quartarone, E. *et al.* PEO-based composite polymer electrolytes. *Solid State Ion.* **110,** 1–14 (1998).

158. Arya, A. & Sharma, A. Insights into the use of polyethylene oxide in energy storage/conversion devices: a critical review. *J. Phys. D: Appl. Phys.* **50,** 443002 (2017).

159. Rosso, M. *et al.* Dendrite short-circuit and fuse effect on Li/polymer/Li cells. *Electrochim. Acta* **51,** 5334–5340 (2006).

160. Tikekar, M. D. *et al.* Design principles for electrolytes and interfaces for stable lithium-metal batteries. *Nat. Energy* **1,** 16114 (2016).

161. Jiang, J. *et al.* Development of the PEO Based Solid Polymer Electrolytes for All-Solid State Lithium Ion Batteries. *Polymers* **10,** 1237 (2018).

162. Arya, A & Sharma, A. L. A glimpse on all-solid-state Li-ion battery (ASSLIB) performance based on novel solid polymer electrolytes: a topical review. *J. Mater. Sci.* **55,** 6242–6304 (2020).

163. Bao, J. *et al.* Polycarbonate-based polyurethane as a polymer electrolyte matrix for all-solid-state lithium batteries. *J. Power Sources* **389,** 84–92 (2018).

164. Tran, H. K. *et al.* Composite Polymer Electrolytes Based on PVA/PAN for All-Solid-State Lithium Metal Batteries Operated at Room Temperature. *ACS Appl. Energy* **3,** 11024–11035 (2020).

165. Cheng, X. *et al.* Gel Polymer Electrolytes for Electrochemical Energy Storage. *Adv. Energy Mater.* **8,** 1702184 (2018).

166. Zhu, M. *et al.* Recent advances in gel polymer electrolyte for high-performance lithium batteries. *J. Energy Chem.* **37,** 126–142 (2019).

167. Sahimi, M. *Applications of Percolation Theory* (Springer, Switzerland, 2023).

168. Osaka, T. *et al.* Performances of lithium/gel electrolyte/polypyrrole secondary batteries. *J. Power Sources* **68,** 392–396 (1997).

169. Zhang, M. Y. *et al.* A Sandwich PVDF/HEC/PVDF Gel Polymer Electrolyte for Lithium Ion Battery. *Electrochim. Acta* **245,** 752–759 (2017).

170. Wu, Y. Advances and prospects of PVDF based polymer electrolytes. *J. Energy Chem.* **64,** 62–84 (2022).

171. Gregorio Jr., R. *et al.* Determination of the α, β, and γ crystalline phases of poly(vinylidene fluoride) films prepared at different conditions. *J. Appl. Polym. Sci.* **100,** 3272–3279 (2006).

172. Abbrent, S. *et al.* Crystallinity and morphology of PVdF–HFP-based gel electrolytes. *Polym.* **42,** 1407–1416 (2001).

173. Quartarone, E. *et al.* Transport properties of porous PVDF membranes. *J. Phys. Chem. B* **106,** 10828–10833 (2002).

174. Capiglia, C. *et al.* Structure and transport properties of polymer gel electrolytes based on PVdF-HFP and LiN(C2F5SO2)2. *Solid State Ion.* **131,** 291–299 (2000).

175. Kataoka, H. *et al.* Conduction Mechanisms of PVDF-Type Gel Polymer Electrolytes of Lithium Prepared by a Phase Inversion Process. *J. Phys. Chem. B* **104,** 11460–11464 (2000).

176. Zhang, X. *et al.* Synergistic coupling between Li6.75La3Zr175Ta0.25O12 and poly(vinylidene fluoride) induces high ionic conductivity, mechanical strength, and thermal stability of solid composite electrolytes. *J. Am. Chem. Soc.* **139,** 13779–13785 (2017).

177. Zhang, X. *et al.* Self-Suppression of Lithium Dendrite in All-Solid-State Lithium Metal Batteries with Poly(vinylidene difluoride)-Based Solid Electrolytes. *Adv. Mater* **31,** 1806082 (2019).

178. Callegari, D. *et al.* Is It Possible to Obtain Solvent-Free, Li+-Conducting Solid Electrolytes Based on Pure PVdF? Comment on "Self-Suppression of Lithium Dendrite in All-Solid-State Lithium Metal Batteries with Poly(vinylidene difluoride)-Based Solid Electrolytes". *Adv. Mater.* **32,** 1907375 (2020).

179. Zhang, X. *et al.* High Cycling Stability for Solid-State Li Metal Batteries via Regulating Solvation Effect in Poly(Vinylidene Fluoride)-Based Electrolytes. *Batteries Supercaps* **3,** 876–883 (2020).

180. Zhang, X. *et al.* Response to Comment on "Self-Suppression of Lithium Dendrite in All-Solid-State Lithium Metal Batteries with Poly(vinylidene difluoride)-Based Solid Electrolytes". *Adv. Mater.* **32,** 2000026 (2020).

181. Shi, K. *et al.* Solid-state polymer electrolytes with polypropylene separator-reinforced sandwich structure for room-temperature lithium ion batteries. *J. Membr. Sci.* **638,** 119713 (2021).

182. Xin, M. *et al.* Enabling high-capacity Li metal battery with PVDF sandwiched type polymer electrolyte. *J. Colloid Interface Sci.* **629,** 980–988 (2023).

183. Reddy, M. V. *et al.* Sulfide and Oxide Inorganic Solid Electrolytes for All-Solid-State Li Batteries: A Review. *Nanomaterials* **10,** 1606 (2020).

184. Ke, X. *et al.* Cell failures of all-solid-state lithium metal batteries with inorganic solid electrolytes: Lithium dendrites. *Energy Storage Mater.* **33,** 309–328 (2020).

185. Nikodimos, Y. *et al.* Chemical stability of sulfide solid-state electrolytes: stability toward humid air and compatibility with solvents and binders. *Energy Environ. Sci.* **15,** 991–1033 (2022).

186. Goodenough, J. B. *et al.* Fast Na+-ion transport in skeleton structures. *Mater. Res. Bull.* **11,** 203–220 (1976).

187. Jian, Z. *et al.* NASICON-Structured Materials for Energy Storage. *Adv. Mater.* **29,** 1601925 (2017).

188. Hou, M. *et al.* Challenges and perspectives of NASICON-type solid electrolytes for all-solid-state lithium batteries. *Nanotechnol.* **31,** 132003 (2020).

189. Hartmann, P. *et al.* Degradation of NASICON-type materials in contact with lithium metal: Formation of mixed conducting interphases (MCI) on solid electrolytes. *J. Phys. Chem. C* **117,** 21064–21074 (2013).

190. Lu, J. & Li, Y. Perovskite-type Li-ion solid electrolytes: a review. *J. Mater. Sci. Mater. Electron.* **32,** 9736–9754 (2021).

191. Yan, S. *et al.* Perovskite Solid-State Electrolytes for Lithium Metal Batteries. *Batteries* **7,** 75 (2021).

192. Zhang, S. *et al.* Characterization of Sr-doped lithium lanthanum titanate with improved transport properties. *Solid State Ion.* **336,** 39–46 (2019).

193. Hu, Z. *et al.* Enhanced Li ion conductivity in Ge-doped Li0.33La0.56TiO3 perovskite solid electrolytes for all-solid-state Li-ion batteries. *New J. Chem.* **42,** 9074–9079 (2018).

194. Thangadurai, V. *et al.* Novel Fast Lithium Ion Conduction in Garnet-Type Li5La3M2O12(M = Nb, Ta). *J. Am. Ceram. Soc.* **86,** 437–440 (2003).

195. Murugan, R. *et al.* Fast Lithium Ion Conduction in Garnet-Type Li7La3Zr2O12. *Angew. Chem. Int. Ed.* **46,** 7778–7781 (2007).

196. Jia, M. *et al.* Comprehensive Investigation into Garnet Electrolytes Toward Application - Oriented Solid Lithium Batteries. *Electrochem. Energy Rev.* **3,** 656–689 (2020).

197. Li, Q. *et al.* Challenges and perspectives of garnet solid electrolytes for all solid-state lithium batteries. *J. Power Source* **389,** 120–134 (2018).

198. Dai, J. *et al.* Interface Engineering for Garnet-Based Solid-State Lithium-Metal Batteries: Materials, Structures, and Characterization. *Adv. Mater.* **30,** 1802068 (2018).

199. Pradel, A. & Ribes, M. Electrical properties of lithium conductive silicon sulfide glasses prepared by twin roller quenching. *Solid State Ion.* **18-19,** 351–355 (1986).

200. Kanno, R. & Murayama, M. Lithium ionic conductor thio-LISICON: the Li2SGeS2P2S5 system. *J. Electrochem. Soc.* **148,** 7 (2001).

201. Lian, P.-J. *et al.* Inorganic sulfide solid electrolytes for all-solid-state lithium secondary batteries. *J. Mater. Chem. A* **7,** 20540 (2019).

202. Duan, Y. *et al.* Research progress and prospect in typical sulfide solid-state electrolytes. *J. Energy Storage* **55,** 105382 (2022).

203. Lau, J. *et al.* Sulfide Solid Electrolytes for Lithium Battery Applications. *Adv. Energy Mater.* **8,** 1800933 (2018).

204. Kamaya, N. *et al.* Sulfide Solid Electrolytes for Lithium Battery Applications. *Nat. Mater.* **10,** 682–686 (2011).

205. Ma, Z. *et al.* Recent achievements on sulfide-type solid electrolytes: crystal structures and electrochemical performance. *J. Mater. Sci.* **53,** 3927–3938 (2018).

206. Zhou, L. *et al.* Local Charge Inhomogeneity and Lithium Distribution in the Superionic Argyrodites Li6PS5X (X = Cl, Br, I). *Inorg. Chem.* **59,** 11009–11019 (2020).

207. Huang, K. J. *et al.* Manufacturing scalability implications of materials choice in inorganic solid-state batteries. *Joule* **5,** 564–580 (2021).

208. Zhou, L. *et al.* Innovative Approaches to Li-Argyrodite Solid Electrolytes for All- Solid-State Lithium Batteries. *Acc. Chem. Res* **54,** 2717–2728 (2021).

209. Yu, C. *et al.* Recent development of lithium argyrodite solid-state electrolytes for solid-state batteries: Synthesys, structure, stability and dynamics. *Nano Ener.* **83,** 3927–3938 (2021).

210. Bai, X. *et al.* Research progress in Li-argyrodite-based solid-state electrolytes. *J. Mater. Chem. A* **48,** 25663–25686 (2020).

211. Oh, D. Y. *et al.* Excellent Compatibility of Solvate Ionic Liquids with Sulfide Solid Electrolytes: Toward Favorable Ionic Contacts in Bulk-Type All-Solid-State Lithium-Ion Batteries. *Adv. Energy Mater.* **5,** 1500865 (2015).

212. Kim, K. J. *et al.* Solid-State Li–Metal Batteries: Challenges and Horizons of Oxide and Sulfide Solid Electrolytes and Their Interfaces. *Adv. Energy Mater.* **11,** 2002689 (2021).

213. Wu, J. *et al.* Reducing the thickness of solid-state electrolyte membranes for high-energy lithium batteries. *Energy Environ. Sci* **14,** 12–36 (2021).

214. Liu, S. *et al.* Filler-Integrated Composite Polymer Electrolyte for Solid-State Lithium Batteries. *Adv. Mater.* **35,** 2110423 (2023).

215. Chen, L. *et al.* PEO/garnet composite electrolytes for solid-state lithium batteries: From "ceramic-in-polymer" to "polymer-in-ceramic". *Nano Energy* **46,** 176–184 (2018).

216. Croce, F. *et al.* Physical and Chemical Properties of Nanocomposite Polymer Electrolytes. *J. Phys. Chem. B* **103,** 10632–10638 (1999).

217. Wieczorek, W. *et al.* Composite polyether based solid electrolytes. The Lewis acid-base approach. *Solid State Ion.* **85,** 67–72 (1996).

218. Croce, F. *et al.* Nanocomposite polymer electrolytes for lithium batteries. *Nature* **394,** 456–458 (1998).

219. Xi, J. *et al.* Nanocomposite polymer electrolyte comprising PEO/LiClO4 and solid super acid: effect of sulphated-zirconia on the crystallization kinetics of PEO. *Polymers* **46,** 5702–5706 (2005).

220. Fan, L. *et al.* Effect of modified SiO2 on the properties of PEO-based polymer electrolytes. *Solid State Ion.* **164,** 81–86 (2003).

221. Choi, J.-H. *et al.* Enhancement of ionic conductivity of composite membranes for all-solid-state lithium rechargeable batteries incorporating tetragonal Li7La3Zr2O12 into a polyethylene oxide matrix. *J. Power Sources* **274,** 458–463 (2015).

222. Li, Q. *et al.* Elucidating the mechanisms of ion conductivity enhancement in polymer nanocomposite electrolytes for lithium ion batteries. *Appl. Phys. Lett* **102,** 243903 (2013).

223. Parejiya, A. *et al.* Understanding slurry formulations to guide solution-processing of solid electrolytes. *J. Power Sources* **544,** 231894 (2022).

224. Wang, Y. *et al.* A thin free-standing composite solid electrolytefilm for solid-state lithium metal batteries. *Chem. Commun.* **58,** 7646 (2022).

225. Riphaus, N. *et al.* Slurry-Based Processing of Solid Electrolytes: A Comparative Binder Study. *J. Electrochem. Soc.* **165,** A3993–A3999 (2018).

226. Sedlmeier, C. *et al.* From Powder to Sheets: A Comparative Electrolyte Study for Slurry-Based Processed Solid Electrolyte/Binder-Sheets as Separators in All-Solid-State Batteries. *J. Electrochem. Soc.* **169,** 070508 (2022).

227. Lee, K. *et al.* Selection of Binder and Solvent for Solution-Processed All-Solid-State Battery. *J. Electrochem. Soc.* **164,** A2075–A2081 (2017).

228. Tron, A. *et al.* Film processing of Li6PS5Cl electrolyte using different binders and their combinations. *J. Energy Storage* **66,** 107480 (2023).

229. Walls, H. J. *et al.* Fumed silica-based composite polymer electrolytes: synthesis, rheology, and electrochemistry. *J. Power Sources* **89,** 156–162 (2000).

230. Didwal, P. N. *et al.* An advanced solid polymer electrolyte composed of poly(propylene carbonate) and mesoporous silica nanoparticles for use in all-solid-state lithium-ion batteries. *Energy Storage Mater.* **37,** 476–490 (2021).

231. Ai, S. *et al.* Nano-silica doped composite polymer chitosan/poly(ethylene oxide)-based electrolyte with high electrochemical stability suitable for quasi solid-state lithium metal batteries. *J. Electroanal.* **895,** 115464 (2021).

232. Mezzomo, L. *et al.* Composite solid-state electrolyte based on hybrid poly (ethylene glycol)-silica fillers enabling long-life lithium metal batteries. *Electrochim. Acta* **41,** 140060 (2022).

233. Scotti, R. *et al.* Shape controlled spherical (0D) and rod-like (1D) silica nanoparticles in silica/styrene butadiene rubber nanocomposites: role of the particle morphology on the filler reinforcing effect. *Polymer* **55,** 1497–1506 (2014).

234. Park, S.-J. *et al.* Influence of crystallinity on ion conductivity of PEO-based solid electrolytes for lithium batteries. *Macromol. Res.* **18,** 336–340 (2010).

235. Zardalidis, G. *et al.* Relating Structure, Viscoelasticity, and Local Mobility to Conductivity in PEO/LiTf Electrolytes. *Macromolecules* **46,** 2705–2714 (2013).

236. Bandara, L. R. A. K. *et al.* Ionic conductivity of plasticized (PEO)-LiCF3SO3 electrolytes. *Electrochim. Acta* **43,** 1447–1451 (1998).

237. Pozyczka, K. *et al.* Ionic conductivity and lithium transference number of poly(ethilene oxide):LiTFSI system. *Electrochim. Acta* **227,** 127–135 (2017).

238. Yang, X. *et al.* Determining the limiting factor of the electrochemical stability window for PEO-based solid polymer electrolytes: main chain or terminal -OH group? *Energy Environ. Sci.* **13,** 1318–1325 (2020).

239. Sun, Q. *et al.* Lithium electrochemistry of SiO2 thin film electrode for lithium-ion batteries. *Appl. Surf. Sci.* **254,** 3774–3779 (2008).

240. Liu, K. *et al.* Extending the Life of Lithium-Based Rechargeable Batteries by Reaction of Lithium Dendrites with a Novel Silica Nanoparticle Sandwiched Separator. *Adv. Mater.* **29,** 1603987 (2016).

241. Liao, C. *et al.* A flame retardant sandwiched separator coated with ammonium polyphosphate wrapped by SiO2 on commercial polyolefin for high performance safety lithium metal batteries. *Appl. Mater. Today* **21,** 100793 (2020).

242. Counihan, M. J. *et al.* The phantom menace of dynamic soft-shorts in solid-state battery research. *Joule* **8,** 1–27 (2024).

243. Colombo, F. *et al.* Polymer-in-Ceramic Nanocomposite Solid Electrolyte for Lithium Metal Batteries Encompassing PEO-Grafted TiO2 Nanocrystals. *J. Electrochem. Soc.* **167,** 070535 (2020).

244. Mezzomo, L. *Nanocomposite solid-state electrolytes for alkali-metal secondary batteries* MA thesis (University of Milano-Bicocca, 2020).

245. Mezzomo, L. *et al.* Exploiting Self-Healing in Lithium Batteries: Strategies for Next-Generation Energy Storage Devices. *Adv. Energy Mater.* **10,** 2002815 (2020).

246. Narayan, R. *et al.* Self-Healing: An Emerging Technology for Next-Generation Smart Batteries. *Adv. Energy Mater.* **12,** 2102652 (2022).

247. Mezzomo, L. *et al.* Unveiling the Role of PEO-Capped TiO2 Nanofiller in Stabilizing the Anode Interface in Lithium Metal Batteries. *Nano Lett.* **21,** 8509–8518 (2022).

248. Selli, D. *et al.* Optimizing PEGylation of TiO2 Nanocrystals through a Combined Experimental and Computational Study. *Chem. Mater.* **31,** 7531–7546 (2019).

249. Besghini, D. *et al.* Time Domain NMR in Polymer Science: From the Laboratory to the Industry. *Appl. Sci.* **9,** 1801 (2019).

250. Sudant, G. *et al.* Electrochemical lithium reactivity with nanotextured anatase-type TiO2. *J. Mater. Chem.* **15,** 1263–1269 (2005).

251. Su, X. *et al.* Advanced titania nanostructures and composites for lithium ion battery. *J. Mater. Sci.* **47,** 2519–2534 (2012).

252. Sudant, G. *et al.* Electrochemical lithium reactivity with nanotextured anatase-type TiO2. *J. Mater. Chem.* **15,** 1263–1269 (2005).

253. Liang, S. *et al.* Anatase titanium dioxide as rechargeable ion battery electrode - A chronological review. *Energy Storage Mater.* **45,** 201–264 (2022).

254. Longoni, G. *et al.* Shape-Controlled TiO2 Nanocrystals for Na-Ion Battery Electrodes: The Role of Different Exposed Crystals Facets on the Electrochemical Properties. *Nano Lett.* **17,** 992–1000 (2017).

255. Wagemaker, M. *et al.* Large Impact of Particle Size on Insertion Reactions. A Case for Anatase LixTiO2. *J. Am. Chem. Soc.* **129,** 4468–4476 (2007).

256. D'Arienzo, M. *et al.* Photogenerated Defects in Shape-Controlled TiO2 Anatase Nanocrystals: A Probe To Evaluate the Role of Crystal Facets in Photocatalytic Processes. *J. Am. Chem. Soc.* **133,** 17652–17661 (2011).

257. Lin, T. *et al.* Effective nonmetal incorporation in black titania with enhanced solar energy utilization. *Energy Environ. Sci.* **7,** 967–972 (2014).

258. Ou, G. *et al.* Tuning defects in oxides at room temperature by lithium reduction. *Nat. Comm.* **9,** 1302 (2018).

259. Tawfilas, M. *et al.* Surface Characterization of TiO2 Polymorphic Nanocrystals through 1H-TD-NMR. *Langmuir* **34,** 9460–9469 (2018).

260. Ohsaka, T. *et al.* Raman spectrum of anatase, TiO2. *J. Raman Spectrosc.* **7,** 321–324 (1978).

261. Otakar, F. *et al.* Raman spectra of titanium dioxide (anatase, rutile) with identified oxygen isotopes (16, 17, 18). *Phys. Chem. Chem. Phys.* **14,** 14567–14572 (2012).

262. Tompsett, G. A. *et al.* The Raman spectrum of brookite, TiO2 (Pbca, Z = 8). *J. Raman Spectrosc.* **726,** 57–62 (1995).

263. Sahoo, S. *et al.* Raman Line Shapes of Optical Phonons of Different Symmetries in Anatase TiO2 Nanocrystals. *J. Phys. Chem. C* **113,** 16927–16933 (2009).

264. Parker, J. C. & Siegel, R. W. Calibration of the Raman spectrum to the oxygen stoichiometry of nanophase TiO2. *Appl. Phys. Lett.* **57,** 943–945 (1990).

265. Rey, I. *et al.* Infrared and Raman study of the PEO-LiTFSI polymer electrolyte. *Electrochim. Acta* **43,** 1505–1510 (1998).

266. Hardwick, L. J. *et al.* Electrochemical lithium insertion into anatase-type TiO2: An in situ Raman microscopy investigation. *Electrochim. Acta* **52,** 5357–5367 (2007).

267. Sorrentino, A. L. *et al.* Quasi-Hexagonal to Lepidocrocite-like Transition in TiO2 Ultrathin Films on Cu(001). *J. Phys. Chem. C* **125,** 10621–10630 (2021).

268. Jackman, M. J. *et al.* Photoelectron Spectroscopy Study of Stoichiometric and Reduced Anatase TiO2(101) Surfaces: The Effect of Subsurface Defects on Water Adsorption at Near-Ambient Pressures. *J. Phys. Chem. C* **119,** 13682–13690 (2015).

269. Kim, K. S. *et al.* Charge transfer shake-up satellites in X-ray photoelectron spectra of cations and anions of SrTiO3, TiO2 and Sc2O3. *Chem. Phys. Lett.* **31,** 312–317 (1975).

270. Beamson, G. & Briggs, D. *High resolution XPS of Organic Polymers: The Scienta ESCA300 Database* (Wiley Interscience, Chichester, UK, 1979).

271. Doring, M. *et al.* Komplexbildung mit sulfonamidsubstituierten Thionoliganden. *Z. Anorg. Allg. Chem.* **563,** 105–115 (1988).

272. Fan, C. *et al.* Black Hydroxylated Titanium Dioxide Prepared via Ultrasonication with Enhanced Photocatalytic Activity. *Sci. Rep.* **5,** 1712 (2015).

273. Klongkan, S. & Pumchusak, J. Effects of the Addition of LiCF3SO3 Salt on the Conductivity, Thermal and Mechanical Properties of PEO-LiCF3SO3 Solid Polymer Electrolyte. *Int. J. Chem. Eng.* **6,** 165–168 (2015).

274. Klongkan, S. & Pumchusak, J. Effects of Nano Alumina and Plasticizers on Morphology, Ionic Conductivity, Thermal and Mechanical Properties of PEO-LiCF3SO3 Solid Polymer Electrolyte. *Electrochim. Acta* **161,** 171–176 (2015).

275. Gireaud, L. *et al.* Lithium metal stripping/plating mechanisms studies: A metallurgical approach. *Electrochem. Commun.* **8,** 1639–1649 (2006).

276. Chassé, W. *et al.* Precise dipolar coupling constant distribution analysis in proton multiple-quantum NMR of elastomers. *J. Chem. Phys.* **134,** 044907 (2011).

277. Fernandez-de Alba, C. *et al.* On the Immobilized Polymer Fraction in Attractive Nanocomposites: Tg Gradient versus Interfacial Layer. *Macromolecules* **54,** 10289–10299 (2021).

278. Counihan, M. J. *et al.* Understanding the Influence of Li7La3Zr2O12 Nanofibers on Critical Current Density and Coulombic Efficiency in Composite Polymer Electrolytes. *ACS Appl. Mater. Interfaces* **15,** 26047–26059 (2023).

279. Vallana, N. *et al.* Host-guest interactions and transport mechanism in poly(vinylidene fluoride)-based quasi solid electrolytes for lithium metal batteries. *ACS Appl. Energy Mater.* **7,** 1606–1617 (2024).

280. Carena, E. *et al.* PVDF-HFP-based quasi-solid nanocomposite electrolytes for lithium metal batteries. *Small* **In press,** 2311805 (2024).

281. Stöber, W. *et al.* Lithium metal stripping/plating mechanisms studies: A metallurgical approach. *J. Colloid Interface Sci.* **26,** 62–69 (1968).

282. Frisch, M. J. *et al. Gaussian 16, Revision C.01* Gaussian Inc. Wallingford CT. 2016.

283. Tomasi, J. *et al.* Quantum Mechanical Continuum Solvation Models. *Chem. Rev.* **105,** 2999–3093 (2005).

284. Schaftenaar, G. *et al.* A Pre-and-Post-Processing Program for Molecular and Electronic Structures. *J. Comput. Aided Mol.* **145,** 123–133 (2000).

285. He, F. *et al.* High Energy Density Solid State Lithium Metal Batteries Enabled by Sub-5 um Solid Polymer Electrolytes. *Adv. Mater.* **33,** 2105329 (2021).

286. Kerner, M. *et al.* Thermal stability and decomposition of lithium bis(fluorosulfonyl)imide (LiFSI) salts. *RSC Adv.* **6,** 23327–23334 (2016).

287. Satapathy, S. *et al.* Effect of annealing on phase transition in poly(vinylidene fluoride) films prepared using polar solvent. *Bull. Mat. Sci.* **34,** 727–733 (2011).

288. Ma, W. *et al.* Crystalline Phase Formation of Poly(vinylidene fluoride) from Tetrahydrofuran/ N,N-dimethylformamide Mixed Solutions. *J. Macromol. Sci. Phys.* **47,** 434–449 (2008).

289. Sim, L. N. *et al.* FTIR studies of PEMA/PVdF-HFP blend polymer electrolyte system incorporated with LiCF3SO3 salt. *Vib. Spectrosc.* **58,** 57–66 (2012).

290. Xu, Y. *et al.* Improved Li-Ion Conduction and (Electro)Chemical Stability at Garnet-Polymer Interface through Metal-Nitrogen Bonding. *Adv. Energy Mater.* **13,** 2204377 (2023).

291. *Kynar Flex 2751-00 specification sheet* Arkema France (2021).

292. Sawyer, J. F. *et al.* Crystal structure, Raman and multinuclear magnetic resonance study of FXEN(SO2F)2, an example of Xenon-Nitrogen bonding. *Inorg. Chem.* **21,** 207–227 (1982).

293. Stakhandske, C. M. V. *et al.* Vibrational Spectroscopic and Force Field Studies of N,N-Dimethylthioformamide, N,N-Dimethylthioformamide, their Deuterated anologues and Bis(N,N-Dimethylthioformamide) Mercury(II) Perchlorate. *Vib. Spectrosc.* **14,** 207–227 (1997).

294. Fuji, K. *et al.* Structural and Electrochemical Properties of Li Ion Solvation Complexes in the Salt-Concentrated Electrolytes Using an Aprotic Donor Solvent, N,N-Dimethylformamide. *J. Phys. Chem. C* **120,** 17196–17204 (2016).

295. Lassègues, J.-C. *et al.* Lithium solvation in bis(trifluoromethanesulfonyl)imide-based ionic liquids. *Phys. Chem. Chem. Phys.* **8,** 5629–5632 (2006).

296. Maier, M. *et al.* A comprehensive study on the ionomer properties of PFSA membranes with confocal Raman microscopy. *J. Memb. Sci.* **669,** 121244 (2023).

297. Albertus, P. *et al.* Challenges for and Pathways toward Li-Metal-Based All-Solid-State Batteries. *Nano Lett.* **6,** 1399–1404 (2021).

298. Li, C. *et al.* Designing Lithium Argyrodite Solid-State Electrolytes for High-Performance All-Solid-State Lithium Batteries. *Batteries Supercaps* **5,** e202100288 (2021).

299. Li, J. *et al.* Processing-Structure-Property Relationships in Practical Thin Solid-Electrolyte Separators for All-Solid-State Batteries. *J. Phys. Energy* **In press** (2024).

300. Kim, S. *et al.* Thin Solid Electrolyte Separators for Solid-State Lithium–Sulfur Batteries. *Nano Lett.* **22,** 10176–10183 (2022).

301. Lee, D.-J. *et al.* Physio-Electrochemically Durable Dry-Processed Solid-State Electrolyte Films for All-Solid-State Batteries. *Adv. Funct. Mater.* **33,** 2301341 (2023).

302. Li, G. *et al.* The influence of polytetrafluorethylene reduction on the capacity loss of the carbon anode for lithium ion batteries. *Solid State Ion.* **90,** 221–225 (1996).

303. Pan, P. *et al.* Garnet ceramic fabric-reinforced flexible composite solid electrolyte derived from silk template for safe and long-term stable All-Solid-State lithium metal batteries. *Energy Storage Mater.* **47,** 279–287 (2022).

304. Hegde, G. S. & Sundara, R. A flexible, ceramic-rich solid electrolyte for room-temperature sodium–sulfur batteries. *Chem. Commun.* **58,** 8794–8797 (2022).

305. Vinayasree, S. *et al.* A microwave absorber based on strontium ferrite–carbon black–nitrile rubber for S and X-band applications. *Compos. Sci. Technol.* **82,** 69–75 (2013).

306. Manna, R. & Srivastava, S. R. Fabrication of functionalized graphene filled carboxylated nitrile rubber nanocomposites as flexible dielectric materials. *Mater. Chem. Front.* **1,** 780–788 (2017).

307. Fu, S.-Y. *et al.* Effects of particle size, particle/matrix interface adhesion and particle loading on mechanical properties of particulate–polymer composites. *Compos. Part B Eng.* **39,** 933–961 (2008).

308. Vollenberg, P. H. T. & Heikens, D. Particle size dependence of the Young's modulus of filled polymers: 1. Preliminary experiments. *Polymer* **30,** 1656–1662 (1989).

309. Nasir, M. *et al.* Effect of γ-mercaptopropyltrimethoxysilane coupling agent on t90, tensile strength and tear strength of silica-filled NR, NBR and SBR vulcanizates. *Eur. Polym. J.* **24,** 961–965 (1988).

310. Fischer, S. & Brown, N. Deformation of polytetrafluoroethylene from 78 to 298 °K and the effects of environmental crazing. *J. Appl. Phys.* **44,** 4322–4327 (1973).

311. Wajge, S. & Das, C. Generating crosslinking network in XNBR based on copper (I) – carboxylate interaction. *Polym. Adv. Technol.* **34,** 998–1007 (2022).

312. Moloney, A. C. *et al.* Parameters determining the strength and toughness of particulate filled epoxide resins. *J. Mater. Sci.* **22,** 381–393 (1987).

313. Doux, J.-M. *et al.* Pressure effects on sulfide electrolytes for all solid-state batteries. *J. Mater. Chem. A.* **8,** 5049–5055 (2020).

314. Hänsel, C. & Kundu, D. The Stack Pressure Dilemma in Sulfide Electrolyte Based Li Metal Solid-State Batteries: A Case Study with Li6PS5Cl Solid Electrolyte. *Adv. Mater. Interfaces* **8,** 2100206 (2021).

315. Porz, L. *et al.* Mechanism of Lithium Metal Penetration through Inorganic Solid Electrolytes. *Adv. Energy Mater.* **7,** 1701003 (2017).